Triaxial models of massive elliptical galaxies

Fabrizio Finozzi

SIGILL · UNIVERSITAT · LUDOVIC · MAXIM

München 2018

Triaxial models of massive elliptical galaxies

Fabrizio Finozzi

Dissertation
an der Fakultät für Physik
der Ludwig–Maximilians–Universität
München

vorgelegt von
Fabrizio Finozzi
aus Legnano

München, den 30. Januar 2018

Erstgutachter: PD Dr. Roberto Saglia
Zweitgutachter: Prof. Dr. Andreas Burkert
Tag der mündlichen Prüfung: 26. Februar 2018

To my wife Federica
for her advice, her patience and her love

Zusammenfassung

Massereiche triaxiale Frühtyp-Galaxien stehen am Ende der Galaxienentwicklung und machen fast ein Drittel der leuchtstärksten Galaxien im lokalen Universum aus. Vermutlich beinhalten Sie die massereichsten Schwarzen Löcher, insbesondere die inaktiven Nachfahren der Schwarzen Löcher, welche im frühen Universum Quasare mit Energie versorgten.

Frühere Studien nahelegen, dass die Eigenschaften und die Dynamik von intrinsisch triaxialen Galaxien nicht vollständig mit achsensymmetrischen Modellen untersucht werden können. Achsensymmetrische Modelle rekonstruieren die Lage von intrinsisch triaxialen Galaxien relativ zur Sichtlinie vermutlich nicht vollständig richtig, weshalb das stellare Masse-zu-Leuchtkraft-Verhältnis bis zur Hälfte seines Wertes unterschätzt werden kann. Dies wiederum führt zu einer schlecht eingegrenzten Ursprünglichen Massenfunktion (engl. Initial Mass Function, IMF) und falschen Massen der Schwarzen Löcher.

Diese Arbeit präsentiert **SCHERPA** (**SCH**warzschild m**E**thod for t**R**iaxial early-ty**P**e g**A**laxies – Schwarzschild-Methode für triaxiale Frühtypgalaxien), eine flexible und effiziente Implementierung der orbit-basierten Schwarzschild-Methode. SCHERPA konstruiert triaxiale Modelle, die die volle Geschwindigkeitsverteilung entlang der Sichtlinie (engl. line-of-sight velocity distribution, LOSVD) realer Galaxien nachbilden. SCHERPA beinhaltet eine Software, um die beobachteten Oberflächenhelligkeitsprofile triaxial zu deprojizieren. Die Software berücksichtigt Veränderungen der Elliptizität und des Positionswinkels der grossen Halbachse als Funktion des Radius. Die sich ergebende triaxiale Leuchtkraftdichte wird interpoliert und integriert, sodass sie die Gesamtmasse der Galaxie, das Gravitationspotential und die Gravitationskräfte berechnet werden können. Die Auswahl der Anfangsbedingungen für die Bibliothek repräsentativer stellarer Orbits passt sich dem jeweiligen Gravitationspotential an. Tatsächlich ist es so, dass das Gravitationspotential von Galaxien durch die massereichen Schwarzen Löcher im Zentrum und durch die Dunkle Materie in den Außenbereichen dominiert wird. Es wurde verifiziert, dass die Methode die Masse (innerhalb von 2%) und die intrinsischen Geschwindingkeitsmomente (innerhalb von 4.5%) von realistischen sphärischen und triaxialen Referenzmodellen reproduziert. Für ein sphärisches Modell fittet SCHERPA die kinematischen Beobachtungen unabhängig von der angenommenen Sichtlinie immer gleich gut, so wie man es aus Symmetrieüberlegungen auch erwartet. Es reproduziert die Beobachtungsrichtung (innerhalb von 7°) und die intrinsische Achsenverhältnisse (innerhalb von 6%) des triaxialen Modells. Die

Genauigkeit bei der Rekonstruktion der intrinsischen Form ist besser als in früheren Publikationen, in denen separable triaxiale Modelle getestet wurden. Die Methode wurde auch an NGC 1600 getestet, einer massereichen Frühtypgalaxie mit einem prominenten zentralen Kern im Oberflächenhelligkeitsprofil. Die Galaxie wurde im Rahmen der MASSIVE-Beobachtungskampagne untersucht. Unter der Annahme, dass die Sichtlinie in der Äquatorialebene der Galaxies liegt, wurden Werte für die Masse des schwarzen Lochs, das stellare Masse-Leuchtkraft-Verhältnis und die Parameter für das Dichteprofil der Dunklen Materie gefunden, die mit früheren Messungen kompatibel sind. Inbesondere ist die für das zentrale Schwarze Loch bestimmte Masse größer als 10 Milliarden Sonnenmasen.

SCHERPA wurde auch auf die zwei-dimensionalen Beobachtungen der massereichen Frühtypgalaxie NGC 5419 angewendet, die mit den Integralfeldspektrographen SINFONI und MUSE am Very Large Telescope der Europäischen Südsternwarte beobachtet wurde. Die Galaxie zeigt einen photometrischen zentralen Kern und kastenförmige Isophoten mit einer Windung in den Positionswinkeln ihrer großen Halbachsen. Die beobachtete Kinematik zeigt die Signatur eines gegenläufig rotierenden zentralen Kerns. Als initialer Test wurde die Photometrie von NGC 5419 entlang einer Beobachtungsrichtung nahe der großen Halbachse der Galaxie deprojiziert. Die triaxialen Modelle ergeben eine Masse für das Schwarze Loch von $2.659^{+0.04}_{-0.06} \cdot 10^9$ $M_\odot$ und sagen einen geringen Anteil an kastenförmigen Orbits (sog. box orbits) innerhalb der Einflussssphäre des Schwarzen Lochs voraus, wo kastenförmige Orbits erwartungsgemäß instabil werden. Darüber hinaus fitten sie korrekt die gegenläufige Rotation in den beobachteten Daten und zeigen, dass die gegenläufige Rotation in NGC 5419 aus dem Zusammenspiel der Projektion von Sternen, die entlang der kleinen und der großen Halbachse der Galaxie rotieren. Die triaxialen Modelle wurden mit einem Edge-On achsensymmetrischen Modell der Galaxie verglichen. Die achsensymmetrischen Abschätzungen der Masse des Schwarzen Lochs und der stellaren Masse innerhalb des Kernradius sind 50% bzw. 15% größer als die triaxialen, was für die gewählte Beobachtungsrichtung erwartet wird. Dies ist das Gegenteil von dem, was für die Frühtyp-Galaxie NGC 3379 behauptet wurde, bei der sich die Masse des schwarzen Lochs im Vergleich zum achsensymmetrischen Ergebnis verdoppelte. Die Anisotropie-Profile sowohl der triaxialen als auch der achsensymmetrischen Modelle sind radial anisotrop und inkompatibel mit den Vorhersagen des Core-Scourings durch gravitativ gebundene Paare von schwarzen Löcher mit gleicher Masse. Eine mögliche Interpretation ist, dass der photometrische Kern früher entstand als die Signatur des Core-Scourings im Anisotropieprofil.

Abstract

Massive triaxial early-type galaxies sit at the end of galaxy evolution and account for almost one third of the most luminous galaxies in the local Universe. They presumably host the highest mass black holes, in particular the dormant descendants of the black holes that powered the Quasars observed at the early stages of the Universe.

Previous studies suggest that the properties and the dynamics of intrinsically triaxial galaxies cannot be fully investigated with axisymmetric modelling. Axisymmetric models are suspected to provide biased reconstructions of the orientation of intrinsically triaxial galaxies with respect to the line-of-sight. As a consequence, the stellar mass-to-light ratio can be underestimated up to one half of its value. This translates in poorly constrained initial mass functions and biased black hole masses.

This work presents **SCHERPA** (**SCH**warzschild m**E**thod for t**R**iaxial early-ty**P**e g**A**laxies) a flexible and efficient triaxial implementation of the orbit-based Schwarzschild method. SCHERPA constructs triaxial models that fit the full line-of-sight velocity distributions of real galaxies. SCHERPA is equipped with a software for triaxial de-projections of the observed surface brightness profile. The software can deal with variations in the ellipticity and with twists of the major axes of the isophotes. The resulting triaxial luminosity density is interpolated and integrated to yield the total mass of the galaxy and to compute the gravitational potential and forces. The initial conditions of the representative stellar orbits are sampled with a technique able to yield a coverage of phase-space that adapts to the changes in the gravitational potential observed in real galaxies. In fact the gravitational potential of galaxies is dominated by the massive black holes in the center and by dark matter in the outskirts.

The method reproduces the mass (within 2 %) and the intrinsic kinematics (within 4.5 %) of realistic spherical and triaxial reference models. For the spherical model, SCHERPA fits the kinematic observations equally well regardless of the line-of-sight along which the model is investigated, as expected from symmetry considerations. It also recovers the viewing direction (within 7°) and intrinsic shape (within 6 %) of the triaxial model. The accuracy on the reconstruction of the intrinsic shape is better than the one reported in previous publications on three-integral triaxial separable Abel models. The method is tested also on the real data of NGC 1600, a massive early-type galaxy with a prominent central core in the surface brightness profile. The galaxy is observed as part of the MASSIVE survey. Edge-on models performed in this Thesis find values of the black hole mass, stellar mass-to-light ratio and of the parameters describing the dark matter density profile that are compatible with previous estimates. In particular the inferred black hole mass is larger than 10 billion solar masses.

SCHERPA is applied to the two-dimensional observations of the massive early-type galaxy NGC 5419, observed with the integral field spectrographs SINFONI and MUSE at the European Southern Observatory Very Large Telescope. The galaxy shows a photometric central core and isophotes with boxy shapes and a twist in the position angles of their major axes. The observed kinematics shows a signature of a counter-rotating central core. As an initial test, the photometry of NGC 5419 is de-projected along a viewing direction close to the intrinsic major axis of the galaxy. The triaxial models yield a black hole mass of $2.659^{+0.04}_{-0.06} \cdot 10^9$ $M_\odot$ and predict a low contribution from box orbits inside the sphere of influence of the black hole, where box orbits are expected to become unstable. Moreover they fit accurately the counter-rotation in the observed data and show that the counter-rotation in NGC 5419 comes from the interplay in projection of stars orbiting respectively around the short and major axes of the galaxy. The triaxial results are compared to edge-on axisymmetric models. The axisymmetric estimates of the black hole mass and of the stellar mass inside the core radius are respectively 50 % and 15 % larger than the triaxial ones, as expected for the chosen viewing direction. This is anyway the opposite of what claimed for the early-type galaxy NGC 3379 where the black hole mass doubled compared to axisymmetric results. The anisotropy profiles of both triaxial and axisymmetric models are radially anisotropic and not compatible with predictions of core scouring by equal-mass binary black holes. A possible interpretation of this result is that the photometric core develops earlier than the signature of core scouring in the anisotropy profile.

Contents

List of Figures

List of Tables

Chapter 1

Introduction

This work describes the development, testing and first application of a fully triaxial implementation of the orbit-based Schwarzschild method for the self-consistent stellar dynamical modelling of massive triaxial elliptical galaxies. After few words of introduction, the chapter deals with the classification and the scaling relations of elliptical galaxies. It then details the evidence for triaxiality in elliptical galaxies. This is followed by the motivational drivers and aims of this project. In the end the chapter focuses on the theory of collisionless systems and their dynamical modelling. The last section presents the outline of the Thesis.

1.1 Elliptical galaxies

On a clear and moonless night it is possible to observe in the sky a pale and irregular stripe as portrayed in Figure (1.1). It is our Galaxy the *Milky Way*. The name comes from the ancient Greek ***galaxías kýklos*** and it has a mythological origin as described by the Latin poet Publius Ovidius Naso [43 BC - 17/18 AD] in the Metamorphoses:

> **Est via sublimis, caelo manifesta sereno; lactea nomen habet, candore notabilis ipso. Hac iter est superis ad magni tecta Tonantis regalemque domum.**
> Accross the height of heaven there runs a road, Clear when the night is bare, the Milky Way, Famed for its sheen of white. Along this way Come the immortals to the royal halls Of the great Thunderer.

Even though Aristotle in the Meteorologica reported that the Greek philosophers Anaxagoras and Democritus believed that the light of the Galaxy originated from that of distant stars, only with the advent of the first telescope it was possible to clarify the origin of the Milky Way (Galilei 1610). Further technological improvements allowed Charles Messier [1730 - 1817 AD] and William Herschel [1] [1738 - 1822 AD] to report the discovery of new *nebolous* objects and to list

---

[1] William Herschel was assisted by his sister Caroline Herschel [1750 - 1848 AD].

them in their catalogues (Messier, 1781; Herschel, 1786). It is interesting to note that at that time it was not clear whether these bodies were part of the Milky Way or were instead extra-galactic objects (the *Island Universes* mentioned by the German philosopher Immanuel Kant [1724 - 1804 AD]). The issue was finally settled by Edwin Hubble [1889 - 1953 AD] who discovered that the Andromeda Nebula was indeed an external galaxy by measuring its distance using Cepheids stars [2] and thus kick-starting the field of extra-galactic Astronomy (Hubble, 1925, 1926). Nowadays galaxies are seen as the fundamental constituents of the visible Universe. The Hubble Ultra Deep Field, the deepest visible-light image of the Universe taken in 2004 with the NASA's Hubble Space Telescope, captured some 10,000 galaxies in an area about 1/100th the size of the full moon. This density implies a total of $\sim$ 200 billion galaxies over the all sky. The estimate includes only the most luminous galaxies. The NASA's planned James Webb Space Telescope will find even fainter galaxies whose light was redshifted to infrared wavelengths by the expansion of the Universe. One of the first steps in the field of extra-galactic Astronomy was to classify galaxies according to their apparent morphology in Elliptical, Spiral, Lenticular and Irregular galaxies (Hubble, 1936). **Elliptical** galaxies owe their name to the fact that their *isophote*s (contours of constant luminous intensity) are ellipses. They are smooth and show almost no structural details except for a bright central concentration. In the Hubble's *tuning-fork* diagram in Figure (1.2) they are denoted by the letter **E** followed by an integer given by $10 \times (1 - q')$ where q' is the observed flattening. **Spiral** galaxies consist of a centrally concentrated bulge and of a prominent flattened disk. The disk is sometimes characterised by the presence of spiral arms where star formation takes place. Conventionally **S** indicates normal spiral galaxies and **SB** barred ones. Bulges in spiral galaxies are observationally classified into **classical** and **pseudo**-bulges. Classical bulges show similar properties of low-luminosity elliptical galaxies. Pseudo-bulges are disk-like structures. Classical and pseudo-bulges are thought to originate from diverse formation scenarios (Kormendy & Kennicutt, 2004; Kormendy et al., 2011; Kormendy & Ho, 2013). Classical bulges are the product of mergers. Pseudo-bulges form gradually in a process denoted as *secular evolution*. **Lenticular** galaxies **(S0)** have a bright central bulge, similar to that of elliptical galaxies, surrounded by an extended disk-like structure with no spiral arms and no on-going formation of new stars. S0 galaxies are thought to be disk galaxies that have used up most of their gas or lost it due to environmental effects (van den Bergh, 2009). **Irregular** galaxies were defined by Hubble as the galaxies that morphologically did not fit in any of the above mentioned classes as for example the Magellanic Clouds. For historical reasons it is customary to refer to Ellipticals as *early-type* galaxies and to Spirals as *late-type* galaxies, since Hubble interpreted the tuning-fork diagram as an evolutionary sequence.

---

[2] A Cepheid is a type of variable star used as a indicator of distance. Its luminosity varies as a function of time and can be determined from the period of variability. By calibrating the method on galactic Cepheids it is then possible to use them as distance indicators where other methods for determining the distance do not work anymore (as for example the Parallax).

Figure 1.1: Image of the Milky Way bulge. The picture was taken in the Kalahari desert of Namibia. Exposure time 60 sec, sensitivity ISO1600, taken with a 8mm FishEye lens attached to a Nikon D7000. Even though the image depicts the sky from the Southern Hemisphere, it gives the idea of what Ovidius meant by *pale and irregular stripe*. Credits: Torben Simm.

Elliptical galaxies are very interesting dynamical systems. Historically, they were considered to be one-component collisionless stellar objects, containing little to no cold gas and mostly evolved stars (Gott, 1977; de Zeeuw & Franx, 1991). This simplistic view has however turned out to be partially incorrect. Modern research found hot X-Ray emissions out to several effective radii (Humphrey et al., 2006) and significant substructures as central regions counter-rotating or having higher rotation and lower velocity dispersion with respect to the rest of the galaxy, with the latter being interpreted as a signature of a central disk (Davies et al., 2001; Emsellem et al., 2004). Intense radio sources, presumably powered by massive black holes, were also detected in the center of these galaxies (Blandford, 1990; Chokshi & Turner, 1992; Kormendy & Richstone, 1995). Elliptical galaxies harbour the most massive black holes. These black holes are possible descendants of the black holes with masses up to several billion solar masses that powered luminous quasars at redshift $z > 6$ (McConnell et al., 2011; Thomas et al., 2016). Studies on their stellar population have revealed that ellipticals in lower-density regions exhibit a younger stellar population (as if they continued to experience star formation also in recent times) than those in dense galaxy clusters (Thomas et al., 2005a, 2010). Furthermore systematic variations in the stellar initial mass function (IMF) were reported (Thomas et al., 2011; Cappellari et al., 2012). The dynamical modelling of elliptical galaxies (in particular of the most massive ones) is the topic of this work.

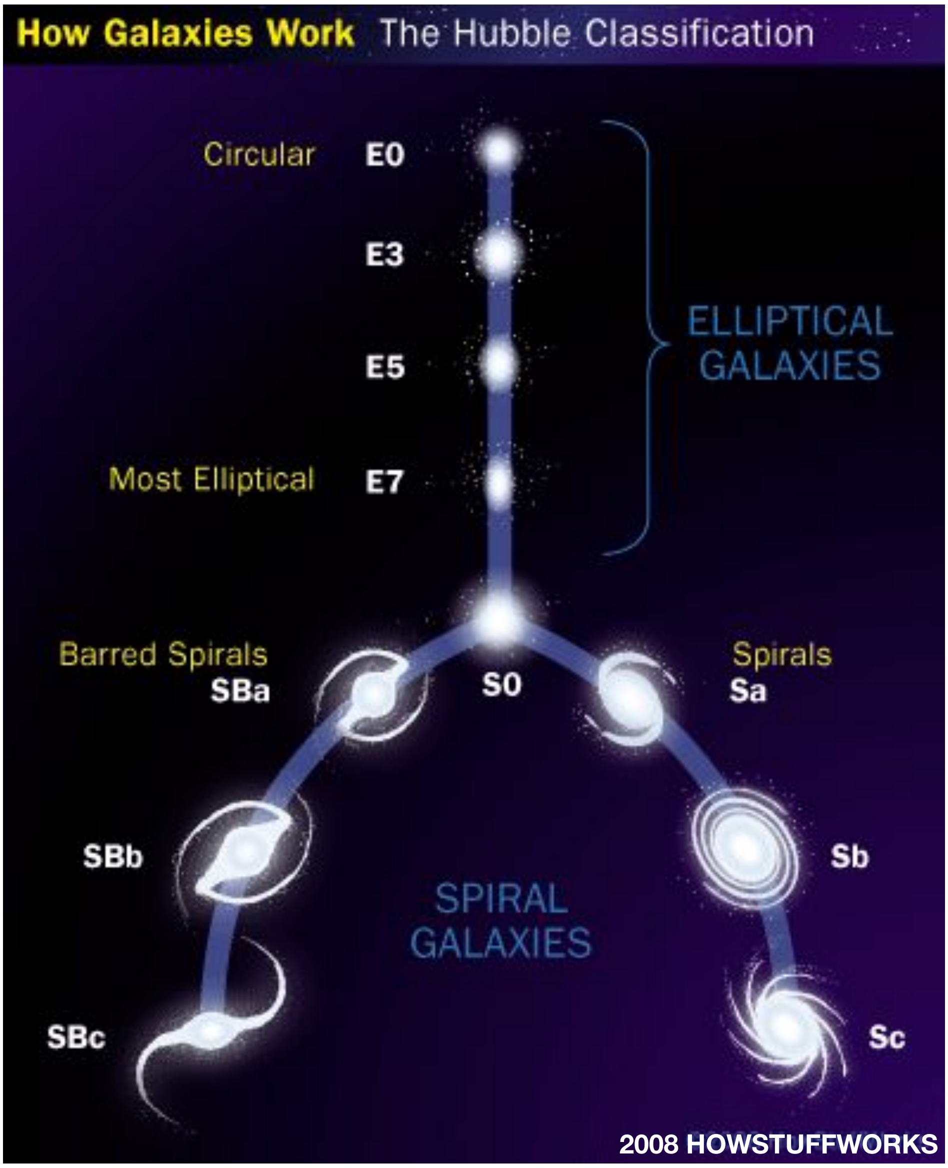

Figure 1.2: Hubble's tuning fork diagram. Credits: 2008 HOWSTUFFWORKS.

1.2 Classification of elliptical galaxies

The classification of elliptical galaxies proposed by Hubble is based on their apparent morphology and suffers from inclination effects (Sandage et al., 1970; Binney & de Vaucouleurs, 1981; Tremblay & Merritt, 1995). Moreover it does not refer to any fundamental physical parameter that can be linked to the formation and past evolution of these objects. Revisions of the Hubble classification were proposed by Tremblay & Merritt (1996) and Kormendy & Bender (1996) based on the correlations among the photometric and kinematic properties of elliptical galaxies. Elliptical galaxies can be photometrically and kinematically divided in two families. The first classification can be performed based on the shape of isophotes. Accurate CCD photometry showed that the shape of the isophotes does not always resemble that of a perfect ellipse (Carter, 1987; Lauer, 1985; Peletier et al., 1990). At first the isophotes are fitted with ellipses. The residuals among isophotes and ellipses are expanded in a Fourier series with coefficients a_k and b_k. The Fourier coefficient a_4 describes the lowest order deviation from elliptical isophotes (lower order coefficients are minimised to zero by the ellipse fit). If $a_4 > 0$ the isophote is disk-shaped and boxy-shaped for negative a_4 (Bender & Moellenhoff, 1987; Bender et al., 1988). A graphical illustration is provided in Figure (1.3(a)). Figure (1.3(b)) shows an example of a boxy elliptical galaxy (NGC 4261) and a disky elliptical galaxy (NGC 4621). Typically $a_4/a \in [0, 2]$ % where a is major axis of the fitted ellipse. Such parametrisation is convenient because it describes the photometry of a galaxy only by means of the ellipticity, the diskyness and boxiness at each projected radius. The classification of elliptical galaxies based on the shape of the isophotes is however the tip of the iceberg of a much profound distinction. There is in fact a striking link among the shape of the isophotes and other properties in the kinematics, X-ray emission intensity and shape of the surface brightness (SB) profiles (Binney & Petrou, 1985; Bender, 1988b; Bender et al., 1989; Rix & White, 1990). Faint ellipticals (absolute magnitude $M_{\mathrm{B}} > -20.6$) have disky isophotes and show a **cusp**, a steep central power-law SB profile (see Section 1.3.1). Moreover they are fast rotators and flattened objects with a shape close to oblate axial symmetry. Bright ellipticals (absolute magnitude $M_{\mathrm{B}} < -20.6$) have boxy isophotes and a flat central SB **core** (Kormendy, 1985; Crane et al., 1993; Lauer et al., 2005; Gebhardt et al., 1996). Such galaxies are slow rotators and are rounder than faint early-types. Bright ellipticals may also present a misalignment between the photometric and kinematic axis known as **kinematic misalignment** (see Section 1.5). Moreover box-shaped ellipticals seem to have higher mass-to-light ratios than those with disky isophotes (Binney & Petrou, 1985; Bender, 1988b; Bender et al., 1989; Rix & White, 1990). The consensus is that this dichotomy originates from two diverse formation scenarios (Emsellem et al., 2007, 2011). The progenitors of faint ellipticals are thought to be disk-dominated galaxies rich in gas (gas-rich merger). The gas is channeled to the center and forms a rotating disk where star formation happens. This could explain the presence of the steep power-law density profile in the center and the

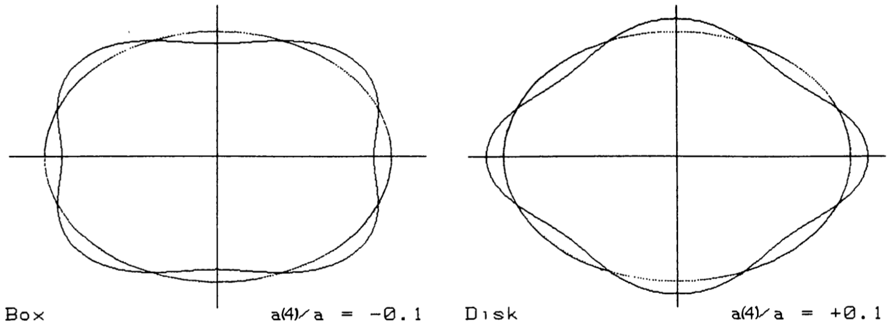

(a) Graphical illustration

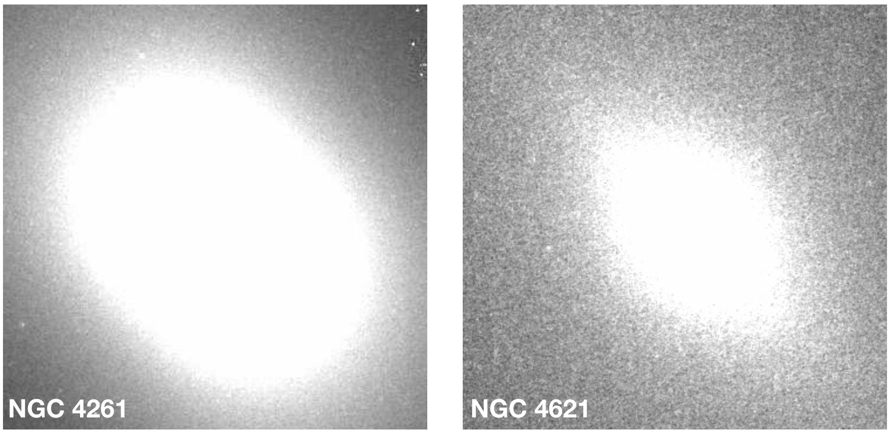

(b) Real galaxies

Figure 1.3: Figure (1.3(a)) portrays drawings illustrating box-shaped ($a_4/a = -0.1$) and disk-shaped ($a_4/a = +0.1$) isophotes from Bender et al. (1988). Figure (1.3(b)) shows HST images of the boxy elliptical galaxy NGC 4261 and disky elliptical galaxy NGC 4621 taken with the instrument ACS/HRC, respectively with the F606W and F330W filters. Exposure times: 782.0 - 1912.0 seconds. Proposal IDs: 9493 - 10435. Box-shaped isophotes are signature of triaxiality.

fast rotating property. In the case of bright ellipticals, the progenitors are poor in gas (gas-dry merger). The super-massive black holes (SMBH) of the progenitor galaxies are channeled to the center and form a binary system that ejects all of the stars that happen to pass in their vicinity in a process known as *core scouring* (Quinlan & Hernquist, 1997; Milosavljević & Merritt, 2001; Thomas et al., 2014b). Confirming evidence for the fact that elliptical galaxies originated from mergers comes from the discovery of fine-structure features (Kormendy, 1984) as central rotating disks (Schweizer, 1982), ripples (Malin & Carter, 1983) and kinematically distinct components in their centres (also known as **kinematically decoupled central cores**, hereafter KDC) (Bender, 1988a). As mentioned in Section (1.5), KDCs could also be seen as a signature of triaxiality. These features are in some cases observed to be metal-enriched (Bender & Surma, 1992) or to have similar ages with respect to the main body of the galaxy (Davies et al., 2001).

1.3 Observations

The section describes the observed photometric and kinematic properties of elliptical galaxies. It delineates how these observations are used as mass tracers.

1.3.1 Photometric observations

Elliptical galaxies are bright in the center and fade away rapidly as the distance from the center increases. This variation is encoded in the surface brightness profile. Figure (1.4) portrays V-band SB profiles for a variety of elliptical galaxies from Lauer et al. (2007) and shows that the shape of the SB profiles exhibits a considerable individuality. As discussed in Section (1.2) bright ellipticals have a flat central core. The extent of the core is given by the **core radius** r_b that usually ranges from 50-600 pc. Faint early-types have a central power-law profile (cusp). It is important to study the shapes of SB profiles since they provide information about galaxy formation (Ebisuzaki et al., 1991; Makino & Ebisuzaki, 1996; Faber et al., 1997). The de Vaucouleurs' profile (de Vaucouleurs, 1948) is an initial description of the SB profile (averaged in concentric circular annuli) as a function of projected radius r

$$SB(r) = SB_e \exp\left\{-7.67\left[\left(\frac{r}{r_e}\right)^{1/4} - 1\right]\right\} \tag{1.1}$$

where r_e (the **effective radius**) contains half of the total light of the galaxy and SB_e is the surface brightness at the r_e. Effective radii range from few hundreds parsecs to 30 Kpc (Binney, J. and Merrifield, 1998; Saglia et al., 2016). The Sérsic profile (Sérsic, 1963, 1968)

$$SB(r) = SB_e \exp\left\{-b_n\left[\left(\frac{r}{r_e}\right)^{1/n} - 1\right]\right\} \tag{1.2}$$

provides a generalisation of the de Vaucouleurs' profile, where b_n is a function of the *Sèrsic index* n and it is defined such that half of the total brightness is within r_e. A Sérsic profile with $n \sim 4$ corresponds to bright ellipticals. Faint ellipticals are described by a Sérsic profile with $1 \leq n \leq 4$ (Caon et al., 1993; Ciotti & Bertin, 1999). Other laws have been proposed in order to account for the SB-cores. Lauer et al. (1995) introduced the *Nuker law*, which was designed to describe the inner $3-10$ arcseconds of nearby early-type galaxies. It reads

$$SB(r) = SB_b \, 2^{(\beta-\gamma)/\alpha} \left(\frac{r}{r_b}\right)^{-\gamma} \left[1 + \left(\frac{r}{r_b}\right)^{\alpha}\right]^{(\gamma-\beta)/\alpha} \tag{1.3}$$

where SB_b is the surface brightness at the core radius, γ and β are the slopes of the power-law profiles respectively inside and outside r_b. This law was however not intended to match the entire SB-profile. This can be achieved by means of the core-Sérsic profile (Graham et al., 2003; Trujillo et al., 2004b)

$$SB(r) = SB'\left[1+\left(\frac{r_b}{r}\right)^{\alpha}\right]^{\gamma/\alpha} \exp\left[-b_n\left(\frac{r^{\alpha}+r_b^{\alpha}}{r_e^{\alpha}}\right)^{1/n\alpha}\right] \tag{1.4}$$

with

$$SB' = SB_b\frac{1}{2^{\gamma/\alpha}} \exp\left[b_n\left(2^{1/\alpha}\,\frac{r_b}{r_e}\right)^{1/n}\right] \tag{1.5}$$

that allows a normal Sérsic profile outside of r_b and a power-law profile with slope γ inside. In Equation (1.3) and (1.4) the parameter α quantifies the sharpness of the transition from the inner to the outer regime.

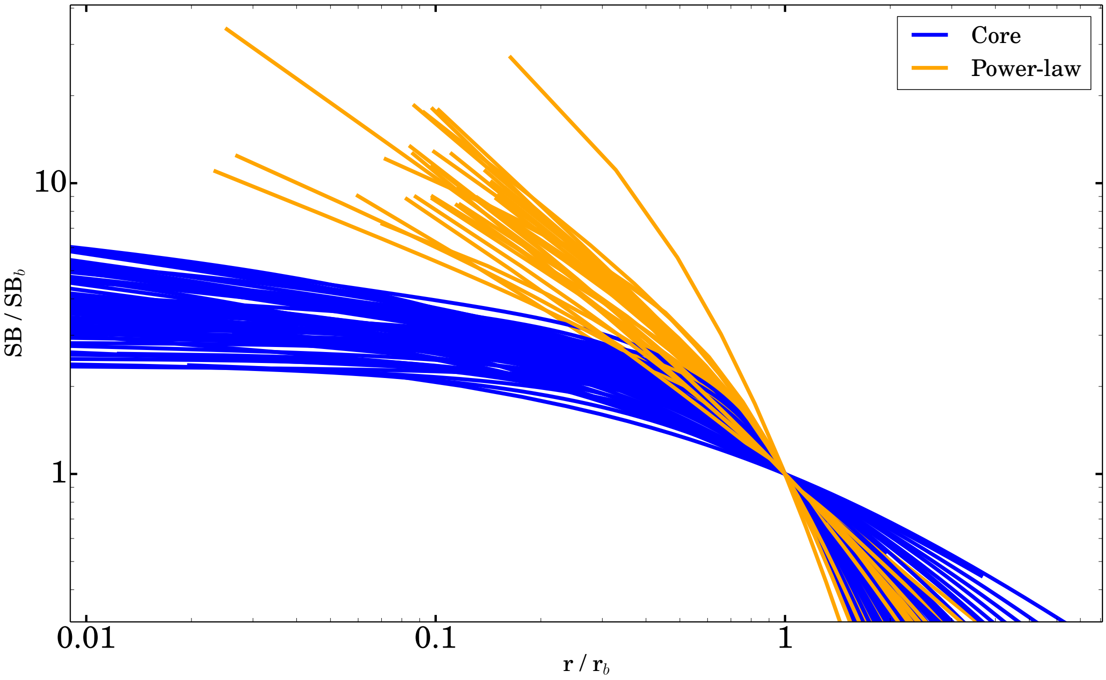

Figure 1.4: HST V-band central surface brightness profiles of elliptical galaxies from the sample of Lauer et al. (2007).

1.3.2 Spectroscopic observations

Spectroscopic observations provide information about the kinematics of galaxies from the broadening of the absorption lines originated in the atmospheres of stars. In the Milky Way (and nearby galaxies) it is possible to observe single stars and resolve their kinematics individually. In distant galaxies it is possible to collect only an integrated spectrum $G(\lambda)$, which is the cumulative result of the absorption lines of stars along the line-of-sight, Doppler-shifted according to their line-of-sight velocities. The integrated spectrum is

$$G(u) \approx \int F(v_{los})\; S(u - v_{los})\; \mathrm{d}v_{los} \tag{1.6}$$

where $u = c \cdot \log(\lambda)$, $S(u - v_{los})$ is a typical unbroadened spectrum of a template star and $F(v_{los})$ is the **line-of-sight velocity distribution** (LOSVD). The LOSVD (also known as velocity profile) provides the fraction of stars with line-of-sight velocities in the interval $[v_{los} - \mathrm{d}v_{los}, v_{los} + \mathrm{d}v_{los}]$ (Binney, J. and Merrifield, 1998). Several methods have been proposed to deconvolve the LOSVD from the integrated spectra (Bender, 1990; Rix & White, 1992; Winsall & Freeman, 1993; van der Marel & Franx, 1993). A number of factors limit the accuracy of these measurements as for example the accuracy in the sky and continuum subtraction, template mismatch or the assumption that the observed galaxy is dust free (Bender et al., 1994). The LOSVDs of elliptical galaxies deviate slightly from Gaussian profiles (e.g. Dejonghe 1987; Franx & Illingworth 1988). They can be best parametrised as a truncated Gauss-Hermite series (Gerhard, 1993; van der Marel & Franx, 1993)

$$F(v_{los}) \approx e^{-\frac{\omega^2}{2}} \left[1 + h_3 \mathscr{H}_3(\omega) + h_4 \mathscr{H}_4(\omega) \right] \tag{1.7}$$

where the zero-th order of the expansion is a Gaussian function. $\omega = \frac{v_{los} - \hat{v}}{\hat{\sigma}}$ and the standard Hermite polynomials (Hermite, 1864) are

$$\begin{aligned} \mathscr{H}_3(\omega) &= \tfrac{2\sqrt{2}\omega^3 - 3\sqrt{2}\omega}{\sqrt{6}} \\ \mathscr{H}_4(\omega) &= \tfrac{4\omega^4 - 12\omega^2 + 3}{\sqrt{24}} \end{aligned} \tag{1.8}$$

with h_3 and h_4 being their respective amplitudes. The fitted quantities $\hat{v}$ and $\hat{\sigma}$ may be different from the line-of-sight mean-rotation velocity $\overline{v}_{\parallel}$ and mean-velocity dispersion $\overline{\sigma}_{\parallel}$ (Bender et al., 1994). Typically the rotational velocity in elliptical galaxies is lower than 150 $\frac{\mathrm{km}}{\mathrm{s}}$ and the velocity dispersion ranges between $100 - 300$ $\frac{\mathrm{km}}{\mathrm{s}}$ (Saglia et al., 2016). The parameters h_3 and h_4 measure respectively asymmetric and symmetric deviations of the LOSVD from a pure Gaussian profile. For example a negative h_3 corresponds to a velocity profile with the prograde wing steeper than the retrograde one. Positive h_4 corresponds to a triangular-shaped LOSVD and a negative h_4 to flat-topped one. Figure (1.5) provides a graphical depiction of how the Gauss-Hermite series varies as a function of h_3 and h_4. Typically $|h_3| \leq 0.2$ and $|h_4| \leq 0.1$. Velocity profiles are a valuable tool for determining the mass distribution of elliptical galaxies and breaking the degeneracy between changes in the mass-to-light ratio and the orbital anisotropy of the stars. Binney & Mamon (1982) showed that both an isotropic system with an increasing central mass-to-light ratio and a system that is increasingly radially anisotropic in the center with a constant mass-to-light ratio are consistent with a central increase of the projected velocity dispersion $\sigma_{\parallel}$. The difference between the two models can be found in the wings of the LOSVDs (Gerhard, 1993).

Luminous ellipticals rotate slowly with respect to faint ellipticals (Bertola & Capaccioli, 1975; Illingworth, 1977). Figure (1.6) portrays the $v/\sigma - \epsilon$ diagram from Davies et al. (1983). The figure shows the ratio between the maximum rotational velocity and the mean velocity dispersion within half of the effective radius against the observed ellipticity ϵ. The solid line is the $v/\sigma - \epsilon$ predicted at an edge-on view by Binney (1978b) from the tensor virial theorem for oblate spheroids of constant ellipticity with isotropic velocity distributions. The diagram shows that luminous ellipticals in the sample of Davies et al. (1983) have a wide range of rotational properties and that most of them present a slower rotation with respect to an oblate rotator. Conversely faint ellipticals (and bulges) follow closely the solid line. Taking into account projection effects (Binney, 2005), a cautious interpretation of the diagram is that faint ellipticals are flattened by rotation and that anisotropy plays a notable role in the kinematics of bright ellipticals. Work from Burkert & Naab (2005) showed that the remnants of unequal-mass mergers of disc galaxies present values of anisotropy similar to those found in equal-mass merger remnants that form slowly rotating ellipticals. The $v/\sigma - \epsilon$ diagram has been recently revisited using two-dimensional kinematic information measurable with integral field spectrographs and applied to the galaxies of the ATLAS 3D sample (Emsellem et al., 2007; Cappellari et al., 2011; Emsellem et al., 2011; Krajnović et al., 2011).

Velocity profiles can also be used to study the mass content of galactic haloes. The velocity dispersion in many ellipticals has been measured to remain constant out to one or more effective radii. Models with an outer dark component for the mass (Saglia et al., 1992, 1993) or with an increasing tangential anisotropy are both able to match the trend in the velocity dispersion. High order moments of the line-of-sight velocity profile allow to exclude the second option and point to the presence of a dark halo (Binney, J. and Merrifield, 1998). The presence of dark matter (DM) has been also confirmed by X-Ray observations of the hot gas surrounding elliptical galaxies (Forman et al., 1985; Fabian et al., 1986; Loewenstein & Mathews, 1987; Loewenstein & White, 1999) and by gravitational lensing (Wilson et al., 2001; Treu & Koopmans, 2004; Gavazzi et al., 2007). Measuring integrated spectra at large radii (more than a couple of r_e) is complicated by the fact that SB-profile of elliptical galaxies decreases rapidly. Planetary nebulae can be observed due to the very distinctive and bright [OIII]λ5007 Å emission line and can be used as a kinematic tracer. For example the planetary nebulae around NGC 5128 (Cen A) rotate faster than the inner luminous part of the galaxy (Wilkinson et al., 1986; Ford et al., 1989). Moreover planetary nebulae were used to determine that the halo of the giant elliptical galaxy M87 has been growing by accreting smaller galaxies (Longobardi et al., 2013, 2015). These findings argue in favour of the model of hierarchical galaxy growth. Planetary nebulae can also be used as tracers for dark matter (e.g. Tremblay et al. 1995; Saglia et al. 2000; Romanowsky et al. 2003; Pierce et al. 2006; Douglas et al. 2007; Napolitano et al. 2009).

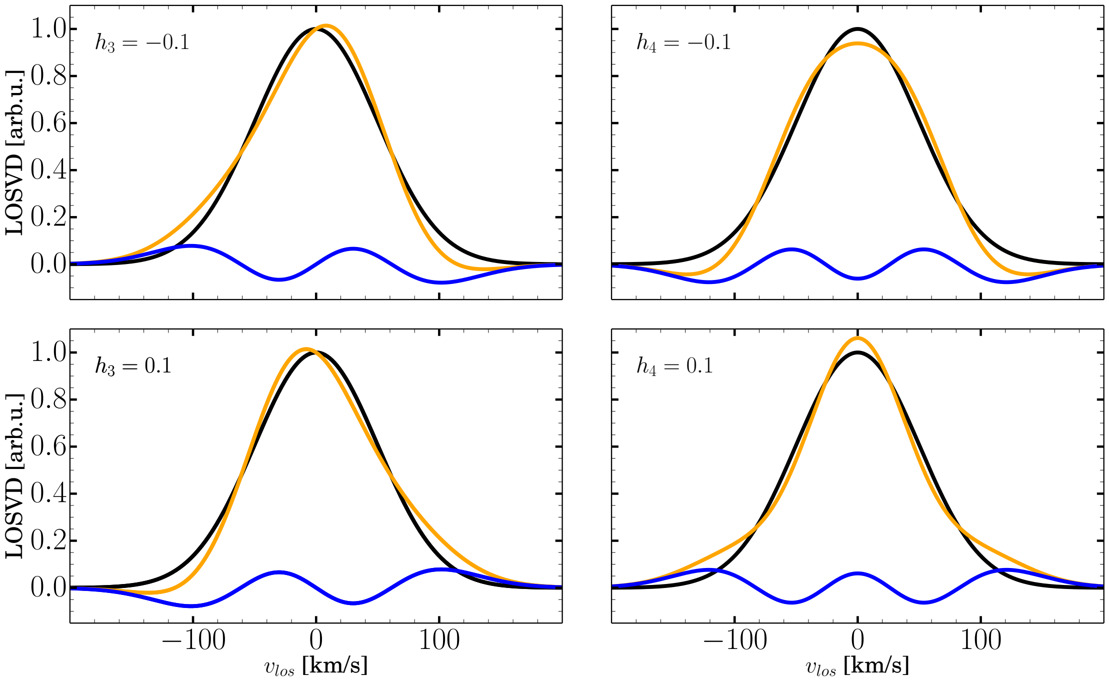

Figure 1.5: Comparison among a pure Gaussian velocity profile (**black**) with $\hat{v} = 0\ \frac{\text{km}}{\text{s}}$ and $\hat{\sigma} = 50\ \frac{\text{km}}{\text{s}}$ and variuos truncated Gauss-Hermite series (**orange**). The difference between the Gaussian profile and the Gauss-Hermite series is plotted in **blue**. On the left-hand side the Gauss-Hermite profiles correspond to $h_4 = 0$. The profiles on the right-hand side correspond to $h_3 = 0$. The plot has been adapted from Bender et al. (1994). Credits: M. Opitsch.

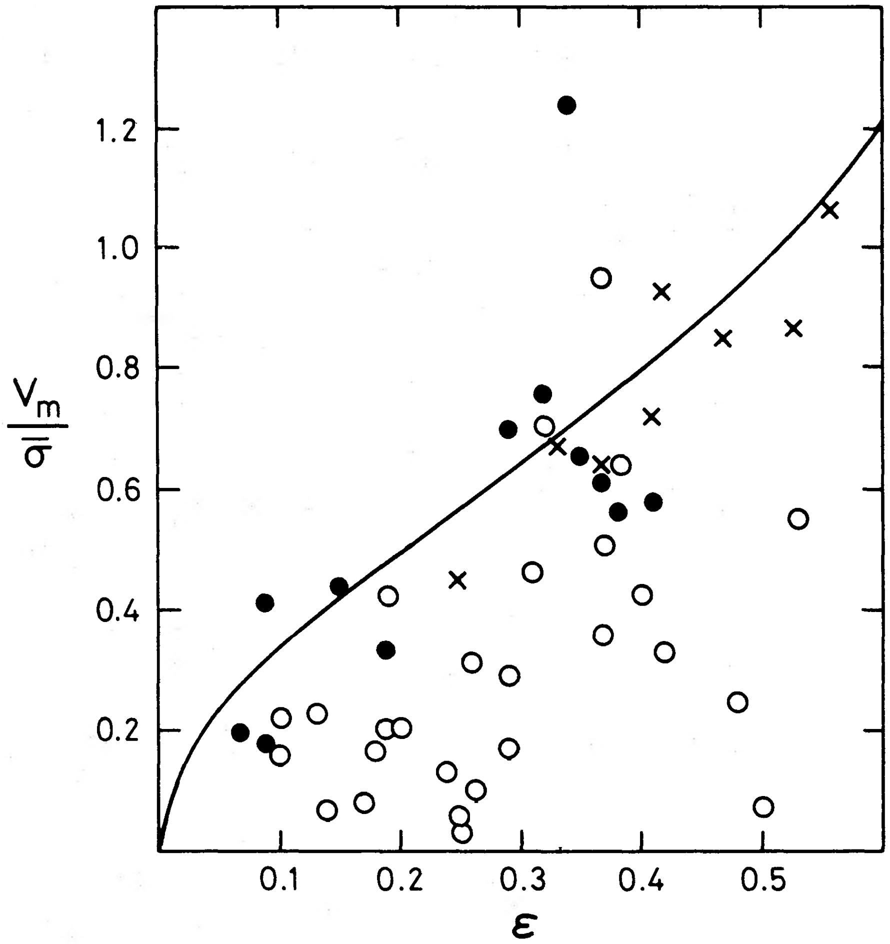

Figure 1.6: The $v/\sigma-\epsilon$ diagram (Davies et al., 1983). The ratio between the maximum rotational velocity and the mean velocity dispersion within half of the effective radius is plotted against the observed ellipticity ϵ. Open circles portray bright elliptical galaxies (absolute magnitude $M_{\rm B} < -20.6$), filled circles faint ellipticals (absolute magnitude $M_{\rm B} > -20.6$) and the crosses the bulges of spiral galaxies. The solid line is the prediction at an edge-on view for an oblate isotropic rotator obtained by Binney (1978b) from the tensor virial theorem.

1.4 Global properties of elliptical galaxies

The topic of this section are the relations among the observed parameters used to describe the properties of elliptical galaxies, as for example the central projected velocity dispersion, the effective radius or the surface brightness. Such relations are excellent tools for understanding the formation and evolution of early-type galaxies. For example the masses of classical bulges and early-type galaxies are known to correlate with the mass of the central SMBH (e.g. Kormendy & Ho 2013). These correlations imply that classical bulges and ellipticals co-evolve with SMBHs.

The Fundamental Plane In logarithmic space, the effective radius, central projected velocity dispersion and the mean surface brightness evaluated at the effective radius are linearly related as

$$\log_{10} r_e = \alpha \log_{10} \sigma_{\parallel} + \beta \overline{SB}_e + \gamma \tag{1.9}$$

with r_e measured in Kpc, $\sigma_{\parallel}$ in $\frac{\mathrm{km}}{\mathrm{s}}$ and $\overline{SB}_e$ in the B band. Reported values are $\alpha = 1.25 \pm 0.1$, $\beta = 0.32 \pm 0.03$ and $\gamma = -8.895$. The last value was determined from the elliptical galaxies of the Coma cluster with an Hubble constant of $H_0 = 50.0 \, \frac{\mathrm{km}}{\mathrm{s}} \frac{1}{\mathrm{Mpc}}$. (Bender et al., 1998). This relation is known as the *Fundamental plane* (Djorgovski & Davis, 1987). The observed relation shows a deviation (tilt) with respect to the one predicted from equilibrium considerations done with the virial theorem ($r_e \sim \sigma_{\parallel}^2 \, \overline{I}_e^{-1}$ with $\overline{SB}_e = -2.5 \log_{10} \overline{I}_e$). This effect is thought to originate either from a non-homology (change of structural parameters) or a variation of the mass-to-light ratio (M/L) with galaxy luminosity (Gerhard et al., 2001; Cappellari et al., 2006) or a combination of both (Trujillo et al., 2004a). The small scatter about the Fundamental Plane makes this relation a useful cosmological probe (e.g. Bender et al. 1998) and a tool for studying the formation and evolution of early-type galaxies (e.g. Kjaergaard et al. 1993; Kelson et al. 1997; Beifiori et al. 2017). Together with the relatively narrow range of kinematic features observed in ellipticals, the small scatter about the Fundamental Plane implies also that only a small range of dynamical models is realised in early-type galaxies. Galaxy clusters were also found to obey a relation similar to the Fundamental Plane (Schaeffer et al., 1993; Lanzoni et al., 2004).

Faber-Jackson relation It is the analog of the Tully-Fisher relation (Tully & Fisher, 1977) for late-type galaxies. It correlates the luminosity (in the B band) of an early-type galaxy with its central projected velocity dispersion and reads

$$L_{\mathrm{B}} \sim \sigma_{\parallel}^4 . \tag{1.10}$$

More luminous galaxies tend to have a larger dispersion (Faber & Jackson, 1976). The Faber-Jackson relation can be seen as a projection of the Fundamental Plane (Binney & Tremaine, 2008).

Kormendy relation Another physically meaningful projection of the Fundamental Plane is the relation between $\log_{10} r_e$ and the mean surface brightness $\overline{SB}_e$ within the effective radius. It is known as the Kormendy relation and reads

$$\overline{SB}_e = \alpha \log_{10} r_e + \beta \tag{1.11}$$

with $\alpha = 2.94$ and $\beta = 19.48$ (Kormendy, 1977; Hamabe & Kormendy, 1986). It points to the fact massive (large) early-type galaxies show on average lower values of the surface brightness than those with smaller r_e.

Morphology-density relation The morphology of galaxies is related to their density in a certain environment. In rich clusters at low redshift one tenth of the galaxies are observed to be spirals, one half are lenticular and 40 % are ellipticals (Dressler, 1980). Clusters at $z = 0.4$ exhibit a 2-3 times smaller occurrence of lenticular galaxies and proportional increase in spiral galaxies. elliptical galaxies still dominate (Dressler et al., 1997). The fact that ellipticals reside in dense environments suggests that mergers play a role in their formation.

The Mg-$\sigma_{\|}$ relation It is a correlation between the strength of the [Mg]λ5150 Å line and the central projected velocity dispersion $\sigma_{\|}$. It reads

$$\mathrm{Mg}_2 = \alpha \log_{10} \sigma_{\|} + \beta \tag{1.12}$$

with $\alpha = 0.2$ and $\beta = -0.166$ (Bender et al., 1993) and the index Mg_2 defined as in Faber et al. (1985). Galaxies with high-velocity dispersion have stronger Magnesium lines (Bender et al., 1993; Ziegler & Bender, 1997). Comparison between measurements in clusters out to $z = 0.4$ are consistent with local relations (Ziegler & Bender, 1997), granted stellar evolution is taken into account. This suggests that the correlation arises due to a higher metal enrichment in high dispersion galaxies.

Scaling relations between black holes and host galaxies The scaling relations between the masses of central black holes and the properties (as for example the central projected velocity dispersion and the K-band absolute magnitude) of their host galaxies are an indication of their co-evolution (Kormendy & Gebhardt, 2001; Kormendy et al., 2011; Kormendy & Ho, 2013; Saglia et al., 2016). The relation between the black hole mass and the central velocity dispersion of the host galaxy was first published by Ferrarese & Merritt (2000) and Gebhardt et al. (2000a) and reads

$$\log_{10}\left(\frac{\mathrm{M_{SMBH}}}{\mathrm{M}_\odot}\right) = \alpha + \beta \log_{10}\left(\frac{\sigma_{\|,e}}{200\,\frac{\mathrm{km}}{\mathrm{s}}}\right) \tag{1.13}$$

with $\sigma_{\parallel,e}$ being the luminosity weighted stellar velocity dispersion inside r_e and the parameters being $\alpha = 8.23 \pm 0.08$ and $\beta = 3.96 \pm 0.42$ for elliptical galaxies with an intrinsic (cosmic) scatter of $\epsilon = 0.31 \pm 0.06$ (Gültekin et al., 2009). Black hole masses correlate also with the K-band absolute magnitude of the host galaxy, even though the scatter for this relation is larger (Kormendy & Ho, 2013). Furthermore in core ellipticals the radius of the sphere of influence of the black hole r_{soi} correlates tightly with the core radius r_b (with an intrinsic scatter $\epsilon = 0.17 \pm 0.04$), hinting that the formation of the depleted stellar cores in massive ellipticals is linked to the presence of central black holes (Thomas et al., 2016).

1.5 Evidence for triaxiality

The distribution of Hubble types for faint elliptical galaxies is clustered around E3. For bright elliptical galaxies it peaks around E1.5 (Tremblay & Merritt, 1995, 1996). It is possible to relate statistically the distribution of Hubble types to that of the intrinsic axes ratios. The intrinsic axes ratios follow as

$$q = \frac{c}{a} \quad p = \frac{b}{a} \tag{1.14}$$

with $a \geq b \geq c$ being respectively the major, intermediate and minor semi-axes and $1 \geq p \geq q > 0$. The triaxiality parameter is defined as

$$T = \frac{1-p^2}{1-q^2}. \tag{1.15}$$

A prolate shape corresponds to $a > b = c$ ($T = 1$, $q = p$). An oblate shape corresponds to $a = b > c$ ($T = 0$, $p = 1$). For faint elliptical galaxies the distribution of Hubble types is consistent with oblate shapes. For bright ellipticals instead triaxial shapes with $0.4 < T < 0.8$ reproduce the observed distribution of ellipticities (Vincent & Ryden, 2005). Furthermore the distribution of the axis ratio q peaks for faint elliptical galaxies at 0.65 and at 0.75 for bright elliptical galaxies (Binney & de Vaucouleurs, 1981; Tremblay & Merritt, 1996).

Isophotes may present a variation in the position angle of their major axes as a function of projected radius (Bertola & Galletta, 1979; Williams & Schwarzschild, 1979). This phenomenon is known as **isophotal twist**. Figure (1.7) shows an example of isophotal twist in the photometry of the early-type galaxy NGC 1549 (Nieto & Bender, 1989). Isophotal twist can be interpreted as a possible signature of triaxiality (King, 1978; Williams, 1981) or it can be caused by a projection effect when the axes ratios of the surfaces of constant density vary radially (Binney, 1978a). Tidal effects due to a massive companion galaxy can also produce a twist in the isophotes (Kormendy, 1977; di Tullio, 1979). Other clues about the intrinsic shapes of elliptical galaxies come from kinematic observations.

The presence of **minor axis rotation** and kinematic misalignment has been reported for several galaxies (Davies & Birkinshaw, 1988; Franx et al., 1989; Jedrzejewski & Schechter, 1989). As discussed in Section (1.9.3) they are tracers for triaxiality (Contopoulos, 1956; Kondratev & Ozernoi, 1979). Elliptical galaxies can also show KDC in their centres (Bender, 1988a). Figure (1.8) shows an example of a KDC in the early-type galaxy NGC 4365. KDCs can be seen as a possible signature of triaxiality (Statler, 1991). They could emerge from the interplay in projection of the major families of tube orbits present in a triaxial potential (see Section 1.9.3).

In the end theoretical works show that the triaxial intrinsic shape is stable. Schwarzschild (1979, 1982) and Statler (1987) showed that self-consistent triaxial equilibrium models can be built from the superposition of a set of representative stellar orbits. Moreover N-body simulations of the violent relaxation of non-equilibrium initial conditions or of the merger of equal-mass disk galaxies were shown to produce triaxial equilibrium models (Aarseth & Binney, 1978; Wilkinson & James, 1982; Barnes, 1992).

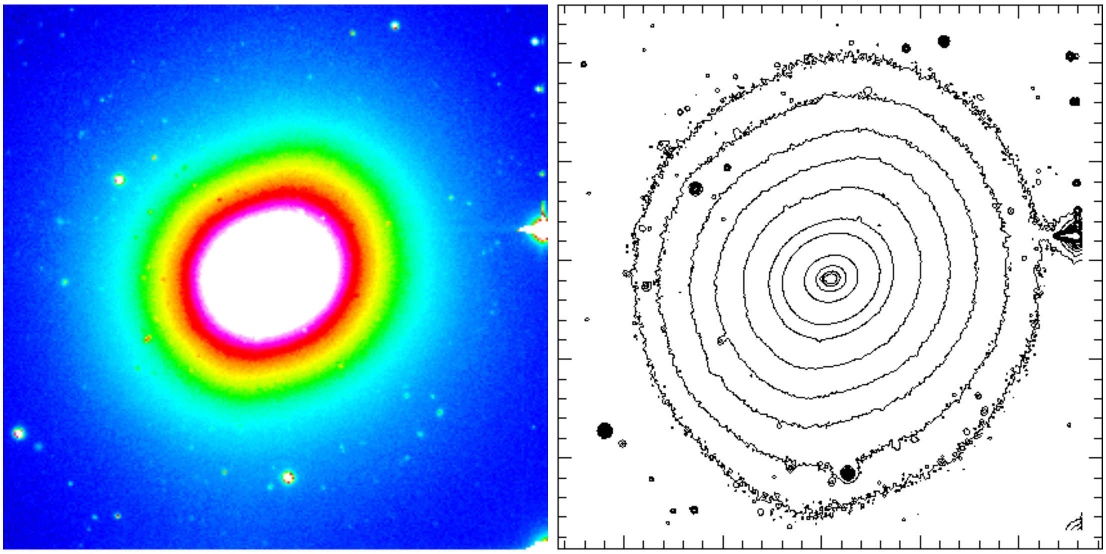

Figure 1.7: NTT+EMMI I-band image of the elliptical galaxy NGC 1549 with its isophotes. Exposure times: 3×200 seconds. The figure provides an example of isophotal twist.

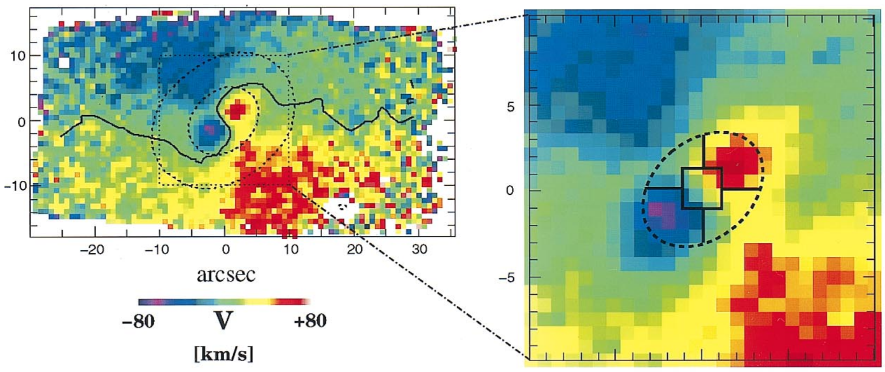

Figure 1.8: Map of the mean streaming velocity from two overlapping SAURON pointings of 4 × 1800 seconds for E3 elliptical galaxy NGC 4365 (Davies et al., 2001). The figure provides an example of a kinematically decoupled central core.

1.6 The need for triaxial modelling

Almost a third of all massive early-type galaxies are thought to be triaxial (Emsellem et al., 2007; Cappellari et al., 2007). The accurate determination of the properties of these galaxies is scientifically important as they represent the last stage of galaxy evolution and may host the relics of the most massive black holes that are postulated to power the Quasars observed at the early stages of the Universe (McConnell et al., 2011). Recent studies however show that axisymmetric models are suspected to provide biased reconstructions of the orientation of triaxial galaxies with respect to the line-of-sight and to underestimate their stellar mass-to-light ratio up to 50 % (Thomas et al., 2007a). In fact a wrong inclination may bring about an underestimation of the luminous kinetic energy and, as a consequence, an undervalued mass-to-light ratio. Biased estimates of the stellar mass-to-light ratio translate in poorly constrained IMFs. The IMF is generally thought to be universal. In the case of the Milky-Way it can be estimated "directly" by counting the stars. In far-away galaxies, where single stars cannot be individually resolved, astrophysicists put constraints on the IMF by measuring the stellar mass-to-light ratio. High values of the mass-to-light ratio correspond to a Salpeter bottom-heavy IMF (Salpeter, 1955), which predicts a high number of low mass (and so low luminosity) stars. On the other hand, low values of mass-to-light ratio translate to Kroupa bottom-light IMF (Kroupa, 2002), which conversely predicts a lower fraction of low mass stars. Thomas et al. (2011) and Cappellari et al. (2012, 2013) claimed systematic variations in the IMF of elliptical galaxies. Moreover the results of Thomas et al. (2014a) hint to the fact that the IMF of power-law galaxies varies as a function of the observed effective velocity dispersion σ_e, ranging from a Kroupa to a Salpeter IMF, and that luminous ellipticals maintain a Kroupa IMF independently from σ_e. The latter could imply diverse IMFs or variations in the distribution of dark matter in core and power-law ellipticals. Triaxial models from van den Bosch & De Zeeuw (2010), performed without dark matter, have also been claimed to yield a doubled SMBH mass of the early-type galaxy NGC 3379 with respect to previous axisymmetric models. However the addition of a DM halo can increase the black hole mass if the mass-to-light ratio is overestimated (Gebhardt & Thomas, 2009; Rusli et al., 2013b). This is because dynamical models constrain the enclosed mass. Hence an overestimated mass-to-light ratio is compensated by a lighter black hole. Accurate estimates of the masses of SMBHs are crucial for advancing the knowledge on the demographics of black holes and for improving the precision in the scaling relations with their host galaxies. These problems serve as clear examples of why accurate triaxial dynamical models are needed. The goal of this Thesis is to write a triaxial implementation of the Schwarzschild method (see Section 1.8.3) starting from the existing axisymmetric code of Thomas et al. (2004). The existing triaxial implementation of the Schwarzschild method from van den Bosch et al. (2008) performs the de-projection of the observed surface brightness profile and the calculation of the gravitational potential and forces using the Multi Gaussian Expansion method from Cappellari (2002). It samples the representative stellar orbits following the recipe from de Zeeuw (1985a) and (Schwarzschild, 1993). The recipe was devised for triaxial separable potentials (see Section 1.8.2). Such potentials are known however to show unnatural central cores. van den Bosch & Van De Ven (2009) showed that their triaxial implementation of the Schwarzschild method recovers the viewing directions, intrinsic shapes and the orbital structures of triaxial separable Abel models. This Thesis advances previous work in the following points; it provides a fully three-dimensional implementation for the calculation of the gravitational potential and forces as an expansion in Spherical Harmonics (see Chapter 2). This implementation is independent from the method used to de-project the surface brightness profile. The gravitational potential of real galaxies varies from the center to the outskirts. In the center it is dominated by the SMBH and in the outer parts by dark matter. This work provides the first technique able to yield a coverage of phase-space with representative stellar orbits that adapts itself to the changes in the gravitational potential of real galaxies (see Chapter 2). The triaxial Schwarzschild code is tested against realistic spherical and triaxial reference models (see Chapter 3) and applied to the massive early-type galaxies NGC 1600 (see Chapter 4) and NGC 5419 (see Chapter 5).

1.7 Derivation of masses and stellar dynamical modelling

Self-consistent stellar dynamical modelling has played a key role in understanding the origin and the properties of elliptical galaxies. It allows for example to determine their total mass distribution and decompose it into luminous and dark components or to find the relics of the formation processes from the present configuration of stellar orbits. This kind of studies are commonly defined as *galactic archeology*. It is possible to model elliptical galaxies focusing on the dynamics of stars because of the low content of gas. This makes the complicated interplay between the motion of the stars and the hydrodynamics of gas negligible. An elliptical galaxy is to a first-order approximation an enormous collection of gravitationally bound stars (on the order of $10^9 - 10^{11}$ stars) spatially distributed over several Kiloparsecs. This means that the density distribution of stars is so low that collisions among them are rare. Quantitatively speaking, this concept can be rephrased by saying that the **relaxation time** $t_{\rm relax}$ [3] is longer than the estimated age of the Universe (Bertin, 2014). Thus early-type galaxies (and galaxies in general) can be considered to be collisionless systems. This implies that stars did not lose memory of their original orbit and so by reconstructing their orbital configuration it is possible to find clues on galaxy formation. The dynamics of collisionless systems can be modelled by computing the probability that a star at time t finds itself in the phase-space volume $\beth$. This is mathematically expressed by means of the phase-space distribution function (DF) defined as

$$f(\mathbf{x}, \mathbf{v}, t)\ \mathrm{d}\mathbf{x}\ \mathrm{d}\mathbf{v}. \tag{1.16}$$

The equation provides the number of stars at position $\mathbf{x}$ and velocity $\mathbf{v}$ at a certain time t in the range d$\mathbf{x}$ and d$\mathbf{v}$. From the phase-space distribution function it is possible to compute any observable $\Im$ of the system at time t by a phase-space projection

$$\Im = \int f(\mathbf{x}, \mathbf{v}, t)\wp(\mathbf{x}, \mathbf{v}, t)\ \mathrm{dV} \tag{1.17}$$

where $\wp$ is a suitable kernel and dV a volume in phase-space. For example the density distribution is

$$\rho(\mathbf{x}, t) = \int \mathrm{d}\mathbf{v} f(\mathbf{x}, \mathbf{v}, t). \tag{1.18}$$

The gravitational potential is related to the density through the Poisson's equation

$$\Delta\Phi = 4\pi \mathrm{G}\rho = 4\pi \mathrm{G} \int \mathrm{d}\mathbf{v} f(\mathbf{x}, \mathbf{v}, t). \tag{1.19}$$

For a collisionless system the DF is a solution of the **Collisionless Boltzmann Equation** (CBE). In cartesian coordinates it reads [4]

$$\frac{\mathrm{d}f}{\mathrm{d}t} = \frac{\partial f}{\partial t} + \mathbf{v} \cdot \frac{\partial f}{\partial \mathbf{x}} - \overrightarrow{\nabla}_x \Phi \cdot \frac{\partial f}{\partial \mathbf{v}} = 0 \tag{1.20}$$

where f is the distribution function, $\mathbf{v}$ the velocity vector, Φ the gravitational potential and $\overrightarrow{\nabla}_x = \frac{\partial}{\partial \mathbf{x}}$ the spatial gradient. The CBE describes how the DF evolves

---

[3] In mathematical terms, the relaxation time corresponds to the interval after which the mean squared variation in the velocity of a given test star due to the cumulative effect of several two-body encounters equals its original velocity, i.e. $\langle(\Delta v)^2\rangle = v^2_{\rm initial}$. For elliptical galaxies $t_{\rm relax}$ is on the order of 10^{14} years and the average dynamical time is on the order of 10^9 years (Bertin, 2014).

[4] The relaxation time decreases if the stellar density is large. In this case the equation becomes the Fokker-Planck equation (Binney & Tremaine, 2008).

in phase-space as a function of time and of the phase-space coordinates. It represents a continuity equation in phase-space and it states that the DF is constant along stellar orbits. Equations (1.19) and (1.20) are called the *fundamental equations of collisionless stellar dynamics* (Chandrasekhar, 1942) since their solution (the DF) provides through Equation (1.17) all the relevant astrophysical quantities describing a galaxy (as the surface brightness or the line-of-sight velocity distribution). Moreover a dynamical system whose potential Φ, density distribution ρ and DF are related by Equations (1.18)-(1.20) is said to be **self-consistent**. If a dynamical system is in equilibrium it is possible to introduce the notion of **integral of motion**. An integral of motion is a function $I(\mathbf{x}, \mathbf{v})$ of the phase-space coordinates that is constant along **all** trajectories. In mathematical terms $\frac{\mathrm{d}I}{\mathrm{d}t}(\mathbf{x}, \mathbf{v}) = 0$. The condition of I being an integral of motion is equivalent to the condition that I is a solution of the CBE. In fact

$$\frac{\mathrm{d}I}{\mathrm{d}t}(\mathbf{x}, \mathbf{v}) = \sum_{l=1}^{3} \frac{\partial I}{\partial x_l} \frac{\mathrm{d}x_l}{\mathrm{d}t} + \frac{\partial I}{\partial v_l} \frac{\mathrm{d}v_l}{\mathrm{d}t} = \mathbf{v} \cdot \vec{\nabla}_x I - \vec{\nabla}_x \Phi \cdot \frac{\partial I}{\partial \mathbf{v}} = 0. \tag{1.21}$$

An important consequence is **Jeans' Theorem** (Jeans, 1915; Binney, 1982).

Theorem 1. *Any steady-state solution of the CBE depends on the phase-space coordinates only through the integrals of motion. Any function of these integrals is a steady-state solution of the CBE.*

Proof. Given a function g of N integral of motions $I_1 \dots I_N$ then

$$\frac{\mathrm{d}g}{\mathrm{d}t}(I_1 \dots I_N) = \sum_{i=1}^{N} \frac{\partial g}{\partial I_i} \frac{\mathrm{d}I_i}{\mathrm{d}t} = 0. \tag{1.22}$$

☐

An integral of motion is **isolating** when it restricts the motion in phase-space to a sub-space of lower dimension. Moreover an integral of motion is usually said to be **classical** if it can be expressed analytically. If the potential is generated by a point mass (Keplerian-case) each orbit satisfies five isolating and classical integrals of motion, the energy (E), the three components of the angular momentum (L_x, L_y, L_z) and the Laplace-Runge-Lenz vector [5]. The motion is confined to an orbital plane where each orbit traces a closed curve. If the potential is spherical, the orbits possess four isolating and classical integrals (E, L_x, L_y, L_z) and lay on an orbital plane where they precess without necessarely closing on themselves. They are confined between a lower (pericentre) and upper (apocentre) radius (*Rosette shape*). Elliptical galaxies have been modelled (see Section 1.2) either as **axisymmetric** (symmetric with respect to a rotation around an axis) or

---

[5] The conservation of the energy and of the angular momentum and Laplace-Runge-Lenz vectors would suggest the presence of seven conserved quantities. In reality there are two equations that relate E, $\vec{L}$ and the Laplace-Runge-Lenz vector. This brings the number of conserved quantities down to five (Goldstein et al., 2002).

fully ellipsoidal (or **triaxial** in the astronomical vocabulary) objects. In both cases most orbits enjoy three isolating integrals of motion, thus being three-dimensional. The axisymmetric potential admits the energy and the component of the angular momentum aligned with symmetry axis (L_z if the potential is oblate and L_x if it is prolate) as classical integrals and a third non-classical integral I_3. In the general triaxial case the only explicitly known integral is E. Lynden-Bell (1962b) showed that a galaxy can be represented by a DF that depends only on isolating integrals of motion if (nearly) all orbits are regular (**Strong Jeans' Theorem**. An orbit is regular if it is confined to an invariant torus (Arnold, 1989).

1.8 Solutions of the CBE

The section provides an overview of the methods used to find a smooth phase-space distribution function that solves the CBE and minimises the deviations among the observables and their model predictions.

1.8.1 Jeans' models

The CBE can be re-written in terms of observable quantities as the mean stellar density or the mean velocity dispersion. This is done by re-casting the CBE in terms of the **moment**s of the DF. The result are the **Jeans' Equation**s

$$\rho\frac{\partial\langle v_k\rangle}{\partial t}+\sum_{l=1}^{3}\left(\frac{\partial(\rho\sigma_{kl}^2)}{\partial x_l}+\rho\frac{\partial\Phi}{\partial x_k}+\rho\langle v_l\rangle\frac{\partial\langle v_k\rangle}{\partial x_l}\right)=0 \tag{1.23}$$

where the mean streaming velocity is defined as $\int v_l\ f\ \mathrm{d}\mathbf{v}\equiv\rho\langle v_l\rangle$ [6] and $\sigma_{kl}^2(\mathbf{x})=\sigma_{kl}^2=\langle v_k\ v_l\rangle-\langle v_k\rangle\langle v_l\rangle$ is the **velocity dispersion tensor**. The tensor is symmetric $\sigma_{kl}=\sigma_{lk}$ and has therefore six independent terms. Jeans' modelling has been used to construct a spherical model of M87 (Binney & Mamon, 1982) and to measure the masses of supermassive black holes in S0 and early-type galaxies (e.g. Magorrian et al. 1998; Cretton & van den Bosch 1999) and their rotation (e.g. Binney et al. 1990, Magorrian & Binney 1994) and the dark matter content in dwarf spheroidal galaxies (Lokas, 2002). Cappellari (2008) presents the Jeans Anisotropic Modelling (JAM), an anisotropic extension of the semi-isotropic axisymmetric Jeans models. The method was applied to the galaxies from the ATLAS^{3D} survey (Cappellari et al., 2011, 2012). It is not clear how physically meaningful Jeans' models are. The solution of the Jeans' equations is not guaranteed to correspond to a (everywhere) non-negative DF. Jeans equations have also difficulties in modelling the higher-order information contained in the kinematic observations and are suspected to yield biased mass-to-light ratios (Li et al., 2016).

---

[6] The explicit dependence of the moment on the position is omitted, i.e. $\rho\langle v_l\rangle(\mathbf{x})=\rho\langle v_l\rangle$

1.8.2 DF-based models

Jeans' models do not yield the total distribution function of an observed system. This can be recovered with DF-based methods. Analytic DF-based models combine the ability of reproducing a large variety of the characteristics of observed galaxies with the fact that many of their properties can be derived analytically. The general requirement for applying these models is that the integrals of motion have analytical form (or are approximated by analytic functions). Isotropic (Dehnen, 1993; Tremaine et al., 1994; Jaffe, 1983; Hernquist, 1990) and anisotropic (Lynden-Bell, 1962a; Hunter, 1975; Wilson, 1975; Lake, 1981a,b; Bertin et al., 1992; Hunter & Qian, 1993) spherical models have been proposed over the years. It is also possible to construct three-integral axisymmetric models where the DF is a function of the energy and of two shape invariants (algebraic transformations of the integrals of motion). Such axisymmetric models allow diverse flattening and have a large variety of observable kinematics (Dehnen & Gerhard, 1993). If the potential is *separable* (of Stäckel form [7]) it is possible to construct axisymmetric and triaxial models where the stellar orbits have three classical isolating integrals of motion. An example is the **Perfect Ellipsoid** where the density distribution is stratified on concentric ellipsoids (de Zeeuw, 1985a; Dejonghe & de Zeeuw, 1988; Hunter & de Zeeuw, 1992). The application of DF-based methods is however limited. Purely spherical and isotropic galaxies do not exist. Separable potentials show unnatural cores. Furthermore the number of potentials for which all the integrals of motion are known analytically is low and sub-classes of DFs that admit only classical integrals, as the axisymmetric (oblate) two-integral models, fail to reproduce simultaneously the observed kinematics of elliptical galaxies along the projected major and minor axes (Bender et al., 1994).

1.8.3 Non-parametric methods

Jeans' models and DF-based methods have limited applicability. Jeans' Equations do not form a closed set of equations and do not guarantee physically meaningful solutions. DF-based methods require the full knowledge of all the isolating integrals of motion. The so-called non-parametric methods pose instead no restriction on the form of the potential and of the DF. They can be extended to arbitrary geometry and allow also to include multiple components as stars, black holes and dark matter haloes.

---

[7] A potential is of Stäckel form if the Hamilton-Jacobi equation separates in confocal ellipsoidal coordinates. Dynamically speaking this property translates in the fact that the stellar orbits can be seen as the sum of three independent motions taking place in each coordinate (de Zeeuw, 1985a).

The made-to-measure method evolves in time an initial self-gravitating N-body model. The model prediction ξ of the observable Ξ is

$$\xi = \sum_{i=1}^{N_{\text{particle}}} w_i \cdot \xi_i, \tag{1.24}$$

where ξ_i and w_i are the contribution to the observable and the **weight** of particle i. The weight quantifies the amount of mass the particle transports. The model is evolved for a small time-step δt by integrating the equations of motion of all particles. The weights are slowly updated so that the model reproduces the observables. The weights are changed by maximising a profit function. The function is given by the difference between an entropy term that ensures the smoothness of the resulting DF and the mean-square difference (χ^2) among the observables and their model predictions. The made-to-measure method (M2M) is a *particle-based* technique since particles are its basic ingredients. The method produces self-consistent models of galaxies in the sense that the particles move in a total potential they all contribute to generate. The accuracy with which the method reproduces the properties of the target galaxy depends on how close the initial N-body model is to the final solution. The method was first introduced by Syer & Tremaine (1996). De Lorenzi et al. (2007) developed the N-particle Made-to-measure Algorithm mInimising Chi squared (NMAGIC), a M2M method capable of fitting the data of real galaxies. M2M methods have been applied to elliptical galaxies (De Lorenzi et al., 2009; Das et al., 2011; Morganti & Gerhard, 2012) and to the Milky Way (Portail et al., 2015a,b, 2016; Pérez-Villegas et al., 2017a,b). Moreover Blaña et al. (2016, 2017) use NMAGIC to reproduce the 2D stellar kinematics of M31 from Opitsch (2016) and Opitsch et al. (2017), finding that M31 has a coexisting classical bulge and a bar of similar masses and a cored dark matter density profile.

The Schwarzschild method (SM) Schwarzschild (1979, 1982) is a rigorous technique that provides self-consistent solutions of the CBE. It finds the most appropriate superposition of a finite number of representative stellar orbits. The DF is given as

$$f = \sum_{i=1}^{N_{\text{orbit}}} w_i \cdot f_i \tag{1.25}$$

where w_i and f_i are respectively the weight and the DF of orbit i and N_{orbit} the number of representative orbits. The weight quantifies the amount of light associated to an orbit. The SM is usually referred to as an *orbit-based* technique. This is because stellar orbits are the building blocks of the model. Combining Equations (1.17) and (1.25), any observable $\Im$ of the system at time t equals the linear combination of the time-averaged orbital contributions $\Im_i$

$$\Im = \sum_{i=1}^{N_{\text{orbit}}} w_i \cdot \int f_i \; \wp(\mathbf{x}, \mathbf{v}, t) \; \mathrm{dV} = \sum_{i=1}^{N_{\text{orbit}}} w_i \cdot \Im_i. \tag{1.26}$$

Schematically the method consists of four steps: (1) After assuming a trial viewing direction for the target galaxy, the observed surface brightness profile is deprojected into a three-dimensional light distribution ν. The total mass density distribution ρ is parametrised as

$$\rho = \rho_* + \rho_{\mathrm{DM}} \tag{1.27}$$

where $\rho_* = \nu \cdot \mathrm{M/L}$ is the stellar mass density distribution. M/L is the stellar mass-to-light ratio of the galaxy and ρ_{DM} is a parametrisation for the density distribution of the dark matter halo. The total gravitational potential corresponding to Equation (1.27) reads

$$\Phi = \Phi_* + \Phi_{\mathrm{DM}} + \Phi_{\mathrm{SMBH}} \tag{1.28}$$

where Φ_{SMBH} is Keplerian contribution of the super-massive black hole (SMBH) of mass $\mathrm{M}_{\mathrm{SMBH}}$ at the center of the galaxy. The parameters defining the dark matter halo parametrisation, together with $\mathrm{M}_{\mathrm{SMBH}}$ and M/L will be hereafter referred to as **input mass parameters**. (2) A set (library) of representative stellar orbits is integrated for a trial mass distribution, given a suitable choice for the input mass parameters. (3) The representative orbits are superimposed so that the observables are fitted and the DF is smooth. (4) The procedure is repeated for different values of the input mass parameters and viewing angles. The best fitting model is selected by minimising χ^2. The effectiveness of the DF reconstruction relies on the **orbit sampling technique**. It is a recipe for sampling the initial conditions of the orbits. The technique makes sure that any combination of the isolating integrals of motion has a counterpart in the library. Further details on the implementation of the SM will be provided in Chapter (2). In principle the only requirement for applying the Schwarzschild method is that the galaxy is collisionless and in a stationary state, without any initial hypothesis on the configuration of the orbits. However implementations often assume particular internal symmetries with the aim of simplifying the modelling effort. Over the years spherical (Richstone & Tremaine, 1984; Rix et al., 1997), axisymmetric (van der Marel et al., 1998; Cretton et al., 1999; Gebhardt et al., 2000b; Thomas et al., 2004; Valluri et al., 2004) and triaxial (van den Bosch et al., 2008) implementations of the SM have been published. The SM has been successfully used to determine the orbital structure, SMBH masses and the SMBH scaling relations of composite bulges and elliptical galaxies (Cretton & van den Bosch, 1999; Cappellari et al., 2002; Verolme et al., 2002; Gebhardt et al., 2003; Siopis et al., 2009; van den Bosch & De Zeeuw, 2010; Nowak et al., 2007, 2008, 2010; Rusli et al., 2011; van den Bosch et al., 2012; Rusli et al., 2013a,b; Thomas et al., 2014b; Erwin et al., 2014; Mazzalay et al., 2016; Saglia et al., 2016; Thomas et al., 2016), the stellar initial mass function and the distribution of DM in early-type galaxies (Cappellari et al., 2006; Thomas et al., 2011), the SMBH mass, stellar M/L and DM halo in the giant elliptical galaxy M87 (Gebhardt & Thomas, 2009) and the DM scaling relations and the assembly epoch of Coma Cluster early-type galaxies (Thomas et al., 2009).

1.9 Equilibrium models

The shapes of individual stellar orbits are closely linked to the overall dynamics and properties of stellar systems. This section will give an overview of the different orbital types (families) commonly found in the gravitational potential of galaxies. The section follows the elegant presentations in Arnold (1989) and Binney & Tremaine (2008). The first subsection will deal with the orbits in a central potential. Subsequently, the section will focus on the orbits in axisymmetric and triaxial potentials. The orbital structures described are those of **non-rotating** potentials corresponding to **integrable** Hamiltonians, i.e. systems for which all orbits are confined to invariant tori (**regular** orbits). Hamiltonians associated to the potentials of real galaxies are instead called **near-integrable** since a large fractions (but not all) of the orbits are indeed regular (Binney & Tremaine, 2008).

1.9.1 Motion in a central potential

A potential is defined to be **central** if it depends only on the distance from the center. The motion in such a potential is characterised by the conservation of the angular momentum L, which is perpendicular to the orbital plane of the star. In polar coordinates the Lagrangian per unit mass reads

$$\mathscr{L} = \frac{1}{2}\left[\dot{r}^2 + (r\dot{\varphi})^2\right] - \Phi(r) \tag{1.29}$$

and the equations of motion are

$$\begin{aligned} \frac{\mathrm{d}}{\mathrm{d}t}\frac{\partial\mathscr{L}}{\partial\dot{r}} - \frac{\partial\mathscr{L}}{\partial r} &= \ddot{r} - r\dot{\varphi}^2 + \frac{\partial\Phi}{\partial r} = 0 \\ \frac{\mathrm{d}}{\mathrm{d}t}\frac{\partial\mathscr{L}}{\partial\dot{\varphi}} - \frac{\partial\mathscr{L}}{\partial\varphi} &= \frac{\mathrm{d}}{\mathrm{d}t}\left(r^2\dot{\varphi}\right) = 0. \end{aligned} \tag{1.30}$$

The second equation is the conservation of the angular momentum vector $L = r^2\dot{\varphi}$ and it allows to re-write the first equation of motion only as a function of the distance from the center. In this way the two-dimensional motion on the orbital plane in the central potential $\Phi(r)$ can be seen as a one-dimensional problem in the *effective potential*

$$\Phi_{\mathrm{eff}}(r) \equiv \Phi(r) + \frac{L^2}{2r^2}. \tag{1.31}$$

Orbits in such potential are dense in annuli (Rosette shape) as shown in Figure (1.9); the azimuthal angle φ increases monotonically and the radius oscillates between a pericentre and an apocentre. A special case is the **Keplerian** potential. It is generated by a point mass M and varies as the inverse of the distance from center. The trajectory of bound orbits is an ellipse.

1.9.2 Motion in axisymmetric (oblate) potentials

As mentioned in Section (1.5), faint elliptical galaxies are rotationally supported and approximate figures of revolution. In cylindrical coordinates, the Lagrangian

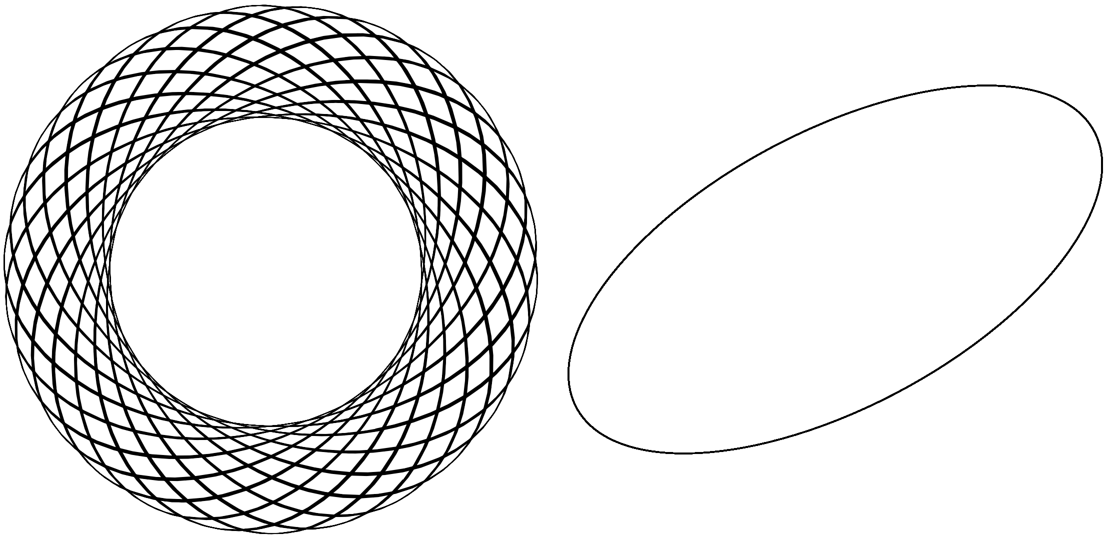

Figure 1.9: Orbit in a central (left) and Keplerian potential (right).

per unit mass reads

$$\mathscr{L} = \frac{1}{2}\left[\dot{R}^2 + \left(R\dot{\phi}\right)^2 + \dot{z}^2\right] - \Phi(R,z) \tag{1.32}$$

and the equations of motion are

$$\begin{aligned}
\tfrac{\mathrm{d}}{\mathrm{d}t}\tfrac{\partial \mathscr{L}}{\partial \dot{R}} - \tfrac{\partial \mathscr{L}}{\partial R} &= \ddot{R} - R\dot{\phi}^2 + \tfrac{\partial \Phi}{\partial R} = 0 \\
\tfrac{\mathrm{d}}{\mathrm{d}t}\tfrac{\partial \mathscr{L}}{\partial \dot{\phi}} - \tfrac{\partial \mathscr{L}}{\partial \phi} &= \tfrac{\mathrm{d}}{\mathrm{d}t}\left(R^2\dot{\phi}\right) = 0 \\
\tfrac{\mathrm{d}}{\mathrm{d}t}\tfrac{\partial \mathscr{L}}{\partial \dot{z}} - \tfrac{\partial \mathscr{L}}{\partial z} &= \ddot{z} + \tfrac{\partial \Phi}{\partial z} = 0,
\end{aligned} \tag{1.33}$$

with $R = r\cos(\theta)$ and the second equation being the conservation of L_z. The dynamics of an axisymmetric three-dimensional system can be described in a **meridional plane** (R,z) that rotates with velocity $\dot{\phi} = \frac{L_z}{R^2}$. The motion in the meridional plane obeys the Hamitonian

$$H(R,\dot{R},z,\dot{z}) = \frac{1}{2}\left[\dot{R}^2 + \dot{z}^2\right] + \Phi_{\text{eff}}(R,z) \tag{1.34}$$

where Φ_{eff} is the effective potential

$$\Phi_{\text{eff}}(R,z) \equiv \frac{L_z^2}{2R^2} + \Phi(R,z). \tag{1.35}$$

The motion is confined within the **zero-velocity curve** (ZVC) given by the points (R,z) where the kinetic energy $E_{\text{kin}} = H - \frac{L_z^2}{2R^2} - \Phi(R,z) = 0$. Orbits with non-vanishing angular momentum feel a centrifugal potential barrier near the center and oscillate between a minimum and maximum radius. They enjoy an effective third integral I_3 that restricts their motion in z and circulate in a fixed sense around the short axis forming a doughnut-like shape as the one shown in Figure (1.10). Such orbits are called **short-axis tubes**. In a prolate axisymmetric potential the x-component of the angular momentum L_x is conserved. In this case there are two types of orbits, the **inner-** and **outer long-axis tubes**. They circulate in a fixed sense around the long axis of the system.

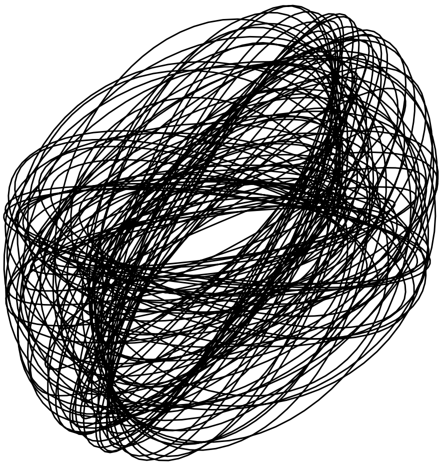

Figure 1.10: Short-axis tube orbit computed in a non-rotating axisymmetric potential.

Surface of section The (isolating) integrals of motion are relations among the phase-space variables. They thereby confine the motion of a star to a hyper-surface within phase-space. The **surface of section** (SOS) is a two-dimensional slice through this hyper-surface (Henon & Heiles, 1964; Richstone, 1982). In an axisymmetric (oblate) potential the motion obeys the Hamiltonian from Equation (1.34) and the phase-space coordinates are $(R, \dot{R}, z, \dot{z})$. An example of surface of section is then the set of points for which the condition $\left\{H(R, \dot{R}, z, \dot{z}) = E,\ z = 0\right\}$ is fullfield. An orbit with energy E leaves an imprint (*consequent*) on this surface of section each time it crosses the $z = 0$ plane. From the topology of the SOS it is possible to determine the nature of an orbit. For example the fact that the consequents lay on a smooth curve (*invariant curve*) is an indication that the orbit conserves a third integral of motion I_3.

1.9.3 Motion in triaxial potentials

In a triaxial potential the orbital structure is richer than that found in the axisymmetric (oblate) case. There are at least four main orbit types as shown in Figure (1.11(a)). Together with the short-axis tubes, there are the inner and outer long-axis tubes and **box orbits**. Tube orbits that rotate around the intermediate axis are unstable (Heiligman & Schwarzschild, 1979). Tube orbits avoid the center of the stellar system. Box orbits instead have no net sense of rotation and are thereby centrophilic. Box orbits play a fundamental role in supporting triaxial shapes (Schwarzschild, 1979; Hunter & de Zeeuw, 1992). As mentioned in Section (1.5) the presence of minor axis rotation can be used a kinematic tracer for triaxiality (Contopoulos, 1956; Kondratev & Ozernoi, 1979). Studies from Miralda-Escude & Schwarzschild (1989), Lees & Schwarzschild (1992) and Schwarzschild (1993) found that the scale-free non-rotating logarithmic triaxial potential [8] can be divided into three sections (a core, a main body and a halo) based on the orbital structure. In the central core region the potential is close to that of a three-dimensional incommensurate harmonic oscillator and all stars follow box orbits (Schwarzschild, 1979; de Zeeuw & Merritt, 1983; de Zeeuw, 1985b). The main body of the potential hosts the four orbit types shown in Figure (1.11(a)) that are peculiar to separable Stäckel potentials (de Zeeuw, 1985a). In the halo part, the three tube families are present and the box orbits are replaced by **Boxlets** and stochastic orbits (Schwarzschild, 1993). Moreover Gerhard & Binney (1985) and Norman et al. (1985) found that the presence of a massive black hole or of a central density cusp renders box orbits unstable. The portion of phase-space formerly occupied by box orbits is taken over by centrophobic boxlets as the banana orbit. The intensity of this phenomenon depends on how massive/cuspy the black hole/density profile is. The disappearance of box orbits rounds the mass distribution, bringing about a loss of triaxiality in the center. A selection of boxlets orbits is shown in Figure (1.11(b)). Moreover Table (1.1) summarises the orbital structure found in the potentials analysed in this section.

Potential	**Orbit dimension**	**Orbital type**
Central	2D	R
Oblate	3D	S
Prolate	3D	IL + OL
Triaxial	3D	S + IL + OL + B

Table 1.1: Summary of the orbital structure discussed in this section, where R = rosette shaped orbit, S = short-axis tube, IL = inner long-axis tube, OL = outer long-axis tube and B = box orbit.

---

[8] The logarithmic potential has the important astronomical feature to produce a flat rotation curve as the one observed in real galaxies.

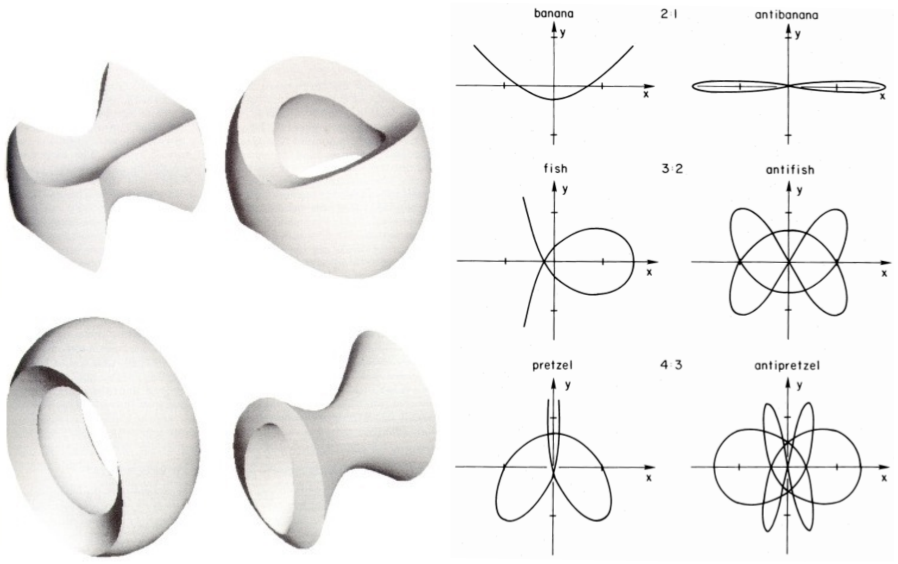

(a) (b)

Figure 1.11: Figure (1.11(a)) portrays the time-averaged orbital density shapes of the main families of orbits in a non-rotating, integrable, triaxial potential from Statler (1987). In the top row a box orbit (left) and short-axis tube (right). In the bottom row an outer (left) and inner (right) long-axis tube. Figure (1.11(b)) shows closed boxlets orbits in a singular logarithmic potential from Miralda-Escude & Schwarzschild (1989). On the left the centrophobic and the right the centrophilic orbits.

1.10 Outline of the Thesis

In this Thesis, a novel triaxial implementation of the Schwarzschild method for the modelling of the density distribution and observed kinematic structure of massive triaxial early-type galaxies has been developed. The implementation allows to measure the total mass of elliptical galaxies and to decompose it into luminous (stars) and dark (dark matter and central black hole) components. Chapter (2) describes the implementation. Chapter (3) describes the testing of the code on a isotropic spherical model and on a triaxial N-body realisations of a stellar system. Chapter (4) presents a three-dimensional axisymmetric model of the massive elliptical galaxy NGC 1600. Chapter (5) provides the first application of the method to the study of the intrinsic and projected dynamics of the massive triaxial early-type galaxy NGC 5419. Chapter (6) concludes the Thesis and provides future perspectives, focusing on the possible improvements of the present implementation and its upcoming applications to increasingly higher resolution data coming in the next decade (for example from instruments as MICADO mounted on the European Sourthern Observatory Extremely Large Telescope [9]) that will allow to close the circle on the origin and the formation of early-type galaxies.

---

[9] Further information about MICADO is available at `https://www.eso.org/public/germany/teles-instr/elt/elt-instr/micado/`.

Chapter 2

SCHERPA

The chapter describes **SCHERPA**, the **SCH**warzschild m**E**thod for t**R**iaxial early-ty**P**e g**A**laxies, a triaxial implementation of the Schwarzschild method. The chapter builds up from what is described in Finozzi (2013) and deals with the refinements and considerable restructuring carried out over the course of this PhD project. Section (2.1) describes how the code is organised. Section (2.2) deals with the de-projection of the observed surface brightness profile. Subsequently the chapter delineates in Section (2.3) how SCHERPA reads-in, interpolates and integrates on appropriate binning grids the input three-dimensional density distribution and, in Section (2.4), how it solves the Poisson Equation to yield the gravitation potential and forces. Section (2.5) focuses on the sampling of the initial conditions and the integration of the representative stellar orbits. Section (2.6) reports on the superposition of the orbit library. Section (2.7) describes the technique used to efficiently search for the best fitting model in the space of the input mass parameters and viewing angles and details the multi-core implementation of SCHERPA.

2.1 Structure of the code

The section overviews the program units (modules) in which SCHERPA [1] is organised. The code is implemented in FORTRAN (FORmula TRANslation) in the F90/F95 standard (Brainerd et al., 1996). Figure (2.1) provides a flowchart description of the main steps in SCHERPA. Module **depromod.f90** implements the de-projection of the surface brightness profile. Module **gdenmod.f90** is responsible for setting the spatial binning grids in which coordinate space is organised and the binning grid for the projected velocity. It reads-in, interpolates and integrates the input three-dimensional density distribution. Module **potforcemod.f90** contains the implementation of the calculation of the gravitational potential and forces. Module **librarymod.f90** comprise the routines responsible

---

[1] The specifications of the code are described in Appendix A.

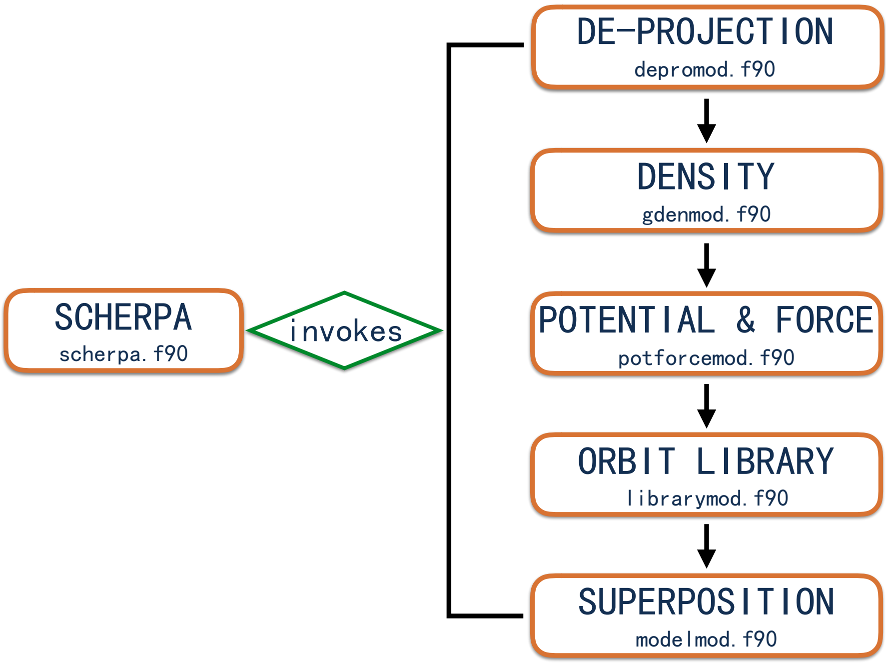

Figure 2.1: A flowchart description of main steps in SCHERPA together with the names of the modules where these steps are implemented.

for the creation of the library of representative stellar orbits and the calculation of their time-averaged properties. Module **modelmod.f90** details how the orbits are superimposed to fit the observables.

2.2 De-projection

The observations of any astrophysical object are projected onto the plane of the sky. It is important to accurately de-project them in order to get the corresponding intrinsic quantities. This section focuses on the de-projection of the surface brightness profile. It yields the three-dimensional light distribution ν. The first subsection provides an introduction on the de-projection problem. The second subsection presents the intrinsic and projected coordinate frames and the viewing angles. The third subsection introduces the Multi Gaussian Expansion method following what described in Cappellari (2002) and van den Bosch et al. (2008). The remaining subsections describe the implementation of the method as detailed in the module **depromod.f90** and its testing.

2.2.1 General introduction

The de-projection of the surface brightness profile is not unique. As discussed in Rybicki (1987) the source of this degeneracy can be understood in terms of the **Fourier Slice Theorem**: the Fourier transform of the surface brightness profile provides information only about the slice of the Fourier transform of ν perpendicular to the line-of-sight. In the spherical case or for a system viewed edge-on this slice is enough to uniquely reconstruct ν. The de-projection is ambiguous for inclinations between the edge-on and face-on views and most degenerate in the face-on case. In fact a region of Fourier space known as *cone of ignorance* remains unconstrained. It is not possible in projection to distinguish among density distributions that differ only for the mass contained in the cone of ignorance. The de-projection of triaxial systems is even less constrained since the range of intrinsic triaxial densities compatible with a given surface brightness profile is greater (Gerhard & Binney, 1996). A first approach to perform the de-projection is to assume the stellar system to have a luminosity density stratified on concentric ellipsoids with ellipsoidal radius $m = \sqrt{x^2 + \frac{y^2}{p^2} + \frac{z^2}{q^2}}$ where $q \leq p \leq 1$ are the axes ratios. Such models project to a surface brightness profile with elliptical isophotes (Contopoulos, 1956; Stark, 1977; Binney, 1985) and are a useful approximation to real elliptical galaxies. They however fail to reproduce ellipticity variations and isophotal twists. Another approach are non-parametric methods (Magorrian, 1999; Bissantz & Gerhard, 2002). They are nevertheless complicated and require a significant time to converge. For these reasons in this project the de-projection of the surface brightness profile will be performed by means of a parametric method the Multi Gaussian Expansion (MGE) introduced by Monnet, G., Bacon, R., Emsellem (1992); Emsellem et al. (1994a); Cappellari (2002) and used to model various galaxies (e.g. Emsellem et al. 1994b; Cretton & van den Bosch 1999; Cappellari 2008). The MGE provides also a method for the computation of the gravitational potential and force components (van den Bosch et al., 2008). In SCHERPA they are computed as an expansion in Spherical Harmonics (see Section 2.4). This implementation has the advantage of being independent from the method used to de-project the surface brightness profile. [2].

2.2.2 Coordinate systems for the Multi Gaussian Expansion

The de-projection involves a transformation from the coordinate system (x', y', z') on the plane of the sky to the intrinsic coordinate system (x, y, z). The line-of-sight coincides with the z'-axis and (x', y') is the plane of the sky. The orientation of the projected coordinate system with respect to the intrinsic frame is specified by the **viewing angles** $(\vartheta, \varphi, \psi)$. As shown in Figure (2.2(a)), ϑ and φ give the orientation of the z'-axis with respect to the intrinsic frame. Angle ψ is a rotation around the line-of-sight. It is chosen to align the major axis of the innermost Gaussian component with the x'-axis. As shown in Figure (2.2(b)), it is measured counter-clockwise from the North to the projected major axis of the galaxy. Projections along the intrinsic major and minor axes correspond respectively to

---

[2] A future prospect of the project is in fact to develop a fully non-parametric method for the triaxial de-projection of the surface brightness profile.

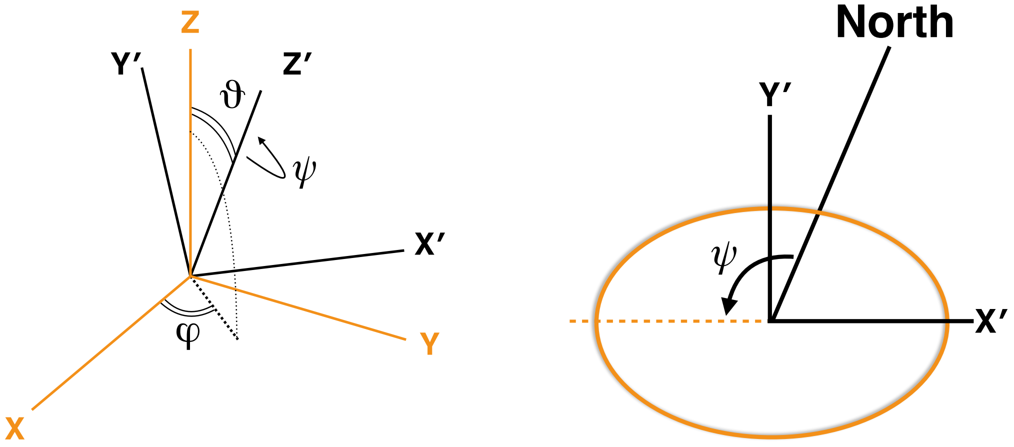

(a) Coordinate systems

(b) Viewing angle ψ

Figure 2.2: On the left, a graphical representation of the intrinsic (**orange**) and projected (**black**) coordinate systems and of the viewing angles $(\vartheta, \varphi, \psi)$. On the right, a depiction of the viewing angle ψ. The orange ellipse is a stylised representation of a galaxy. The dashed line portrays the projected major axis of the galaxy.

$(\vartheta = \frac{\pi}{2}, \varphi = 0)$ and $(\vartheta = 0, \varphi = 0, \ldots, \frac{\pi}{2})$. The coordinate systems are related as

$$\begin{pmatrix} x' \\ y' \\ z' \end{pmatrix} = \mathbf{R} \cdot \mathbf{P} \cdot \begin{pmatrix} x \\ y \\ z \end{pmatrix} \tag{2.1}$$

where matrix **P** is responsible for the projection onto the plane of the sky and **R** expresses the rotation around the line-of-sight by angle ψ. The matrices are

$$\mathbf{P} = \begin{pmatrix} -\sin\varphi & \cos\varphi & 0 \\ -\cos\vartheta\cos\varphi & -\cos\vartheta\sin\varphi & \sin\vartheta \\ \sin\vartheta\cos\varphi & \sin\vartheta\sin\varphi & \cos\vartheta \end{pmatrix} \tag{2.2}$$

$$\mathbf{R} = \begin{pmatrix} \sin\psi & -\cos\psi & 0 \\ \cos\psi & \sin\psi & 0 \\ 0 & 0 & 1 \end{pmatrix} \tag{2.3}$$

Appendix (B.1) provides the expressions of $\mathbf{P}^{-1}$ and $\mathbf{R}^{-1}$.

2.2.3 Multi Gaussian Expansion

The MGE finds the intrinsic luminosity density ν that projects to a surface brightness profile parametrised as a sum of N_{comp} two-dimensional Gaussian functions (components)

$$SB(r_{\text{sky}}, \theta_{\text{sky}}) = \sum_{j=1}^{N_{\text{comp}}} \frac{L_j}{2\pi\sigma_j'^2 q_j'} \exp\left[-\frac{1}{2\sigma_j'^2}\left(x_j'^2 + \frac{y_j'^2}{q_j'^2}\right)\right] \tag{2.4}$$

where $r_{\rm sky}$ and $\theta_{\rm sky}$ are the polar coordinates on the plane of the sky and

$$\begin{aligned} x'_j &= r_{\rm sky}\sin(\theta_{\rm sky}-\psi'_j) \\ y'_j &= r_{\rm sky}\cos(\theta_{\rm sky}-\psi'_j). \end{aligned} \tag{2.5}$$

The parameters q'_j, σ'_j and L_j are the projected flattening of the Gaussian function, its length scale along the projected major axis and its luminosity (weight). The projected flattening assumes values $0 \leq q'_j \leq 1$. Angle ψ'_j is the position angle measured counter-clockwise from the y'-axis to the major axis of the Gaussian. It is given by

$$\psi'_j = \psi + \Delta\psi'_j \quad \text{with} \quad \Delta\psi'_1 \equiv 0 \tag{2.6}$$

where $\Delta\psi'_j$ is the isophotal twist. The surface brightness profile from Equation (2.4) corresponds to the intrinsic luminosity density

$$\nu(x,y,z) = \sum_{j=1}^{N_{\rm comp}} \frac{L_j}{(\sigma_j\sqrt{2\pi})^3 p_j q_j} \exp\left[-\frac{1}{2\sigma_j^2}\left(x^2+\frac{y^2}{p_j^2}+\frac{z^2}{q_j^2}\right)\right] \tag{2.7}$$

where q_j, p_j qnd σ_j are the **intrinsic shape parameters**. The components in Equation (2.7) are three-dimensional coaxial Gaussian functions with ellipsoidal shape. The first step in the MGE method is to fit the parametric expression from Equation (2.4) to the observed surface brightness profile in order to determine the parameters L_j, σ'_j, q'_j and $\Delta\psi'_j$. This is done by means of the software from Michele Cappellari (Cappellari, 2002) freely available at `http://www-astro.physics.ox.ac.uk/~mxc/software/` in Python and IDL. The number of Gaussian components to be used is initially set to $N_{\rm comp} = 10$. As discussed in Cappellari (2002), Gaussians are then added until the fit does not vary appreciably (e.g. the variations in the χ^2 are lower than 1 %). Fits where the components are required to have the same position angle can be performed using the fully linear version of the algorithm [3]. In this case $N_{\rm comp}$ is determined autonomously by the code. The intrinsic shape parameters for a given viewing direction are

$$1-{q_j}^2 = \frac{\delta'_j \cdot \left\{2\cos 2\psi'_j + \sin 2\psi'_j \cdot \left[\sec\vartheta\cdot\cot\varphi - \cos\vartheta\cdot\tan\varphi\right]\right\}}{2\sin^2\vartheta\cdot\left[\delta'\cdot\cos\psi'_j\cdot\left(\cos\psi'_j + \cot\varphi\cdot\sec\vartheta\cdot\sin\psi'_j\right)-1\right]} \tag{2.8}$$

$${p_j}^2-{q_j}^2 = \frac{\delta'_j \cdot \left\{2\cos 2\psi'_j + \sin 2\psi'_j \cdot \left[\cos\vartheta\cdot\cot\varphi - \sec\vartheta\cdot\tan\varphi\right]\right\}}{2\sin^2\vartheta\cdot\left[\delta'\cdot\cos\psi'_j\cdot\left(\cos\psi'_j + \cot\varphi\cdot\sec\vartheta\cdot\sin\psi'_j\right)-1\right]} \tag{2.9}$$

---

[3] Details about the fully linear version of the MGE software are available in Section (3.4) of Cappellari (2002).

$$\sigma_j^2 = \frac{q_j' \cdot {\sigma_j'}^2}{\sqrt{p_j^2 \cdot \cos^2\vartheta + q_j^2 \cdot \sin^2\vartheta\left(p_j^2 \cdot \cos^2\varphi + \sin^2\varphi\right)}} \tag{2.10}$$

where $\delta_j' = 1 - (q_j')^2$ and $0.2 < q_j \leq p_j \leq 1$ [4]. A physically meaningful de-projection may not be found for every combination of the viewing angles (Bertola et al., 1991). Each component has different observed flattening q_j' and photometric twists $\Delta\psi_j'$. The volume in the space of the viewing angles for which the de-projection of the galaxy is allowed is given by the intersection of the volumes of single components (Williams, 1981). Components with $q_j' = 1$ can be de-projected along any viewing direction. The flatter the component the tinier its allowed volume will be (van den Bosch et al., 2008). If a component is photometrically twisted with respect to the others the final allowed volume for the galaxy will be even smaller. The volume of allowed viewing directions for a galaxy is limited by the $\min(q_j')$ and the $\max\left(|\Delta\psi_j'|\right)$ as discussed in Cappellari (2002) and van den Bosch et al. (2008). Galaxies with high $\min(q_j')$ and low $\max\left(|\Delta\psi_j'|\right)$ have the largest allowed volume. The MGE allows axisymmetric and triaxial de-projections. For an oblate axisymmetric de-projection $\psi = \frac{\pi}{2}$ (van den Bosch et al., 2008) and Equation (2.8) and (2.9) become respectively

$$q_j = \sqrt{1 - \frac{\delta_j'}{\sin^2(\vartheta)}} \quad \text{and} \quad p_j = 1. \tag{2.11}$$

The de-projection is triaxial if ψ_j' are different (Cappellari, 2002). One important limitation of the MGE method is that it does not allow to investigate the densities in the cone of ignorance. In fact the MGE provides just one de-projected density ν for a given combination of the viewing angles $(\vartheta, \varphi, \psi)$. Moreover the de-projection is always axisymmetric if all $\Delta\psi_j' = 0$ and $\psi = \frac{\pi}{2}$. This is true even if, as discussed in Section (3.2.5), the galaxy is intrinsically triaxial. In this case triaxial shapes are probed by treating ψ as a free parameter and setting it to $\psi \neq \frac{\pi}{2}$.

2.2.4 Implementation

The MGE method has been implemented in four routines. The first routine (**read_input()**) reads-in the output of Michele Cappellari's code. The output comes in the form shown in Table (2.1). For each Gaussian component Table (2.1) shows the total counts counts$_j$, the sigma σ_j' in units of pixel, the observed flattening q_j' and the isophotal twist $\Delta\psi_j'$ expressed in degrees. The routine checks if the position angles ψ_j' are the same. If so, it sorts the components from the flattest to the roundest. The second routine (**angles()**) verifies if a given viewing direction $(\vartheta, \varphi, \psi)$ corresponds to a physically meaningful de-projection. When the position angles differ the viewing direction is accepted if

$$0.2 < q_j \leq p_j \leq 1 \quad \forall j = 1 \ldots N_{\text{comp}}. \tag{2.12}$$

---

[4] It is easy to show that the Equations (2.8)-(2.10) are valid for $\vartheta \in (0, \frac{\pi}{2}) \cup (\frac{\pi}{2}, \pi)$ and $\varphi \in (0, \frac{\pi}{2}) \cup (\frac{\pi}{2}, \pi) \cup (\pi, \frac{3}{2}\pi) \cup (\frac{3}{2}\pi, 2\pi)$.

The statistical considerations on the intrinsic shape of elliptical galaxies from the observed distribution of Hubble types mentioned in Section (1.5) rule out intrinsic shapes for which $q < 0.2$. If the position angles are equal it is sufficient to check that the flattest (first) component satisfies Equation (2.12). The third routine (**physical_units()**) converts the observed total counts and σ'_j to solar luminosities and arcseconds. The final routine (**depro_density()**) computes the intrinsic shapes parameters and stores them into arrays. Afterwards it defines a grid in spherical coordinates where it evaluates the de-projected density. The routine uses a linear binning for $\theta \in [-\frac{\pi}{2}, \frac{\pi}{2}]$ and $\phi \in [0, \pi]$ and a logarithmic one for $r \in [r_{\rm min}, r_{\rm max}]$. The minimum and maximum radii are computed from the minimum and maximum value of the σ_j of the components as $r_{\rm min} = \sigma_{\rm min}/100$ and $r_{\rm max} = 3 \times \sigma_{\rm max}$. The number of bins is $N_{r,\rm dens} = 300$ and $N_{\theta,\rm dens} = N_{\phi,\rm dens} = 101$ (see Section 2.3.4). The density ν has a flat central core and falls down as $\sim \exp(-r^2)$ for large radii. Therefore the routine samples ν coarsely for $r \leq r_{\rm medium} = \sigma_{\rm max}/100$ at $N_{r,\text{dens-inner}} = N_{r,\rm dens}/3$ radii. For $r > r_{\rm medium}$ the density is sampled with a finer binning at $N_{r,\text{dens-outer}} = N_r - N_{r,\text{dens-inner}}$ radii. Figure (2.3) provides a flowchart representation of the implementation.

Component	**counts$_j$**	$\boldsymbol{\sigma'_j}$	**q$'_j$**	$\boldsymbol{\Delta\psi'_j}$
1	8198.48	0.38000	1.000000	0.0
2	44161.1	5.88124	0.899775	0.0
3	215881.0	13.5803	0.672745	0.0
4	348640.0	21.8192	0.815558	0.0
5	1.26569×10^6	46.0376	0.681965	0.0
6	2.17338×10^6	82.7561	0.775966	0.0
7	1.97307×10^6	149.808	0.714511	0.0
8	3.86588×10^6	246.401	0.738354	0.0
9	4.41886×10^6	478.825	0.732588	0.0
10	8.42750×10^6	870.403	0.733947	0.0
11	2.76482×10^7	2777.72	0.774998	0.0

Table 2.1: Parameters obtained from the MGE fit to an HST/WFPC2/F814W image of IC1459 from *Getting Started with the MGE_FIT_SECTORS Package* available at `http://www-astro.physics.ox.ac.uk/~mxc/software/`, where σ'_j is expressed in units of pixel and $\Delta\psi'_j$ in degrees.

2.2.5 Test of the implementation

The test of the MGE algorithm is carried out on a toy-model introduced in Finozzi (2013). The model is given by the sum of ten Gaussian components with different

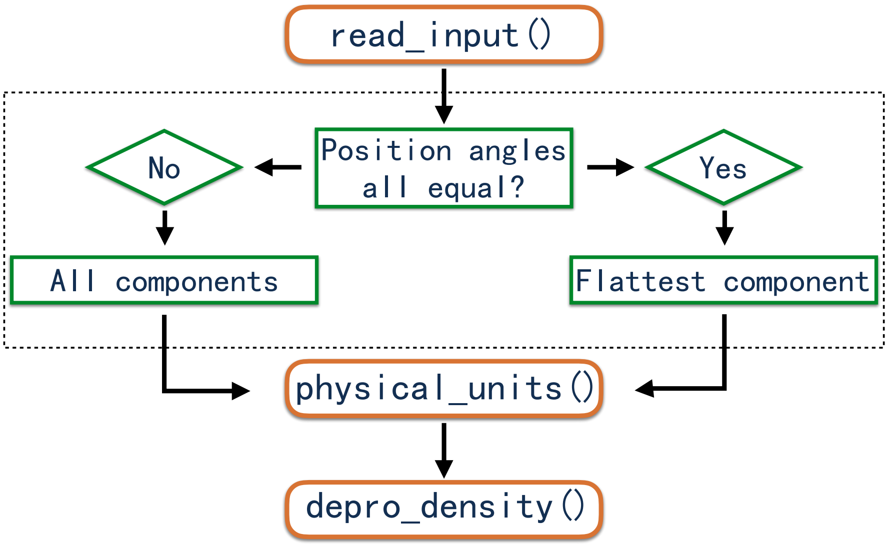

Figure 2.3: A flowchart description of the MGE algorithm as implemented in the module **depromod.f90**. The content of the dashed block describes the implementation of the routine **angles()**.

intrinsic shapes (from oblate/prolate to fully triaxial). Table (2.2) shows the luminosities $\mathrm{L}_{\mathrm{orig}}$ and the intrinsic shape parameters σ_{orig}, $\mathrm{p}_{\mathrm{orig}}$ and $\mathrm{q}_{\mathrm{orig}}$ of the components. The model is projected onto the plane of the sky along the line-of-sight $(\vartheta = 30\,^{\circ}, \varphi = 20\,^{\circ}, \psi = 90\,^{\circ})$. The projected quantities are shown in Table (2.3). Figure (2.4) verifies that $(\vartheta = 30\,^{\circ}, \varphi = 20\,^{\circ}, \psi = 90\,^{\circ})$ belongs to the volume of allowed line-of-sights. The figure portrays also the corresponding intrinsic axes ratios $\langle p \rangle$ and $\langle q \rangle$. They are given by the luminosity weighted averages of the axes ratios p_j and q_j of the single components. For the line-of-sight used for the projection $\langle p \rangle = 0.7850$ and $\langle q \rangle = 0.4591$. The viewing angles are sampled linearly in the ranges $\vartheta, \varphi \in [0\,^{\circ}, 90\,^{\circ}]$ and $\psi \in [0\,^{\circ}, 180\,^{\circ}]$ in steps $\Delta\vartheta, \varphi, \psi = 1\,^{\circ}$. Table (2.4) shows that the intrinsic shape parameters found after the de-projection along the line-of-sight $(\vartheta = 30\,^{\circ}, \varphi = 20\,^{\circ}, \psi = 90\,^{\circ})$ agree with the original values. A meaningful estimate of this agreement can be expressed by means of the RMS of the fractional difference for σ, q and p. The RMS of the fractional difference for σ is computed as

$$\Delta\mathrm{RMS}\ \sigma = \sqrt{\frac{\sum_{i=1}^{N_{\mathrm{comp}}} \left(\frac{\sigma_{\mathrm{orig},i} - \sigma_i}{\sigma_{\mathrm{orig},i}}\right)^2}{N_{\mathrm{comp}}}}. \tag{2.13}$$

The same relation applies to the intrinsic axes ratios. Figure (2.5) portrays the ΔRMS as a function of viewing angles. The line-of-sight that best reproduces the original values of the intrinsic shape parameters is $(\vartheta = 30\,^{\circ}, \varphi = 20\,^{\circ}, \psi = 90\,^{\circ})$ with values of

$$\begin{aligned} \Delta\mathrm{RMS}\ \sigma &= 0.367\ \mathrm{E\text{-}03} \\ \Delta\mathrm{RMS}\ p &= 0.710\ \mathrm{E\text{-}04} \\ \Delta\mathrm{RMS}\ q &= 0.893\ \mathrm{E\text{-}02}. \end{aligned} \tag{2.14}$$

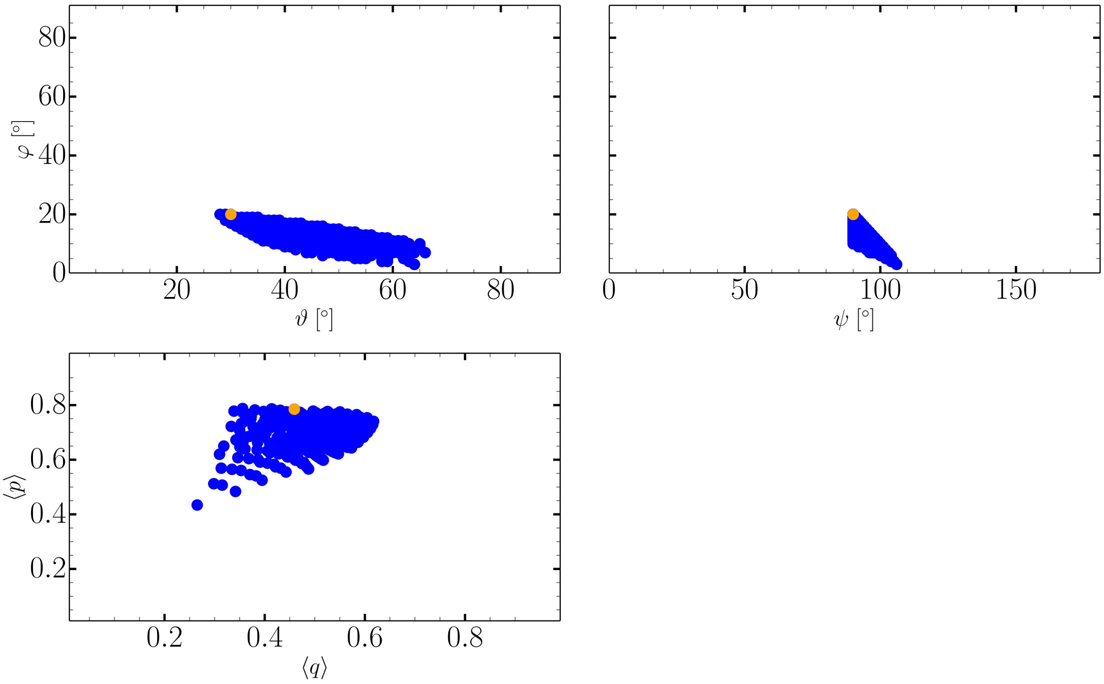

Figure 2.4: Viewing directions corresponding to physically meaningful de-projections for the toy-model (details in text). The viewing direction ($\vartheta = 30\,°, \varphi = 20\,°, \psi = 90\,°$) is highlighted by the orange dots. The axes ratios $\langle q\rangle$ and $\langle p\rangle$ are the luminosity weighted averages of the axes ratios of the single components.

It can be concluded that the implementation of the MGE method works as expected. The de-projected density corresponding to the line-of-sight ($\vartheta = 30\,°, \varphi = 20\,°, \psi = 90\,°$) is integrated in the radial interval $r_{\rm min} = 5 \cdot 10^{-2}$ Kpc and $r_{\rm max} = 8$ Kpc over a three-dimensional spatial grid. The grid is defined as in Section (2.3.4). The total luminosity is $\mathrm{L} = 0.9967\ \mathrm{L}_\odot$. The three-dimensional integration is carried out also for the densities de-projected along the line-of-sights

$$\begin{array}{cccccc} \boldsymbol{\vartheta}\ [°] & \boldsymbol{\varphi}\ [°] & \boldsymbol{\psi}\ [°] & \langle \mathbf{p}\rangle & \langle \mathbf{q}\rangle & \mathbf{L}\ [\mathbf{L}_\odot] \\ 51.0 & 11.0 & 95.0 & 0.6872 & 0.5451 & 0.9861 \\ 64.0 & 3.0 & 106.0 & 0.4341 & 0.2652 & 0.9421 \end{array} . \tag{2.15}$$

The table lists the viewing angles, the luminosity weighted axes ratios and the total luminosity. The first line-of-sight corresponds to a difference in intrinsic shape of $\Delta\langle p\rangle \approx 0.1$ and $\Delta\langle q\rangle \approx 0.1$. This translates in a total luminosity 1.06 % smaller than the one obtained for ($\vartheta = 30\,°, \varphi = 20\,°, \psi = 90\,°$). The $\Delta\langle p\rangle$ and $\Delta\langle q\rangle$ for the first line-of-sight are on the order of the step used in van den Bosch et al. (2008) to investigate in a grid search the intrinsic shape of NGC 4365. The second viewing direction corresponds to the intrinsic shape that maximises $\Delta\langle p\rangle$ and $\Delta\langle q\rangle$ (in absolute terms) with $\Delta\langle p\rangle \approx 0.35$ and $\Delta\langle q\rangle \approx 0.2$. The integration of this density yields a variation of 5.48 % in the total luminosity.

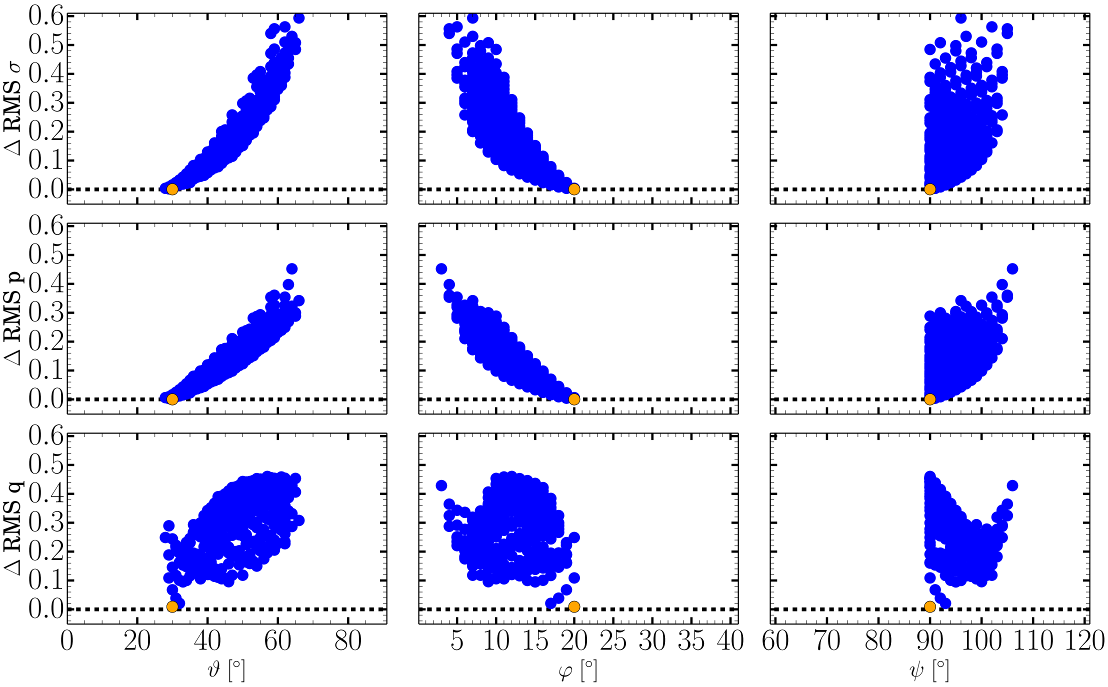

Figure 2.5: Deviations as a function of the viewing angles between the original values of the intrinsic shape parameters from Table (2.2) and the de-projected ones corresponding to the allowed line-of-sights. The viewing direction ($\vartheta = 30^\circ, \varphi = 20^\circ, \psi = 90^\circ$) is highlighted by the orange dots.

Component	$\mathbf{L_{orig}}$	$\boldsymbol{\sigma}_{\mathbf{orig}}$	$\mathbf{p_{orig}}$	$\mathbf{q_{orig}}$
1	0.100	0.5	1.00	0.60
2	0.100	0.8	1.00	0.60
3	0.100	1.1	1.00	0.50
4	0.100	1.4	0.95	0.50
5	0.100	1.7	0.90	0.40
6	0.100	2.0	0.80	0.40
7	0.100	2.3	0.70	0.40
8	0.100	2.6	0.60	0.40
9	0.100	2.9	0.50	0.40
10	0.100	3.2	0.40	0.40

Table 2.2: Luminosity and intrinsic shape parameters of the Gaussian components of the toy-model (details in text). The luminosity is expressed in units of $L_{\odot}$ and σ_{orig} in units of arcseconds.

Component	**L**	$\boldsymbol{\sigma'}$	$\mathbf{q'}$	$\boldsymbol{\Delta\psi'}$
1	0.100	0.500	0.916	90.000
2	0.100	0.800	0.916	90.000
3	0.100	1.100	0.901	90.000
4	0.100	1.343	0.931	103.140
5	0.100	1.580	0.927	120.420
6	0.100	1.819	0.861	145.440
7	0.100	2.083	0.761	152.280
8	0.100	2.350	0.656	154.980
9	0.100	2.619	0.550	156.420
10	0.100	2.888	0.443	157.140

Table 2.3: Projected quantities of the Gaussian components of the toy-model (details in text). Viewing direction ($\vartheta = 30\,°, \varphi = 20\,°, \psi = 90\,°$). The luminosity is expressed in units of $L_{\odot}$, σ' in units of arcseconds and $\Delta\psi'$ in degrees.

Component	L	σ	p	q
1	0.100	0.500	1.000	0.600
2	0.100	0.800	1.000	0.600
3	0.100	1.100	1.000	0.500
4	0.100	1.400	0.950	0.500
5	0.100	1.700	0.900	0.400
6	0.100	2.000	0.800	0.401
7	0.100	2.300	0.700	0.400
8	0.100	2.601	0.600	0.398
9	0.100	2.899	0.500	0.404
10	0.100	3.203	0.400	0.390

Table 2.4: De-projected quantities of the Gaussian components for the toy-model. Viewing direction ($\vartheta = 30\,^\circ, \varphi = 20\,^\circ, \psi = 90\,^\circ$). The luminosity is expressed in units of $\mathrm{L}_\odot$ and σ in units of arcseconds.

2.3 Spatial and velocity grids and the density

The de-projected luminosity and the dark matter densities are binned on appropriate three-dimensional grids. They are interpolated and integrated with the aim of computing the gravitational potential and forces by solving the Poisson equation. This section details how the spatial and velocity binning are set in SCHERPA and how the interpolation and integration of the density are carried out. The routines mentioned in this section are implemented in module **gdenmod.f90**.

2.3.1 Spatial and velocity binning

Coordinate space is described in the spherical coordinates (r, θ, ϕ) and organised in a grid of N_{grid} bins. The number of bins is provided by the user. Angles θ and ϕ are the altitude and azimuthal angles. The radius varies in the interval $[r_{\min}, r_{\max}]$ where $r_{\min} \approx r_e/100$ and $r_{\max} \approx 10 \times r_e$, with r_e being the effective radius of the galaxy. The radial grid is defined by

$$i_{\mathrm{r}} = \frac{1}{a} \log\left(1 + \frac{a}{b} r\right) \tag{2.16}$$

where i_{r} is the radial binning index. The factors a and b are such that $r_{\min}$ is located in the first radial bin and $r_{\max}$ in the last. The grid has bins of size b linearly spaced near the center and bins of size a logarithmically spaced in the outer parts (Siopis et al., 2009). This scheme adapts the resolution of the grid to the amount of information available. The altitude angle θ varies in the interval $[-\frac{\pi}{2}, \frac{\pi}{2}]$ where $\theta = \pm\frac{\pi}{2}$ identifies the *minor axis* and $\theta = 0$ the *equatorial plane*. The bins are linearly spaced. The azimuthal angle ϕ varies in $[0, 2\pi]$ and the bins are linearly spaced. The azimuth $\phi = 0$ identifies the *major axis*. The spatial binning is set in routines **getbinr()**, **getbinth()** and **getbinphi()**. They use specific binning functions from module **mod_binfunc_lib.f90** to relate the physical values of the coordinates with the corresponding indexes $(i_{\mathrm{r}}, i_\theta, i_\phi)$. The spatial binning on the plane of the sky is that of the kinematic observations. The line-of-sight projected velocities are binned in N_{vel} velocity bins. The bins are linearly spaced in the interval $[-v_{\|,\max}, v_{\|,\max}]$. The bin size is

$$\Delta v_{\|} = 2 \times \frac{v_{\|,\max}}{N_{\mathrm{vel}}} \tag{2.17}$$

where $v_{\|,\max}$ is the maximum projected velocity considered in the model.

2.3.2 Definition of the mass density

The mass density distribution of the stars follows as $\rho_* = \mathrm{M/L} \cdot \nu$. The total mass density distribution ρ is given by Equation (1.27). The equation includes a parametrisation for the dark matter halo ρ_{DM}. The possible choices for ρ_{DM} are a Dehnen/Plummer profile (Plummer, 1911; Dehnen, 1993), a Navarro-Frenk-White (NFW) profile (Navarro et al., 1996) and a logarithmic profile (Binney & Tremaine, 2008). The code offers also the possibility to discard dark matter.

2.3.3 Interpolation and integration of the density

Routine **gden()** reads-in the de-projected luminosity densities ν. The density is given on $N_{\mathrm{dens}} = N_{r,\mathrm{dens}} \times N_{\theta,\mathrm{dens}} \times N_{\phi,\mathrm{dens}}$ points with coordinates $(r_{\mathrm{dens}}, \theta_{\mathrm{dens}}, \phi_{\mathrm{dens}})$. The number N_{dens} is chosen as described in Section (2.3.4). Routine **bin_data()** performs the three-dimensional interpolation of the logarithm (with base 10) of the stellar luminosity density ν and the total mass density ρ. Figure (2.6) provides a schematic representation of the interpolation scheme. Given a position of coordinates (r, θ, ϕ), routine **bin_data()** finds the indexes j_{r}, j_θ and j_ϕ with $1 \leq j_{r,\theta,\phi} \leq N_{r,\theta,\phi,\mathrm{dens}}$ such that

$$\begin{array}{lcl} r_{\mathrm{dens}}(j_r) & < r < & r_{\mathrm{dens}}(j_r + 1) \\ \theta_{\mathrm{dens}}(j_\theta) & < \theta < & \theta_{\mathrm{dens}}(j_\theta + 1) \\ \phi_{\mathrm{dens}}(j_\phi) & < \phi < & \phi_{\mathrm{dens}}(j_\phi + 1). \end{array} \tag{2.18}$$

The densities are bi-linearly interpolated on two concentric spheres of radii $r_{\mathrm{dens}}(j_r)$ and $r_{\mathrm{dens}}(j_r{+}1)$ among the points $Q_{1,1} = (\theta_{\mathrm{d}}(j_\theta), \phi_{\mathrm{d}}(j_\phi))$, $Q_{1,2} = (\theta_{\mathrm{d}}(j_\theta), \phi_{\mathrm{d}}(j_\phi + 1))$, $Q_{2,1} = (\theta_{\mathrm{d}}(j_\theta + 1), \phi_{\mathrm{d}}(j_\phi))$, $Q_{2,2} = (\theta_{\mathrm{d}}(j_\theta + 1), \phi_{\mathrm{d}}(j_\phi + 1))$ and $P_{1,1}$, $P_{1,2}$, $P_{2,1}$, $P_{2,2}$. This yields the interpolation points Q and P. The densities are linearly interpolated in the logarithm of the radius between Q and P. This results in the

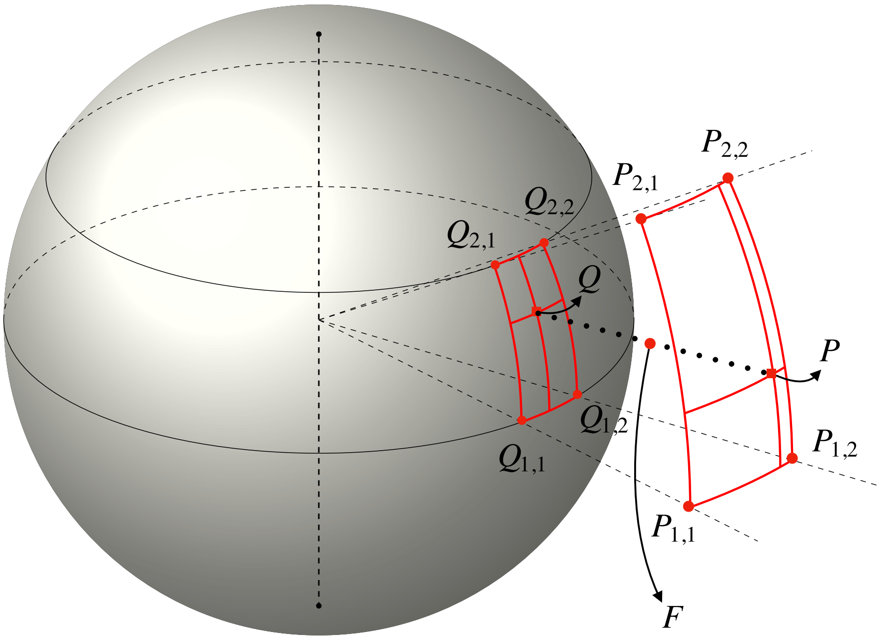

Figure 2.6: Schematic representation of the interpolation scheme for the density implemented in the module **gdenmod.f90**. The density is first bi-linearly interpolated on two concentric spheres of different radius yielding the interpolation points Q and P. Afterwards the density is linearly interpolated in the logarithm of the radius along the dotted line connecting Q and P. This results in the final interpolation point F. The image has been modified from an example available at `http://www.texample.net/tikz/examples/spherical-and-cartesian-grids/`.

final interpolation point F. Subsequently, **bin_data()** integrates the interpolated densities via a 10-point Gaussian quadrature algorithm from Press et al. (1996) yielding the total luminosity and total mass, the luminosities of the two stellar components and the dark matter halo mass in each spatial bin. The integration is carried out between the boundaries of the bins of the fine grid.

2.3.4 Test of the implementation

The interpolation and integration schemes are tested on spherical and triaxial density distributions. The binning grid is composed of $N_{r,\mathrm{grid}} = 20$, $N_{\theta,\mathrm{grid}} = 5$ and $N_{\phi,\mathrm{grid}} = 10$ bins, resulting in a total number of $N_{\mathrm{grid}} = 1000$ bins. The chosen number of bins ensures that the mass is well reproduced.

Spherical density The spherical model is the isotropic Hernquist sphere (Hernquist, 1990). The density profile reads

$$\rho(r) = \frac{M}{2\pi} \frac{r_{\mathrm{s}}}{r(r+r_s)^3} \tag{2.19}$$

where r_s is the scaling radius and M the total mass. The scaling radius relates to the effective radius as $r_e \approx 1.8153\ r_s$. The enclosed mass is given by

$$M(<r) = M\frac{r^2}{(r+r_s)^2}. \tag{2.20}$$

The total mass is $M = 1.5 \cdot 10^{12}\ \mathrm{M}_\odot$. The effective radius is $r_e = 10$ Kpc ($r_s \approx 5.51$ Kpc). The model is placed at a distance $d = 65$ Mpc and studied in the radial interval $r_{\min} = 3 \cdot 10^{-2}$ Kpc and $r_{\max} = 101$ Kpc. The deviations between the input ρ and interpolated ρ_{interp} densities are expressed by means of the RMS of the fractional difference

$$\Delta\text{RMS} = \sqrt{\frac{\sum_{i=1}^{N_{\text{dens}}} \left(\frac{\rho(\mathbf{x}_i)-\rho_{\text{interp}}(\mathbf{x}_i)}{\rho(\mathbf{x}_i)}\right)^2}{N_{\text{dens}}}} \tag{2.21}$$

where $N_{\text{dens}} = N_{r,\text{dens}} \times N_{\theta,\text{dens}} \times N_{\phi,\text{dens}}$ is the number of positions $\mathbf{x}_i = (r, \theta, \phi)$ where the comparison is performed. Figure (2.7) shows the behaviour of the ΔRMS as a function of the number of points on which the input density ρ is sampled. The panel on the left-hand side portrays the behaviour of the ΔRMS as a function of $N_{r,\text{dens}}$ for $N_{\theta,\text{dens}} = N_{\phi,\text{dens}} = 101$ [5]. The agreement between the theoretical and interpolated densities improves as $N_{r,\text{dens}}$ increases. The ΔRMS becomes essentially constant for $N_{r,\text{dens}} \geq 300$. The panel on the right-hand side shows that the ΔRMS is independent from the number of points in the angular coordinates (when $N_{\theta,\text{dens}}$ is varied $N_{\phi,\text{dens}} = 101$ and vice-versa). This is expected for a spherical density. It is possible to conclude that a spherical density should be sampled on at least $N_{r,\text{dens}} = 300$ radial points for the interpolation to work well. Figure (2.8) shows the comparison between the expected enclosed mass from Equation (2.20) and the one obtained from the integration of the interpolated density over the spatial grid. The RMS of the fractional difference between the curves is 7.633 E-04.

Triaxial density The triaxial model is the Perfect Ellipsoid (de Zeeuw, 1985a). The density profile reads

$$\rho(m) = \frac{\rho_0}{(1+m^2)^2} \tag{2.22}$$

where

$$m = \sqrt{\frac{x^2}{a^2}+\frac{y^2}{b^2}+\frac{z^2}{c^2}} \quad \text{with} \quad a \geq b \geq c \geq 0. \tag{2.23}$$

The density ρ approaches ρ_0 for small radii and falls off as $\frac{1}{m^4}$ in the outer parts. The enclosed mass is obtained by solving numerically the integral

$$M(<r) = \int_0^r dr' \int_{-\frac{\pi}{2}}^{\frac{\pi}{2}} d\theta \cos\theta \int_0^{2\pi} d\phi\ \frac{\rho_0}{(1+m^2)^2} \tag{2.24}$$

---

[5] The angular coordinates (θ, ϕ) are sampled linearly on an odd number of points to ensure that $\theta = \phi = 0$ are included.

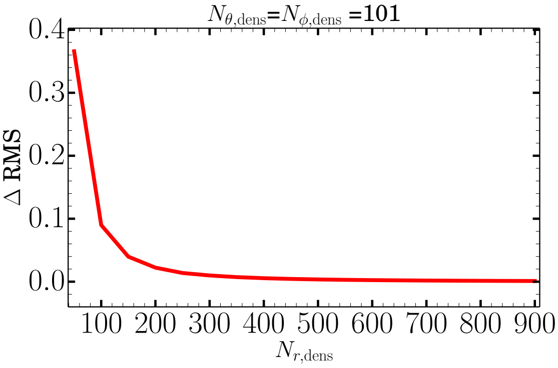

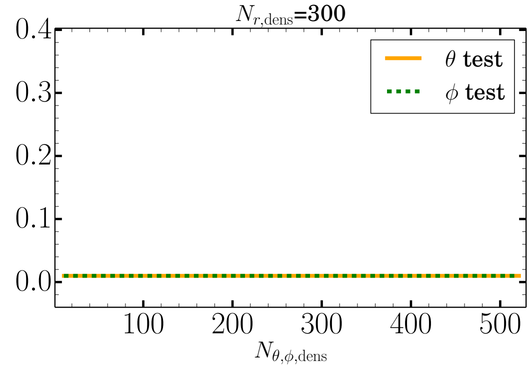

Figure 2.7: Deviations between the input ρ and interpolated density ρ_{interp} expressed as the RMS of the fractional difference. On the left the deviations as a function of $N_{r,\mathrm{dens}}$ for $N_{\theta,\mathrm{dens}} = N_{\phi,\mathrm{dens}} = 101$. On the right the deviations as a function of the number of angular points for $N_{r,\mathrm{dens}} = 300$. When $N_{\theta,\mathrm{dens}}$ is varied $N_{\phi,\mathrm{dens}} = 101$ and vice-versa. The spherical mass model is the isotropic Hernquist sphere (details in text).

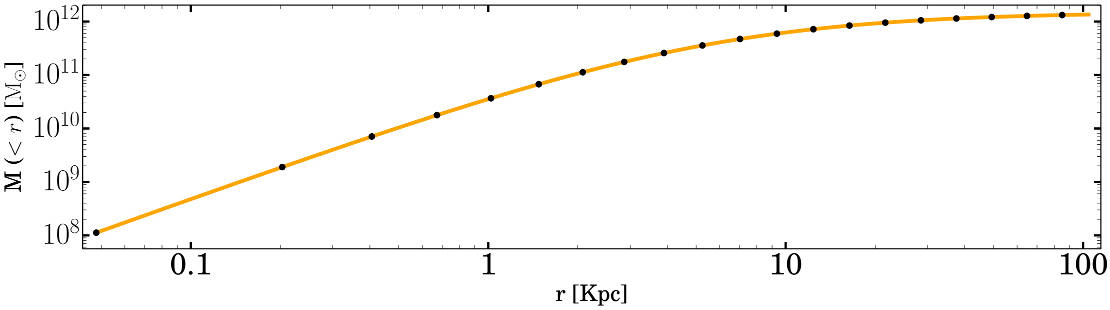

Figure 2.8: Graphical comparison between the **theoretical** and the model enclosed mass for the isotropic Hernquist sphere (details in text).

with

$$\begin{aligned} x &= (r')^2 \cos\theta \cos\phi \\ y &= (r')^2 \cos\theta \sin\phi \\ z &= (r')^2 \sin\theta . \end{aligned} \tag{2.25}$$

The total mass is $M = \pi^2 abc\rho_0$. The profile has $M = 1.5 \cdot 10^{12}$ $\mathrm{M}_\odot$ with axes lengths $a = 7.65$ Kpc, $b = 6.5025$ Kpc and $c = 5.355$ Kpc. The axes ratios are $q = \frac{c}{a} = 0.7$ and $p = \frac{b}{a} = 0.85$. They correspond to a triaxiality parameter $T = \frac{1-p^2}{1-q^2} \approx 0.55$. As mentioned in Section (1.5), these values are chosen since the distribution of the intrinsic axes ratios of elliptical galaxies peaks between $q \approx 0.6 - 0.8$ (Binney & de Vaucouleurs, 1981; Tremblay & Merritt, 1996). Furthermore the distribution of intrinsic shapes for bright elliptical galaxies is consistent with $0.4 < T < 0.8$ (Vincent & Ryden, 2005). The model is placed at a distance $d = 16.83$ Mpc and studied in the radial interval $r_{\mathrm{min}} = 8 \cdot 10^{-2}$ Kpc and $r_{\mathrm{max}} = 120$ Kpc. Figure (2.9) shows the behaviour of the ΔRMS as a function of the number of points on which the input density ρ is sampled. The panel on the left-hand side portrays the behaviour of ΔRMS as a function of $N_{r,\mathrm{dens}}$ for $N_{\theta,\mathrm{dens}} = N_{\phi,\mathrm{dens}} = 101$. For low values of $N_{r,\mathrm{dens}}$ the agreement between the two functions is worse than in the spherical case. In fact the performance of a linear interpolation scheme worsens for a flat density profile. Nevertheless $\Delta\mathrm{RMS} \to 0$ as $N_{r,\mathrm{dens}}$ increases. The panel on the right-hand side shows the behaviour of ΔRMS as a function of $N_{\theta,\phi,\mathrm{dens}}$ for $N_{r,\mathrm{dens}} = 300$. When $N_{\theta,\mathrm{dens}}$ is varied $N_{\phi,\mathrm{dens}} = 101$ and vice-versa. The ΔRMS decreases as $N_{\theta,\phi,\mathrm{dens}}$ become larger. At low values of $N_{\theta,\phi,\mathrm{dens}}$ the interpolation performs better in θ rather than in ϕ. This is because the evaluations of ρ in the azimuthal direction are spread over the larger interval $\phi \in [0, 2\pi]$ rather than $\theta \in [-\frac{\pi}{2}, \frac{\pi}{2}]$. It is possible to conclude that a triaxial density should be sampled on at least $N_{r,\mathrm{dens}} = 300$ and $N_{\theta,\mathrm{dens}} = N_{\phi,\mathrm{dens}} = 101$ points for the interpolation scheme to perform well. Figure (2.10) shows the comparison between the expected enclosed mass from Equation (2.24) and the one obtained from the integration of the interpolated density over the spatial grid. The RMS of the fractional difference between the curves is 1.263 E-03.

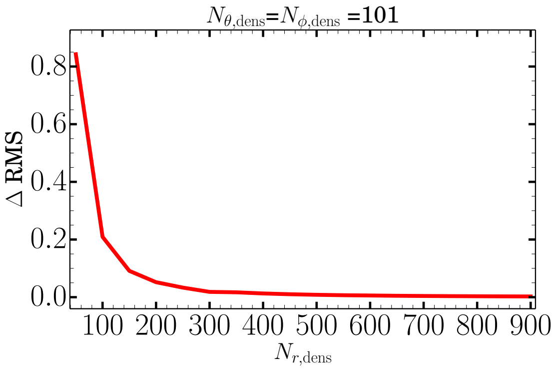

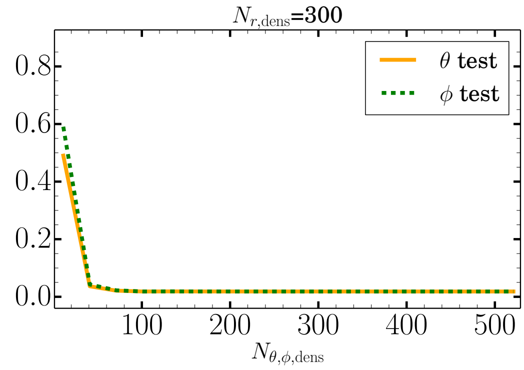

Figure 2.9: Deviations between the input ρ and interpolated density ρ_{interp} expressed as the RMS of the fractional difference. On the left the deviations as a function of $N_{r,\mathrm{dens}}$ for $N_{\theta,\mathrm{dens}} = N_{\phi,\mathrm{dens}} = 101$. On the right the deviations as a function of the number of angular points for $N_{r,\mathrm{dens}} = 300$. When $N_{\theta,\mathrm{dens}}$ is varied $N_{\phi,\mathrm{dens}} = 101$ and vice-versa. The triaxial mass model is the Perfect Ellipsoid (details in text).

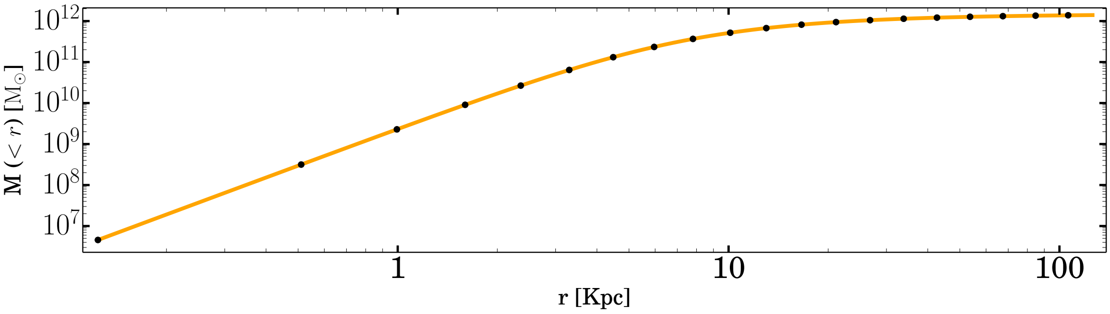

Figure 2.10: Graphical comparison between the **theoretical** and the model enclosed mass for the Perfect Ellipsoid (details in text).

2.4 Potential and force calculation

The section describes the implementation for the calculation of the gravitational potential and forces and its testing. The routines are detailed in module **potforcemod.f90**.

2.4.1 Description of the implementation

The total gravitation potential is modelled as in Equation (1.28). The stellar and dark matter halo terms are computed as an expansion in **spherical harmonics** $Y_{l,m}(\theta,\phi)$ (Binney & Tremaine, 2008). A potential $\Phi(r,\theta_{\text{sh}},\phi)$ generated by a density distribution $\rho(r,\theta_{\text{sh}},\phi)$ is expanded as

$$\begin{aligned}\Phi(r,\theta_{\text{sh}},\phi) = -4\pi G\sum_{l=0}^{\infty}\sum_{m=-l}^{l}\frac{Y_{l,m}(\theta_{\text{sh}},\phi)}{2l+1}&\left[r^{-(l+1)}\int_0^r s^{l+2}\rho_{l,m}(s)\;ds\right.\\ &\left.+\,r^l\int_0^{+\infty} s^{1-l}\rho_{l,m}(s)\;ds\right]\end{aligned}\tag{2.26}$$

where

$$\rho_{l,m}(s) = \int_0^{2\pi} d\phi\int_0^{\pi}\sin\theta_{\text{sh}}\;Y^*_{l,m}(\theta_{\text{sh}},\phi)\;\rho(s,\theta_{\text{sh}},\phi)\;d\theta_{\text{sh}}\tag{2.27}$$

and $\theta_{\text{sh}} = \frac{\pi}{2}-\theta$. The spherical harmonics read

$$Y_{l,m}(\theta_{\text{sh}},\phi) = \sqrt{\frac{2l+1}{4\pi}\frac{(l-m)!}{(l+m)!}}P_l^m(\cos\theta_{\text{sh}})\mathrm{e}^{im\phi}\tag{2.28}$$

where $P_l^m(\cos\theta_{\text{sh}})$ are the **associated Legendre polynomials** and $l,m\in\mathbb{N}$ with $l\geq 0$ and $m\in[-l,l]$. Equation (2.26) is implemented by means of the **real spherical harmonics**

$$y_{l,m}\equiv\begin{cases}\sqrt{2}K_l^mP_l^m(\cos\theta_{\text{sh}})\cos(m\phi) & m>0\\ \sqrt{2}K_l^{|m|}P_l^{|m|}(\cos\theta_{\text{sh}})\sin(|m|\phi) & m<0\\ K_l^0P_l^0(\cos\theta_{\text{sh}}) & m=0\end{cases}\tag{2.29}$$

where $K_l^m = \sqrt{\frac{2l+1}{4\pi}\frac{(l-|m|)!}{(l+|m|)!}}$ (Morse & Feshbach 1953). The expansion becomes

$$\begin{aligned}\Phi(r,\theta_{\text{sh}},\phi) = -2G\sum_{l=1}^{\infty}\sum_{m=1}^{l}\frac{(l-m)!}{(l+m)!}P_l^m(\varsigma)&\Bigg(\sin(|m|\phi)\left[r^{-(l+1)}A_{l,|m|}\right.\\ &\left.+\,r^lB_{l,|m|}\right]+\cos(m\phi)\left[r^{-(l+1)}A_{l,m}+r^lB_{l,m}\right]\Bigg)\\ &-G\sum_{l=0}^{\infty}P_l^0(\varsigma)\left[r^{-(l+1)}A_{l,0}+r^lB_{l,0}\right]\end{aligned}\tag{2.30}$$

where $\cos\theta_{\rm sh} = \varsigma$ [6]. The coefficients of the expansion read

$$\begin{aligned}
A_{l,|m|} &= \sqrt{2}K_l^{|m|} \int_0^r s^{l+2}ds \int_0^{2\pi} d\phi \sin(|m|\phi) \int_{-1}^1 d\varsigma P_l^{|m|}(\varsigma)\ \rho(s,\varsigma,\phi)\\
A_{l,m} &= \sqrt{2}K_l^m \int_0^r s^{l+2}ds \int_0^{2\pi} d\phi \cos(m\phi) \int_{-1}^1 d\varsigma P_l^m(\varsigma)\ \rho(s,\varsigma,\phi)\\
B_{l,|m|} &= \sqrt{2}K_l^{|m|} \int_r^{+\infty} s^{1-l}ds \int_0^{2\pi} d\phi \sin(|m|\phi) \int_{-1}^1 d\varsigma P_l^{|m|}(\varsigma)\ \rho(s,\varsigma,\phi)\\
B_{l,m} &= \sqrt{2}K_l^m \int_r^{+\infty} s^{1-l}ds \int_0^{2\pi} d\phi \cos(m\phi) \int_{-1}^1 d\varsigma P_l^m(\varsigma)\ \rho(s,\varsigma,\phi)\\
A_{l,0} &= K_l^0 \int_0^r s^{l+2}ds \int_0^{2\pi} d\phi \int_{-1}^1 d\varsigma P_l^0(\varsigma)\ \rho(s,\varsigma,\phi)\\
B_{l,0} &= K_l^0 \int_r^{+\infty} s^{1-l}ds \int_0^{2\pi} d\phi \int_{-1}^1 d\varsigma P_l^0(\varsigma)\ \rho(s,\varsigma,\phi).
\end{aligned} \tag{2.31}$$

The components of the force per unit mass are obtained by differentiating Equation (2.30) with respect to r, $\theta_{\rm sh}$ and ϕ. They read

$$\begin{aligned}
\frac{\partial\Phi}{\partial r} = -2G\sum_{l=1}^{\infty}\sum_{m=1}^{l}\frac{(l-m)!}{(l+m)!}P_l^m(\varsigma)\Bigg(&\sin(|m|\phi)\Big[-(l+1)r^{-l-2}A_{l,|m|}\\
&+ lr^{l-1}B_{l,|m|}\Big] + \cos(m\phi)\Big[-(l+1)r^{-l-2}A_{l,m} + lr^{l-1}B_{l,m}\Big]\Bigg)\\
&- G\sum_{l=0}^{\infty}P_l^0(\varsigma)\Big[-(l+1)r^{-l-2}A_{l,0} + lr^{l-1}B_{l,0}\Big]
\end{aligned} \tag{2.32}$$

$$\begin{aligned}
\frac{\partial\Phi}{\partial\theta_{\rm sh}} = -2G\sum_{l=1}^{\infty}\sum_{m=1}^{m=l}\frac{(l-m)!}{(l+m)!}\frac{\partial P_l^m}{\partial\varsigma}\frac{\partial\varsigma}{\partial\theta_{\rm sh}}\Bigg(&\sin(|m|\phi)\Big[r^{-(l+1)}A_{l,|m|}\\
&+ r^lB_{l,|m|}\Big] + \cos(m\phi)\Big[r^{-(l+1)}A_{l,m} + r^lB_{l,m}\Big]\Bigg)\\
&- G\sum_{l=0}^{\infty}\frac{\partial P_l^0}{\partial\varsigma}\frac{\partial\varsigma}{\partial\theta_{\rm sh}}\Big[r^{-(l+1)}A_{l,0} + r^lB_{l,0}\Big]
\end{aligned} \tag{2.33}$$

$$\begin{aligned}
\frac{\partial\Phi}{\partial\phi} = -2G\sum_{l=1}^{\infty}\sum_{m=1}^{m=l}\frac{(l-m)!}{(l+m)!}P_l^m(\varsigma)\Bigg(&|m|\cos(|m|\phi)\Big[r^{-(l+1)}A_{l,|m|}\\
&+ r^lB_{l,|m|}\Big] - m\sin(m\phi)\Big[r^{-(l+1)}A_{l,m} + r^lB_{l,m}\Big]\Bigg).
\end{aligned} \tag{2.34}$$

The derivative $\frac{\partial P_l^m}{\partial\varsigma}\frac{\partial\varsigma}{\partial\theta_{\rm sh}} = \left(-\sqrt{1-\varsigma^2}\right)\frac{(l-m+1)P_{l+1}^m(\varsigma)-(l+1)\varsigma P_l^m(\varsigma)}{\varsigma^2-1}$(Abramowitz & Stegun, 1972). Routines **tables()** and **halotables()** implement the calculation of the coefficients of the expansion for the stellar and dark matter densities. The dark matter density is known analytically. The stellar density is interpolated in three dimensions for $r \in [r_{\rm min}, r_{\rm max}]$ as in Section (2.3.3). The stellar density is

---

[6] The last term of Equation (2.30) is the only one that does not vanish when the potential is axisymmetric.

extrapolated for $r < r_{\min}$ as a power-law with exponent $\gamma = \gamma_{\text{inner}}$ (with γ_{inner} provided by the user) and with $\gamma_{\text{outer}} = 4$ for $r > r_{\max}$ [7]. The integration of the densities is performed by means of the Gauss-Kronrod 21-point integration rule. The integration method is implemented in routine **qags()**. The routine has been adapted over the course of this project to the Fortran 90 standard starting from the Fortran 77 version of the QUADPACK library freely available at `http://nines.cs.kuleuven.be/software/QUADPACK/`. **Tables()** and **halotables()** yield tabulated values of the expansion coefficients evaluated on a grid of radii. The stellar and dark matter coefficients are added in **addtables()** and cubic-spline interpolated in the logarithm (base 10) of the radius in **tables_splines()**. Routines **potential()** and **force()** evaluate the total potential and the corresponding components of the gravitational force by implementing Equation (2.30) and Equations (2.32)-(2.34). The routines account also for the Keplerian contribution of the central SMBH. The existing triaxial implementation of the Schwarzschild method from van den Bosch et al. (2008) performs the calculation of the gravitational potential and forces using the Multi Gaussian Expansion method from Cappellari (2002). The implementation described in this work is instead independent from the method used to de-project the surface brightness profile.

2.4.2 Test of the implementation

The implementation is tested on spherical and triaxial potentials. The method is also compared to a composite potential generated by a triaxial stellar density distribution combined with a central black hole and a dark matter halo. The spatial binning grid of the models is composed of $N_{r,\text{grid}} = 20$, $N_{\theta,\text{grid}} = 5$ and $N_{\phi,\text{grid}} = 10$ bins. The expansion in Equation (2.30) is computed to order $l = 6$. This is enough to guarantee that the gravitational potential and the components of the force are accurate.

Spherical potential The spherical reference model is the isotropic Hernquist sphere with the same characteristics as that used in Section (2.3.4). The gravitational potential Φ and the corresponding force components F are given by

$$\Phi(r) = -\frac{GM}{r + r_\text{s}}, \quad F(r) = -\frac{GM}{(r + r_\text{s})^2}, \quad F(\theta) = F(\phi) = 0. \tag{2.35}$$

The comparison between the model predictions and the theoretical values is carried out by means of the RMS of the fractional difference for Φ and F_r and of the difference for F_θ and F_ϕ (the theoretical value is zero). The number of points on which the comparison is performed is $N = 960400$. The results are given in Table (2.5) and show that the implementation functions as expected. Figure (2.11) provides a graphical comparison.

---

[7] As an example consider that $\gamma_{\text{inner}} = -0.2$ for NGC 1600 (see Chapter 4). This value is determined from the average slope of the density profile. The value $\gamma_{\text{outer}} = 4$ is for the convergence of the integral.

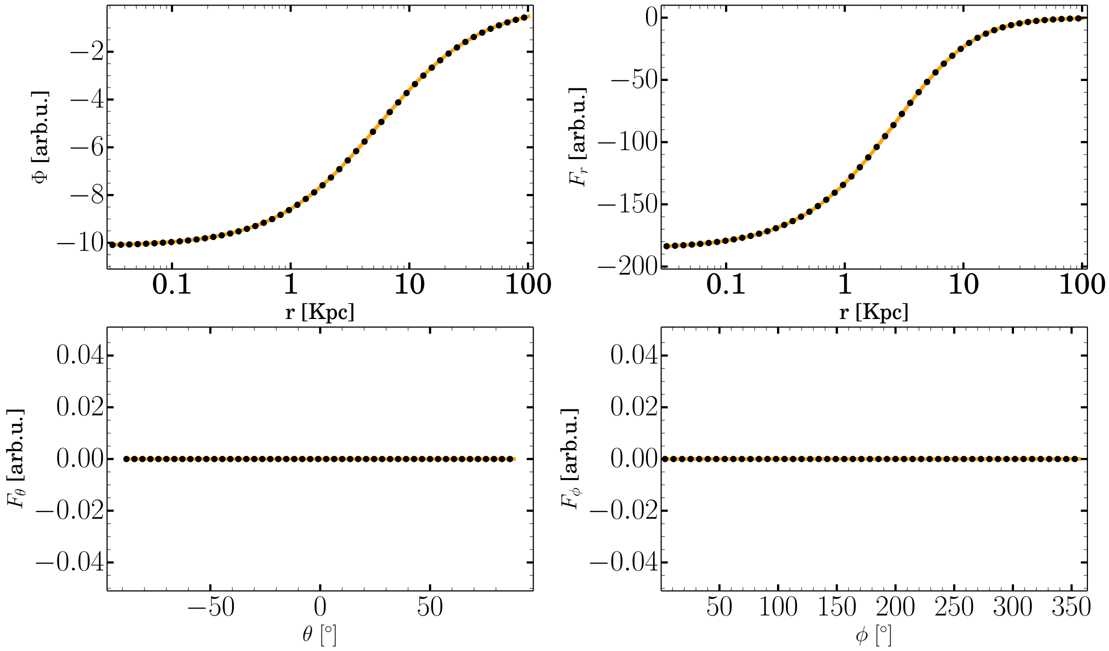

Figure 2.11: Graphical comparison between the **theoretical** and the **model** gravitational potential and forces for an isotropic Hernquist sphere (details in text). The top left and top right panels show the potential and radial component of the force as a function of radius along the major axis. The bottom left and bottom right panels show for $r = r_{\rm min}$ the altitude component of the force as a function of θ along the major axis and the azimuthal component of the force as a function of ϕ on the equatorial plane.

	Δ RMS
Φ	0.348 E-02
$\mathbf{F_r}$	0.158 E-03
$\mathbf{F_\theta}$	0.531 E-11
$\mathbf{F_\phi}$	0.184 E-10

Table 2.5: Comparison between the model predictions and the theoretical values of the gravitational potential and forces for an isotropic Hernquist sphere (details in text).

Triaxial potential The triaxial reference model is the Perfect Ellipsoid. The parameters of the model are those used in Section (2.3.4). The gravitational potential reads

$$V(\lambda,\mu,\nu) = -\left(\frac{F(\lambda)}{(\lambda-\mu)(\lambda-\nu)} + \frac{F(\mu)}{(\mu-\nu)(\mu-\lambda)} + \frac{F(\nu)}{(\nu-\lambda)(\nu-\mu)}\right) \tag{2.36}$$

where (λ,μ,ν) are the confocal ellipsoidal coordinates and function F is given in Equation (21) of de Zeeuw (1985a). The components of the force are obtained by computing the gradient $\left(\frac{\partial V}{\partial \lambda}, \frac{\partial V}{\partial \mu}, \frac{\partial V}{\partial \nu}\right)$ of Equation (2.36). The gradient is transformed to cartesian coordinates as

$$\left(\frac{\partial V}{\partial x}, \frac{\partial V}{\partial y}, \frac{\partial V}{\partial z}\right) = \frac{\partial(\lambda, \mu, \nu)}{\partial(x, y, z)} \left(\frac{\partial V}{\partial \lambda}, \frac{\partial V}{\partial \mu}, \frac{\partial V}{\partial \nu}\right) \tag{2.37}$$

where $\frac{\partial(\lambda,\mu,\nu)}{\partial(x,y,z)}$ is given in Equation (14) from de Zeeuw et al. (1986). The final conversion to spherical coordinates is obtained using Equation (B.5). The comparison between the model predictions and the theoretical values is carried out by means of the RMS of the fractional difference on a number of points equal to that used for the test on the spherical potential. The results are given in Table (2.6) and show that the implementation works as expected. Figure (2.12) provides a graphical comparison.

	Δ RMS
Φ	0.253 E-02
$\mathbf{F_r}$	0.468 E-03
$\mathbf{F}_\theta$	0.327 E-02
$\mathbf{F}_\phi$	0.596 E-02

Table 2.6: Comparison between the model predictions and the theoretical values of the gravitational potential and forces for a Perfect Ellipsoid (details in text).

Composite potential The implementation is tested against a model given by a triaxial stellar density distribution with a central black hole of mass $M_{\rm SMBH} = 1.7 \cdot 10^{10}$ $\rm M_\odot$ and a dark matter halo that follows the profile of a Plummer sphere with mass $M_{\rm DM} = 1.2 \cdot 10^{12}$ $\rm M_\odot$ and scaling radius $r_{\rm plm} = 40$ Kpc. The parameters used for the triaxial stellar density distribution are those of Section (2.3.4). The model is placed at a distance $d = 16.83$ Mpc and studied in the radial interval $r_{\rm min} = 8 \cdot 10^{-2}$ Kpc and $r_{\rm max} = 120$ Kpc. The contribution to the gravitation potential and the components of the force from the black hole is compared to

$$\Phi(r) = -\frac{GM_{\rm SMBH}}{r}, \quad F(r) = -\frac{GM_{\rm SMBH}}{r^2}, \quad F(\theta) = F(\phi) = 0 \tag{2.38}$$

and from the dark matter halo to

$$\Phi(r) = -\frac{GM_{\rm DM}}{\sqrt{r^2 + r_{\rm plm}^2}}, \quad F(r) = -\frac{GM_{\rm DM}\ r}{(r^2 + r_{\rm plm}^2)^{\frac{3}{2}}}, \quad F(\theta) = F(\phi) = 0. \tag{2.39}$$

The comparison between the model predictions and the theoretical values from Equation (2.36), (2.38) and (2.39) is carried out by means of the RMS of the fractional difference on a number of points equal to that used for the test on the central potential. The results are given in Table (2.7) and Figure (2.13) provides a graphical comparison.

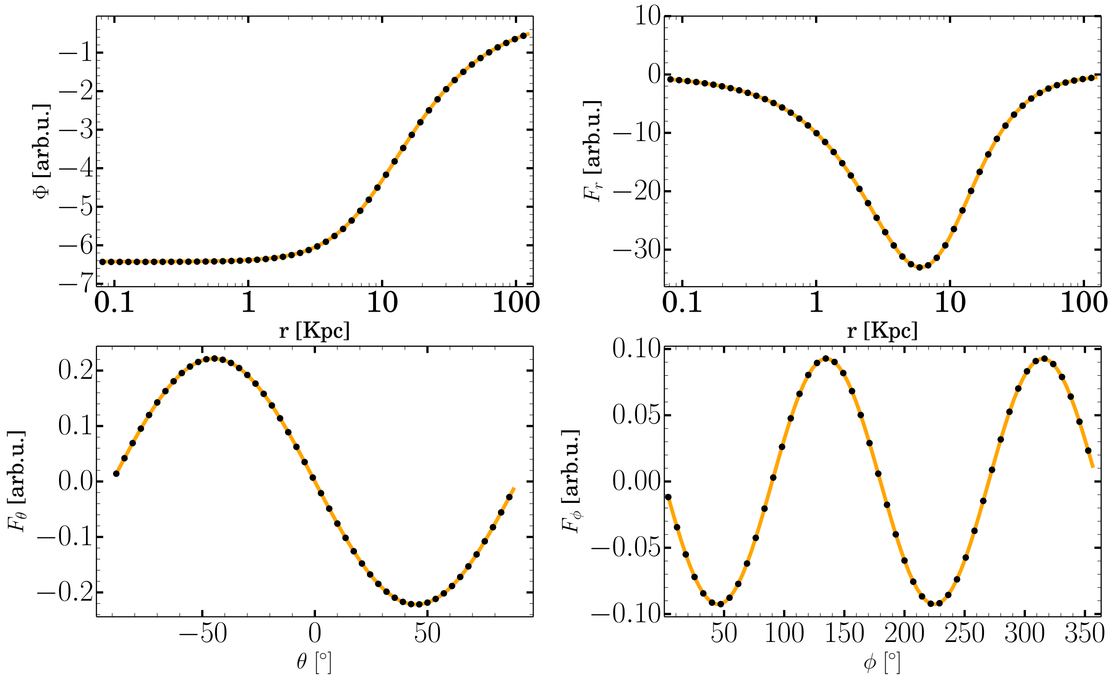

Figure 2.12: Graphical comparison between the **theoretical** and the **model** gravitational potential and forces for a Perfect Ellipsoid (details in text). The top left and top right panels show the potential and radial component of the force as a function of radius along the major axis. The bottom left and bottom right panels show for $r = r_{\min}$ the altitude component of the force as a function of θ along the major axis and the azimuthal component of the force as a function of ϕ on the equatorial plane.

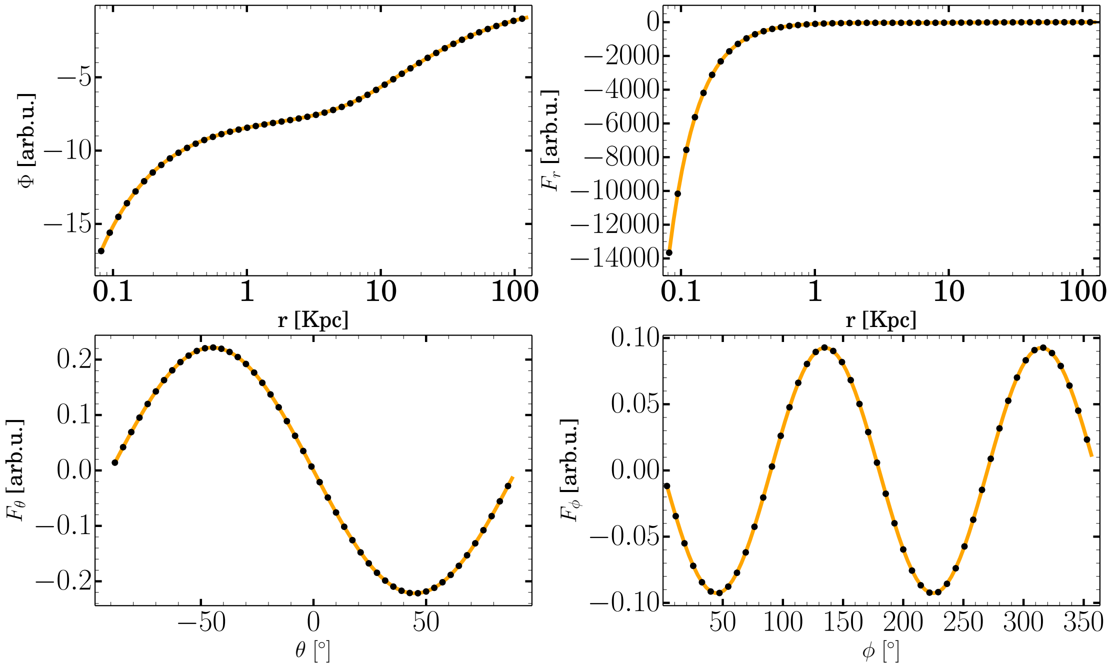

Figure 2.13: Graphical comparison between the **theoretical** and the **model** gravitational potential and forces for a triaxial stellar density distribution with a central black hole and a dark matter halo (details in text). The top left and top right panels show the potential and radial component of the force as a function of radius along the major axis. The bottom left and bottom right panels show for $r = r_{\mathrm{min}}$ the altitude component of the force as a function of θ along the major axis and the azimuthal component of the force as a function of ϕ on the equatorial plane.

	Δ RMS
$\mathbf{\Phi}$	0.155 E-02
$\mathbf{F_r}$	0.384 E-03
$\mathbf{F}_\theta$	0.327 E-02
$\mathbf{F}_\phi$	0.596 E-02

Table 2.7: Comparison between the model predictions and the theoretical values of the gravitational potential and forces for a triaxial stellar density distribution with a central black hole and a dark matter halo (details in text).

2.5 The library of the representative stellar orbits

The section introduces the sampling of the initial conditions of the representative stellar orbits and describes how the integration of the equations of motion is performed. It focuses also on the classification of the orbits and the calculation of their

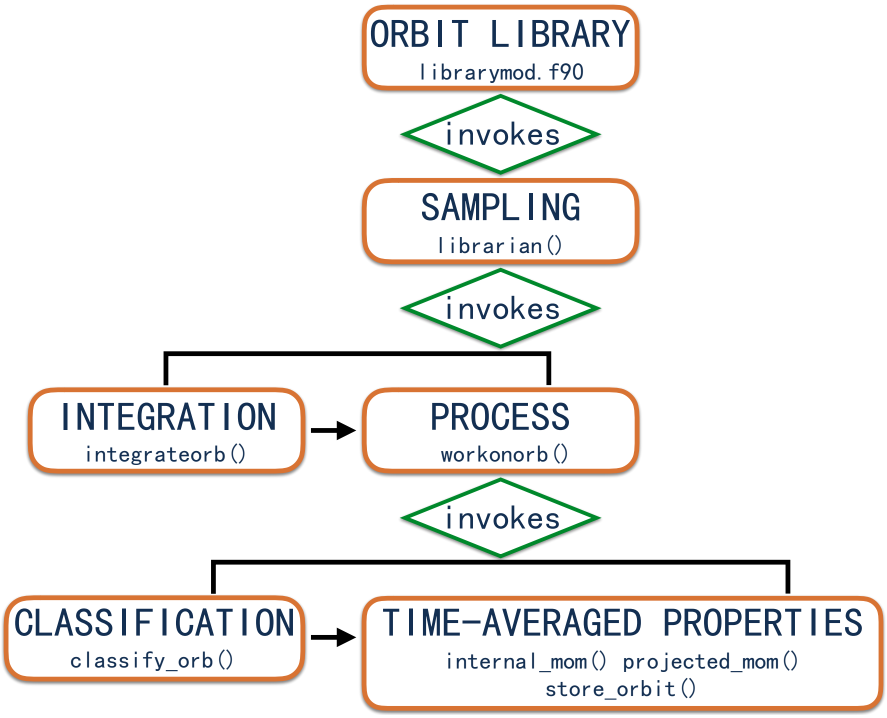

Figure 2.14: A flowchart description of main steps in module **librarymod.f90** together with the names of the routine where these steps are implemented.

time-averaged properties. Afterwards the section deals with the test performed to verify the validity of the code. Figure (2.14) provides a flowchart representation of the implementation. The routines are detailed in module **librarymod.f90**.

2.5.1 Sampling of the initial conditions

In the Schwarzschild method the DF of a stellar system is reconstructed by means of a set (library) of representative stellar orbits. Each orbit corresponds to a combination of the isolating integrals of motion (and vice-versa). They restrict the motion in phase-space to a sub-space S of dimension $N_{\mathrm{S}} = N_{\text{phase-space}} - N_{\text{int}}$ with $N_{\text{phase-space}} = 6$. N_{int} is the number of isolating integrals of motion necessary to uniquely identify an orbit. This number depends on the potential as described in Section (1.7). The reconstruction of the DF is reliable if the library fully reproduces the structure of phase-space. This is achieved if, to some degree, the library renders any allowed combination of the integrals of motion. In other words, if the library homogeneously samples all the dimensions of the sub-space S. This condition can be complicated to satisfy in a real galaxy since the geometry of the potential varies from the centre to the outskirts. The potential is Keplerian in the immediate vicinity of the SMBH and it is dominated by dark matter in the outer parts. The sampling technique has been implemented in the routine **librarian()**. The library of representative orbits is organised in **energy shell**s. They are groups of orbits that share the value E of the energy. Each energy shell is in turn subdivided in groups of orbits denoted as **sequence**s. The orbits belonging to a sequence share the same initial value L_z of the z-component of the angular momentum [8]. The routine **initel()** invoked in **librarian()** samples the value E of the energy as

$$E = \Phi(r_{\text{energy}}, \theta_{\text{energy}} = 0, \phi_{\text{energy}}) \quad \text{with} \quad E < 0. \tag{2.40}$$

Radius r_{energy} is binned as in Equation (2.16). The potential is assumed to be symmetric in all octants and to have its extremal values along the major and intermediate axes. Hence $\phi_{\text{energy}} = 0, \frac{\pi}{2}$. For each energy shell the routine computes the minimum $L_{z,\text{min}}$ and maximum $L_{z,\text{max}}$ values of

$$L_z(r, \phi) = r\sqrt{2(E - \Phi(r, \theta = 0, \phi))}. \tag{2.41}$$

It evaluates $L_z(r, \phi)$ for radii logarithmically spaced in $[r_{\text{min}}/10, r_{\text{energy}}]$ with $\phi = \phi_{\text{energy}}$. The initial value of the angular momentum associated to a given sequence is obtained from a linear binning in the interval $[L_{z,\text{min}}, L_{z,\text{max}}]$. For each sequence routine **periapo()** computes on the equatorial plane the radial interval where the motion of the stars is allowed. This is done along the major and intermediate axes by means of the root-finding algorithm of Brent (1971) as implemented in Press et al. (1996). The routine searches where the kinetic energy

$$E_{\text{kin}} = E - \Phi(r, \theta = 0, \phi) - \frac{L_z^2}{2r^2} \tag{2.42}$$

vanishes for $r \in [r_{\text{min}}/1000, 2 \times r_{\text{max}}]$. The minimum and maximum radius allowed for orbits in a given sequence is identified as the pericentre $r_{\text{peri-seq}}$ and apocentre $r_{\text{apo-seq}}$ of the sequence.

The initial conditions of the representative stellar orbits are

$$r_i \quad \theta_i \quad \phi_i \quad v_{r,i} \quad v_{\theta,i} \quad v_{\phi,i}. \tag{2.43}$$

They are sampled for each sequence in two steps: (1) **librarian()** randomly generates $N_{r,\text{grid}} \cdot N_{\phi,\text{grid}}$ values of (r_i, ϕ_i) for $r \in [r_{\text{peri-seq}}, r_{\text{apo-seq}}]$ and $\phi \in [0, 2\pi]$. The component $v_{\phi,i}$ of the velocity follows as

$$v_{\phi,i} = \frac{L_z(r_i, \phi_i)}{r_i}. \tag{2.44}$$

The maximum radial velocity is

$$v_{r,\text{max}} = \sqrt{2(E - \Phi(r_i, 0, \phi_i)) - v_{\phi,i}^2}. \tag{2.45}$$

The radial component $v_{r,i}$ is linearly sampled in $[0, v_{r,\text{max}}]$. Component $v_{\theta,i}$ is derived from the conservation of energy as

$$v_{\theta,i} = \sqrt{2(E - \Phi(r_i, 0, \phi_i)) - v_{\phi,i}^2 - v_{r,i}^2}. \tag{2.46}$$

---

[8] The library is partitioned in this way so that the sampling technique includes as a special case the method used for potentials where the angular momentum is an integral of motion.

Every orbit crosses the equatorial plane and leaves a footprint in the three-dimensional space (r, ϕ, v_r). For convenience the equatorial plane is divided in $N_{\text{sector}} = N_{\phi,\text{grid}}$ azimuthal sectors and the orbital imprints are stored in a corresponding SOS. The SOS is given by the radii r and radial velocities v_r of the upward crossings of the equatorial plane. For example Figure (2.15(a)) depicts the imprints that a short-axis tube orbit integrated in an axisymmetric potential leaves on the equatorial plane. The equatorial plane is organised in $N_{\text{sector}} = 4$ azimuthal sectors. Figure (2.15(b)) portrays the SOSs. Figure (2.16(a)) and Figure (2.16(b)) show the same for a long-axis tube orbit integrated in a triaxial potential. The short-axis tube and long-axis tube orbits from Figure (2.15) and (2.16) are integrated in axisymmetric and triaxial potentials as those considered in Section (2.5.4). (2) The SOS incorporates all available orbital shapes. The sampling is representative if the SOSs of all the azimuthal sectors are homogeneously filled with orbital imprints. Angle ϕ_i is randomly generated. The SOS related to the corresponding azimuthal sector is completed by sampling the point $(r_i, v_{r,i})$ that maximises the distance from the nearest imprint. The components $v_{\phi,i}$ and $v_{\theta,i}$ are generated as before.

It is interesting to report that the existing triaxial implementation of the Schwarzschild method from van den Bosch et al. (2008) samples the representative stellar orbits from two 2D starting spaces following the recipe from de Zeeuw (1985a) and Schwarzschild (1993). The first space is the (x,z)-start space from which orbits are started with $y_i = v_{x,i} = v_{z,i} = 0$ and $v_{y,i}$ obtained from the conservation of energy $(x_i, y_i, z_i, v_{x,i}, v_{y,i}, v_{z,i}$ are the initial conditions of the orbits). As found by Schwarzschild (1993) using numerical models, the (x,z)-space does not account for all box and boxlets orbits of triaxial near-integrable potentials (see Section 1.9.3). These orbits are sampled in the second 2D starting space (the *stationary start space*) from equipotential surfaces. The recipe was devised for triaxial separable potentials (see Section 1.8.2) and yields a high fraction of box orbits inside the sphere of influence of the black hole in NGC 3379 (van den Bosch & De Zeeuw, 2010). Separable potentials are known however to show unnatural central cores and black holes make box orbits unstable (see Section 1.9.3).

2.5.2 Integration of the equations of motion

Given a set of initial conditions **librarian()** invokes the routine **integrateorb()**. The routine performs the integration of the equations of motion in cartesian coordinates by means of the Cash-Karp algorithm Cash & Karp (1990) as implemented in Press et al. (1996). The algorithm is a fifth-order Runge-Kutta method that returns the estimate of the local truncation error. The integration step-size is adaptive and provided by the algorithm itself. The equations of motion are

$$\frac{dv_{x_i}}{dt} = -\frac{\partial \Phi}{\partial x_i} \tag{2.47}$$

where x_i equals either x, y or z. The components of the force per unit mass are obtained by a coordinate transformation from Equation (2.32)-(2.34) as detailed in

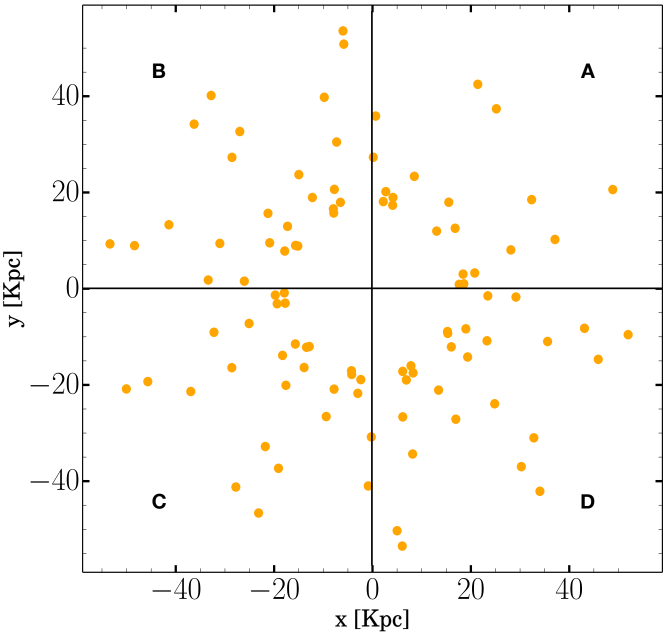

(a) Equatorial plane

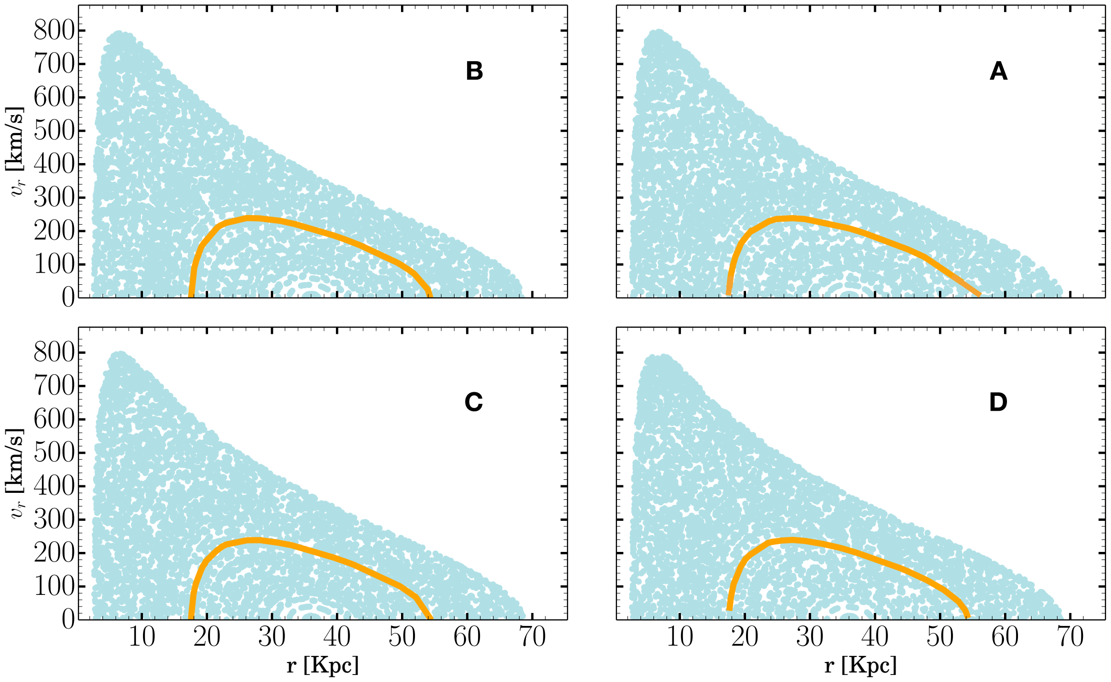

(b) Surfaces of section

Figure 2.15: Upwards crossings of the equatorial plane of a short-axis tube orbit integrated in an axisymmetric potential (2.15(a)) and the SOSs corresponding to the azimuthal sectors in which the equatorial plane is organised (2.15(b)). The orange points are the imprints of the short-axis tube orbit. In light blue the imprints of the other orbits belonging to the sequence. A short-axis tube circulates around the short-axis of the system. Hence it crosses the equatorial plane upwardly in all azimuthal sectors.

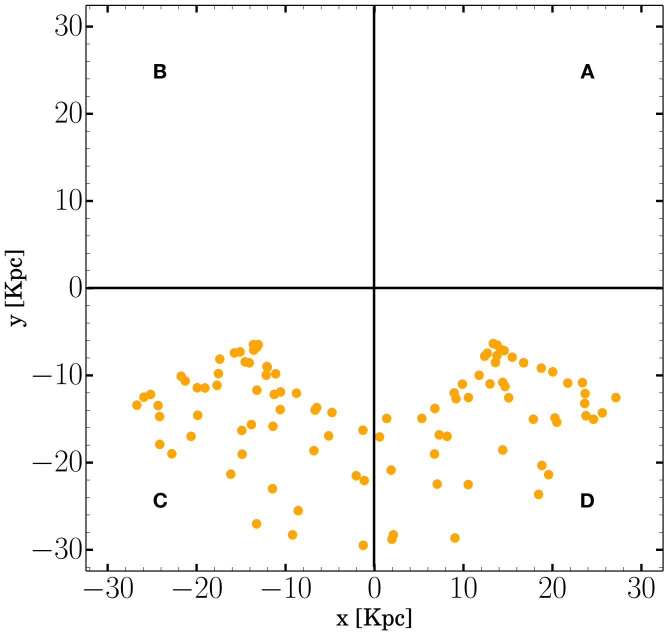

(a) Equatorial plane

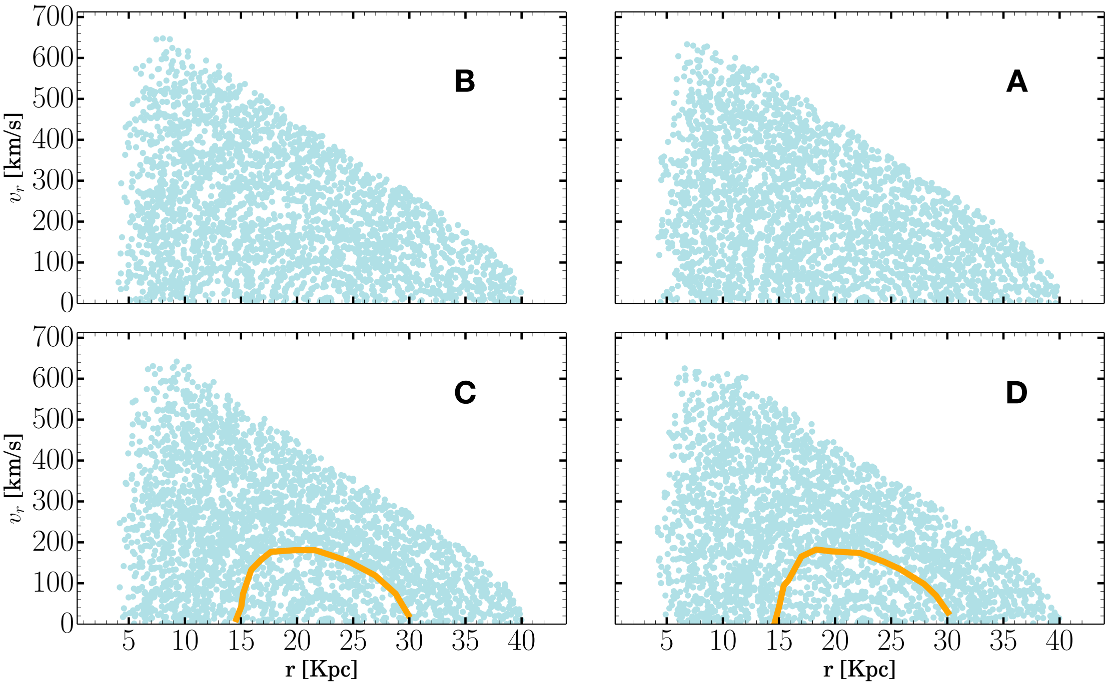

(b) Surfaces of section

Figure 2.16: Upwards crossings of the equatorial plane of a long-axis tube orbit integrated in a triaxial potential (2.16(a)) and the SOSs corresponding to the azimuthal sectors in which the equatorial plane is organised (2.16(b)). The orange points are the imprints of the long-axis tube orbit. In light blue the imprints of the other orbits belonging to the sequence. The long-axis tube circulates around the long-axis of the system. Hence it crosses upwardly only in one half of the equatorial plane.

Appendix (B.2). As in Siopis et al. (2009), the equations of motion are integrated for a number $N_{\rm step}$ of time-steps such that the corresponding orbit crosses the equatorial plane upwardly for $N_{\rm SOS} = 100$ times [9].

2.5.3 Processing the representative orbits

During the integration of the equations of motion the positions and velocities of the representative orbits at each time-step are stored in appropriate arrays. Routine **librarian()** invokes **workonorb()**. This routine classifies the representative orbits and computes their time-averaged properties.

The classification of the representative orbits The number of orbits to be sampled in order to ensure a complete coverage of the SOSs of all the azimuthal sectors may be very large. The situation is extreme in a Keplerian potential where each orbit leaves only one upward imprint in the SOS. In order to reduce the computational effort the orbits are classified following the scheme of van den Bosch et al. (2008). Routine **classify_orb()** checks the sign of the components of the angular momentum as the orbits cross the equatorial plane and categorises them in one of the following classes:

1. **Short-axis tube orbit**: if the orbit conserves the sign of the z-component of the angular momentum;
2. **Keplerian/Spherical-like orbit**: if the orbit conserves the sign of all the components of the angular momentum;
3. **Long-axis tube orbit**: if the orbit conserves the sign of the x-component of the angular momentum;
4. **Box orbit**: the orbit does not conserve the sign of any of the components of the angular momentum. In fact orbits belonging to this class oscillate in all three directions.

As described in the next paragraph, this classification is used to shorten the calculation of the orbital time-averaged properties and to reduce the number of representative orbits to be computed. The classification scheme does not allow to distinguish between inner- and outer long-axis tubes. This is however irrelevant since the two families of orbits are treated in the same way.

The time-averaged properties of the representative orbits At each time-step SCHERPA stores the contribution of orbit i to the luminosity and internal velocity moments and to the projected kinematics. This is done taking into account the contribution from the point spread function (PSF), which is parametrised as

---

[9] This ensures the accuracy of the time-averaged properties of the representative stellar orbits introduced in Section (2.5.3).

a two dimensional Gaussian or given by an image. The projection onto the plane of the sky is carried out as in Equation (2.1). Following Thomas et al. (2004) the set of integration time-steps Δt_j such that the orbit lays in the bin k with $1 \leq k \leq N_{\text{bin}}$ is defined as

$$\Lambda_k \equiv \Big\{ j : \Big(r(\Delta t_j),\ \theta(\Delta t_j),\ \phi(\Delta t_j) \Big) \in \text{bin } k \Big\} \tag{2.48}$$

where $N_{\text{bin}} = N_{\text{r, grid}} \times N_{\theta,\text{grid}} \times N_{\phi,\text{grid}}$. The contribution LIGHT_i^k of orbit i to the luminosity LIGHT^k in bin k can be computed by means of the time-average theorem (if the orbit is regular and it is not a resonance) as

$$\text{LIGHT}_i^k = \sum_{j \in \Lambda_k} \frac{\Delta t_j}{T_i} \tag{2.49}$$

where $T_i = \sum_{j=1}^{N_{\text{step}}} \Delta t_j$ is the total integration time of orbit i. The contribution in spatial bin k of orbit i to the internal velocity moments of order l, m, n is given by

$$\langle v_r^l v_\theta^m v_\phi^n \rangle_i^k = \sum_{j \in \Lambda_k} v_r^l v_\theta^m v_\phi^n \frac{\Delta t_j}{T_i}. \tag{2.50}$$

The normalised contribution of orbit i to the kinematics in projected bin $1 \leq b \leq N_{\text{x,sky}} \times N_{\text{y,sky}}$ and velocity bin $1 \leq g \leq N_{\text{vel}}$ is denoted as $\text{LOSVD}_i^{b,g}$.

Routine **workonorb()** processes the representative orbits differently based on their classification. Keplerian/Spherical-like orbits whose initial conditions differ only in ϕ are identical under symmetry reasons. Therefore the routine produces $N_{\text{sector}} - 1$ copies in the azimuthal direction of an orbit belonging to this class. The routine invokes **intrinsic_mom()** for computing the luminosity and intrinsic velocity moments and **projected_mom()** for the projected kinematics of the orbits. The trajectories of the prograde and retrograde motion of Tube and Keplerian/Spherical-like orbits are identical. Therefore it suffices to consider their velocity mirrored copies at the superposition stage. Box orbits have instead no net sense of rotation. Their velocity mirrored copies are then not considered. These operations are performed in **store_orbit()**.

2.5.4 Test of the implementation

The method for the integration of the equations of motion is tested by verifying the conservation of the integrals of motion along the representative stellar orbits. The test is performed for a spherical, an axisymmetric (oblate) and a triaxial density distribution. The library contains $N_{\text{orbit}} = 74020$ orbits. The binning grid is composed of $N_{r,\text{grid}} = 20$, $N_{\theta,\text{grid}} = 5$ and $N_{\phi,\text{grid}} = 10$ bins. During the integration of orbit i the code stores for each integral of motion the maximum of the relative deviations

$$\Delta_{\max,i} = \max \left(\frac{val(t) - val(t=0)}{val(t=0)} \right) \tag{2.51}$$

between the value of the integral of motion at time t and its initial value $val(t=0)$. When the integration of the library of orbits is complete the code computes for each integral the average

$$\langle \Delta_{\rm max} \rangle = \frac{1}{N_{\rm orbit}} \sum_{i=1}^{N_{\rm orbit}} \Delta_{{\rm max},i}. \tag{2.52}$$

The spherical model is the isotropic Hernquist sphere. The parameters of the model are those used in Section (2.3.4). The orbits in a spherical potential are expected to conserve the energy and the three components of the angular momentum. Table (2.8) shows that the averages of the maxima of the relative deviations for the four integrals are all below 0.001.

	$\langle \boldsymbol{\Delta}_{\rm max} \rangle$
Energy	7.660 E-07
$\mathbf{L_x}$	7.351 E-07
$\mathbf{L_y}$	7.351 E-07
$\mathbf{L_z}$	7.352 E-07

Table 2.8: Averages over $N_{\rm orbit}$ representative stellar orbits of the maxima of the relative deviations of the integrals of motion conserved in a central potential (details in text).

The axisymmetric (oblate) model is a Perfect Ellipsoid with total mass $M = 1.5 \cdot 10^{12}$ $\mathrm{M}_\odot$ and axis lengths $a = b = 7.65$ Kpc and $c = 5.355$ Kpc. The axes ratios are therefore $q = \frac{c}{a} = 0.7$ and $p = \frac{b}{a} = 1.0$. The model is placed at a distance $d = 16.83$ Mpc and studied in the radial interval $r_{\rm min} = 8 \cdot 10^{-2}$ Kpc and $r_{\rm max} = 120$ Kpc. The orbits in an axisymmetric (oblate) model conserve the energy and the z-component of the angular momentum as shown in Table (2.9). The averages of the maxima of the relative deviations in E and L_z are lower than 0.001.

	$\langle \boldsymbol{\Delta}_{\rm max} \rangle$
Energy	1.123 E-06
$\mathbf{L_z}$	7.008 E-07

Table 2.9: Averages over $N_{\rm orbit}$ representative stellar orbits of the maxima of the relative deviations of the integrals of motion conserved in an axisymmetric (oblate) potential (details in text).

As a final test the validity of the method for the integration of the equations of motion is tested against a triaxial model equal to that used in Section (2.3.4). The energy is the only analytical integral of motion in a triaxial potential. Moreover the orbital structure is richer. There are short- and long-axis tube orbits and box

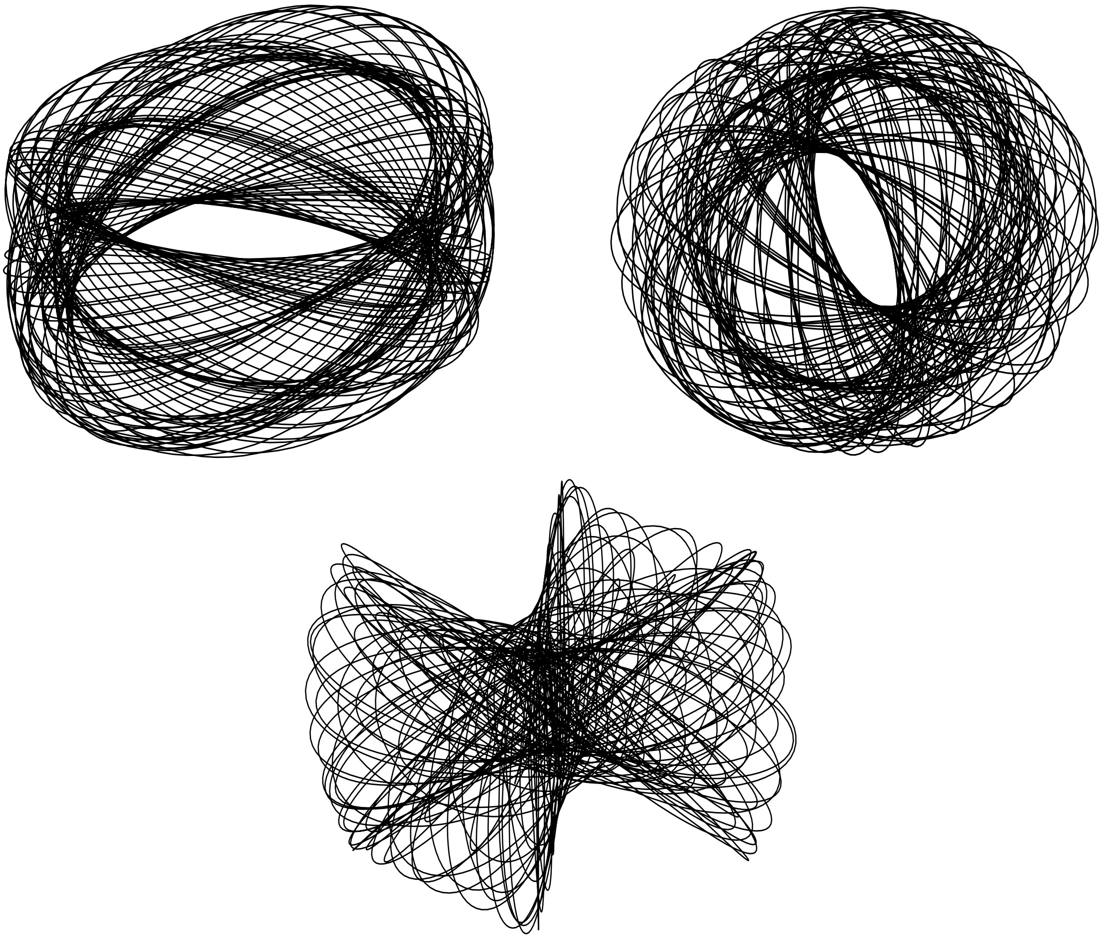

Figure 2.17: A short-axis tube orbit (top left), a long-axis tube orbit (top right) and a box orbit (bottom), sampled and integrated in the potential of the triaxial Perfect Ellipsoid model described in the text.

orbits as those portrayed in Figure (2.17). Table (2.10) shows the averages of the maxima of the relative deviations over each orbit class. The averages are computed over $N_{\text{short}} = 33487$, $N_{\text{long}} = 21790$ and $N_{\text{box}} = 18743$ representative orbits. The energy is well conserved. It is therefore possible to conclude that the integration scheme performs as expected for all the density distributions considered regardless of the complexity of the orbital shapes.

	$\langle \boldsymbol{\Delta}_{\text{max}} \rangle$ **Short-axis tube**	$\langle \boldsymbol{\Delta}_{\text{max}} \rangle$ **Long-axis tube**	$\langle \boldsymbol{\Delta}_{\text{max}} \rangle$ **Box orbit**
Energy	1.348 E-06	1.329 E-06	1.263 E-06

Table 2.10: Averages over each orbital class of the maxima of the relative deviations of the energy in a triaxial potential (details in text).

2.6 Orbit superposition

The section details the superposition of the representative stellar orbits as implemented in module **modelmod.f90** and routine **analyse_model()**. After introducing the maximum entropy technique and the method used to compute the orbital weights, the section focuses on how SCHERPA computes the model estimates of the observables.

2.6.1 Maximum entropy technique

The representative stellar orbits are superimposed in order to match the observed kinematics and to exactly reproduce the de-projected density. The latter guarantees that the orbit model is consistent with the observed surface brightness profile. The contribution of each orbit i to the superposition is quantified by a non-negative **orbital weight** w_i [10] that represents the amount of light carried by the given orbit. The superposition is performed by means of the maximum entropy technique of Richstone & Tremaine (1988) as described in Siopis et al. (2009). The orbital weights are determined by maximising the entropy-like quantity

$$\hat{S} \equiv S - \alpha\, \chi^2, \tag{2.53}$$

where the term S is the Boltzmann entropy

$$S \equiv - \int f \ln(f)\; d^3r\; d^3v \approx - \sum_{i=1}^{N_{\rm orbit}} w_i \ln\left(\frac{w_i}{V_i}\right) \tag{2.54}$$

with V_i being the phase-space volume associated with orbit i and where

$$\chi^2 \equiv \sum_{b=1}^{N_{\rm losvd}} \sum_{g=1}^{N_{\rm vel}} \left(\frac{{\rm LOSVD}^{b,g}_{\rm model} - {\rm LOSVD}^{b,g}_{\rm data}}{\Delta{\rm LOSVD}^{b,g}_{\rm data}}\right)^2 \tag{2.55}$$

measures the deviations among the model and data LOSVDs in the projected bin $1 \leq b \leq N_{\rm x,sky} \times N_{\rm y,sky}$ and in the velocity bin $1 \leq g \leq N_{\rm vel}$. For Hamiltonians corresponding to a spherical/axisymmetric system the orbital phase-space volumes follow as

$$V_i \approx 2\pi \times \Delta E \times \Delta L_z \times \int_{\rm SOS} T(r, v_r)\; dr\; dv_r. \tag{2.56}$$

$T(r, v_r)$ is the time elapsed between two consecutive crossings of the equatorial plane and $\Delta E \times \Delta L_z$ is the area of the cell on the (E, L_z)-plane around the value of the energy and of the angular momentum of the orbit (Binney et al., 1985; Thomas et al., 2004). In SCHERPA the orbital phase-space volumes are set to

$$V_i = \frac{1}{N_{\rm orbit}} \quad \text{for} \quad i = 1, \ldots, N_{\rm orbit} \tag{2.57}$$

---

[10] The orbital weights are also known as *occupation numbers*.

so that

$$\sum_{i=1}^{N_{\mathrm{orbit}}} V_i = 1. \tag{2.58}$$

This approximation is used also in De Lorenzi et al. (2007). The Boltzmann entropy term guarantees that the model corresponds to a smooth DF. The minimisation of the χ^2 ensures that the model is able to reproduce the observed kinematics. The **regularisation (smoothing)** parameter α sets the relative importance of the entropy maximisation with respect to the χ^2-minimisation. A large value of α corresponds to a low regularisation, i.e. the minimisation of χ^2 is more important than the maximisation of the entropy. Determining how much smoothing is necessary to reproduce the properties of a galaxy depends on the quality and spatial coverage of the observed data set (Thomas et al., 2005b). $\hat{S}$ is a function of the regularisation parameter α. Therefore the maximisation of $\hat{S}$ is iterated for different values of α. The program starts with $\alpha = 0$ and then increases it slowly until the value of the χ^2 is stable around its minimum (Thomas et al., 2005b). For each value of the regularisation parameter, the maximisation of $\hat{S}$ is performed by the method of the Lagrange multipliers. The values of the weights are adjusted iteratively using the Newton's method (see Appendix B.3). These steps involve linear algebra operations, performed by means of the routines from the LAPACK library (`http://www.netlib.org/lapack/`).

2.6.2 Model estimates of the observables

Routine **analyse_model()** estimates the model predictions of the observables. The total luminosity of the library in bin k is obtained as

$$\mathrm{LIGHT}^k_{\mathrm{model}} = \sum_{i=1}^{N_{\mathrm{orbit}}} w_i\ \mathrm{LIGHT}^k_i. \tag{2.59}$$

The velocity moments are given by

$$\langle v_r^l v_\theta^m v_\varphi^n \rangle^k_{\mathrm{model}} = \frac{1}{\mathrm{LIGHT}^k_{\mathrm{model}}} \sum_{i=1}^{N_{\mathrm{orbit}}} w_i\ \langle v_r^l v_\theta^m v_\varphi^n \rangle^k_i. \tag{2.60}$$

The contribution to the projected kinematics follows as

$$\mathrm{LOSVD}^{b,g}_{\mathrm{model}} = \sum_{i=1}^{N_{\mathrm{orbit}}} w_i\ \mathrm{LOSVD}^{b,g}_i. \tag{2.61}$$

The routine fits a Gauss-Hermite series to the $\mathrm{LOSVD}^{b,g}_{\mathrm{model}}$ to obtain the Gauss-Hermite Parameters (GHP)

$$\mathrm{GHP}^{b,g}_{\mathrm{model}} = \{\gamma^{b,g}, v^{b,g}, \sigma^{b,g}, h_3^{b,g}, h_4^{b,g}\}. \tag{2.62}$$

2.7 Optimisation of SCHERPA

The section deals with the improvements performed to SCHERPA in order to optimise the search of the best fitting model in the multi-dimensional space of the input mass parameters and viewing angles and to shorten the computation of each model. This part of the project has been carried out with the assistance of Dr. Alexey Krukau and Dr. Frederik Beaujean from the C^2PAP cluster (Computational Center for Particle And Astrophysics) [11].

2.7.1 Searching for the best fitting model

The Schwarzschild method is a flexible technique that allows to study the properties of galaxies without any a priori assumption on the orbital configuration or the potential. It is however computationally expensive. It requires to explore the multi-dimensional space of the input mass parameters and viewing angles in order to find the model that best reproduces the observed data. So far this has been done by means of a grid search. This procedure is costly in terms of computation time due to the high number of models to be probed (usually 20.000 for an axisymmetric galaxy). Moreover each model involves the computation and superposition of thousands of representative stellar orbits. The common practice to reduce the computation effort is to narrow down parameter space by assuming the M/L to be constant throughout the galaxy or a 2-parameters expression for the DM profile. This diminishes the number of models to be computed. Such approach may however not be physically reliable; the real DM profile could be unlike any of those proposed or the M/L could vary. Furthermore in the triaxial case the parameter space becomes larger due to the fact that the viewing direction of a galaxy is identified by two viewing angles. These issues motivate the introduction of NOMAD (**N**onlinear **O**ptimisation by **M**esh **A**daptive **D**irect search), a C++ software designed for time-consuming constrained **black-box** optimisations. In this type of problem the function to optimise is noisy and it is evaluated by means of a computer code (Audet & Dennis, 2006; Le Digabel, 2011). The software investigates the space of the input mass parameters and viewing angles with a **direct-search** scheme, where the exploration is driven only by the function evaluations. The advantage of NOMAD is its efficiency in converging to the best fitting model regardless of the number of dimensions of the space of parameters. It is also able to execute different function calls in parallel. The disadvantage of NOMAD is that it is not suited to estimate the errors on the input mass parameters. NOMAD can be freely downloaded from the webpage `https://www.gerad.ca/nomad/Project/Home.html` together with a detailed documentation. Dr. Alexey Krukau and Dr. Frederik Beaujean implemented and tested an algorithm in Python that interfaces NOMAD with SCHERPA in order to run multiple function calls in parallel.

---

[11] The C^2PAP cluster (`http://www.universe-cluster.de/c2pap/`) is an initiative of the Excellence Cluster Universe.

2.7.2 Multi-core implementation

The modelling of triaxial elliptical galaxies is computationally demanding. The space of the parameters becomes larger and each model is three-dimensional. Furthermore the number of representative stellar orbits to be integrated increases as well as the number of density constraints. The implementation of SCHERPA has been modified in order to run on multiple computer cores. The serial implementation was executed using the profiling options of the Intel compiler. This yielded the amount of computation time spent in each of the program units illustrated in Figure (2.1). The first three steps (de-projection, density and potential calculation) require less than 20 % of the total computation time. Hence they were not parallelised. The remaining computation time is equally spent in the generation of the library of orbits and in the linear algebra operations needed for their superposition. The parallelised routines developed by Dr. Alexey Krukau with the MPI (Message Passing Interface) library (MPIstandard) for the axisymmetric implementation of Thomas et al. (2004) have been migrated to SCHERPA.

A parallel program shares the workload among different processes. Each process runs a serial application. The number of processes is provided by the user when executing the code. The communicator assigns an identifier (**rank**) to every process and connects them. The communication among processes can be either **point-to-point** or **collective**. In the first case the communication involves only two processes. In the second case all processes partecipate. Program **scherpa.f90** initialises the MPI communication by invoking **MPI_INIT()**. Afterwards it executes **MPI_COMM_SIZE()** and **MPI_COMM_RANK()** to get the number of processes (the size of the communicator) and assign a rank to each of them. Given a de-projected density, each process runs independently the second and third step of the flowchart in Figure (2.1). Most of the changes that regard the generation of the library of orbits happen in the routines responsible for the sampling of the initial conditions. In Schwarzschild models the representative orbits can be integrated independently from any other with the only complication that the initial conditions of orbits belonging to the same sequence are derived in order to fill empty parts of phase-space. Routine **librarian()** invokes **distribute_orbits()** which divides the library in groups (**piles**) made up of a certain number of sequences so that the amount of orbits in each pile is similar. Afterwards every pile is assigned to a particular process that will integrate the orbits and compute their time-averaged properties. In the end, the library is gathered and shared with all processes by means of a collective communication. The routine **distribute_orbits()** was developed by Dr. Jens Thomas and tested by Dr. Alexey Krukau. With respect to the superposition of the orbits, the changes consist mainly in performing in parallel the linear algebra operations described in Appendix (B.3). This is achieved by substituting the routines from the LAPACK library with their parallel versions from ScaLAPACK (`http://www.netlib.org/scalapack/`). The tests described in this chapter were repeated for the multi-core implementation of the code and yielded the same results.

Chapter 3

The recovery of the mass and viewing direction of a spherical and triaxial reference model

The chapter tests how well SCHERPA reproduces the luminosity density distribution, fits the projected velocity profiles and estimates the intrinsic kinematics of a spherical and a triaxial reference model. It thereby verifies the accuracy of the techniques described in Chapter (2) for the sampling of the initial conditions of the representative stellar orbits and for their superposition. The chapter validates also the recovery of the values of the input mass parameters and of the viewing angles.

3.1 Spherical model

The spherical model is the isotropic Hernquist sphere with total mass $M = 1.5 \cdot 10^{12}\ \mathrm{M}_\odot$ and effective radius $r_e = 10$ Kpc ($r_s \approx 5.51$ Kpc). The models is placed at a distance $d = 65$ Mpc and studied in the radial interval $r_{\mathrm{min}} = 3 \cdot 10^{-2}$ Kpc and $r_{\mathrm{max}} = 101$ Kpc. The mass-to-light ratio is $\mathrm{M/L} = 1\ \frac{\mathrm{M}_\odot}{\mathrm{L}_\odot}$. The model is oriented along the line-of-sight ($\vartheta = 90\,^\circ, \varphi = 0\,^\circ, \psi = 90\,^\circ$) and contains no dark matter and no black hole. The velocity profiles $\mathrm{LOSVD}_{\mathrm{original}}$ fitted by the code are obtained from a Monte-Carlo sampling of the model performed by J. Thomas with one billion equal-mass particles, distributed in phase-space according to the DF of the isotropic Hernquist sphere. It reads

$$
\begin{aligned}
f(E) = {} & \frac{M}{8\sqrt{2}\ \pi^3\ r_s^3\ v_s^3} \frac{1}{(1-q^2)^{\frac{5}{2}}} \\
& \times \left[3\arcsin(q) + q\sqrt{1-q^2}(1-2q^2)(8q^4-8q^2-3) \right]
\end{aligned}
\tag{3.1}
$$

where $q = \sqrt{-\frac{E\ r_s}{GM}}$ and $v_s = \sqrt{\frac{GM}{r_s}}$ is the circular velocity at the scaling radius. The velocity profiles are binned in $N_{\mathrm{vel}} = 27$ velocity bins with $v_{\parallel,\mathrm{max}} = 1500\ \frac{\mathrm{km}}{\mathrm{s}}$.

The number of velocity profiles is $N_{\mathrm{losvd}} = 48$. This is the number of velocity profiles used in general when modelling real galaxies. The velocity profiles are distributed along angular rays in the projected radial interval $r \in (0.31, 10)$ Kpc. They are distributed only in the first quadrant $(x' > 0, y' > 0)$ of the plane of the sky. No PSF convolution is applied during the projection. The binning grid is composed of $N_{r,\mathrm{grid}} = 20$, $N_{\theta,\mathrm{grid}} = 5$ and $N_{\phi,\mathrm{grid}} = 10$ bins. A library of $N_{\mathrm{orbit}} = 2 \times 45010$ representative stellar orbits is used to reproduce $N_{r,\mathrm{grid}} \times N_{\theta,\mathrm{grid}} \times N_{\phi,\mathrm{grid}} = 1000$ constraints from the three-dimensional intrinsic luminosity density and to fit $N_{\mathrm{kindata}} = 1083$ kinematic data points. The three-dimensional input density is given by Equation (2.19). It is sampled on $N_{r,\mathrm{dens}} = 300$ radial points and on $N_{\theta,\mathrm{dens}} = N_{\phi,\mathrm{dens}} = 101$ angular points. The intrinsic velocity dispersion is such that

$$\sigma_r = \sigma_\theta = \sigma_\phi. \tag{3.2}$$

The anisotropy parameter follows as

$$\beta = 1 - \frac{\sigma_\theta^2 + \sigma_\phi^2}{2\sigma_r^2} = 0. \tag{3.3}$$

The LOSVDs are fitted with a truncated Gauss-Hermite series. For a non-rotating spherical system $v = h_3 = 0$. The values for h_4 are from Baes et al. (2005). The projected velocity dispersion $\sigma_P(r)$ reads

$$\begin{aligned} \sigma_P^2(r) = \frac{GM^2}{12\ \pi\ r_s^3\ SB(r)\ \mathrm{M/L}} \Bigg(\frac{1}{2} \frac{1}{(1-s^2)^3} \times \Big[-3s^2\ \Xi(s) \\ \big(8s^6 - 28s^4 + 35s^2 - 20\big) - 24s^6 + 68s^4 - 65s^2 + 6\Big] - 6\pi s \Bigg). \end{aligned} \tag{3.4}$$

The surface brightness profile is

$$SB(r) = \frac{M}{2\ \pi\ r_s^2 (1-s^2)^2\ \mathrm{M/L}} \left[(2+s^2)\ \Xi(s) - 3 \right] \tag{3.5}$$

where $s = \frac{r}{r_s}$ and

$$\begin{aligned} \Xi(s) &= \tfrac{1}{\sqrt{1-s^2}} \ln\left(\tfrac{1+\sqrt{1-s^2}}{s}\right) && \text{for} \quad 0 \le s \le 1 \\ \Xi(s) &= \tfrac{1}{\sqrt{s^2-1}} \arccos(\tfrac{1}{s}) && \text{for} \quad 1 \le s < \infty. \end{aligned} \tag{3.6}$$

Figure (3.1) portrays the reconstruction of the intrinsic properties and the fit to the observed kinematics. The comparison among the model predictions and the theoretical values is carried out by means of the RMS of the fractional difference. The RMS of the difference is used for v and h_3 since their theoretical value is zero. The RMS is computed for radii between the innermost and outermost projected data points. The deviations are computed over 450 points and are reported in Table (3.1). The table shows that the code reproduces the properties of the target

	Δ RMS
$\boldsymbol{\rho}$	1.323 E-02
$\boldsymbol{\sigma_r}$	6.848 E-03
$\boldsymbol{\sigma_\theta}$	6.174 E-03
$\boldsymbol{\sigma_\phi}$	8.950 E-03
$\boldsymbol{v}$	6.078 E-05
$\boldsymbol{\sigma_P}$	4.969 E-03
$\boldsymbol{h_3}$	1.773 E-04
$\boldsymbol{h_4}$	8.816 E-04

Table 3.1: Comparison between the model predictions and the theoretical values of the intrinsic and projected properties of an isotropic Hernquist sphere (details in text).

model within 1.5 %. The fits in Figure (3.1(b)) correspond to $\chi^2_{\rm min} = 13.602$ and were obtained for $\alpha = 1.024$ E-04 where α is the regularisation parameter from Equation (2.53). The orbital phase space volumes are evaluated as in Equation (2.56).

3.1.1 Recovery of the mass-to-light ratio and of the orientation

The verification of the recovery of the mass-to-light ratio and of the orientation is carried out by fitting three noisy realisations of the velocity profiles $\mathrm{LOSVD}_{\rm original}$. They are identified as Noise A, Noise B and Noise C. SCHERPA is tested on more than one realisation in order to limit the influence of a particular noise pattern on the results. A noisy realisation of $\mathrm{LOSVD}^b_{\rm original}$ is equal to

$$\mathrm{LOSVD}^{b,g}_{\rm noisy} = \mathrm{LOSVD}^{b,g}_{\rm original} + y_{\rm ran} \tag{3.7}$$

with $1 \leq b \leq N_{\rm x,sky} \times N_{\rm y,sky}$, $1 \leq g \leq N_{\rm vel}$ and $y_{\rm ran} = x_{\rm ran} \times \mathrm{HSD}^{b,g}$. The value $x_{\rm ran}$ is a normally distributed random number with zero mean and unit variance generated from the algorithm of Box & Muller (1958) as implemented in Press et al. (1996). Factor $\mathrm{HSD}^{b,g}$ equals half of the standard deviation of the values $\mathrm{LOSVD}^{b,g}_{\rm GH,noise}$. $\mathrm{LOSVD}_{\rm GH,noise}$ indicates a set of $N_{\rm noise} = 2000$ realisations generated from noisy GHPs obtained from adding normally distributed noise with zero mean and unit variance to the GHPs of $\mathrm{LOSVD}_{\rm original}$. The uncertainty on $\mathrm{LOSVD}^{b,g}_{\rm noisy}$ equals $\mathrm{HSD}^{b,g}$. The specifications (number of orbits etc.) used to fit the three noisy realisations are those used for the model portrayed in Figure (3.1).

Recovery of the mass-to-light ratio The recovery of the mass-to-light ratio is done by means of a grid search. The mass-to-light ratio is varied in the interval $0.7\,\frac{\mathrm{M}_\odot}{\mathrm{L}_\odot} \leq \mathrm{M/L} \leq 1.4\,\frac{\mathrm{M}_\odot}{\mathrm{L}_\odot}$ in steps $\Delta\mathrm{M/L} = 0.05\,\frac{\mathrm{M}_\odot}{\mathrm{L}_\odot}$. The models are oriented according to $(\vartheta = 90\,^\circ, \varphi = 0\,^\circ, \psi = 90\,^\circ)$. Figure (3.2) quantifies the level of regularisation required for the best fitting mass-to-light ratio to equal the

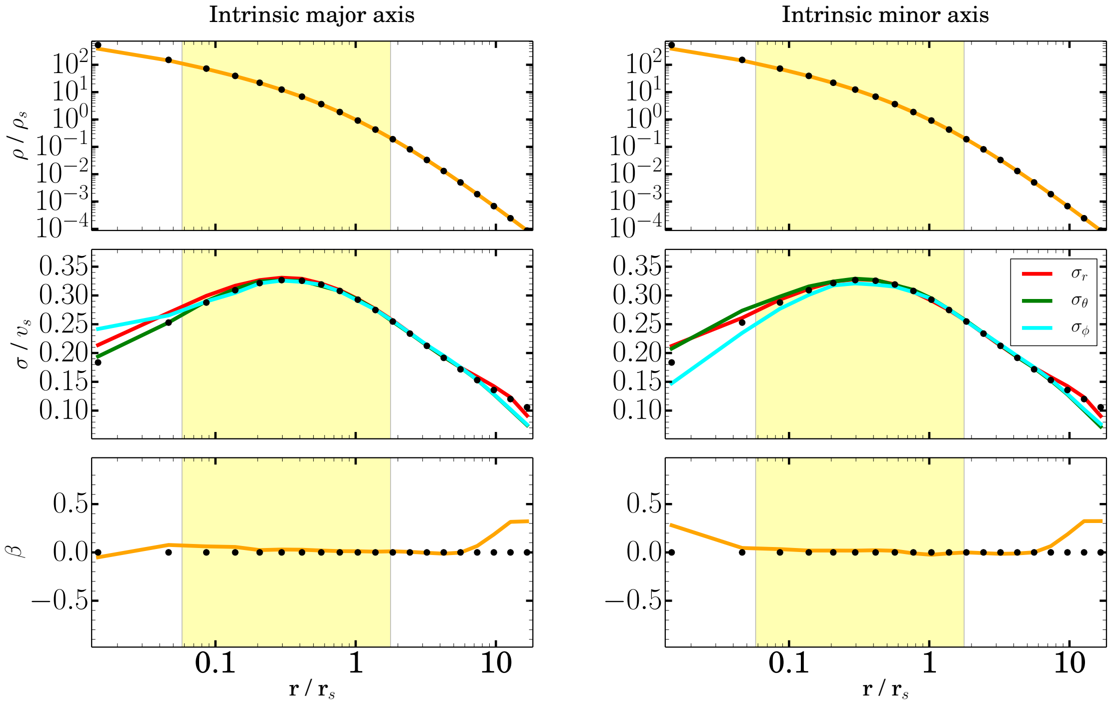

(a) Intrinsic properties

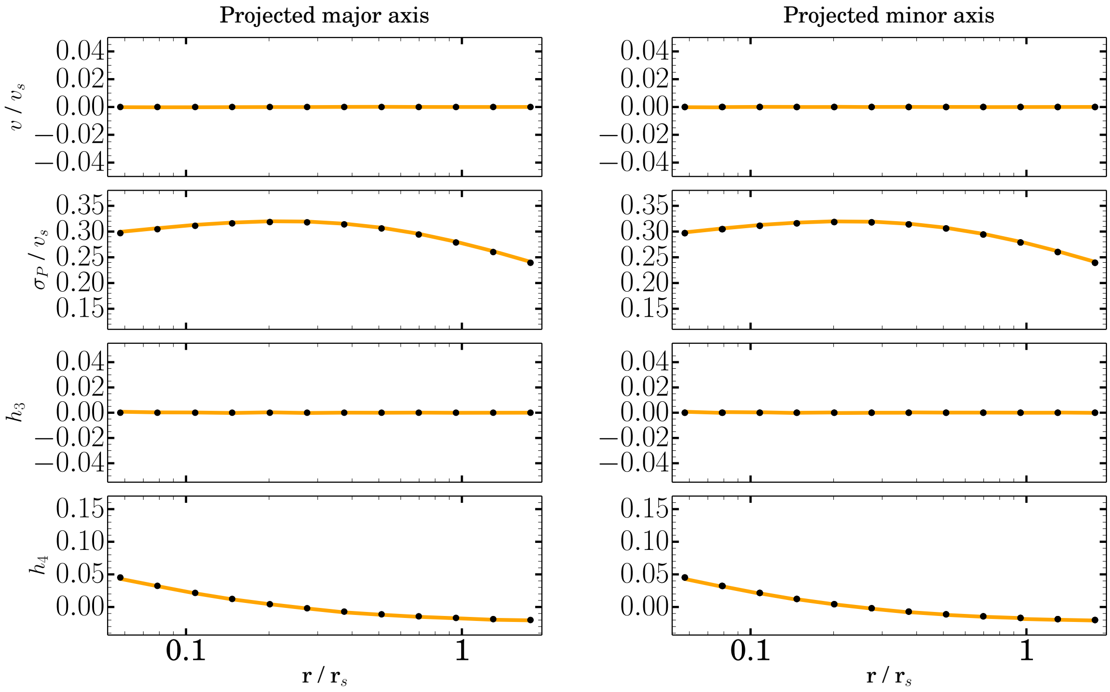

(b) Projected properties

Figure 3.1: Reconstruction of the intrinsic properties (3.1(a)) and fit to the projected kinematics (3.1(b)) for an isotropic Hernquist sphere (details in text) along the major and minor axes. ρ_s is the density at the scaling radius. The black dots represent the theoretical expectations and the coloured lines the results of the modelling. The vertical shaded yellow area in the upper panels highlights the radial interval on the sky where the LOSVDs are distributed.

expected value of $\mathrm{M/L} = 1\,\frac{\mathrm{M}_\odot}{\mathrm{L}_\odot}$. The test is carried out for $N_\alpha = 32$ values of the regularisation parameter α. For all noisy realisations $i_\alpha = 15$. This corresponds to $\alpha = 1.024$ E-04. Figure (3.3) shows the $\Delta\chi^2 = \chi^2 - \chi^2_{\mathrm{min}}$ as a function of mass-to-light ratio. Table (3.2) provides the values χ^2_{min} and the number of kinematic data points for the noisy realisations. Moreover Figure (3.4) portrays the reconstruction of the intrinsic properties and the fit to the noisy realisation Noise C for the best fitting mass-to-light ratio.

Noise Realisation	χ^2_{min}	$\mathrm{N}_{\mathrm{kindata}}$
Noise A	714.370	1095
Noise B	739.079	1090
Noise C	710.512	1086

Table 3.2: Value of χ^2_{min} for the models corresponding to the best fitting mass-to-light ratio and the number of kinematic data points for three noisy realisations of the velocity profiles $\mathrm{LOSVD}_{\mathrm{original}}$ of an isotropic Hernquist sphere (details in text).

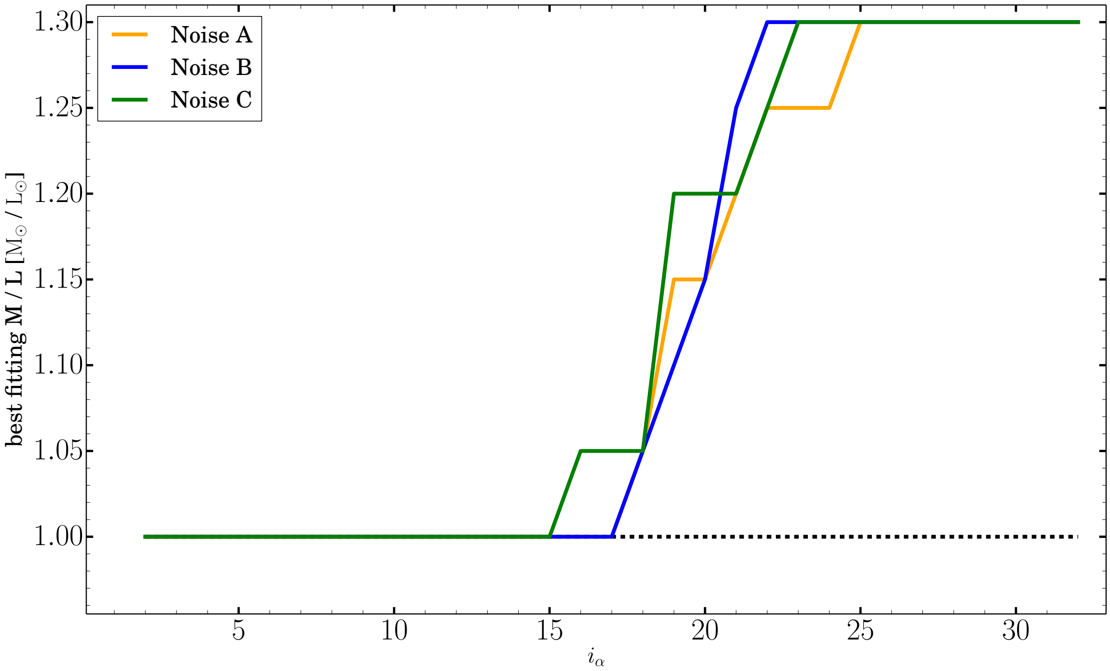

Figure 3.2: Best fitting mass-to-light ratio as a function of the regularisation parameter α for three noisy realisations of the velocity profiles $\mathrm{LOSVD}_{\mathrm{original}}$ of an isotropic Hernquist sphere (details in text).

Recovery of the viewing direction The recovery of the viewing direction is investigated through a grid search. For $\mathrm{M/L} = 1\,\frac{\mathrm{M}_\odot}{\mathrm{L}_\odot}$ and $(\varphi, \psi) = (0\,^\circ, 90\,^\circ)$ the altitude angle ϑ is varied in the interval $0\,^\circ \leq \vartheta \leq 90\,^\circ$ in steps $\Delta\vartheta = 10\,^\circ$. Figure (3.5(a)) shows the $\Delta\chi^2$ as a function of ϑ. The plot compares the results from

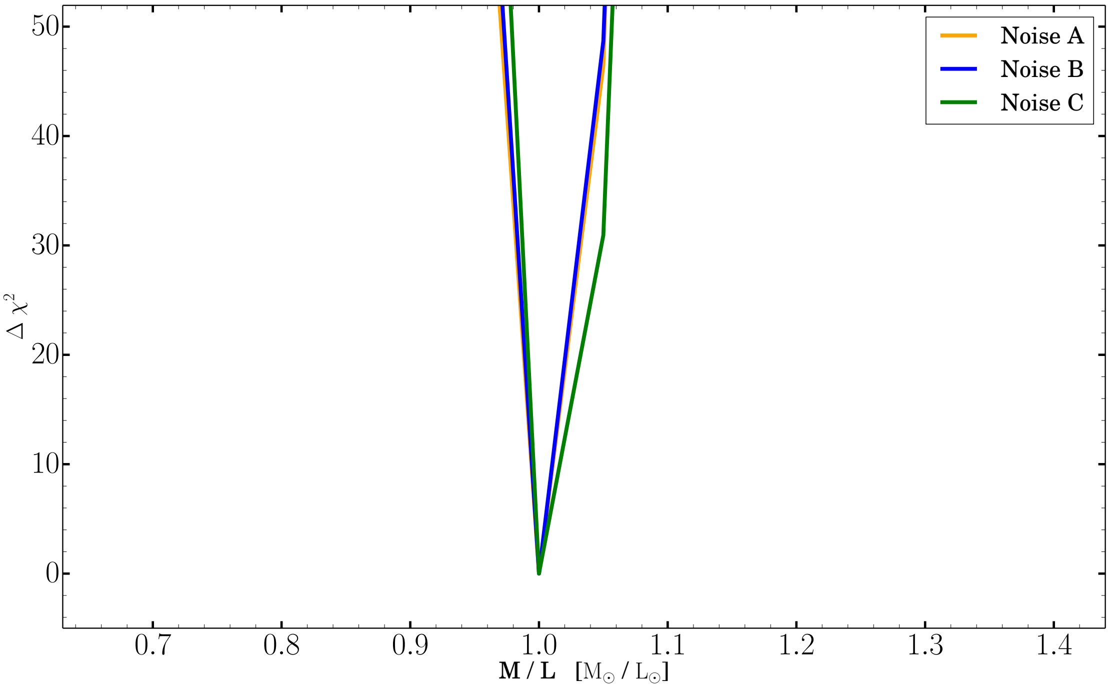

Figure 3.3: The $\Delta\chi^2 = \chi^2 - \chi^2_{\mathrm{min}}$ as a function of the mass-to-light ratio for three noisy realisations of the velocity profiles $\mathrm{LOSVD}_{\mathrm{original}}$ of an isotropic Hernquist sphere (details in text).

SCHERPA with the axisymmetric models obtained using the code from Thomas et al. (2004). The axisymmetric models fit the kinematics with $N_{\mathrm{orbit}} = 2 \times 7000$ and a regularisation corresponding to $\alpha = 1.677$. The expectation for a spherical system is that the velocity profiles can be fitted equally well regardless of the viewing direction. While axisymmetric models fit the profiles better for an edge-on view, the models from SCHERPA show no coherent dependence on ϑ. The grid search is repeated for $\mathrm{M/L} = 1\,\frac{\mathrm{M}_\odot}{\mathrm{L}_\odot}$ and $\vartheta = \psi = 90^\circ$ by varying the azimuthal angle φ in the same interval probed for ϑ. Figure (3.5(b)) shows that the $\Delta\chi^2$ presents no clear dependence on φ. These results are presumably due to the fact that SCHERPA produces fully three-dimensional models where all four integrals of motion of the spherical potential are sampled. The models have then more freedom in fitting the noisy data. Axisymmetric models are instead two-dimensional. They sample only three integrals of motion, integrate the representative orbits in two-dimensions and smooth them in the azimuthal direction. Edge-on axisymmetric models are able to balance the retrograde and prograde motion in order to reproduce the noisy data. Face-on axisymmetric models are such that the position angle on the sky corresponds to the intrinsic azimuthal angle, as a function of which they are constant by construction. Therefore they fail to reproduce the noise in the kinematics (Thomas et al., 2007a).

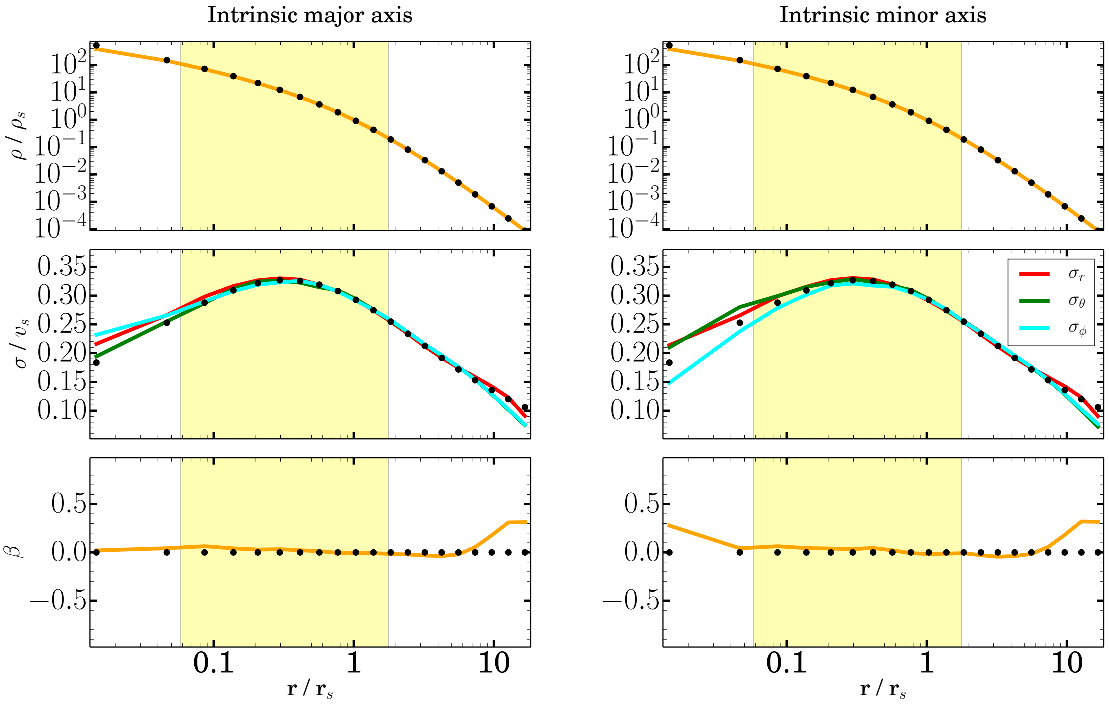

(a) Intrinsic properties

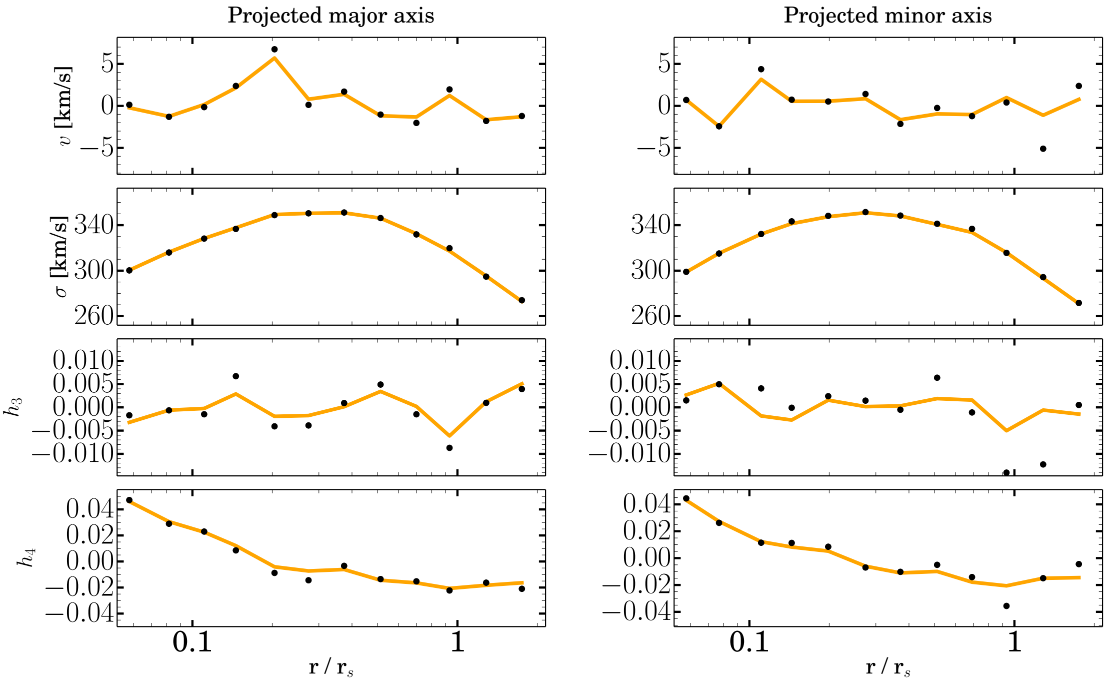

(b) Projected properties

Figure 3.4: Reconstruction of the intrinsic properties (3.4(a)) and fit to the noisy realisation Noise C (3.4(b)) for an isotropic Hernquist sphere (details in text) along the major and minor axes. The model corresponds to the best fitting mass-to-light ratio. ρ_s is the density at the scaling radius. The black dots represent the theoretical expectations for the intrinsic properties and the kinematic data for the projected properties and the coloured lines the results of the modelling. The vertical shaded yellow area in the upper panels highlights the radial interval on the sky where the LOSVDs are distributed.

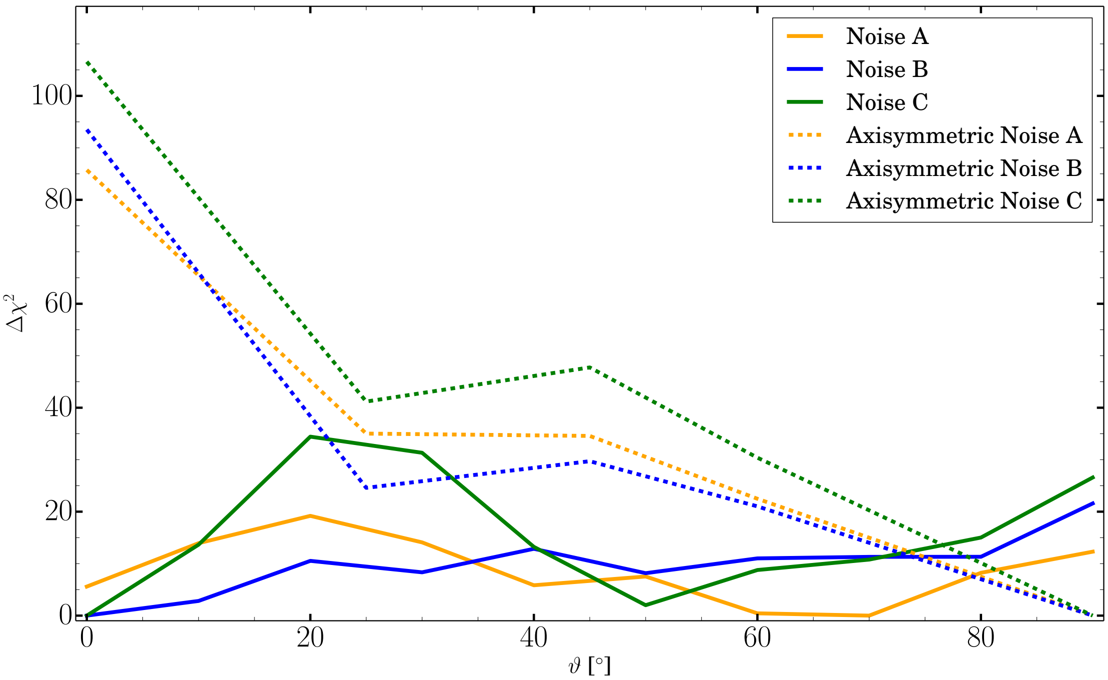

(a) Viewing angle ϑ

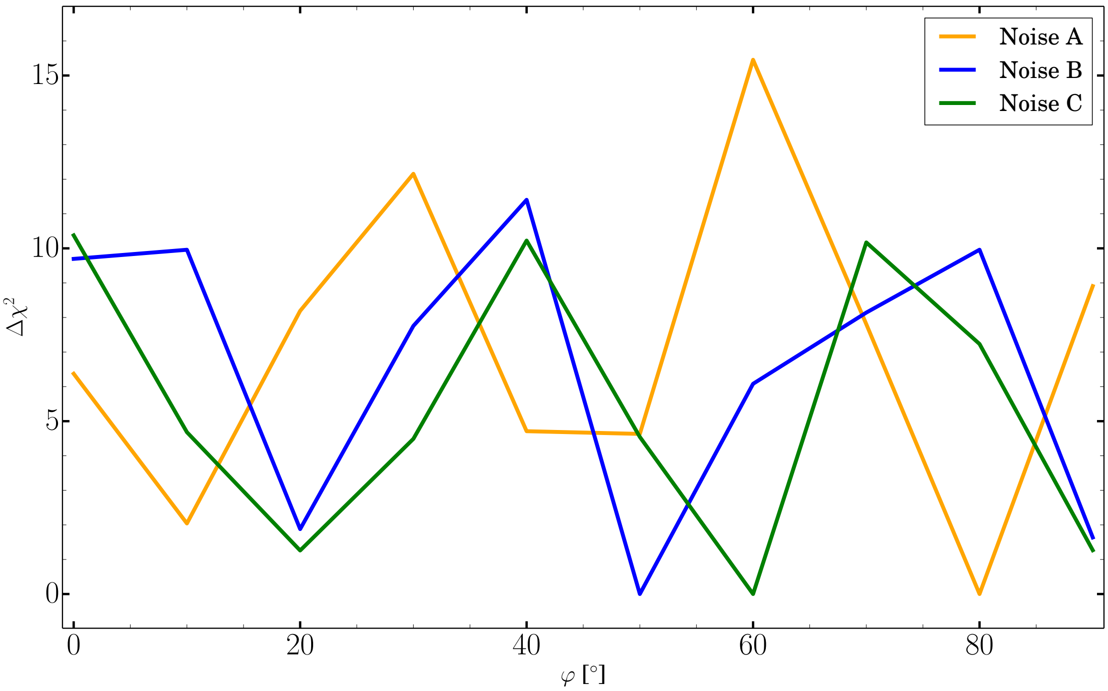

(b) Viewing angle φ

Figure 3.5: The $\Delta\chi^2 = \chi^2 - \chi^2_{\mathrm{min}}$ as a function of the viewing angle ϑ (3.5(a)) and the viewing angle φ (3.5(b)) for three noisy realisations of the velocity profiles $\mathrm{LOSVD}_{\mathrm{original}}$ of an isotropic Hernquist sphere (details in text). The coloured full lines represent the models computed by means of SCHERPA and the dashed lines the models computed with the axisymmetric code from Thomas et al. (2004).

3.2 Triaxial model

Previous work from Van De Ven et al. (2008) and van den Bosch & Van De Ven (2009) tested the triaxial implementation of the Schwarzschild method from van den Bosch et al. (2008) on triaxial separable Abel models. However, as explained in Section (1.8.2), models with separable potentials are unrealistic. SCHERPA is tested on a triaxial reference model produced by I. Soeldner-Rembold starting from an initial spherical N-body model. The particles in the initial model are distributed in phase-space according to a DF obtained by solving iteratively the Eddington's formula (Eddington, 1916). The spherical density originates from the major axis profile of the de-projected density of the massive early-type galaxy NGC 4649. The de-projection was performed in Das et al. (2011) using the code from Magorrian (1999) in the radial interval $[0.3, 201.0]$ Kpc. The initial model is evolved self-consistently by means of the N-body made-to-measure code NMAGIC (De Lorenzi et al., 2007). As explained in Section (1.8.3), NMAGIC changes the masses of the particles maximising a profit function. NMAGIC squashes the model rigidly along the principal axes. It enforces a triaxiality of $T = \frac{1-p^2}{1-q^2} \approx 0.55$ with $q = 0.7$ and $p = 0.85$ for radii $r \leq 122.4$ Kpc. The mass enclosed within this radius is $\approx 97\%$ of the total mass of the model. The intrinsic shape was chosen based on the fact that, as discusses in Section (1.5), the distribution of the axis ratio q of elliptical galaxies peaks between $q \approx 0.6 - 0.8$ (Binney & de Vaucouleurs, 1981; Tremblay & Merritt, 1996). Furthermore the distribution of intrinsic shapes of bright elliptical galaxies is consistent with $0.4 < T < 0.8$ (Vincent & Ryden, 2005). The stability of the system is verified by evolving it without forcing any triaxiality. Figure (3.6) provides a view of the resulting triaxial model along the three principal axes [1]. The model is composed of four million unequal-mass particles and contains no central black hole and no dark matter. The calculation of its intrinsic and projected properties is implemented in the program **extractnbodyfold.f90**.

3.2.1 Three-dimensional density distribution of the model

The program reads-in the masses m_i and the phase-space coordinates $x_i,\ y_i,\ z_i$ and $v_{x,i},\ v_{y,i},\ v_{z,i}$ of each particle. These quantities are expressed in natural units. In these units the total mass of the system is

$$M_{\text{tot}} = \sum_{i=1}^{N_{\text{particle}}} m_i \approx 1.0 \tag{3.8}$$

and the gravitational constant is

$$\mathrm{G} = 1\ u_{\mathrm{d}}\ u_{\mathrm{M}}^{-1}\ u_{\mathrm{v}}^{2} \tag{3.9}$$

---

[1] In Figure (3.6), the triaxiality of the system stands out especially from the fact that the central $r < 20$ Kpc region appears flattened in all three projections.

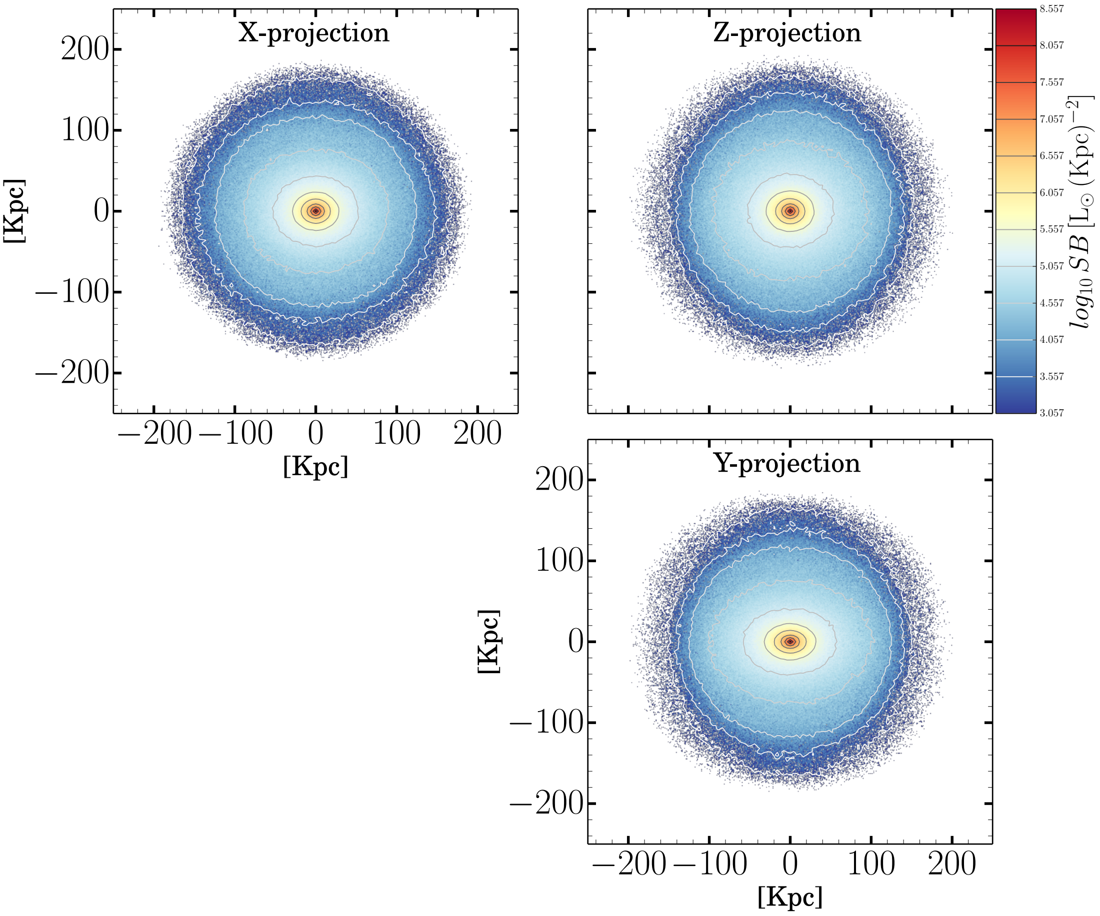

Figure 3.6: Views of a four million unequal-mass particles triaxial reference model along the three principal axes (details in text).

where $u_\mathrm{d} = 1$ Kpc, $u_\mathrm{M} = 10^{10}$ $\mathrm{M}_\odot$ and $u_\mathrm{v} = \sqrt{\frac{\mathrm{G}\ u_\mathrm{M}}{u_\mathrm{d}}}\ \frac{\mathrm{km}}{\mathrm{s}}$ are the length, mass and velocity scales and G = 4.301 E-06 $\frac{\mathrm{Kpc}}{\mathrm{M}_\odot}\left(\frac{\mathrm{km}}{\mathrm{s}}\right)^2$. The masses and phase-space coordinates of the particles are converted to physical units (Kpc, $\frac{\mathrm{km}}{\mathrm{s}}$, $\mathrm{M}_\odot$). The mass-to-light ratio is set to M/L = 1 $\frac{\mathrm{M}_\odot}{\mathrm{L}_\odot}$. To increase the particle-count the particles are folded in the octant $(x > 0, y > 0, z > 0)$ by taking the absolute values of their spatial coordinates. The program creates a three-dimensional grid in the spherical coordinates (r, θ, ϕ) with θ and ϕ binned linearly in $[0, \frac{\pi}{2}]$ and the radius binned as in Equation (2.16) in the interval $r \in [8 \cdot 10^{-2}, 122.4]$ Kpc. The grid is organised in $N_\mathrm{nbody} = N_{r,\mathrm{nbody}} \times N_{\theta,\mathrm{nbody}} \times N_{\phi,\mathrm{nbody}}$ bins with $N_{r,\mathrm{nbody}} = 23$, $N_{\theta,\mathrm{nbody}} = 10$ and $N_{\phi,\mathrm{nbody}} = 25$. The set of particles laying in the spatial bin k with $1 \le k \le N_\mathrm{nbody}$ is

$$P_k \equiv \Big\{ j : \Big(r_j,\ \theta_j,\ \phi_j \Big) \in \mathrm{bin}\ k \Big\}. \tag{3.10}$$

The three-dimensional density ρ_{fold} obtained from the sum of the masses of the particles in bin k is given by

$$\rho_{\mathrm{fold},k} = \frac{M_k}{V_k} \tag{3.11}$$

where

$$M_k = \sum_{j \in P_k} m_j \tag{3.12}$$

is the total mass of the particles in spatial bin k and V_k is the volume of the grid cell. The particle-count is low for radii $r < 1$ Kpc. In this region the density is computed in cartesian coordinates. The grid cells are cubes of side $l = \frac{r(i+1)-r(i)}{2}$ with $i = 1, \ldots, N_{r,\mathrm{nbody}}$ centred on the mid-points of the cells of the spherical grid. In the end ρ_{fold} is cubic-spline interpolated in (r, θ) on $N_{\phi,\mathrm{nbody}}$ meridional planes. It is then sampled in each meridional plane on $N_{r,\mathrm{dens}} = 300$ radial points and $N_{\theta,\mathrm{dens}} = 51$ angular points. The density ρ_{fold} is unfolded in the other octants yielding ρ_{nbody}. Figure (3.7) portrays ρ_{nbody} along the three principal axes as a function of the distance from the center. The density is integrated in a spatial grid composed of $N_{r,\mathrm{grid}} = 20$, $N_{\theta,\mathrm{grid}} = 5$ and $N_{\phi,\mathrm{grid}} = 10$ bins. Figure (3.8) shows the comparison between the expected enclosed mass obtained from the sum of the masses of the particles and the one coming from the integration of ρ_{nbody}. The RMS of the fractional difference between the curves is 4.667 E-03. This confirms that the ρ_{nbody} has been estimated accurately.

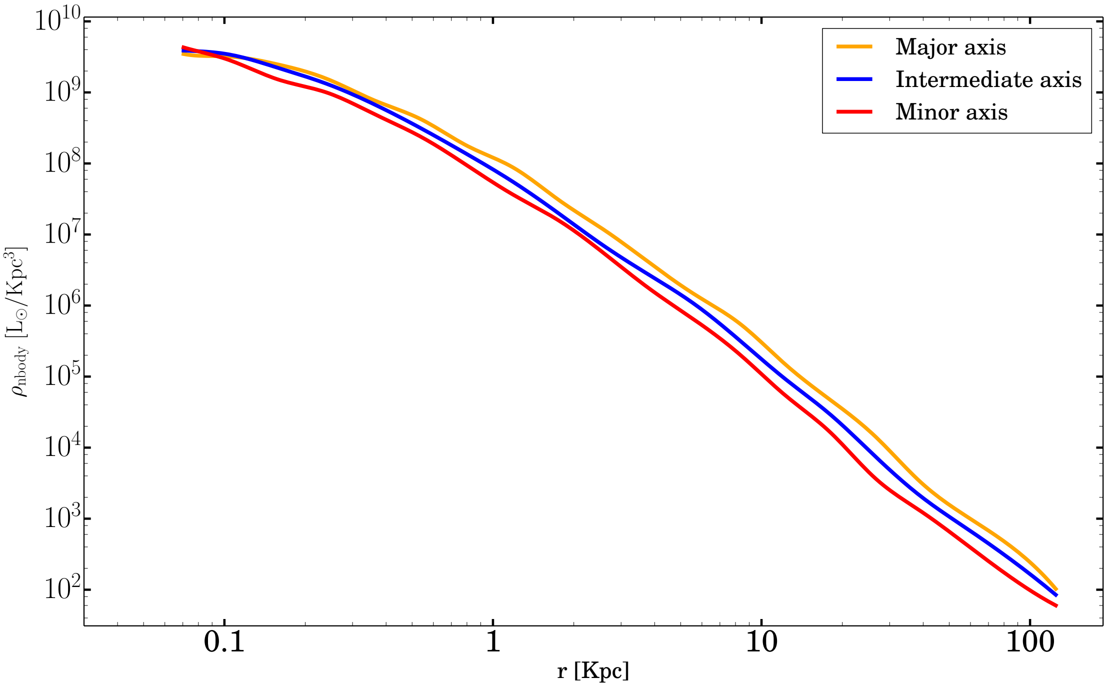

Figure 3.7: The three-dimensional density ρ_{nbody} of a four million unequal-mass particles triaxial N-body model (details in text) computed from the sum of the masses of the particles. The density is plotted along the three principal axes.

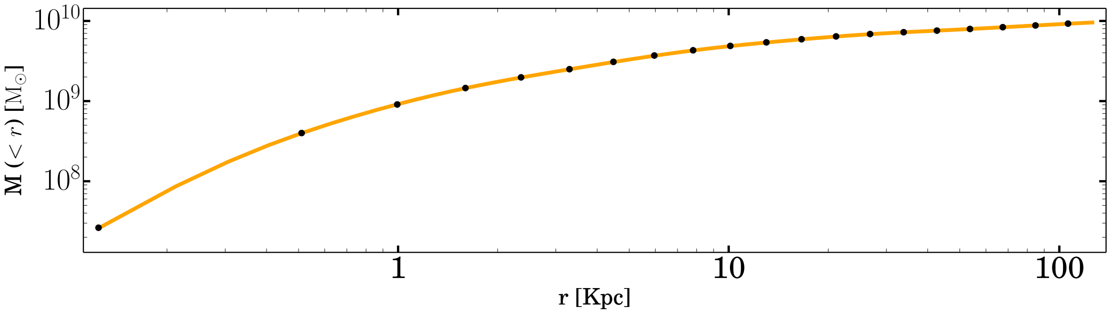

Figure 3.8: Graphical comparison between the **expected** and the **model** enclosed mass for a four million unequal-mass particles triaxial reference model (details in text). The model enclosed mass is computed from the integration of ρ_{nbody}.

3.2.2 Photometry

The plane of the sky is organised in a squared grid in the cartesian coordinates (x', y'). The abscissa x' and the ordinate y' are binned linearly in the interval $[-\text{coord}_{\text{max}}, \text{coord}_{\text{max}}]$ where

$$\text{coord}_{\text{max}} = \max\Big(\max|x'_i|, \max|y'_i|\Big) \quad \text{for} \quad i = 1, \ldots, N_{\text{particle}}. \tag{3.13}$$

The grid is organised in $N_{\text{bin}} = 4000 \times 4000$ bins to ensure a good resolution in the photometry. The particles are projected onto the plane of the sky according to Equation (2.1). No PSF convolution is applied. The set of particles laying in the bin γ with $1 \leq \gamma \leq N_{\text{bin}}$ is

$$\Gamma_\gamma \equiv \Big\{ j : \Big(x'_j,\ y'_j \Big) \in \text{bin } \gamma \Big\}. \tag{3.14}$$

The program sums the masses of the particles laying in bin γ and stores the result in a matrix. The matrix is then converted to the FITS (Flexible Image Transport System) format.

3.2.3 Kinematics of the model

The calculation of the intrinsic and projected kinematics of the triaxial model is performed with particles with radii $r_i \leq 122.4$ Kpc and masses $m_i < 10^5$ M$_\odot$. This is done to reduce the influence of the particle noise on the kinematics.

Intrinsic kinematics The program creates a three dimensional grid in spherical coordinates with θ and ϕ binned linearly in the intervals $[-\frac{\pi}{2}, \frac{\pi}{2}]$ and $[0, 2\pi]$. The radius is binned as in Equation (2.16) in the interval $r \in [8 \cdot 10^{-2}, 122.4]$ Kpc. The grid is made up of $N_\sigma = N_{r,\sigma} \times N_{\theta,\sigma} \times N_{\phi,\sigma}$ bins with $N_{r,\sigma} = 20$, $N_{\theta,\sigma} = 5$ and $N_{\phi,\sigma} = 10$ bins. The set of particles laying in the spatial bin a with $1 \leq a \leq N_\sigma$ is

$$\Sigma_a \equiv \Big\{ j : \Big(r_j,\ \theta_j,\ \phi_j \Big) \in \text{bin } a \Big\}. \tag{3.15}$$

The intrinsic velocity dispersion is computed as

$$\sigma_r^a = \sqrt{\frac{1}{M_a}\sum_{j\in\Sigma_a} m_j\ v_{r,j}^2 - \Big(\frac{1}{M_a}\sum_{j\in\Sigma_a} m_j\ v_{r,j}\Big)^2}. \tag{3.16}$$

Equation (3.16) is valid also for σ_θ and σ_ϕ. The anisotropy parameter is computed as in Equation (3.3). As depicted in Figure (3.11)-(3.13), (3.14)-(3.16) and (3.17)-(3.19) the model becomes on average radially anisotropic as the distance from the center increases.

Projected kinematics The plane of the sky is organised in a grid in polar coordinates $(r_{\rm sky}, \theta_{\rm sky})$. The radius $r_{\rm sky}$ is logarithmically binned in $[1.08, 8.87]$ Kpc. The angle $\theta_{\rm sky}$ is linearly binned in $[-\frac{\pi}{2}, \frac{\pi}{2}]$. This is because the projected properties of triaxial systems are mostly point symmetric with respect to the projected center. Hence triaxial systems need to be investigated in at least one half of the sky (van den Bosch et al., 2008). The grid is organised in $N_{r,\rm sky} = 8$ and $N_{\theta,\rm sky} = 5$ bins ($N_{\rm losvd} = 40$). The projected velocity is binned according to Equation (2.17) in $N_{\rm vel} = 23$ velocity bins with

$$v_{\parallel,\rm max} = \eta \cdot \max(v_\parallel) \tag{3.17}$$

where $\max(v_\parallel)$ is the maximum line-of-sight velocity in the projected radial interval $[1.08, 8.87]$ Kpc and $\eta = 1.15$. The factor η is introduced to ensure that the wings of the velocity profiles are not truncated. In fact as explained in Section (1.3.2) the wings of the velocity profiles are important for the dynamical modelling. The phase-space coordinates of the particles are projected onto the plane of the sky as in Equation (2.1). No PSF convolution is applied. The velocity profiles read

$${\rm LOSVD}^b_{\rm nbody} = \frac{\sum_{j\in\Xi_b} m_{\rm j}\ v_{\parallel,j}}{\sum_{j\in\Xi_b} m_{\rm j}} \tag{3.18}$$

where $1 \leq b \leq N_{r,\rm sky} \times N_{\theta,\rm sky}$ and

$$\Xi_b \equiv \Big\{ j : \Big(r_{\rm sky,j},\ \theta_{\rm sky,j}\Big) \in {\rm bin}\ b \Big\} \tag{3.19}$$

is the set of particles laying in the projected bin b. In order to reduce the particle noise, $\rm LOSVD_{nbody}$ are computed by folding the particles to the half of the plane of the sky corresponding to $x' \geq 0$. This is done by considering the opposite of the coordinates (x', y') and of $v_\parallel$. The uncertainties on the velocity profiles are given by

$$\Delta{\rm LOSVD}^{b,g}_{\rm nbody} = \sqrt{\Delta{\rm noise}^2_{b,g} + \Delta\text{two-halves}^2_{b,g}} \tag{3.20}$$

with $1 \leq b \leq N_{r,\rm sky} \times N_{\theta,\rm sky}$ and $1 \leq g \leq N_{\rm vel}$. The first term quantifies the particle noise. The second term the difference between the LOSVDs in the two halves of the sky. The particle noise is given by $\Delta{\rm noise} = \frac{1}{\sqrt{N_e}}$, where N_e is the effective number of particles. It is defined as in De Lorenzi et al. (2007) and reads $N_e \equiv N_{\rm particle}\frac{\overline{m}^2}{\overline{m^2}}$, where $\overline{m}$ and $\overline{m^2}$ are the mean and mean-square particle masses. The effective number of particles reduces to $N_{\rm particle}$ for equal-mass particles. As shown in Figure (3.20)-(3.22) the model shows on average little rotation in projection (as observed in the kinematics of massive early-type galaxies) and vanishing h_3. Moreover $h_4 \approx -0.02$.

3.2.4 Models of the principal axes projections

The subsection tests how well SCHERPA recovers the mass-to-light ratio of the triaxial N-body model, while estimating its intrinsic properties and fitting the projected velocity profiles. The three-dimensional density used is $\rho_{\rm nbody}$, which is computed from the sum of the masses of the particles. As a first test, the model is projected along the three principal axes. The sets of velocity profiles are identified as X-projection, Y-projection and Z-projection and correspond to the line-of-sights

$$\begin{array}{llll} \textbf{X-projection} & \vartheta = 90\,^\circ & \varphi = 0\,\,^\circ & \psi = 90\,^\circ \\ \textbf{Y-projection} & \vartheta = 90\,^\circ & \varphi = 90\,^\circ & \psi = 90\,^\circ \\ \textbf{Z-projection} & \vartheta = \;\,0\,^\circ & \varphi = 90\,^\circ & \psi = 90\,^\circ \;\; . \end{array} \tag{3.21}$$

Angle ψ is chosen as explained in Section (2.2.2). The decision to model the projections along the principal axes comes from the fact that the principal axes are the symmetry axes of the different families of orbits (see Section 1.9.3). This means that the observational properties of the model will reach their maximum/minimum at these projections. The model is placed at a distance d = 16.83 Mpc and investigated in the radial interval $r_{\rm min} = 8 \cdot 10^{-2}$ Kpc and $r_{\rm max} = 122.4$ Kpc. The binning grid is made up of $N_{r,\rm grid} = 20$, $N_{\theta,\rm grid} = 5$ and $N_{\phi,\rm grid} = 10$ bins. A library of $N_{\rm orbit} = 46580$ representative stellar orbits is used to reproduce $N_{r,\rm grid} \times N_{\theta,\rm grid} \times N_{\phi,\rm grid} = 1000$ constraints from the three-dimensional luminosity density and to fit

$$\begin{array}{lll} \mathbf{N_{kindata}} & \textbf{X-projection} & 517 \\ \mathbf{N_{kindata}} & \textbf{Y-projection} & 528 \\ \mathbf{N_{kindata}} & \textbf{Z-projection} & 534 \end{array} \tag{3.22}$$

kinematic data points. The phase-space volumes follow from Equation (2.57). The mass-to-light ratio is varied in the interval $0.7\ \frac{\rm M_\odot}{\rm L_\odot} \leq {\rm M/L} \leq 1.3\ \frac{\rm M_\odot}{\rm L_\odot}$ in steps $\Delta{\rm M/L} = 0.05\ \frac{\rm M_\odot}{\rm L_\odot}$. In the interval $0.9\ \frac{\rm M_\odot}{\rm L_\odot} \leq {\rm M/L} \leq 1.1\ \frac{\rm M_\odot}{\rm L_\odot}$ the step equals $\Delta{\rm M/L} = 0.01\ \frac{\rm M_\odot}{\rm L_\odot}$. The models are oriented as in Equation (3.21). Figure (3.9) quantifies the level of regularisation required to minimise for all projections the difference between the best fitting mass-to-light ratio and the expected value of ${\rm M/L} = 1\ \frac{\rm M_\odot}{\rm L_\odot}$. The test is carried out for $N_\alpha = 32$ values of the regularisation parameter α. For all three projections $i_\alpha = 15$. This corresponds to $\alpha = 1.024$ E-04. Figure (3.10) shows the $\Delta\chi^2 = \chi^2 - \chi^2_{\rm min}$ as a function of the mass-to-light ratio. The best fitting mass-to-light ratios and the corresponding $\chi^2_{\min}$ are

$$\begin{array}{cccc} & \textbf{X-projection} & \textbf{Y-projection} & \textbf{Z-projection} \\ \mathbf{M/L}\left[\frac{\mathrm{M}_\odot}{\mathrm{L}_\odot}\right] & 0.98 & 0.98 & 1.0 \\ \boldsymbol{\chi}^2_{\min} & 305.813 & 199.869 & 435.714 \end{array} \quad . \tag{3.23}$$

SCHERPA is able to reproduce the mass-to-light ratio of a four million unequal-mass particles triaxial reference model within 2 % accuracy for all the projections considered. Figure (3.11)-(3.13), (3.14)-(3.16) and (3.17)-(3.19) portray the reconstruction of the intrinsic kinematics along the principal axes for the best fitting mass-to-light ratios. Figure (3.20)-(3.22) display the fit to the projected kinematics. The comparison among the model predictions and the expected values of the intrinsic kinematics is carried out by means of the RMS of the fractional difference. The RMS is computed for radii between the innermost and outermost projected data points. The deviations are computed over 350 points and are

$$\begin{array}{cccc} & \textbf{X-projection} & \textbf{Y-projection} & \textbf{Z-projection} \\ \boldsymbol{\Delta}\ \textbf{RMS}\ \boldsymbol{\sigma_r} & 2.505\ \text{E-02} & 3.273\ \text{E-02} & 3.901\ \text{E-02} \\ \boldsymbol{\Delta}\ \textbf{RMS}\ \boldsymbol{\sigma_\theta} & 2.824\ \text{E-02} & 2.530\ \text{E-02} & 2.500\ \text{E-02} \\ \boldsymbol{\Delta}\ \textbf{RMS}\ \boldsymbol{\sigma_\phi} & 2.363\ \text{E-02} & 2.446\ \text{E-02} & 4.468\ \text{E-02} \end{array} \quad . \tag{3.24}$$

The code recovers the intrinsic kinematics within 4.5 %. This accuracy is similar to the one reported by Van De Ven et al. (2008) on triaxial separable Abel models.

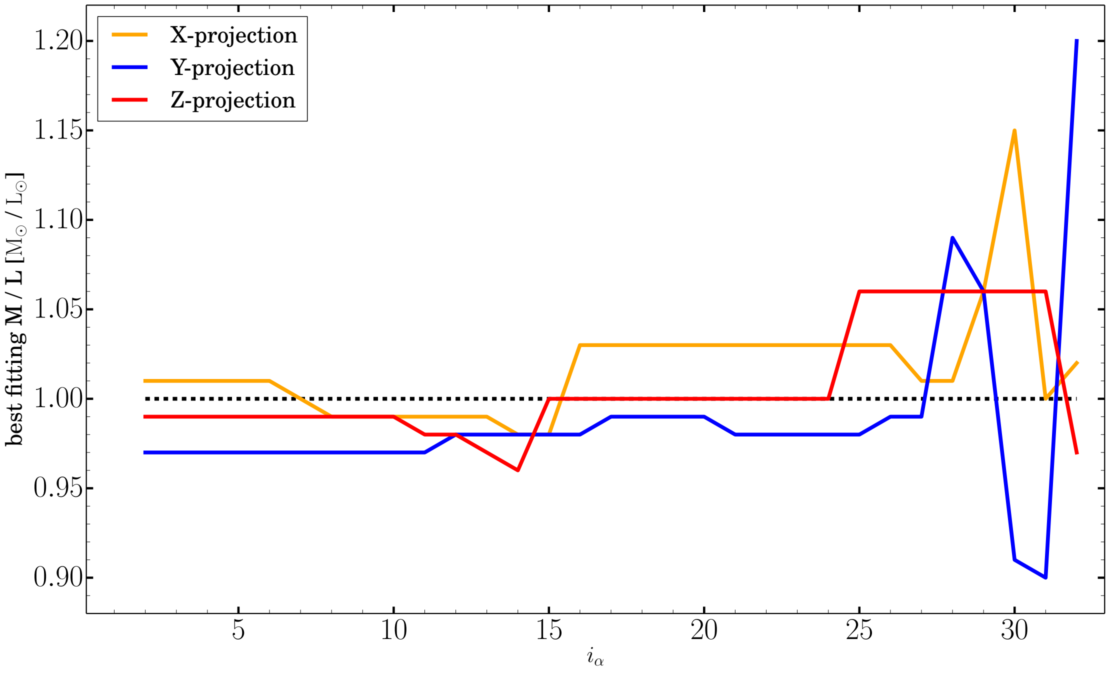

Figure 3.9: Best fitting mass-to-light ratio as a function of the regularisation parameter α for the projections along the principal axes of a four million unequal-mass particles triaxial reference model (details in text).

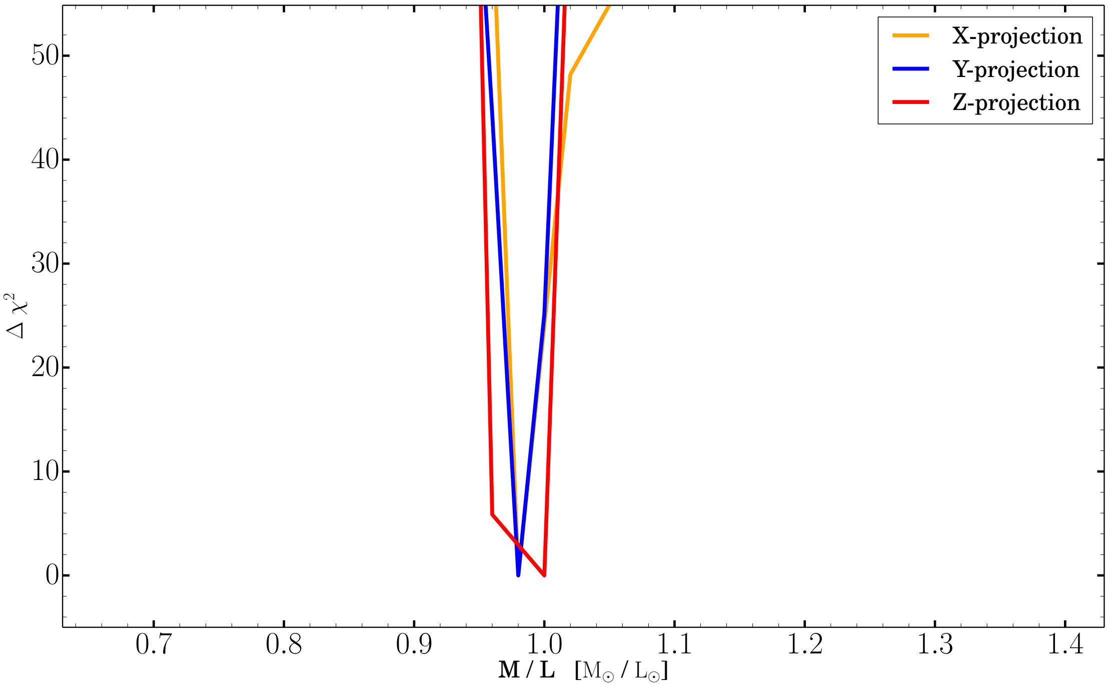

Figure 3.10: The $\Delta\chi^2 = \chi^2 - \chi^2_{\mathrm{min}}$ as a function of the mass-to-light ratio for the projections along the principal axes of a four million unequal-mass particles triaxial reference model (details in text).

3.2.5 Models along a different line-of-sight

The subsection repeats the test performed in Section (3.2.4) and compares the results obtained with the MGE de-projected density ρ_{MGE} and ρ_{nbody}. For projections along the principal axes the model shows no isophotal twist (Jedrzejewski, 1987) and $\psi = 90\,^\circ$ to align the major axis of the innermost Gaussian to the x'-axis. As explained in Section (2.2.3) this results in only axisymmetric de-projections. In order to test triaxial de-projections, the model is studied along the line-of-sight $(\vartheta = 45\,^\circ, \varphi = 45\,^\circ, \psi = 112\,^\circ)$ as it is maximally distant from the principal axes. The FITS file is created as described in Section (3.2.2) and it is fitted with the code of Michele Cappellari. As depicted in Figure (3.23), the model shows low isophotal twist ($\Delta\mathrm{PA} < 5\,^\circ$) along the selected line-of-sight. The fit requires each Gaussian component to have the same position angle. The number of Gaussian components is determined autonomously by the code (see Section 2.2.3). Figure (3.24) portrays the set of line-of-sights (see Section 2.2.3) along which the MGE de-projection is allowed. The figure portrays also the corresponding intrinsic axes ratios $\langle p\rangle$ and $\langle q\rangle$. They are given by the luminosity weighted averages of the axes ratios of the single Gaussian components. Table (3.3) shows the output of the MGE fit and Table (3.4) the luminosity and intrinsic shape parameters found after the de-projection along the line-of-sight $(\vartheta = 45\,^\circ, \varphi = 45\,^\circ, \psi = 112\,^\circ)$. The de-projection corresponds to a triaxial intrinsic shape with $\langle p\rangle = 0.89$, $\langle q\rangle = 0.75$ and $T = \frac{1-p^2}{1-q^2} = 0.5$. Figure (3.25) compares ρ_{nbody} and ρ_{MGE} along the principal axes. The deviations between the density profiles along the principal axes are computed as the RMS of the fractional difference and are $\Delta\text{RMS}\ \rho_{\text{major}} = 6.42\ \%$, $\Delta\text{RMS}\ \rho_{\text{intermediate}} = 6.44\ \%$ and $\Delta\text{RMS}\ \rho_{\text{minor}} = 11.81\ \%$. Figure (3.26) shows the expected enclosed mass obtained from the sum of the masses of the particles and the one coming from the integration of ρ_{MGE}. The MGE density is integrated in a spatial grid composed of $N_{r,\text{grid}} = 20$, $N_{\theta,\text{grid}} = 5$ and $N_{\phi,\text{grid}} = 10$ bins. The RMS of the fractional difference between the curves is 2.119 E-02. The model is placed at a distance $d = 16.83$ Mpc and investigated in the radial interval $r_{\text{min}} = 8 \cdot 10^{-2}$ Kpc and $r_{\text{max}} = 122.4$ Kpc. The binning grid is the one used for the integration of ρ_{MGE}. A library of $N_{\text{orbit}} = 46580$ representative stellar orbits is used to reproduce $N_{r,\text{grid}} \times N_{\theta,\text{grid}} \times N_{\phi,\text{grid}} = 1000$ constraints from the three-dimensional luminosity density and to fit $N_{\text{kindata}} = 519$ kinematic data points. The phase-space volumes follow from Equation (2.57). The mass-to-light ratio is varied as in Section (3.2.4). The test is carried out for $N_\alpha = 32$ values of the regularisation parameter α. Figure (3.27) shows that for $i_\alpha = 15$ ($\alpha = 1.024$ E-04) SCHERPA recovers within 2 % the expected value of the mass-to-light ratio. This is true both for ρ_{nbody} and ρ_{MGE}. This level of regularisation is chosen for a better comparison with the results obtained for the projections along the principal axes. The best fitting mass-to-light ratios and the corresponding χ^2_{min} are

$$\begin{array}{lcc} & \textbf{Nbody} & \textbf{MGE} \\ \textbf{M/L}\left[\frac{\text{M}_\odot}{\text{L}_\odot}\right] & 0.98 & 0.98 \\ \boldsymbol{\chi}^2_{\text{min}} & 569.047 & 582.094 \end{array} \quad . \tag{3.25}$$

The comparison among the model predictions and the expected values of the intrinsic kinematics is carried out by means of the RMS of the fractional difference for radii between the innermost and outermost projected data points. The deviations are computed over 350 points and are

$$\begin{array}{lcc} & \textbf{Nbody} & \textbf{MGE} \\ \boldsymbol{\Delta}\ \textbf{RMS}\ \boldsymbol{\sigma_r} & 3.590\text{ E-02} & 3.668\text{ E-02} \\ \boldsymbol{\Delta}\ \textbf{RMS}\ \boldsymbol{\sigma_\theta} & 2.730\text{ E-02} & 2.895\text{ E-02} \\ \boldsymbol{\Delta}\ \textbf{RMS}\ \boldsymbol{\sigma_\phi} & 3.190\text{ E-02} & 3.455\text{ E-02} \end{array} \quad . \tag{3.26}$$

The code recovers the intrinsic kinematics of the target model within 3.7 %. The ΔRMS and χ^2_{min} obtained with the MGE density are as expected larger than those found with ρ_{nbody}. Figure (3.28) portrays the cumulative light carried by each orbit type as a function of the average of the peri- and apocentres of the orbits. The figure compares the result obtained at the best fitting mass-to-light ratio for models computed with ρ_{nbody} and ρ_{MGE}. Over the entire library, the light carried by the orbit types is subdivided in

$$\begin{array}{lcc} & \textbf{Nbody} & \textbf{MGE} \\ \textbf{Short-axis tube orbit} & 60.85\ \% & 63.11\ \% \\ \textbf{Long-axis tube orbit} & 30.82\ \% & 28.82\ \% \\ \textbf{Box orbit} & 8.33\ \% & 8.28\ \% \end{array} \quad . \tag{3.27}$$

The values obtained from models with ρ_{nbody} and ρ_{MGE} differ by less than 3 %.

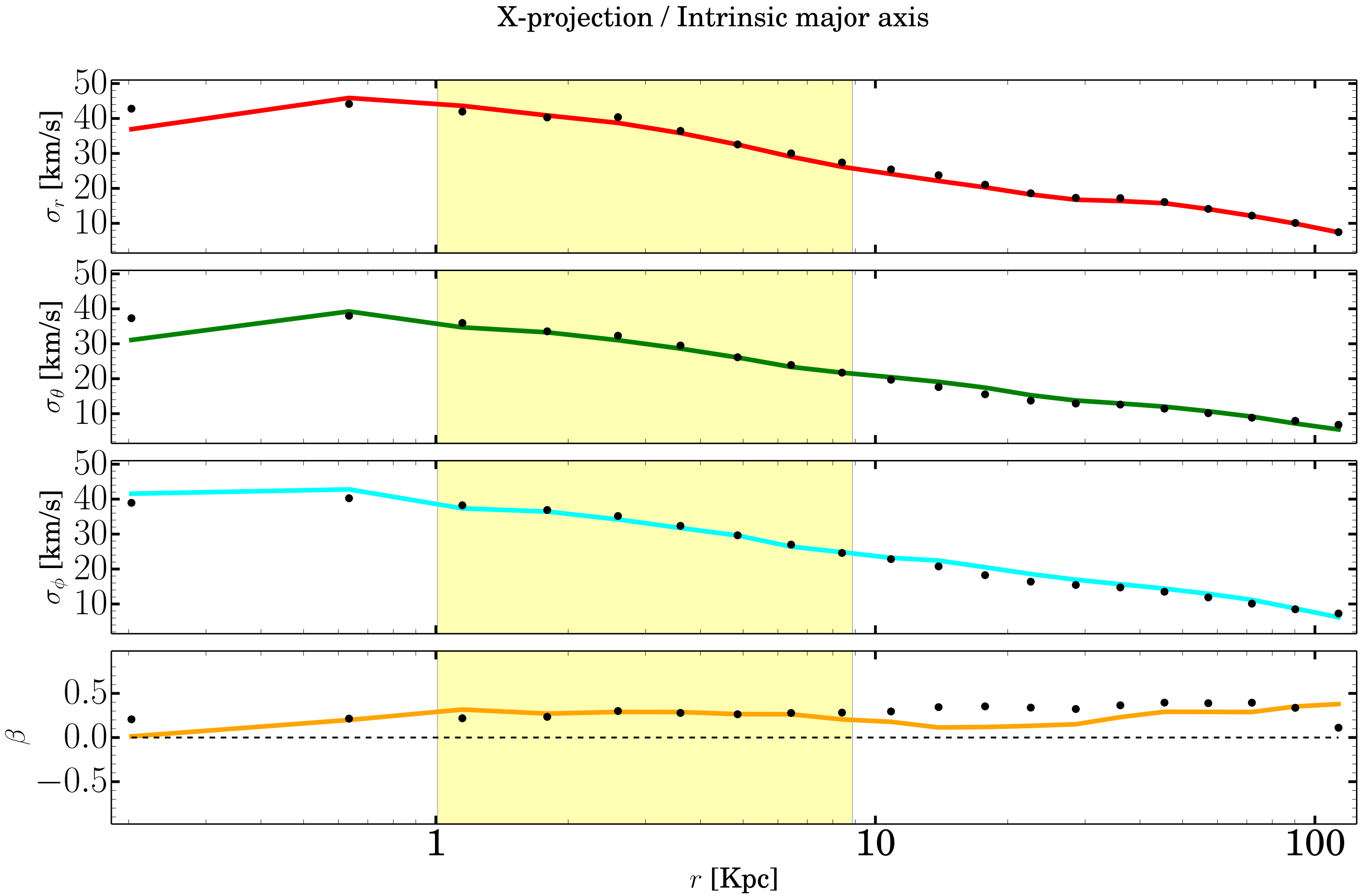

Figure 3.11: Reconstruction of the intrinsic kinematics along the major axis of a four million unequal-mass particles triaxial reference model (details in text) for the X-projection and at the best fitting mass-to-light ratio. The dots represent the expectations and the coloured lines the results of the modelling. The vertical shaded yellow area highlights the radial interval on the sky where the LOSVDs are distributed.

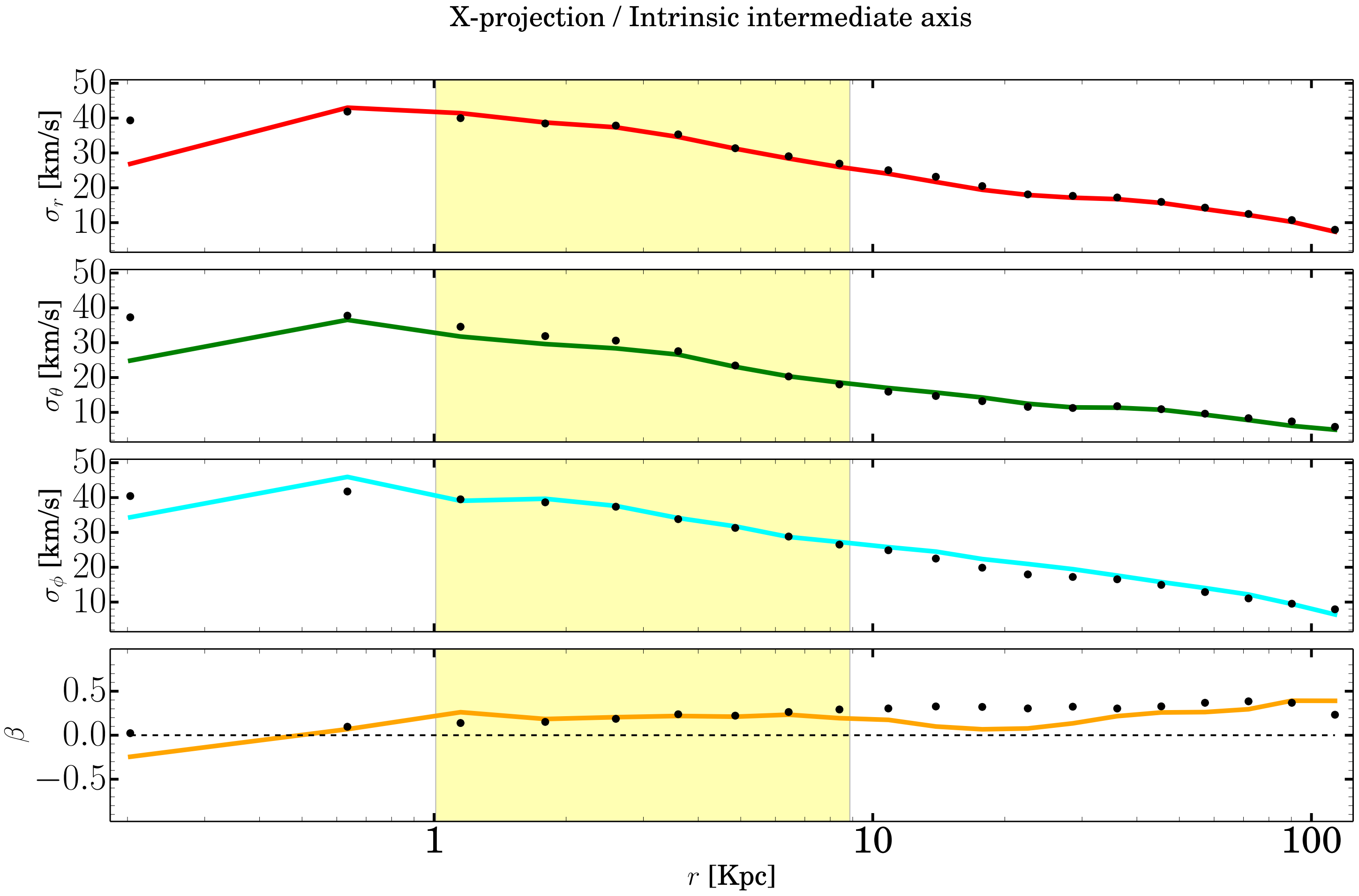

Figure 3.12: Reconstruction of the intrinsic kinematics along the intermediate axis of a four million unequal-mass particles triaxial reference model (details in text) for the X-projection and at the best fitting mass-to-light ratio. The dots represent the expectations and the coloured lines the results of the modelling. The vertical shaded yellow area highlights the radial interval on the sky where the LOSVDs are distributed.

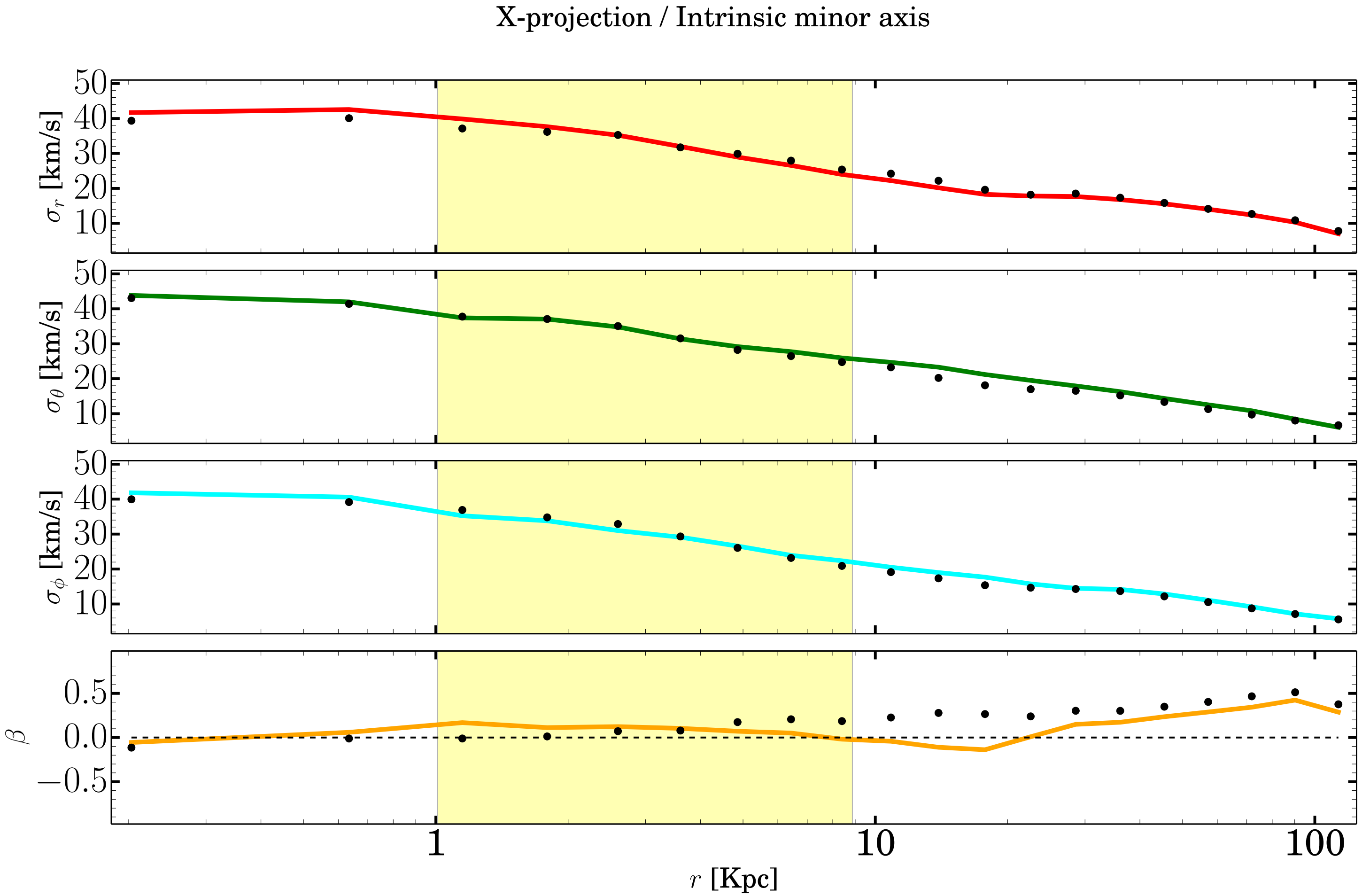

Figure 3.13: Reconstruction of the intrinsic kinematics along the minor axis of a four million unequal-mass particles triaxial reference model (details in text) for the X-projection and at the best fitting mass-to-light ratio. The dots represent the expectations and the coloured lines the results of the modelling. The vertical shaded yellow area highlights the radial interval on the sky where the LOSVDs are distributed.

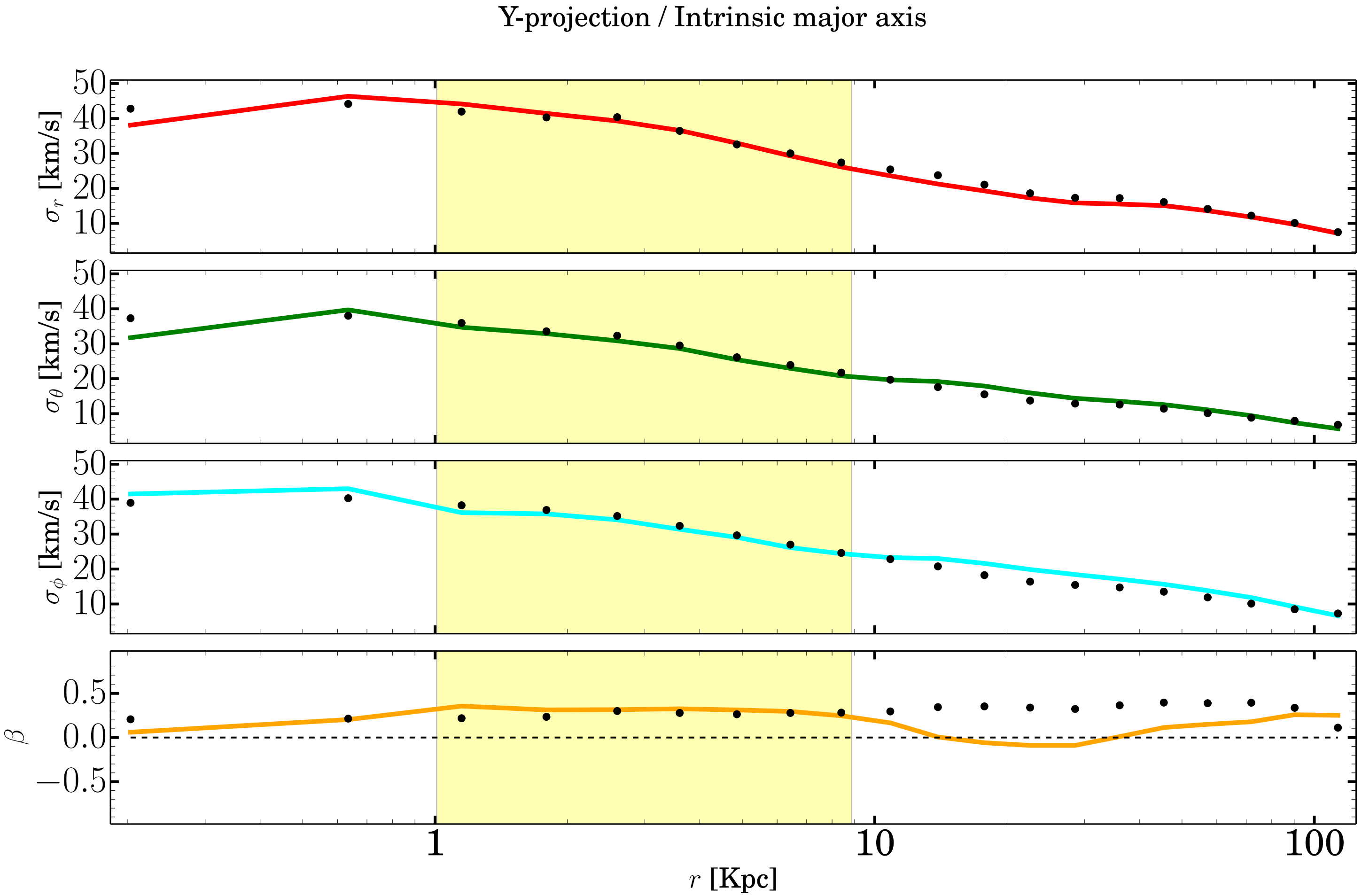

Figure 3.14: Reconstruction of the intrinsic kinematics along the major axis of a four million unequal-mass particles triaxial reference model (details in text) for the Y-projection and at the best fitting mass-to-light ratio. The dots represent the expectations and the coloured lines the results of the modelling. The vertical shaded yellow area highlights the radial interval on the sky where the LOSVDs are distributed.

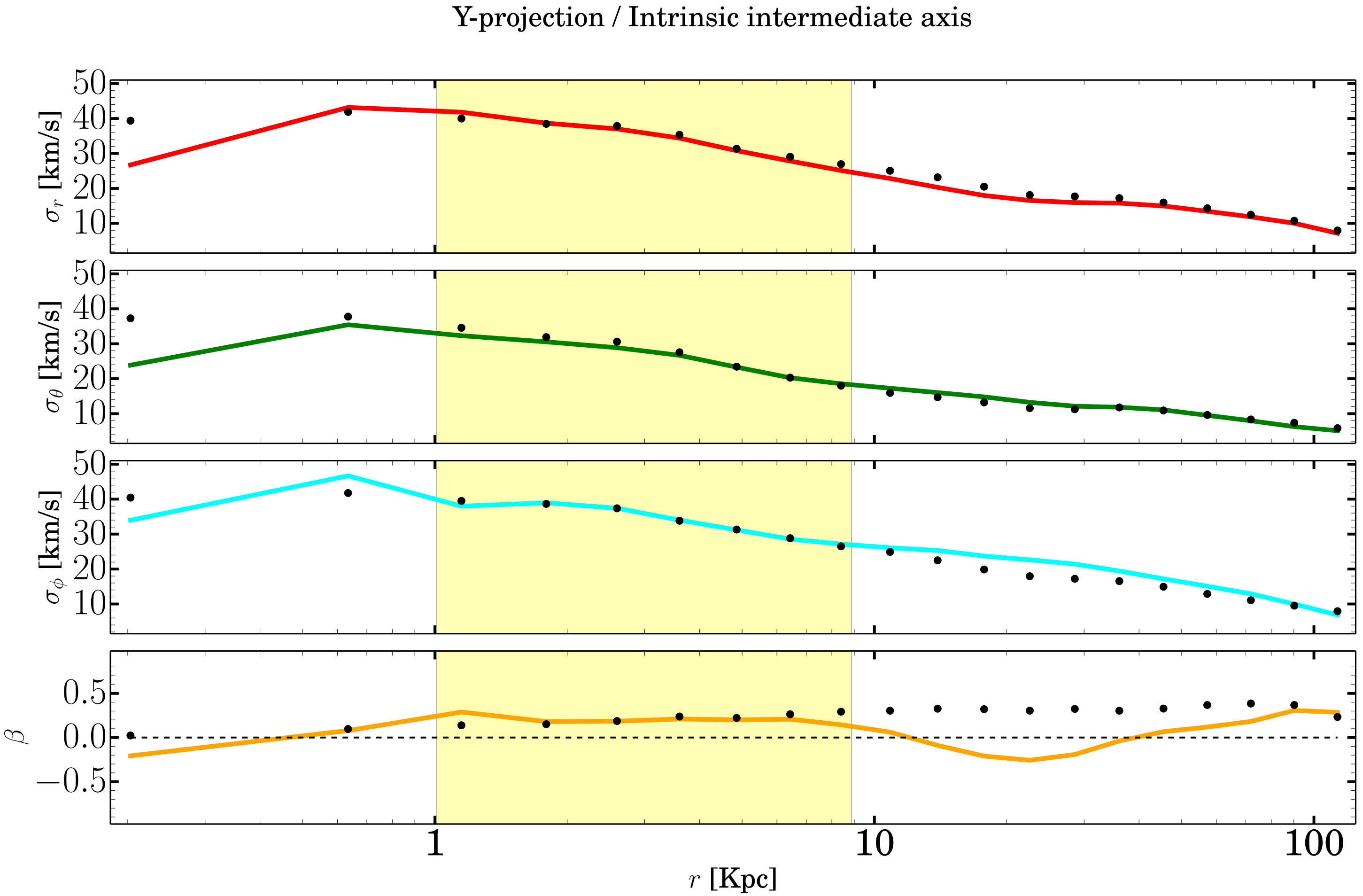

Figure 3.15: Reconstruction of the intrinsic kinematics along the intermediate axis of a four million unequal-mass particles triaxial reference model (details in text) for the Y-projection and at the best fitting mass-to-light ratio. The dots represent the expectations and the coloured lines the results of the modelling. The vertical shaded yellow area highlights the radial interval on the sky where the LOSVDs are distributed.

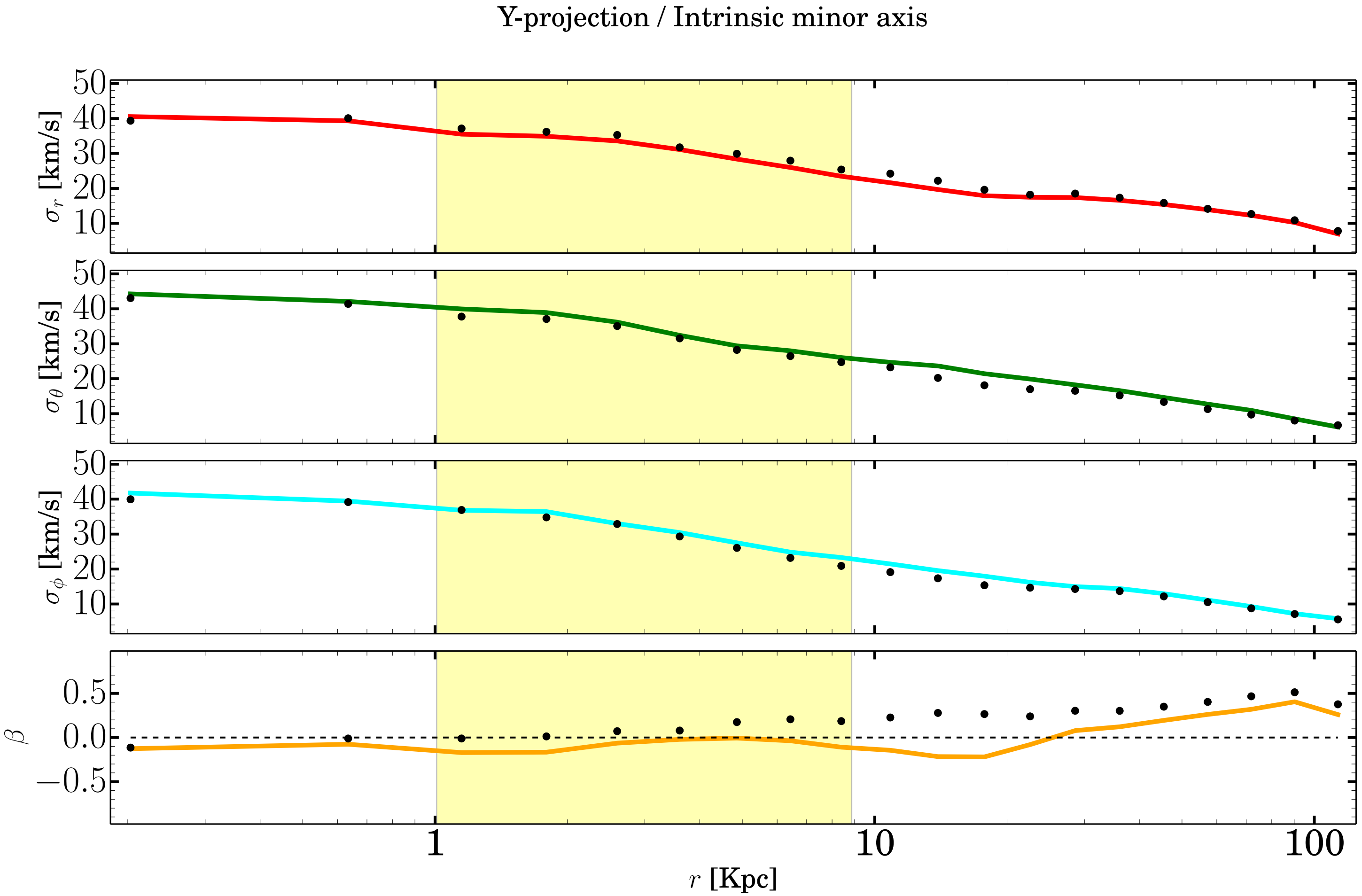

Figure 3.16: Reconstruction of the intrinsic kinematics along the minor axis of a four million unequal-mass particles triaxial reference model (details in text) for the Y-projection and at the best fitting mass-to-light ratio. The dots represent the expectations and the coloured lines the results of the modelling. The vertical shaded yellow area highlights the radial interval on the sky where the LOSVDs are distributed.

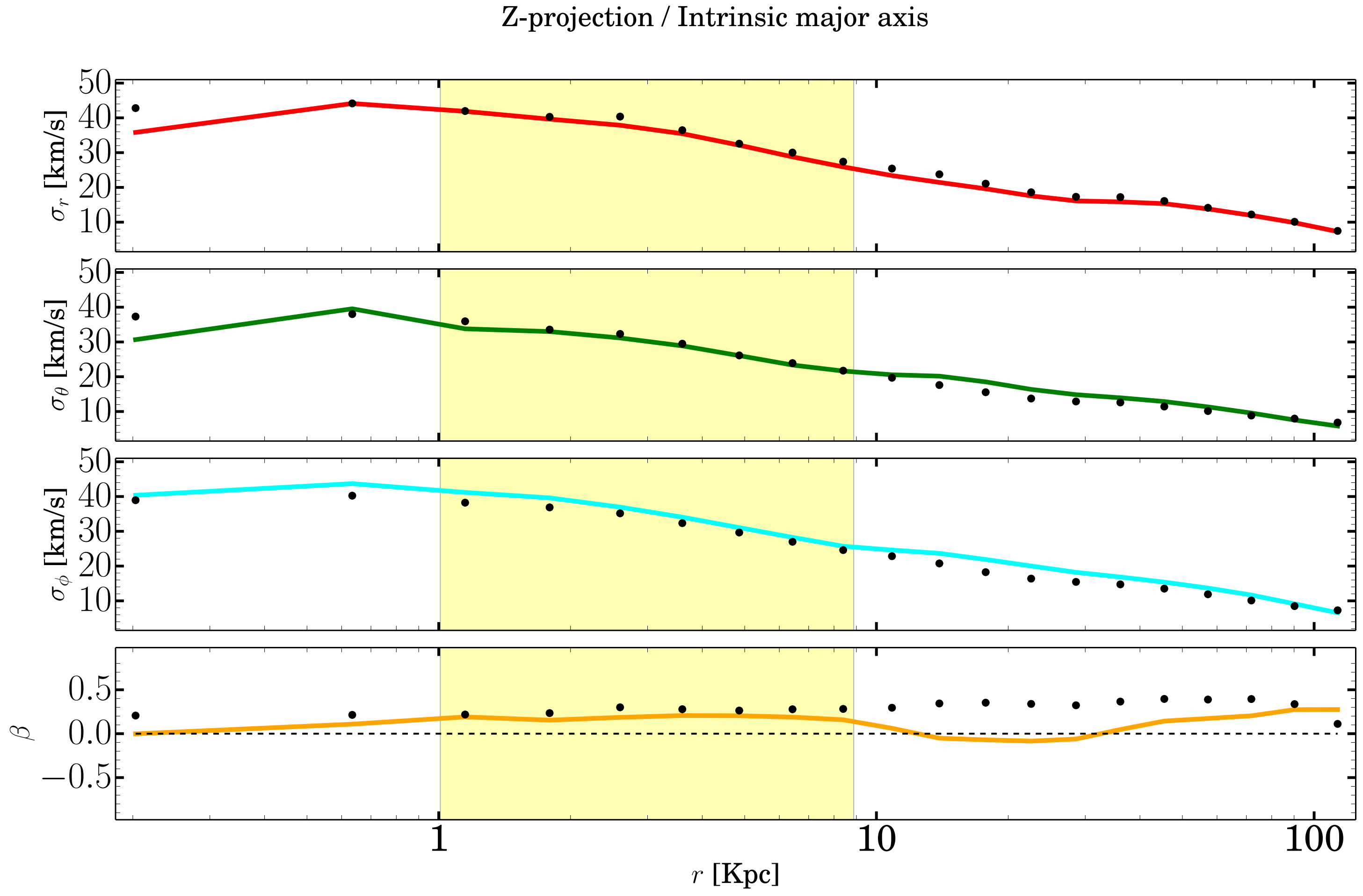

Figure 3.17: Reconstruction of the intrinsic kinematics along the major axis of a four million unequal-mass particles triaxial reference model (details in text) for the Z-projection and at the best fitting mass-to-light ratio. The dots represent the expectations and the coloured lines the results of the modelling. The vertical shaded yellow area highlights the radial interval on the sky where the LOSVDs are distributed.

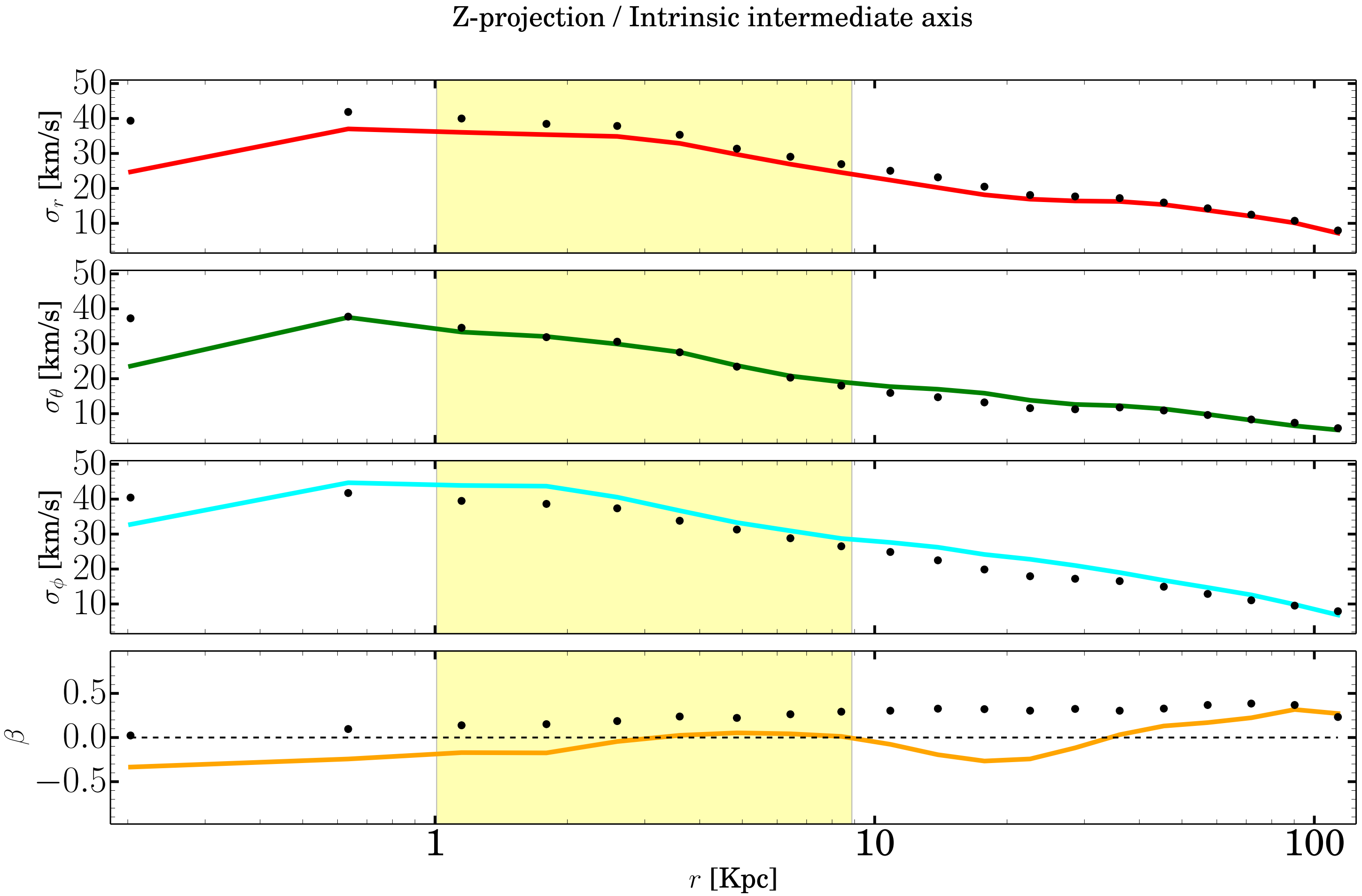

Figure 3.18: Reconstruction of the intrinsic kinematics along the intermediate axis of a four million unequal-mass particles triaxial reference model (details in text) for the Z-projection and at the best fitting mass-to-light ratio. The dots represent the expectations and the coloured lines the results of the modelling. The vertical shaded yellow area highlights the radial interval on the sky where the LOSVDs are distributed.

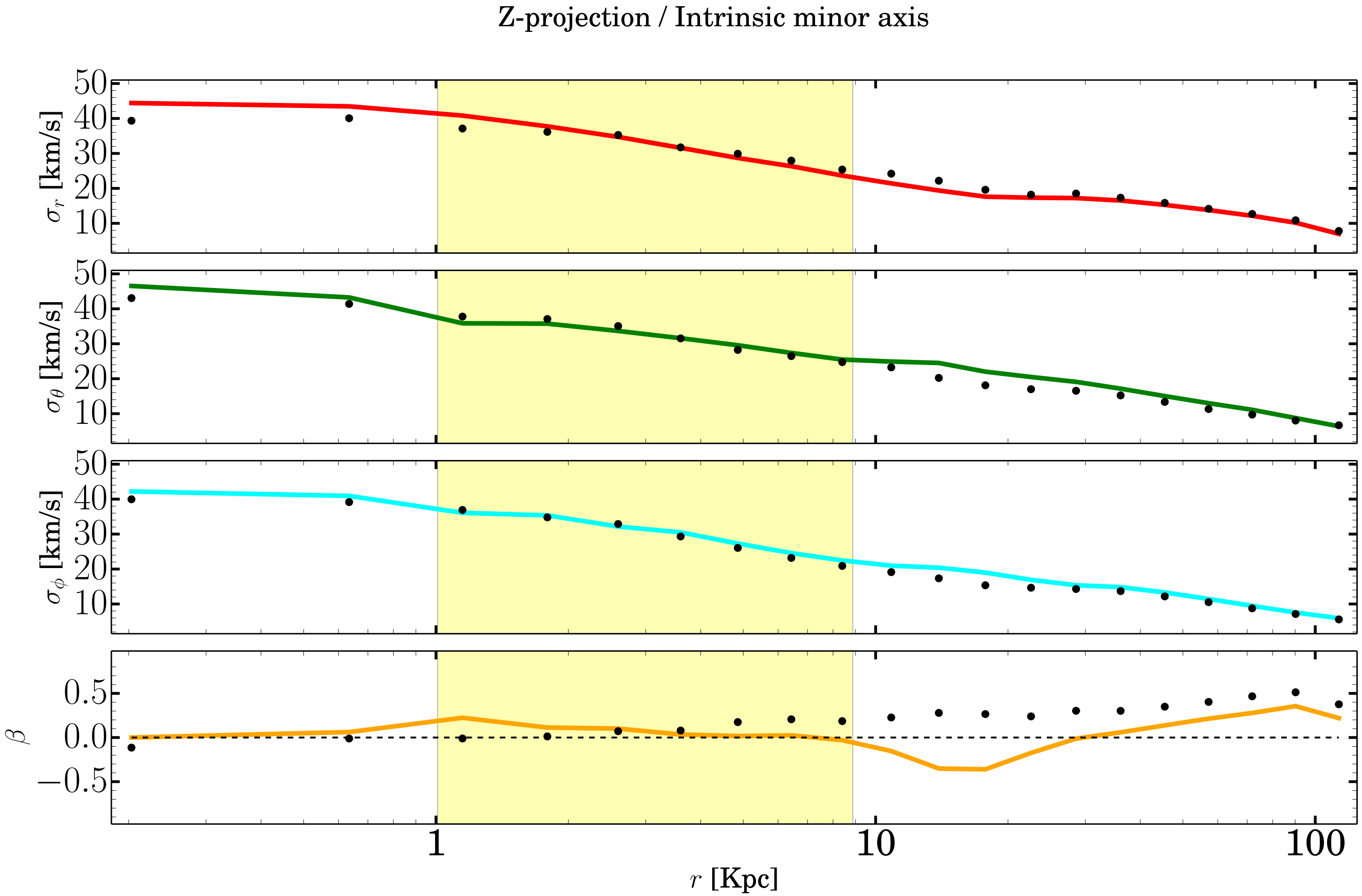

Figure 3.19: Reconstruction of the intrinsic kinematics along the minor axis of a four million unequal-mass particles triaxial reference model (details in text) for the Z-projection and at the best fitting mass-to-light ratio. The dots represent the expectations and the coloured lines the results of the modelling. The vertical shaded yellow area highlights the radial interval on the sky where the LOSVDs are distributed.

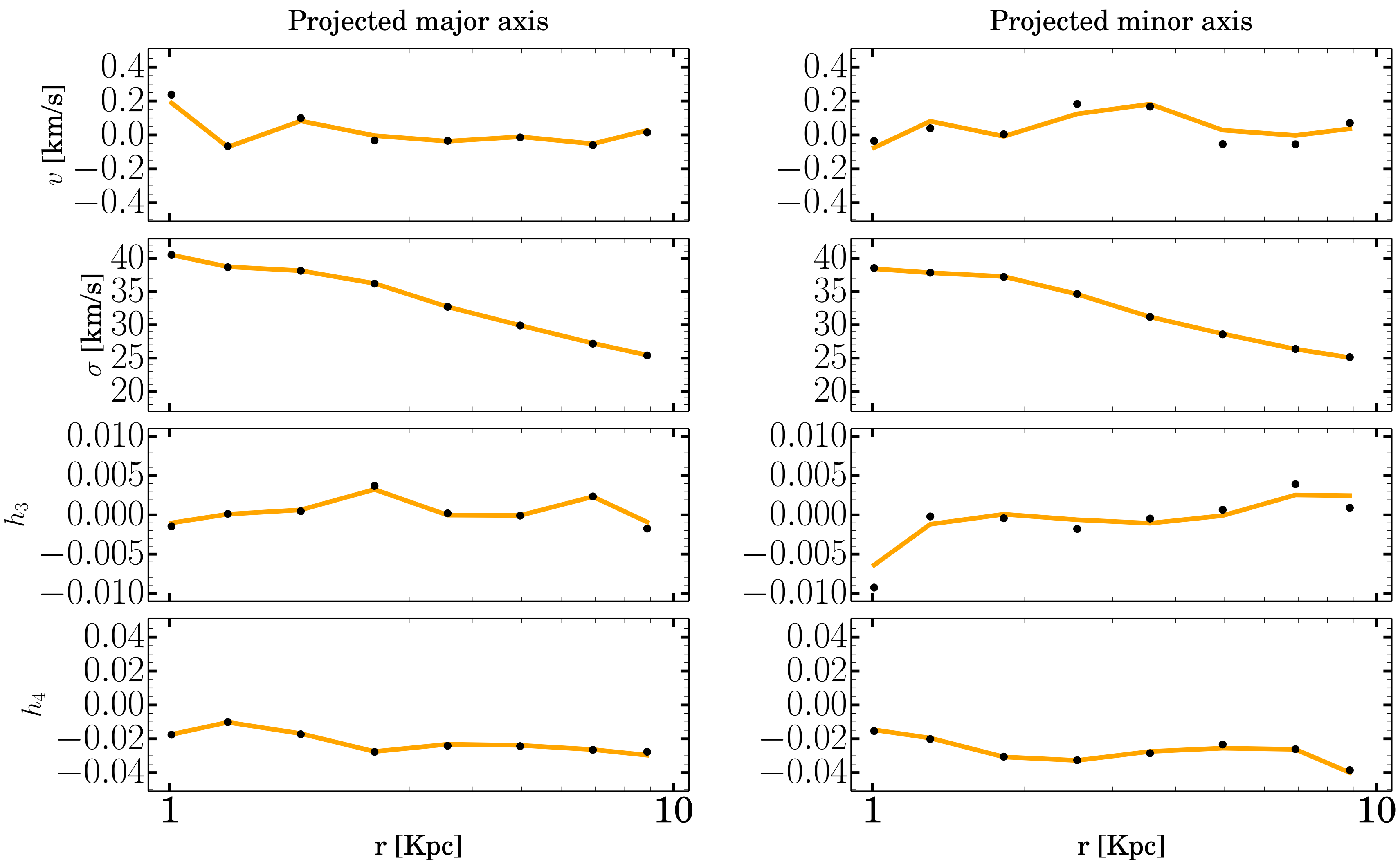

Figure 3.20: Fit to the velocity profiles of the X-projection of a four million unequal-mass particles triaxial reference model (details in text) along the projected major and minor axes. The model corresponds to the best fitting mass-to-light ratio. The dots represent the expectations and the coloured lines the results of the modelling.

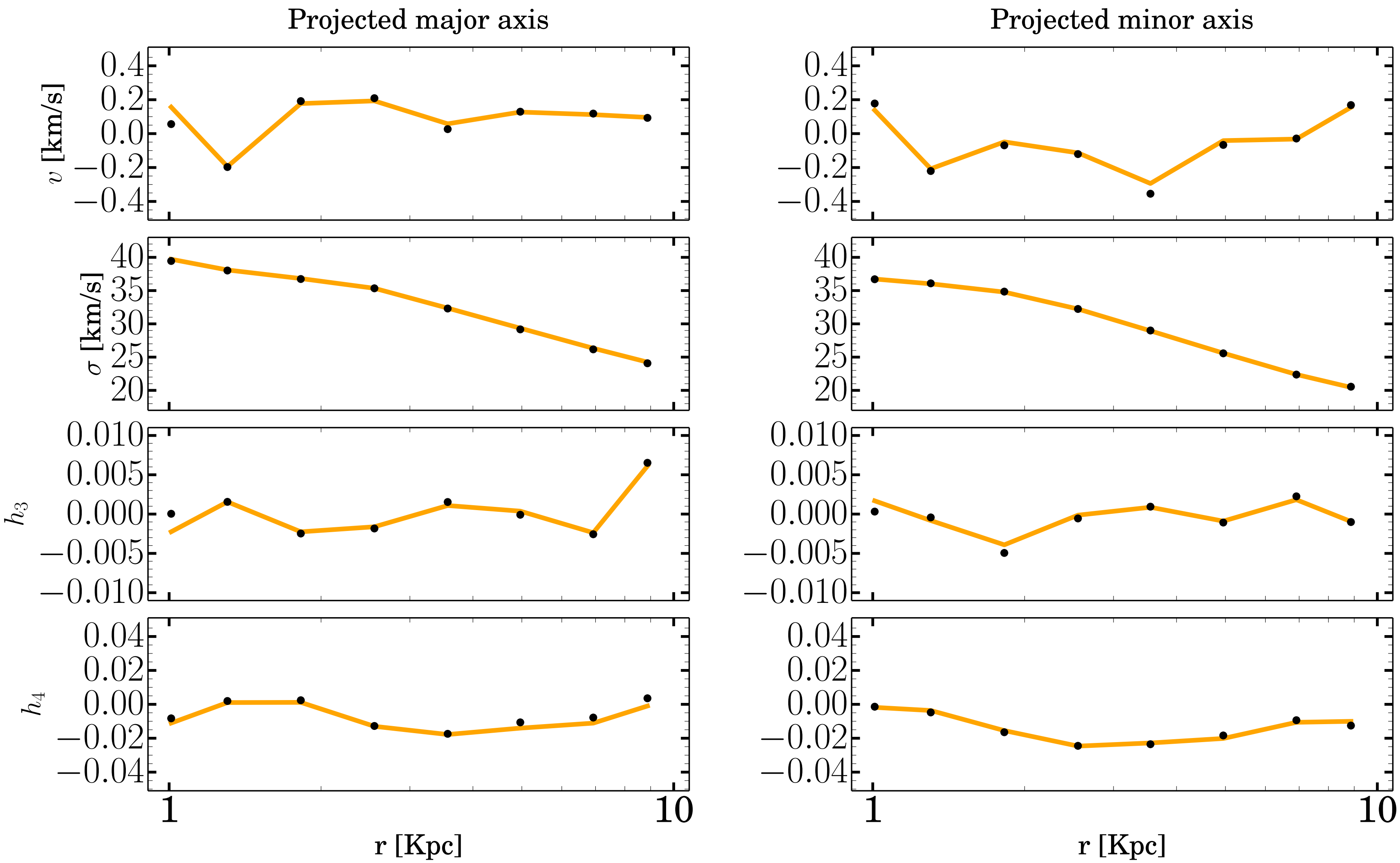

Figure 3.21: Fit to the velocity profiles of the Y-projection of a four million unequal-mass particles triaxial reference model (details in text) along the projected major and minor axes. The model corresponds to the best fitting mass-to-light ratio. The dots represent the expectations and the coloured lines the results of the modelling.

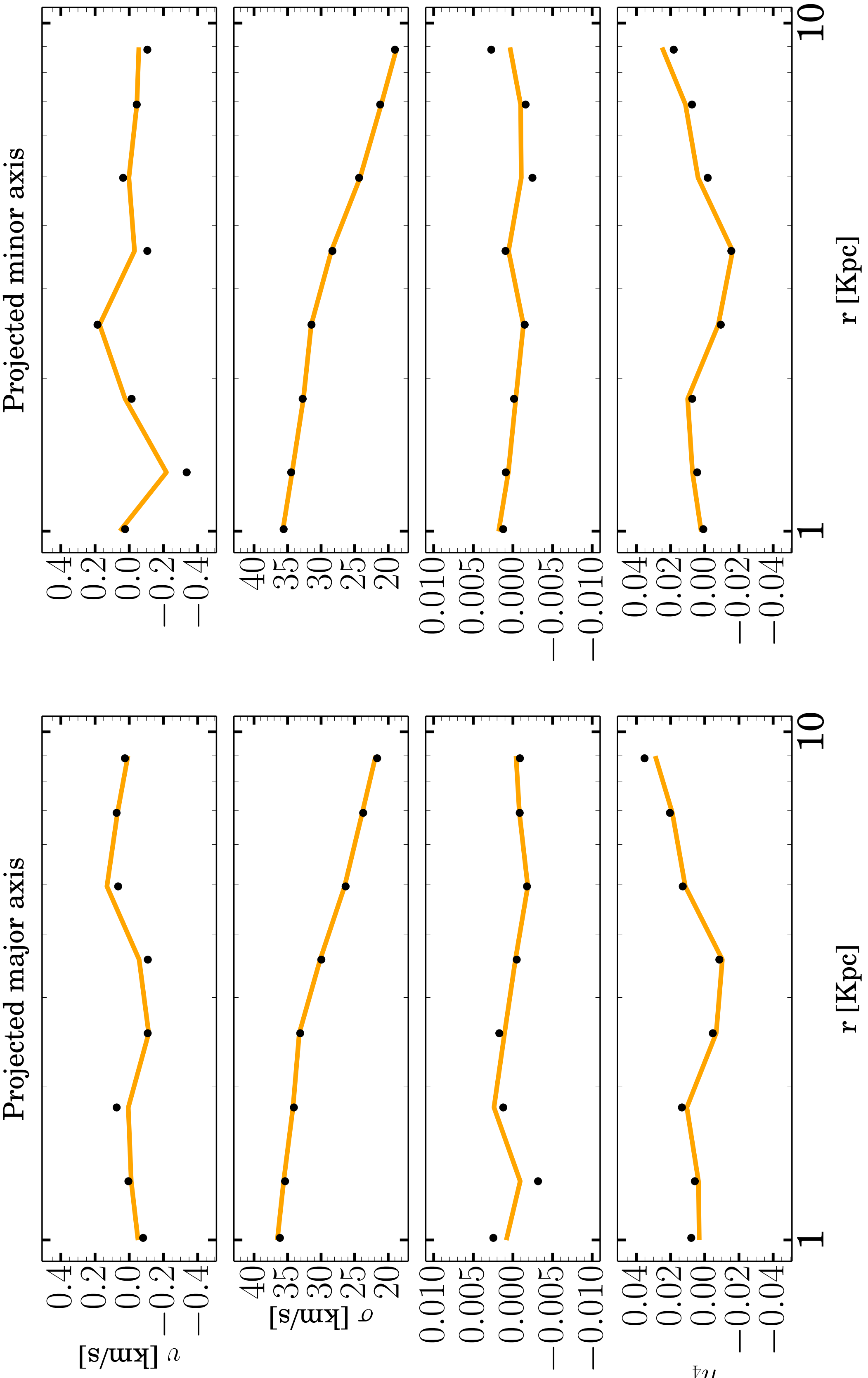

Figure 3.22: Fit to the velocity profiles of the Z-projection of a four million unequal-mass particles triaxial reference model (details in text) along the projected major and minor axes. The model corresponds to the best fitting mass-to-light ratio. The dots represent the expectations and the coloured lines the results of the modelling.

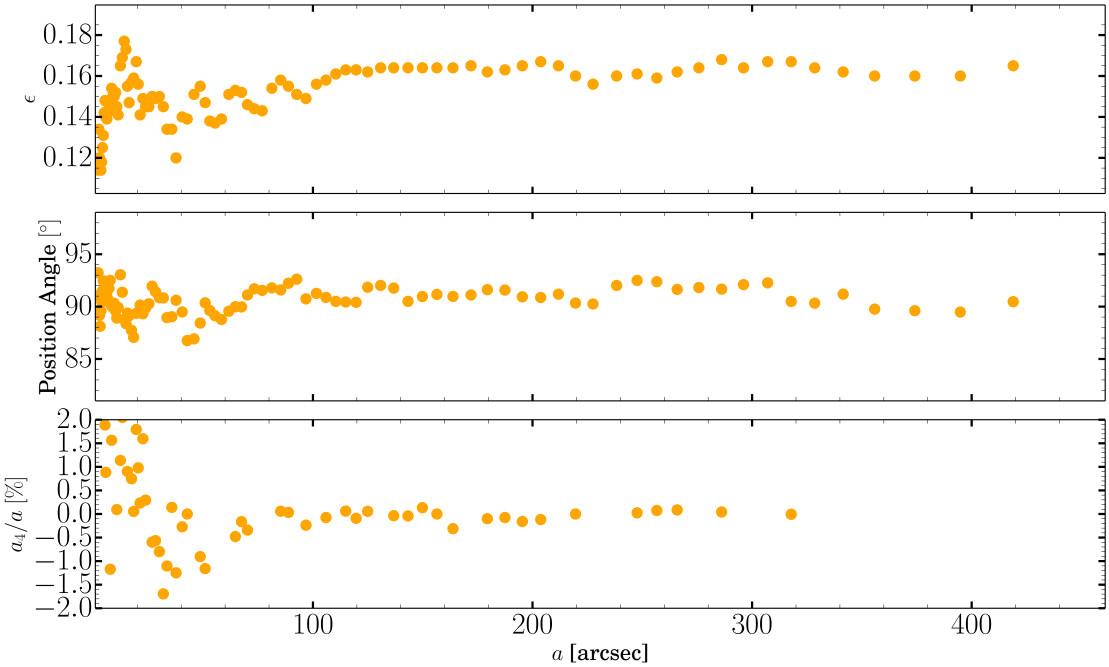

Figure 3.23: Ellipticity, major axis position angle and normalised a_4/a as a function of the semi-major axis a for a four million unequal-mass particles triaxial reference model (details in text). The model is projected along the viewing direction ($\vartheta = 45\,°, \varphi = 45\,°, \psi = 112\,°$). The ellipse fit is performed with the software from Bender & Moellenhoff (1987) using a FITS file computed as in Section (3.2.2).

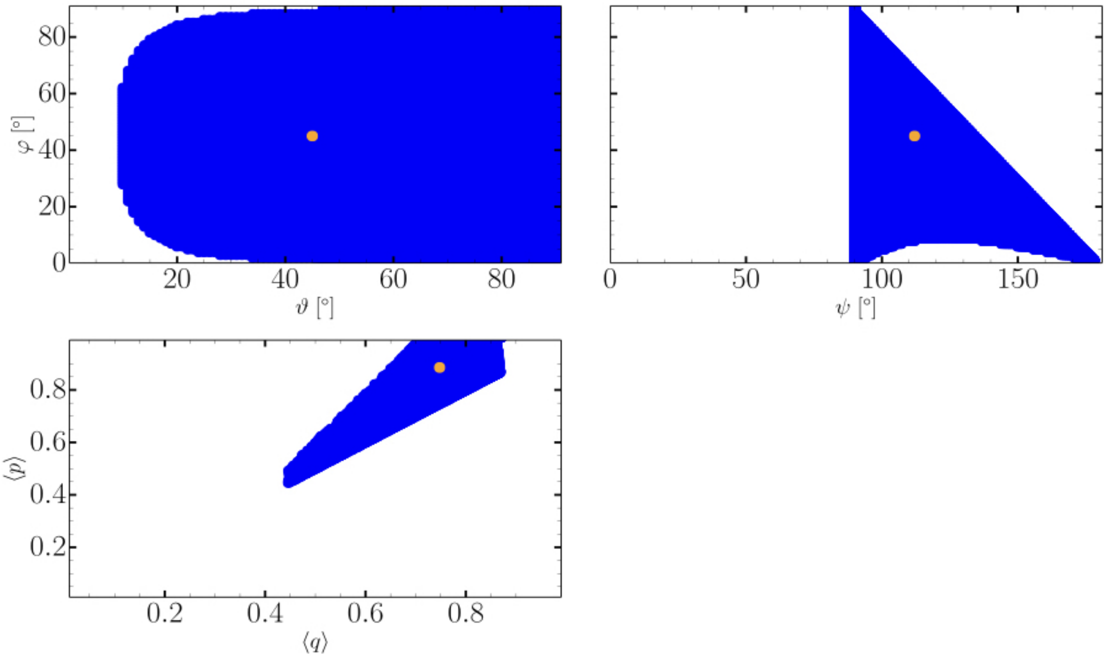

Figure 3.24: Viewing directions corresponding to physically meaningful de-projections for a four million unequal-mass particles triaxial reference model (details in text). The viewing direction ($\vartheta = 45\,^\circ, \varphi = 45\,^\circ, \psi = 112\,^\circ$) is highlighted by the orange dots. The axes ratios $\langle q \rangle$ and $\langle p \rangle$ are the luminosity weighted averages of the axes ratios of the single components.

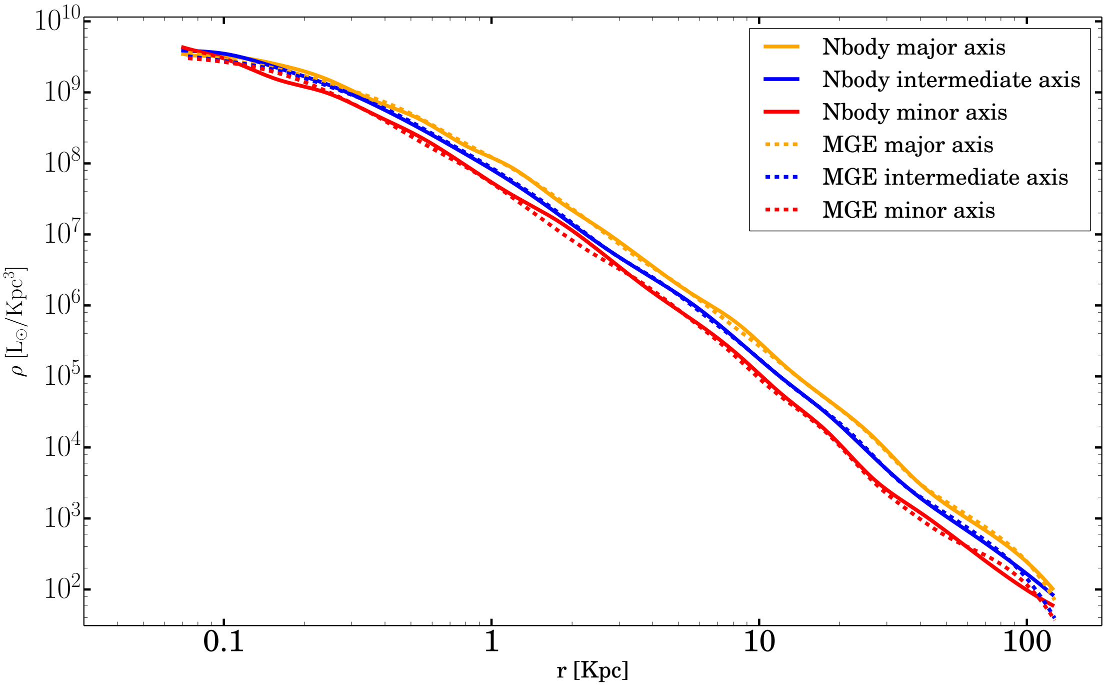

Figure 3.25: Graphical comparison along the three principal axes between the density ρ_{nbody} of a four million unequal-mass particles triaxial reference model (details in text) computed from the sum of the masses of the particles and the density ρ_{MGE} from the MGE de-projection along the viewing direction ($\vartheta = 45\,°, \varphi = 45\,°, \psi = 112\,°$).

Component	**counts$_\mathrm{j}$**	$\boldsymbol{\sigma'_\mathrm{j}}$	**q$'_\mathrm{j}$**	$\boldsymbol{\Delta\psi'_\mathrm{j}}$
1	5200.02	0.380000	0.700000	0.0
2	253925.0	1.16970	0.967399	0.0
3	1.31737×10^6	2.64721	0.851890	0.0
4	893871.0	3.96808	1.00000	0.0
5	859232.0	5.70228	0.700000	0.0
6	1.82134×10^6	6.88689	0.881303	0.0
7	3.65159×10^6	10.8487	0.875498	0.0
8	1.20116×10^6	11.9033	0.700000	0.0
9	6.99359×10^6	24.1981	0.865197	0.0
10	6.69103×10^6	42.8901	0.885772	0.0
11	4.31042×10^6	61.0163	0.815027	0.0
12	1.06551×10^7	116.356	0.844407	0.0
13	4.05622×10^6	226.913	0.842573	0.0
14	3.66189×10^6	451.829	0.700000	0.0
15	9.80094×10^6	530.318	1.000000	0.0

Table 3.3: Parameters obtained from the MGE fit to the photometry of a four million unequal-mass particles triaxial reference model (details in text) projected along the viewing direction ($\vartheta = 45\,°, \varphi = 45\,°, \psi = 112\,°$). σ'_j is expressed in units of pixel and $\Delta\psi'_j$ in degrees. The pixel scale is 1.196 arcsec.

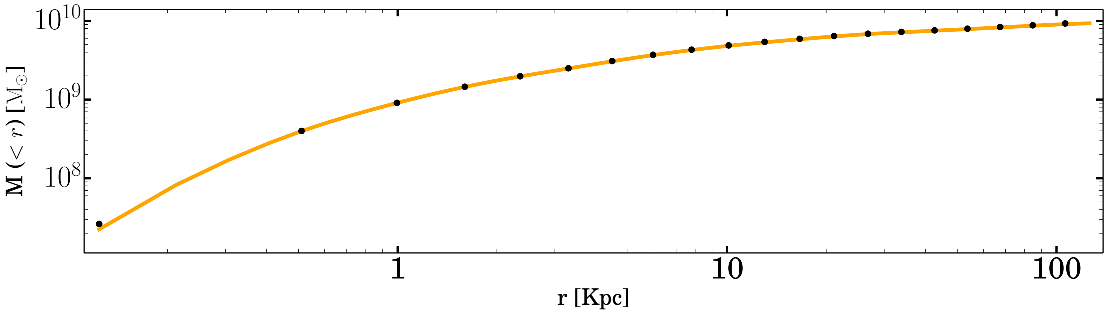

Figure 3.26: Graphical comparison between the **expected** and the **model** enclosed mass for a four million unequal-mass particles triaxial reference model (details in text). The model enclosed mass is computed from the integration of the MGE de-projected density along the viewing direction ($\vartheta = 45\,°, \varphi = 45\,°, \psi = 112\,°$).

Component	**L**	σ	**p**	**q**
1	0.88115261×10^{6}	0.49357	0.75830	0.40639
2	0.43028042×10^{8}	1.41491	0.96869	0.93752
3	0.22323068×10^{9}	3.31561	0.86844	0.71912
4	0.15146803×10^{9}	4.74683	1.00000	1.00000
5	0.14559839×10^{9}	7.40658	0.75830	0.40639
6	0.30862929×10^{9}	8.55512	0.89250	0.77483
7	0.61876840×10^{9}	13.49896	0.88768	0.763867
8	0.20353869×10^{9}	15.46098	0.75830	0.40639
9	$0.11850762 \times 10^{10}$	30.19694	0.87921	0.74438
10	$0.11338069 \times 10^{10}$	53.21104	0.89624	0.78326
11	0.73040831×10^{9}	77.17039	0.83960	0.64835
12	$0.18055256 \times 10^{10}$	146.03092	0.86247	0.70486
13	0.68733367×10^{9}	284.92430	0.86102	0.70136
14	0.62051376×10^{9}	586.87252	0.75830	0.40638
15	$0.16607867 \times 10^{10}$	634.39498	1.00000	1.00000

Table 3.4: Luminosity and intrinsic shape parameters of the Gaussian components from an MGE de-projection along the viewing direction ($\vartheta = 45\,°, \varphi = 45\,°, \psi = 112\,°$) for a four million unequal-mass particles triaxial reference model (details in text). The luminosity is expressed in units of $\mathrm{L}_\odot$ and σ in units of arcseconds.

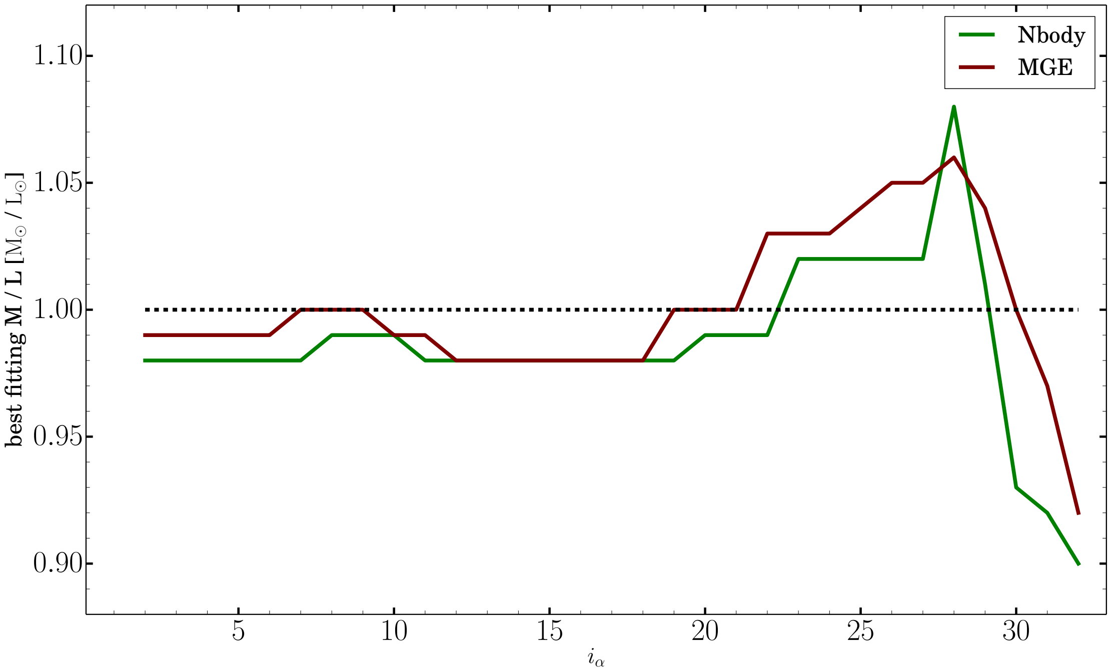

Figure 3.27: Best fitting mass-to-light ratio as a function of the regularisation parameter α for the projection along the line-of-sight ($\vartheta = 45\,°, \varphi = 45\,°, \psi = 112\,°$) of a four million unequal-mass particles triaxial reference model (details in text).

3.2.6 Recovery of the mass-to-light ratio, the viewing direction and the intrinsic shape

The verification of the recovery of the mass-to-light ratio, the viewing direction and intrinsic shape is carried out by fitting the velocity profiles obtained for ($\vartheta = 45\,°, \varphi = 45\,°, \psi = 112\,°$). The specifications of the model (i.e. number of orbits etc.) are the same used in Section (3.2.5). The density is obtained from the MGE de-projection of the observed surface brightness profile. The mass-to-light ratio is varied in the interval $0.7\,\frac{\mathrm{M}_\odot}{\mathrm{L}_\odot} \leq \mathrm{M/L} \leq 1.3\,\frac{\mathrm{M}_\odot}{\mathrm{L}_\odot}$. The viewing angles are varied in $\vartheta, \varphi \in [0\,°, 90\,°]$ and $\psi \in [0\,°, 180\,°]$. The minimisation of the χ^2 is performed with NOMAD for $i_\alpha = 15$ ($\alpha = 1.024$ E-04). NOMAD converges to the best fitting solution after 569 models. Figure (3.29(a)) shows the $\Delta\chi^2 = \chi^2 - \chi^2_{\mathrm{min}}$ as a function of the mass-to-light ratio and the viewing angles and Figure (3.29(b)) as a function of the axes ratios. The axes ratios $\langle p \rangle$ and $\langle q \rangle$ are the luminosity weighted averages of the axes ratios of the single Gaussian components. The expected values of the mass-to-light ratio, viewing angles and axes ratios and the

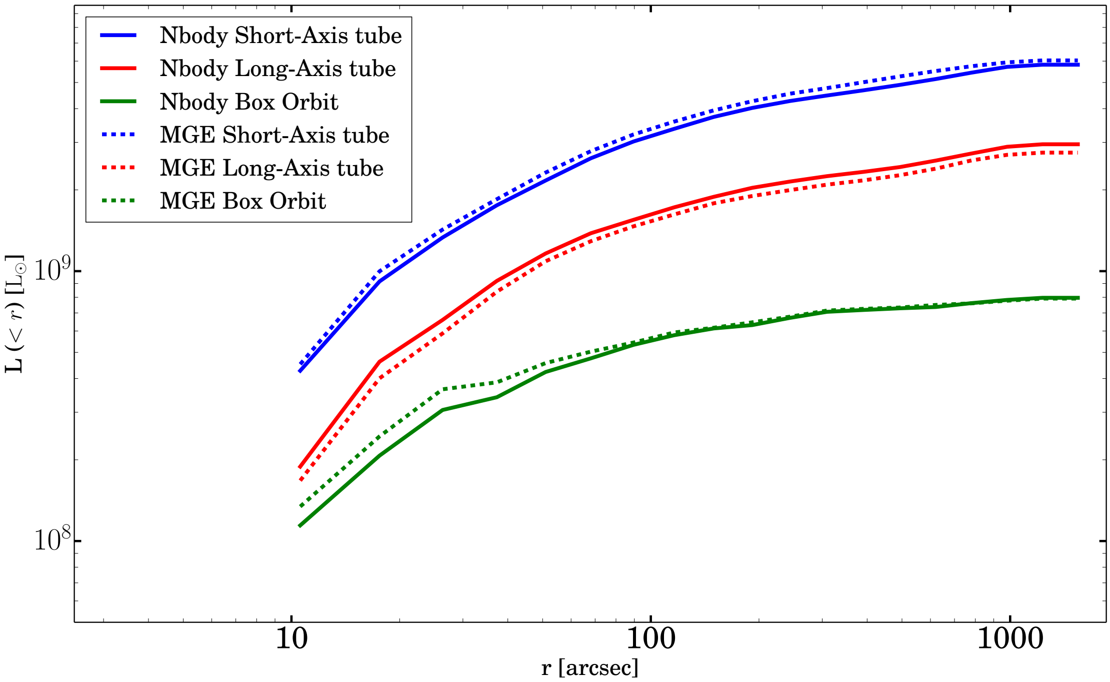

Figure 3.28: Cumulative light carried by the different orbit types as a function of the average of the peri- and apocentres of the orbits for a four million unequal-mass particles triaxial reference model (details in text) at the best fitting mass-to-light ratio. The figure compares a model obtained with the density ρ_{nbody} computed from the sum of the masses of the particles to a model obtained with the density ρ_{MGE} computed from the MGE de-projection along the viewing direction ($\vartheta = 45\,^\circ, \varphi = 45\,^\circ, \psi = 112\,^\circ$).

best fitting values corresponding to $\chi^2_{\text{min}} = 407.081$ are

$$\begin{array}{ccc} & \textbf{Expected} & \textbf{Best-fit} \\ \mathbf{M/L}\left[\frac{\mathrm{M}_\odot}{\mathrm{L}_\odot}\right] & 1.0 & 1.0062 \\ \boldsymbol{\vartheta}[^\circ] & 45.0 & 48.91 \\ \boldsymbol{\varphi}[^\circ] & 45.0 & 51.73 \\ \boldsymbol{\psi}[^\circ] & 112.0 & 108.65 \\ \langle\mathbf{q}\rangle & 0.7478 & 0.7946 \\ \langle\mathbf{p}\rangle & 0.8855 & 0.8867 \end{array} . \tag{3.28}$$

SCHERPA recovers the mass-to-light ratio, the viewing angles (recovered within 7 [°] of the input values) and the intrinsic shape (reconstructed within 6 %). The accuracy on the reconstruction of the intrinsic shapes is better than the one reported by (van den Bosch & Van De Ven, 2009) on triaxial separable Abel models.

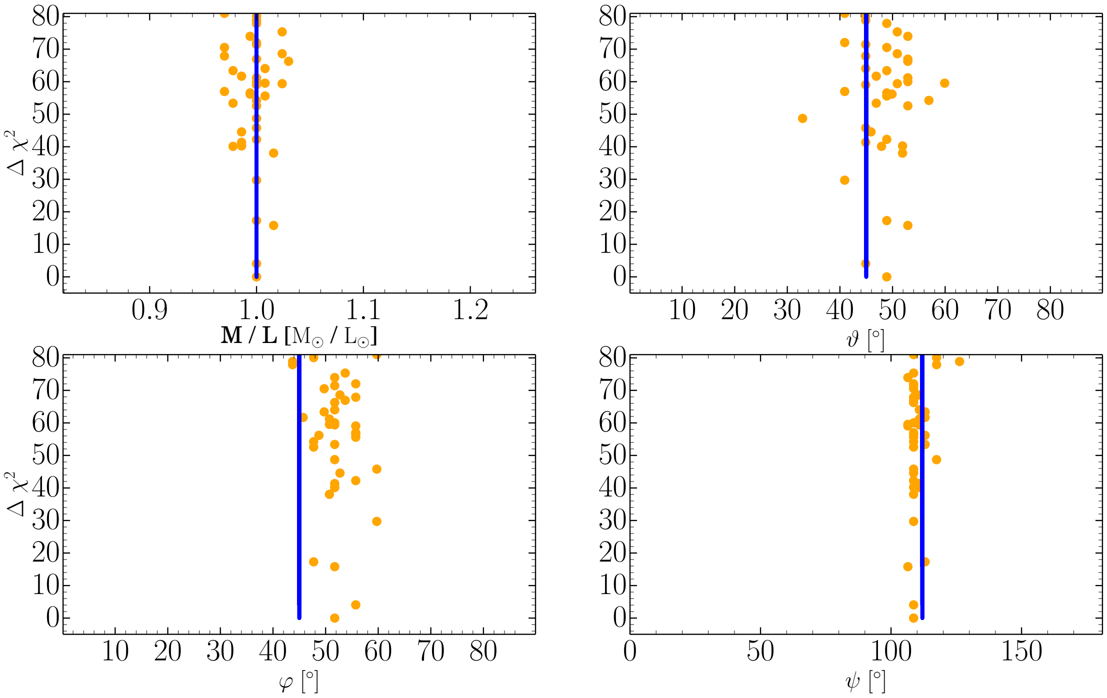

(a) Mass-to-light ratio and viewing angles

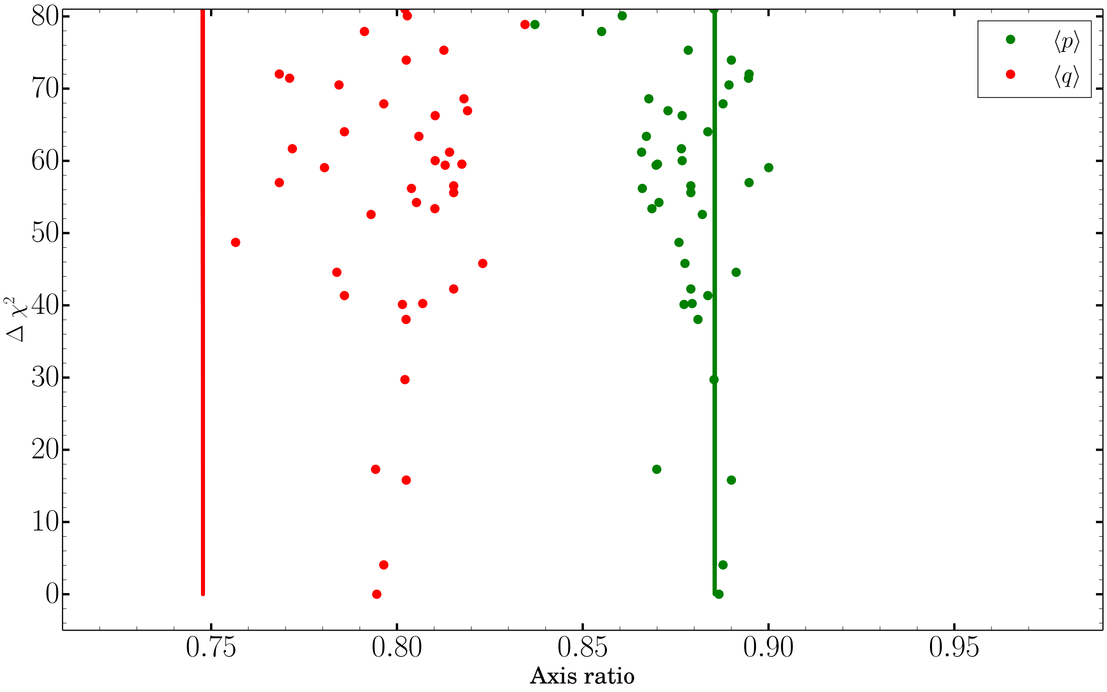

(b) Axes ratios

Figure 3.29: The $\Delta\chi^2 = \chi^2 - \chi^2_{\mathrm{min}}$ as a function of the mass-to-light ratio and the viewing angles (3.29(a)) and of the axes ratios (3.29(b)). The axes ratios $\langle q\rangle$ and $\langle p\rangle$ are the luminosity weighted averages of the axes ratios of the single components. The coloured lines represent the expected values for the various parameters.

Chapter 4

A three-dimensional axisymmetric model of the massive early-type galaxy NGC 1600

The aim of the chapter is to test SCHERPA in the axisymmetric regime and to verify how the code behaves when fitting the data of a real galaxy. The chapter reports on the three-dimensional axisymmetric modelling performed with SCHERPA of the massive early-type galaxy NGC 1600. After introducing the general properties of the galaxy, the chapter describes the spectroscopic and photometric data used and the results of the modelling.

4.1 Introduction

NGC 1600, portrayed in Figure (4.1), is a bright (M_{B} = -23.17) early-type galaxy located at 63.8 Mpc from Earth. It is classified as E3-E4 in the Hubble diagram. It has boxy isophotes and an effective radius $r_e = 14.85$ Kpc. The galaxy has little rotation. Most measured values are below 20 $\frac{\mathrm{km}}{\mathrm{s}}$. The maximum rotation is $v_{\parallel} \approx 30\ \frac{\mathrm{km}}{\mathrm{s}}$. The line-of-sight velocity dispersion reaches a maximum of $\sigma_{\parallel} \approx 360\ \frac{\mathrm{km}}{\mathrm{s}}$ near the center. It degrades to $\approx 235 - 275\ \frac{\mathrm{km}}{\mathrm{s}}$ in the outskirts. The small rotation along the projected minor axis is evidence of the fact that the stellar velocity distribution is aligned with the light distribution. This suggests, together with the low isophotal twist ($\Delta\mathrm{PA} < 2\,^{\circ}$), that the galaxy is nearly oblate (Bender et al., 1994; Matthias & Gerhard, 1999). NGC 1600 has the largest central core in the surface brightness profile among the 219 early-type galaxies observed with HST (Lauer et al., 2007). Moreover it harbours one of the most massive central black holes with $\mathrm{M_{SMBH}} = 1.7 \cdot 10^{10}\ \mathrm{M}_{\odot}$ (Thomas et al., 2016). NGC 1600 is a relatively isolated galaxy. This makes its black hole, together with those in NGC 3842 and NGC 4889 (McConnell et al., 2011), a possible dormant descendant of the massive black holes that presumably powered highly luminous quasars at

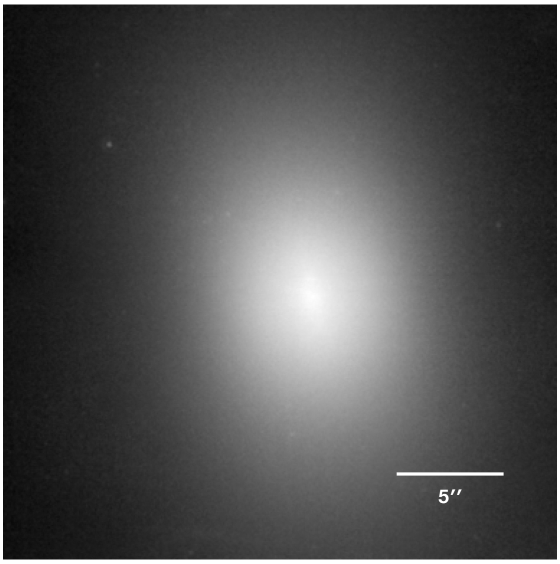

Figure 4.1: HST image of the galaxy NGC 1600 taken with the instrument NICMOS/NIC2 with the F160W filter. Exposure time: 640 seconds. Proposal ID: 7886.

redshift $z > 6$. The galaxy shows evidence of core scouring (Quinlan & Hernquist, 1997; Milosavljević & Merritt, 2001; Thomas et al., 2014b). The orbit distribution is tangential within the core radius and radial outside.

4.2 Spectroscopic data

NGC 1600 has been observed as part of the MASSIVE survey (Ma et al., 2014). MASSIVE is a multi-wavelength, integral field spectroscopic (IFS) and photometric survey of the one hundred most massive early-type galaxies within 108 Mpc from Earth. The galaxies have an absolute K-band magnitude $M_K < -25.3$, declination $\delta > -6°$ and galactic extinction $A_V < 0.6$. MASSIVE targets galaxies that have stellar masses greater than $5 \cdot 10^{11}$ $\mathrm{M}_{\odot}$. The survey aims at constraining the scaling relations between black holes and massive early-type galaxies and probing their dark matter distribution and IMF. The survey collets wide-field IFS data up to two effective radii from the Mitchell Spectrograph (Hill et al., 2008) at the McDonald Observatory in Texas (USA) and additional high-spatial resolution IFS data of the central regions of the galaxies with adaptive optics. This is done to resolve the sphere of influence of the central black holes. The data for the central 5×7 arcsec region of NGC 1600 was obtained with GMOS-N (Gemini Multi-Object Spectrograph) at the 8-meter Gemini North Telescope (`http://www.gemini.edu`) in Hawaii (USA). The spectra are centred on the triplet of calcium absorption lines in the wavelengths regime from $\lambda = 8480$ Å to $\lambda = 8680$ Å. This region is suitable for the measurements of the stellar kinematics (Barth et al., 2002; McConnell et al., 2012). The spectra are binned in order to achieve a signal-to-noise ratio of about 100 per pixel and kinematic observations that are symmetric over the four quadrants of the plane of the sky. This is performed with the Voronoi tessellation scheme from Cappellari & Copin (2003). The kinematic data resolves the central region of NGC 1600 to about 200 pc, where the influence of the black hole is maximum.

4.3 Photometric data

NGC 1600 has a remarkably faint and flat core. In fact the galaxy has a lower central surface brightness than any other galaxy within the MASSIVE sample. The circularised surface brightness profile of NGC 1600 was constructed from an ellipse fit to an high-resolution HST image for the inner 8 arcsec and ground-based photometric data observed at the Kitt Peak National Observatory (`https://www.noao.edu/kpno/`) for larger projected radii (Peletier et al., 1990). The high-resolution image was taken with NICMOS, a near-infrared camera and multi-object spectrometer instrument on the HST, in the F160W bandpass. The pixel scale of the image is of 0.05 arcsec and the total exposure time is of 460 seconds. The two images were combined by calibrating the NICMOS data to the R-band of the ground-based image in the radial range $r \in (2, 10)$ arcsec where the two data sets overlap, so that the magnitude squared differences are minimised. The surface brightness profile is well described by a core-Sèrsic profile with core radius $r_b = 2.15$ arcsec (see Section 1.3.1). The three-dimensional intrinsic luminosity density used in the model of NGC 1600 is obtained in the axisymmetric regime from an edge-on de-projection of the observed surface brightness profile. This is done by means of the non-parametric algorithm from Magorrian (1999) reproducing the ellipticity profile and boxiness of the galaxy.

4.4 Results

NGC 1600 is studied in the radial interval $r_{\text{min}} = 1.5 \cdot 10^{-2}$ Kpc and $r_{\text{max}} = 62$ Kpc. The LOSVDs are binned in $N_{\text{vel}} = 23$ velocity bins with $v_{\parallel,\text{max}} = 1600\ \frac{\text{km}}{\text{s}}$ and distributed in the first quadrant of the plane of the sky in the projected radial interval $r \in (0.2, 14)$ Kpc. In the model are considered $N_{\text{losvd}} = 85$ velocity profiles. The contribution of each representative orbit to the projected kinematics is convolved with the PSF of the observations, which is modelled as a Gaussian-PSF with an FWHM of 0.6 arcsec for the GMOS-N data and FWHM of 2.3 arcsec for the wide-field observations. Three-dimensional space is organised in a grid of $N_{r,\text{grid}} = 20$, $N_{\theta,\text{grid}} = 5$ and $N_{\phi,\text{grid}} = 10$ bins. A library of $N_{\text{orbit}} = 46580$ representative stellar orbits is used to reproduce $N_{r,\text{grid}} \times N_{\theta,\text{grid}} \times N_{\phi,\text{grid}} = 1000$ constraints from the three-dimensional luminosity distribution and to fit $N_{\text{kindata}} = 1955$ kinematical data points. The galaxy is studied along the line-of-sight ($\vartheta = 90\,°, \varphi = 0\,°, \psi = 90\,°$) as in Thomas et al. (2016). The phase-space volumes follow from Equation (2.57). The black hole mass is varied in the interval $1 \cdot 10^9\ \text{M}_\odot \leq \text{M}_{\text{SMBH}} \leq 4 \cdot 10^{10}\ \text{M}_\odot$ and the R-band mass-to-light ratio in $2\ \frac{\mathrm{M}_\odot}{\mathrm{L}_\odot} \leq \mathrm{M}/\mathrm{L}_\mathrm{R} \leq 8\ \frac{\mathrm{M}_\odot}{\mathrm{L}_\odot}$. The dark matter halo follows a spherical (cored) logarithmic profile given by

$$\rho_{\mathrm{DM}} = \frac{v_0^2}{4\ \pi\ \mathrm{G}} \frac{3r_c^2 + r^2}{(r_c^2 + r^2)^2}, \tag{4.1}$$

where $5\ \mathrm{Kpc} \leq r_c \leq 60\ \mathrm{Kpc}$ is the core radius inside which the profile is constant and $500\ \frac{\mathrm{km}}{\mathrm{s}} \leq v_0 \leq 1500\ \frac{\mathrm{km}}{\mathrm{s}}$ is the asymptotic circular velocity. The minimisation of the χ^2 is performed with NOMAD for a low level of regularisation corresponding to $\alpha = 13.42$. This is done to compare the results from SCHERPA at the same level of regularisation used in Thomas et al. (2016). The best fitting solution is obtained after 2907 models and corresponds to $\chi^2_{\mathrm{min}} = 1441.919$ and $\mathrm{M}_{\mathrm{SMBH}} = 1.352 \cdot 10^{10}\ \mathrm{M}_\odot$, $\mathrm{M}/\mathrm{L}_\mathrm{R} = 4.8\ \frac{\mathrm{M}_\odot}{\mathrm{L}_\odot}$, $r_c = 31.5$ Kpc and $v_0 = 1100\ \frac{\mathrm{km}}{\mathrm{s}}$. Figure (4.2) shows the $\Delta\chi^2 = \chi^2 - \chi^2_{\mathrm{min}}$ as a function of the input mass parameters. The plot compares the results from SCHERPA with those from Thomas et al. (2016). The models from Thomas et al. (2016) fit the kinematics with $N_{\mathrm{orbit}} = 29000$ representative stellar orbits. Figure (4.3) shows the luminosity weighted spherically averaged anisotropy parameter β (see Equation 3.3) as a function of the radius. The radius is scaled by the core radius r_b. Figure (4.4) portrays the fits to the projected kinematics. The figures correspond to the best fitting model. It is possible to conclude that the best fitting three-dimensional axisymmetric model recovers the core scouring signature and corresponds to a black hole with a mass larger than $10^{10}\ \mathrm{M}_\odot$. This confirms that NGC 1600 presumably hosts a dormant descendant of the massive black holes powering distant Quasars. The best fitting input mass parameters are within 20 % of the values found in Thomas et al. (2016). The black hole and mass-to-light ratio are respectively 20 % smaller and larger than previous estimates. In fact dynamical models can only constrain the enclosed mass. Hence the black hole mass decreases in order to compensate for the higher stellar mass (see Section 1.6).

As discussed in Section (4.1), photometric and kinematic evidence hint to the fact that NGC 1600 is nearly oblate (Bender et al., 1994; Matthias & Gerhard, 1999). As a future prospect, the modelling of NGC 1600 will be repeated allowing for triaxial intrinsic shapes. It will be interesting to see how this will affect the best fitting values of the input mass parameters, in particular of the black hole mass. Furthermore Figure (4.3) hints to the fact that a smaller black hole mass translates in a model that is less anisotropic. Core scouring changes the orbital distribution in galaxies. Radial orbits that pass in the vicinity of the central black hole binary are gravitationally slingshotted outwards. Intuitively it is then fair to expect that a less massive black hole will scouter less radial orbits out. A more conclusive answer can be drawn from the analysis of simulated galaxy mergers that explore a wide range of initial conditions (something that is planned as a future prospect of this project).

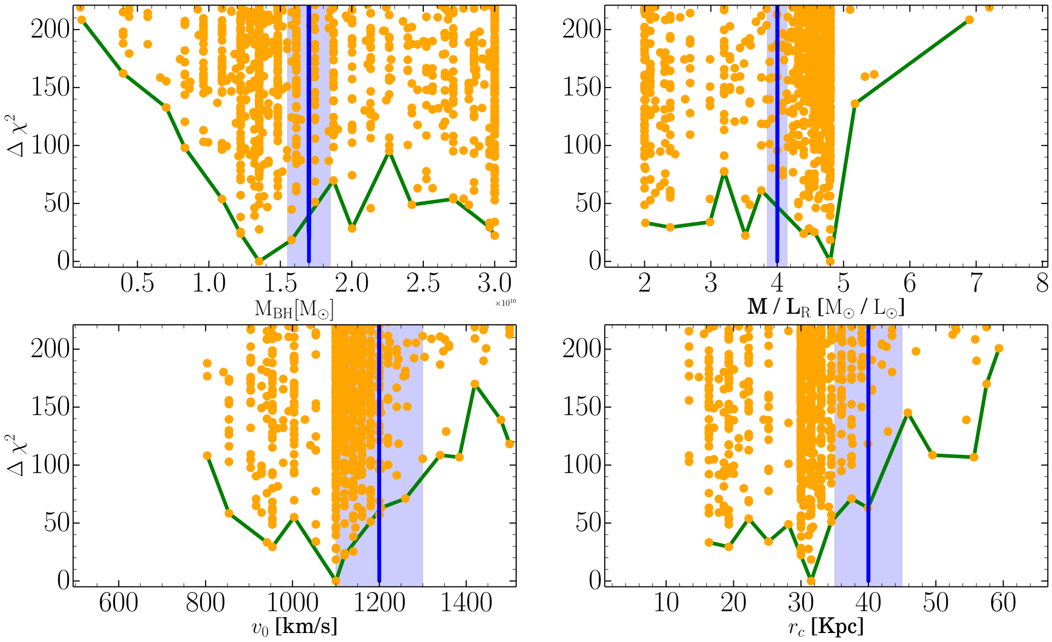

Figure 4.2: The $\Delta\chi^2 = \chi^2 - \chi^2_{\text{min}}$ as a function of the input mass parameters. The blue vertical line shows the best fitting values of the input mass parameters from Thomas et al. (2016) and the shaded blue areas the confidence intervals.

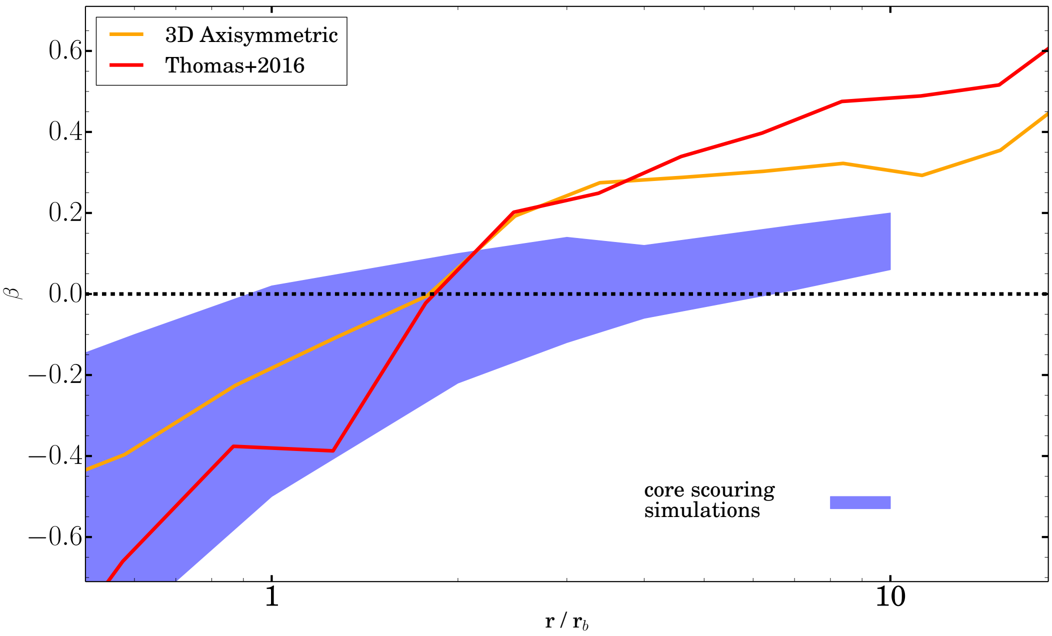

Figure 4.3: Luminosity weighted spherically averaged anisotropy parameter β as a function of the radius for the best fitting model of NGC 1600. The radius is scaled by the core radius r_b. The shaded area portrays the prediction of core scouring by equal-mass binary black holes from N-body simulations of Quinlan & Hernquist (1997) and Milosavljević & Merritt (2001).

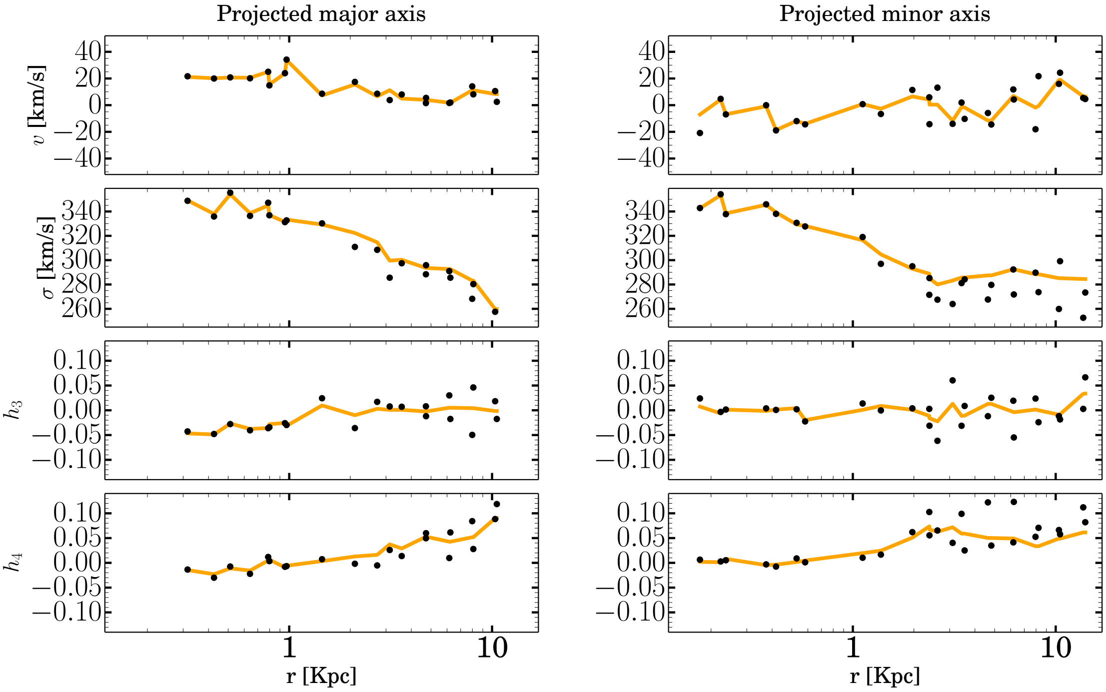

Figure 4.4: Fit to the velocity profiles of NGC 1600 along the projected major and minor axes for the best fitting model. The dots represent the data and the coloured lines the results of the modelling.

Chapter 5

The black hole of the massive triaxial early-type galaxy NGC 5419

The chapter reports on the first triaxial modelling of the massive early-type galaxy NGC 5419 and discusses in particular how allowing for a triaxial intrinsic shape changes the estimate of the black hole mass. After introducing the general properties of the galaxy, the chapter describes the spectroscopic and photometric data and the results of the modelling.

5.1 Introduction

NGC 5419, portrayed in Figure (5.1), is a bright ($M_{\mathrm{V}} = -23.1$) early-type galaxy located at 56.2 Mpc (Mazzalay et al., 2016) from Earth in the cluster Abell 753. It has an effective radius $r_e = 14.66$ Kpc (Saglia et al., 2016). As portrayed in Figure (5.2), the galaxy has boxy isophotes and an isophotal twist of $\Delta\mathrm{PA} \approx 20\,^{\circ}$. HST images of the center ($r < 0.4$ arcsec) of the galaxy from Lauer et al. (2005) show evidence of a double nucleus. Radio (Goss et al., 1987; Subrahmanyan et al., 2002) and X-rays (Balmaverde et al., 2006) observations point to the presence of a central low-luminosity AGN. The galaxy rotates slowly ($v_{\|} < 50\ \frac{\mathrm{km}}{\mathrm{s}}$) and shows a line-of-sight velocity dispersion that peaks at $\sigma_{\|} \approx 350\ \frac{\mathrm{km}}{\mathrm{s}}$. In the region of the double nucleus it reaches a maximum of $\approx 450\ \frac{\mathrm{km}}{\mathrm{s}}$. The sharp increase in $\sigma_{\|}$ suggests that the two nuclei correspond presumably to two SMBHs separated in projection by 70 pc (Mazzalay et al., 2016). In the outer parts the velocity dispersion decreases to $\approx 270\ \frac{\mathrm{km}}{\mathrm{s}}$. The center counter-rotates with respect to the outer parts of the galaxy as shown in Figure (5.3). The transition takes place at 5-6 arcsec. The low rotation, the boxy isophotes, the isophotal twist and the KDC suggest that NGC 5419 is triaxial (see Section 1.5). This makes the galaxy an interesting object to be modelled with SCHERPA.

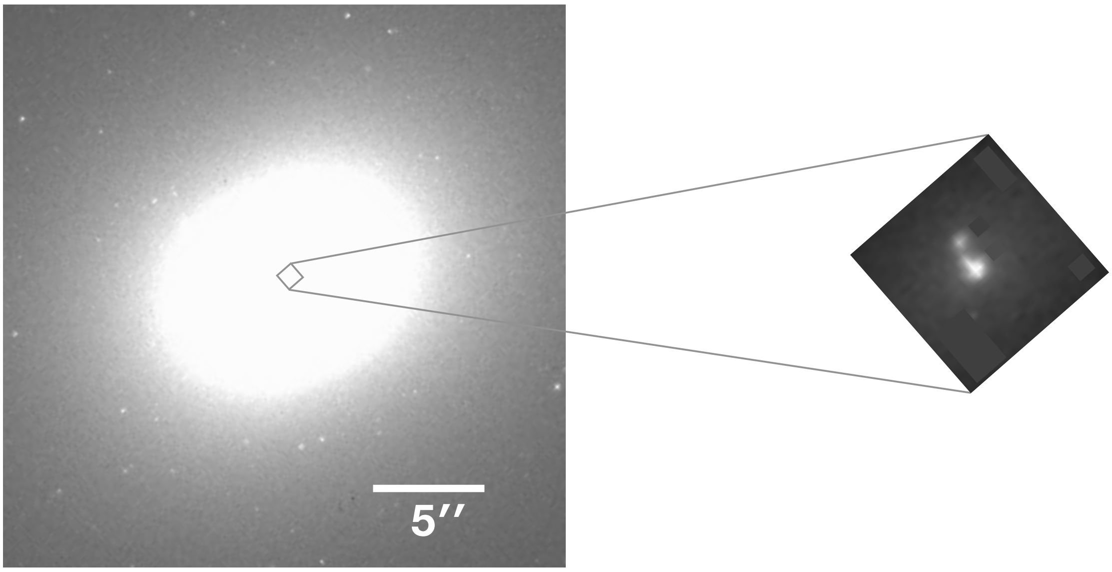

Figure 5.1: HST/WFPC2 image of the galaxy NGC 5419 and of its central double nucleus in the F555W filter. Exposure time: 800 seconds. Proposal ID: 6587.

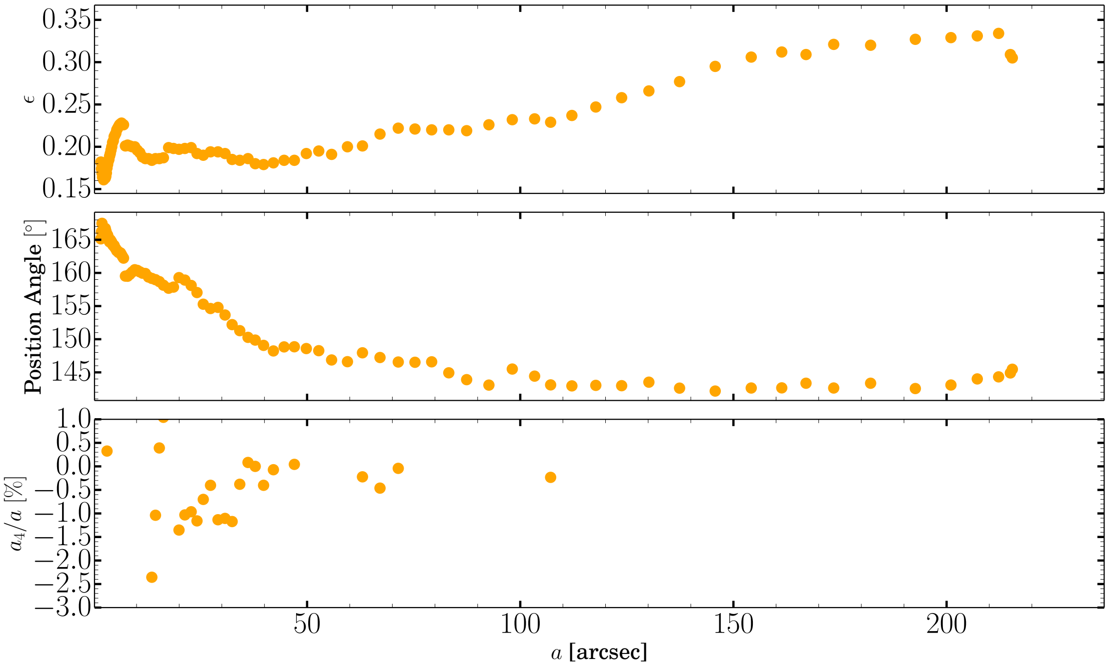

Figure 5.2: Ellipticity, major axis position angle and normalised a_4/a as a function of the semi-major axis a. The ellipse fit is performed with the software from Bender & Moellenhoff (1987) using an high-resolution HST/WFPC2 image (Proposal ID: 6587, PI = D. Richstone) for the inner 7 arcsec and the wide-field Spitzer IRAC1 3.6 μm image (Proposal ID: 30318, PI = G. Fazio) for larger projected radii.

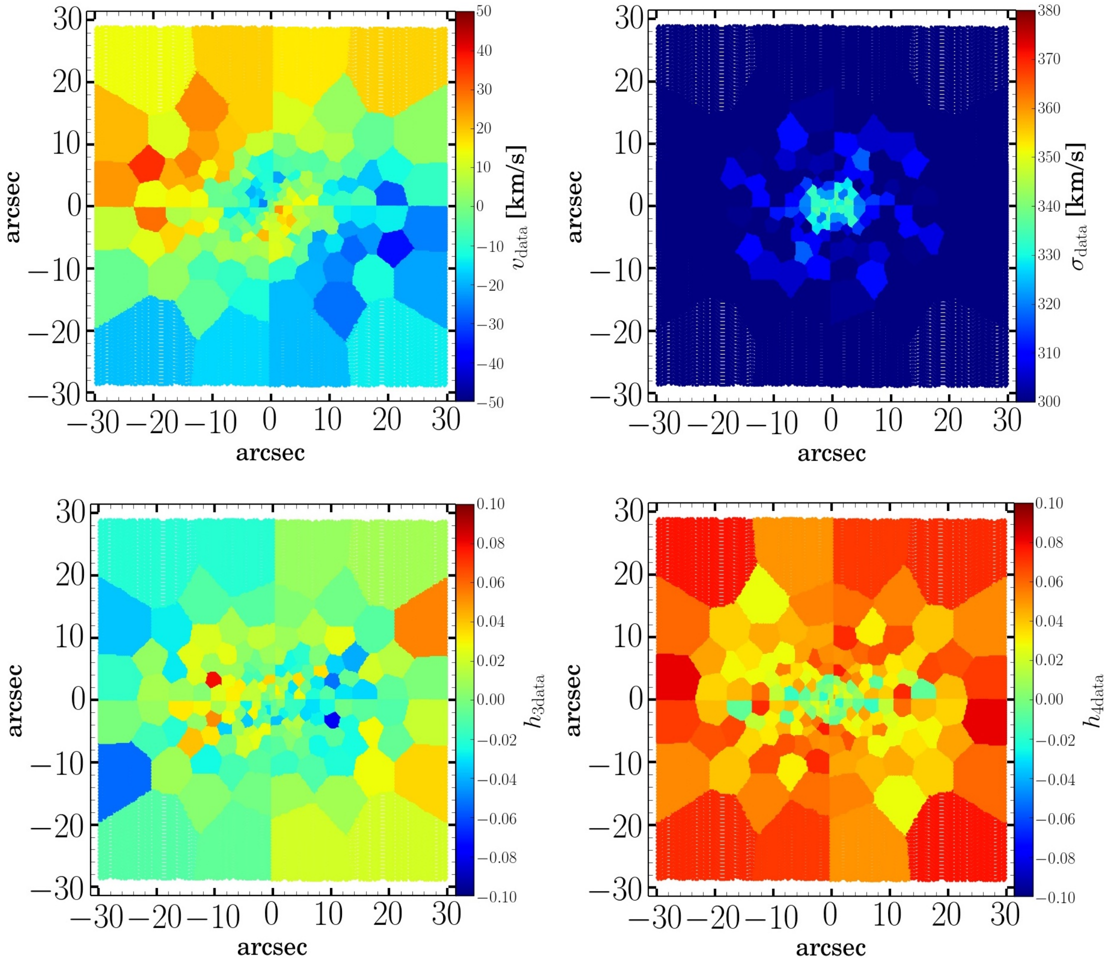

Figure 5.3: Kinematic maps from SINFONI and MUSE pointings of the elliptical galaxy NGC 5419. The map of the mean streaming velocity shows that the galaxy has a counter-rotating core.

5.2 Photometric data

The photometric data of NGC 5419 come from the high-resolution HST/WFPC2 image (Proposal ID: 6587, PI = D. Richstone) for the inner 7 arcsec and the wide-field Spitzer IRAC1 3.6 μm image (Proposal ID: 30318, PI = G. Fazio) for larger projected radii. The high-resolution image was taken in the F555W bandpass. The central region ($r < 0.4$ arcsec) of the HST image corresponding to the AGN has been masked out. The HST data are calibrated to the IRAC1 image by determining the sky subtraction level and relative scaling that minimise the magnitude square differences in the radial range $r \in (5, 18)$ arcsec where the two data sets overlap. The sky background is estimated from the Spitzer image as the galaxy fills the entire field of view of the HST image. As discussed in Mazzalay et al. (2016), the SB profile is well described by a core-Sèrsic profile with core radius r_b = 1.58 arcsec (see Section 1.3.1). The photometry of the galaxy is fitted with the MGE method. The MGE model is fitted simultaneously to the HST and IRAC1 images with $N_{\mathrm{comp}} = 12$ Gaussian components. The number of Gaussian components is determined as detailed in Section (2.2.3). Figure (5.4(a)) shows the comparison between the contours of the MGE model and the data. Figure (5.4(b)) shows the maps of the residuals obtained from the subtraction of the MGE model from the data. The subtraction is performed with IMFIT (`http://www.mpe.mpg.de/~erwin/code/imfit/index.html`) from Erwin (2015). The MGE model fits well the photometric data of the galaxy. Table (5.1) shows the output of the MGE fit.

Component	**$\mathrm{counts}_\mathrm{j}$**	**σ'_j**	**q'_j**	**$\Delta\psi'_\mathrm{j}$**
1	50.54	0.83417	0.686336	5.00
2	159.11	1.75580	0.500000	0.28
3	6778.79	2.53739	0.881305	5.00
4	11692.6	4.99838	0.750501	5.00
5	16446.2	8.37790	0.772485	5.00
6	3094.52	10.4358	0.500000	-28.69
7	24525.3	11.5528	0.866750	5.00
8	30072.1	22.5915	0.746456	0.69
9	56175.0	32.7715	0.849173	-14.82
10	67135.5	66.5264	0.771376	-12.34
11	17574.3	71.7851	1.000000	0.0
12	187799.0	161.954	0.702489	-19.40

Table 5.1: Parameters obtained from the MGE fit to the photometry of NGC 5419. The images used are an HST/WFPC2 F555W image (Proposal ID: 6587, PI = D. Richstone) for the inner 7 arcsec and a Spitzer IRAC1 3.6 μm (Proposal ID: 30318, PI = G. Fazio) for larger radii. σ'_j is expressed in units of pixel and $\Delta\psi'_j$ in degrees. The pixel size is 0.6 arcsec and the photometric zero point of 21.121, such that $SB = -2.5\log_{10}\frac{\mathrm{counts}}{2\pi\sigma' q'} + 21.121$.

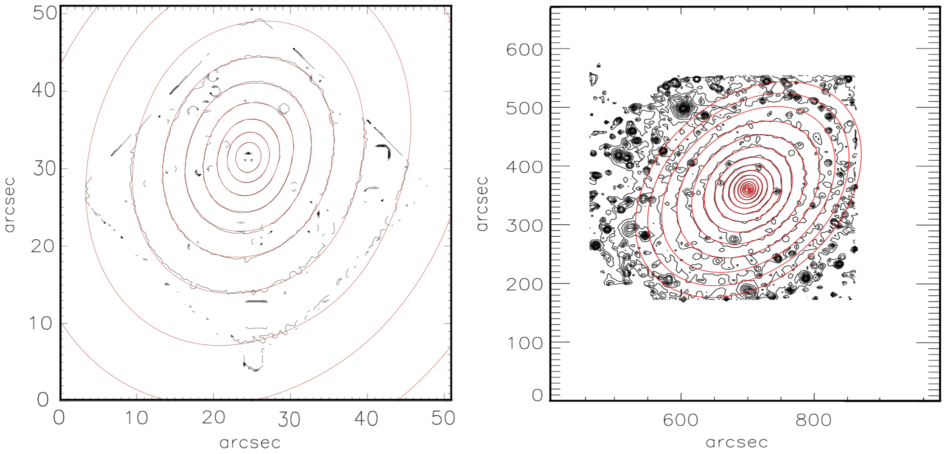

(a) Contour maps

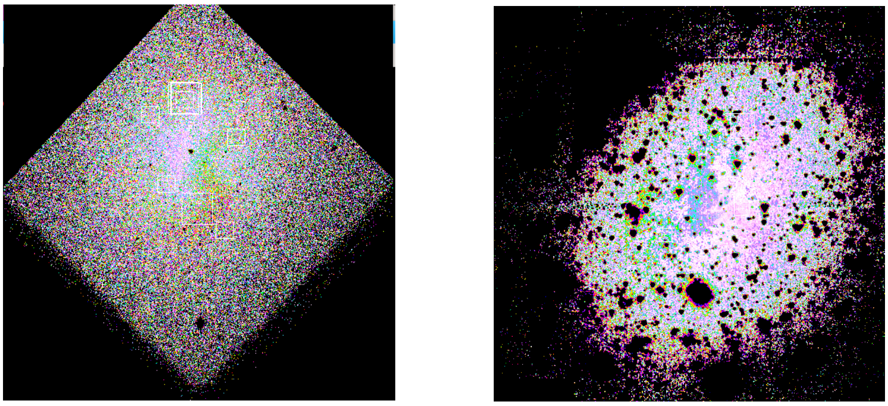

(b) Residual maps

Figure 5.4: On the left the HST/WFPC2 F555W image (Proposal ID: 6587, PI = D. Richstone) of the early-type galaxy NGC 5419. On the right the Spitzer IRAC1 3.6 μm (Proposal ID: 30318, PI = G. Fazio) image. Figure (5.4(a)) portrays the comparison between the contours of the **MGE model** and the **data**. The MGE model is convolved with the proper PSF. Figure (5.4(b)) shows the residuals obtained from the subtraction of the MGE model from the data (Roberto P. Saglia, private communication). The white areas correspond to residuals on the order of 3 %. The black areas correspond to residuals on the order of 10 %.

5.3 Spectroscopic data

The central 3×3 arcsec of NGC 5419 have been observed in the near-infrared as part of the MPE SINFONI (Spectrograph for INtegral Field Observations in the Near Infrared) black hole survey (Nowak et al., 2007, 2008, 2010; Rusli et al., 2011, 2013a,b; Thomas et al., 2014b; Mazzalay et al., 2016; Saglia et al., 2016) with the integral field spectrograph SINFONI (Eisenhauer et al., 2003; Bonnet et al., 2004) at European Southern Observatory Very Large Telescope. This is done to resolve the sphere of influence of the black hole. The SINFONI data are coupled with wide-field IFS data up to 31 arcsec from the MUSE (Multi Unit Spectroscopic Explorer) spectrograph also at the European Southern Observatory Very Large Telescope (Henault et al., 2003; Bacon et al., 2004). The SINFONI spectra are binned as in Gebhardt et al. (2003) and the MUSE spectra with the Voronoi tesselation scheme from Cappellari & Copin (2003) to achieve a signal-to-noise ratio of approximately 40-50.

5.4 Results

The three-dimensional intrinsic luminosity density used in the model of NGC 5419 is obtained from a triaxial de-projection of the observed surface brightness profile. This is carried out by means of the MGE method. Given the output of the MGE fit to the HST and IRAC1 images from Table (5.1), Figure (5.5) portrays the set of line-of-sights (see Section 2.2.3) along which the MGE de-projection is allowed. The figure portrays also the corresponding intrinsic axes ratios $\langle p \rangle$ and $\langle q \rangle$. They are given by the luminosity weighted averages of the axes ratios of the single Gaussian components (see Section 2.2.5). As an initial test, the viewing direction is set to $(\vartheta = 63\,°, \varphi = 33\,°, \psi = 124\,°)$. It corresponds to the roundest of the allowed triaxial intrinsic shapes with $\langle p \rangle = 0.8$, $\langle q \rangle = 0.61$ and $T = \frac{1-p^2}{1-q^2} = 0.57$. This triaxiality lies in the interval $0.4 < T < 0.8$ found by Vincent & Ryden (2005) to reproduce the observed distribution of ellipticities of bright elliptical galaxies. The galaxy is studied in the radial interval $r_{\text{min}} = 6.8 \cdot 10^{-3}$ Kpc and $r_{\text{max}} = 68$ Kpc. The LOSVDs are binned in $N_{\text{vel}} = 23$ velocity bins with $v_{\parallel,\text{max}} = 1238\ \frac{\text{km}}{\text{s}}$ and distributed in the half of the plane of sky corresponding to $x' > 0$ in the projected radial interval $r \in (0.11, 8.47)$ Kpc. Kinematic data points inside $r < 0.1$ Kpc are omitted in order to avoid the region of the central double nucleus. In the model are considered $N_{\text{losvd}} = 120$ velocity profiles. The contribution of each representative orbit to the projected kinematics is convolved with the PSF of the observations, which is modelled as a Gaussian-PSF with an FWHM of 0.92 arcsec for the MUSE data and given by an image for the SINFONI observations as done in Rusli et al. (2013a). Three-dimensional space is organised in a grid of $N_{r,\text{grid}} = 20$, $N_{\theta,\text{grid}} = 5$ and $N_{\phi,\text{grid}} = 10$ bins. A library of $N_{\text{orbit}} = 46580$ representative stellar orbits is used to reproduce $N_{r,\text{grid}} \times N_{\theta,\text{grid}} \times N_{\phi,\text{grid}} = 1000$ constraints from the three-dimensional luminosity distribution and to fit $N_{\text{kindata}} = 2760$ kinematical data points. The phase-space volumes follow from Equation (2.57). The black hole mass is varied in the interval $1 \cdot 10^9\ \mathrm{M}_\odot \leq \mathrm{M}_\mathrm{SMBH} \leq 1 \cdot 10^{10}\ \mathrm{M}_\odot$ and the 3.6 μm-band mass-to-light ratio in $0.4\ \frac{\mathrm{M}_\odot}{\mathrm{L}_\odot} \leq \mathrm{M/L}_{3.6\mu\mathrm{m}} \leq 1.2\ \frac{\mathrm{M}_\odot}{\mathrm{L}_\odot}$. The dark matter halo follows a spherical (cored) logarithmic profile given by Equation (4.1) where 5 Kpc $\leq r_c \leq$ 50 Kpc is the core radius and $500\ \frac{\mathrm{km}}{\mathrm{s}} \leq v_0 \leq 1100\ \frac{\mathrm{km}}{\mathrm{s}}$ is the asymptotic circular velocity. The minimisation of the χ^2 is performed with NOMAD for a low level of regularisation corresponding to $\alpha = 13.42$. The best fitting solution is obtained after 3045 models and corresponds to $\chi^2_\mathrm{min} = 2093.518$ and $\mathrm{M/L}_{3.6\mu\mathrm{m}} = 1.127^{+0.04}_{-0.03}\ \frac{\mathrm{M}_\odot}{\mathrm{L}_\odot}$, $r_c = 45.5^{+0.18}_{-0.22}$ Kpc and $v_0 = 882.8^{+1}_{-6}\ \frac{\mathrm{km}}{\mathrm{s}}$. The black hole mass is $\mathrm{M}_\mathrm{SMBH} = 2.659^{+0.041}_{-0.060} \cdot 10^9\ \mathrm{M}_\odot$. Figure (5.6(a)) shows the $\Delta\chi^2 = \chi^2 - \chi^2_\mathrm{min}$ as a function of the input mass parameters and Figure (5.6(b)) the 1-σ error on the input mass parameters, determined as in Gebhardt et al. (2000b). Figure (5.7) portrays the fits to the projected kinematics. Figure (5.8) quantifies how accurately the best fitting triaxial model recovers the input kinematics of the galaxy. This is estimated by

$$\left(\frac{v - v_\mathrm{data}}{\Delta v_\mathrm{data}}\right)^2. \tag{5.1}$$

Equation (5.1) is valid also for σ, h_3 and h_4. The uncertainties on the LOSVDs were estimated from 100 Monte Carlo simulations of the galaxy spectra from which the velocity profiles are derived. Figure (5.9) shows the cumulative light carried by each orbit type as a function of the average of their peri- and apocentres. The figures correspond to the best fitting model. Figure (5.7) and (5.8) show that the best fitting model is able to reproduce the central counter-rotation of the galaxy and to fit well the input kinematics. The enclosed stellar mass within the core radius for the best fitting triaxial model is $\mathrm{M}_\mathrm{star,triaxial}(< r_b) = 6.8 \cdot 10^9\ \mathrm{M}_\odot$. A NOMAD search for a high level of regularisation corresponding to $\alpha = 1.024\mathrm{E}\text{-}04$ yields a black hole mass ($\mathrm{M}_\mathrm{SMBH} = 2.913^{+0.007}_{-0.023} \cdot 10^9\ \mathrm{M}_\odot$) similar to the non-regularised one and an enclosed stellar mass within the core radius of $6.11 \cdot 10^9\ \mathrm{M}_\odot$. This seems to be in agreement with Thomas et al. (2007b), where it was found that the total reconstructed mass is not significantly affected by the the balance between the fit to the data and the regularisation. Figure (5.10) compares the fits to the projected kinematics for the best fitting triaxial models corresponding to a low and high level of regularisation.

With respect to the orbital distribution of the triaxial model, it is possible to note in Figure (5.9) that Keplerian/Spherical-like orbits account for 0.4 % of the light inside the core radius r_b. The contribution of box orbits is negligible. The presence of a massive black hole renders box orbits unstable. Triaxial models from van den Bosch & De Zeeuw (2010) for the early-type galaxy NGC 3379 are instead dominated by box orbits inside the sphere of influence of the black hole (55 % of all orbits). As portrayed in Figure (5.9), short-axis and long-axis tube orbits carry over 89 % of the total light within the region of the KDC ($r \leq 6$ arcsec). The light is almost equally portioned between the two orbit types (46 % for the short-axis tubes and 43 % for the long-axis tube). Box orbit carry the remaining ≈ 11 % of the light with a small contribution coming from Keplerian/Spherical-like orbits (less than 0.3 %). As discussed in Sections (1.5) and (1.9.3), one possible explanation for the origin of KDCs is that these structures emerge from the interplay in projection of the major families of tube orbits present in a triaxial potential. This seems to be the case for the KDC in NGC 5419. Over the entire orbit library, the light carried by the orbit types is subdivided in

Keplerian/Spherical-like orbit	0.004 %	
Short-axis tube orbit	51.400 %	(5.2)
Long-axis tube orbit	33.400 %	
Box orbit	15.196 %.	

The results from SCHERPA are compared to an axisymmetric modelling of the galaxy performed with the code from Thomas et al. (2004). The axisymmetric models fit the kinematics edge-on with $N_{\mathrm{orbit}} = 30000$ orbits and a low level of regularisation corresponding to $\alpha = 13.42$. The best fitting black hole mass is $\mathrm{M_{SMBH}} = 4^{+0.4}_{-0.4} \cdot 10^9\ \mathrm{M_\odot}$. The enclosed stellar mass within the core radius r_b amounts to $\mathrm{M_{star,axisymmetric}}(< r_b) = 7.74 \cdot 10^9\ \mathrm{M_\odot}$. The axisymmetric model yields a black hole mass that is $\approx 50\%$ larger than the triaxial estimate. The axisymmetric enclosed stellar mass inside r_b is also ≈ 15 % larger than the triaxial result. Probably more modelling along different line-of-sights is needed in order to understand if these overestimations are systematic. For the moment it is possible to say that axisymmetric models overestimate the black hole mass of NGC 5419. This is expected, given the chosen line-of-sight near the intrinsic major axis of the galaxy. This is the opposite of what reported in van den Bosch & De Zeeuw (2010) for NGC 3379, where the black hole mass from triaxial models is claimed to be almost two times larger than previous axisymmetric estimates from Shapiro et al. (2006). In both Shapiro et al. (2006) and van den Bosch & De Zeeuw (2010) the models are computed without dark matter and the best fitting I-band mass-to-light ratio is $\approx 3.00\ \frac{\mathrm{M_\odot}}{\mathrm{L_\odot}}$ regardless of the fact that the best fitting inclinations are close respectively to a face-on and edge-on view. Gebhardt & Thomas (2009) showed that dark halo can increase the black hole mass if the constant M/L is overestimated. Moreover Thomas et al. (2007a) showed that edge-on axisymmetric models of face-on merger remnants underestimate the M/L. This seems however not to be the case in NGC 3379 since the best fitting M/L is very close to the one derived from the stellar population (Cappellari et al., 2006). Figure (5.11) and (5.12) show how accurately the best fitting axisymmetric model recovers the input kinematic of the galaxy. It is possible to see that the axisymmetric model is not able to reproduce the KDC. This is probably because of the lack of long-axis tubes in an axisymmetric potential. NGC 5419 was modelled as an axisymmetric system also in Mazzalay et al. (2016). The models implied a black hole mass of $7.2^{+2.7}_{-1.9} \cdot 10^9\ \mathrm{M_\odot}$ and an enclosed stellar mass within the core radius of $5.68 \cdot 10^9\ \mathrm{M_\odot}$. It has to be noted however that the data used in this modelling were different. The SINFONI velocity profiles were combined to long slits obtained at the Southern African Large Telescope (SALT) out to 20 arcsec along the photometric major axis and 10 arcsec along the projected minor axis.

Figure (5.13) compares the luminosity weighted spherically averaged anisotropy parameter β (see Equation 3.3) for the best fitting triaxial and axisymmetric models. The anisotropy profiles are not compatible with the predictions of core scouring by equal-mass binary black holes from N-body simulations of Quinlan & Hernquist (1997) and Milosavljević & Merritt (2001). It seems that the core scouring signature in the anisotropy profile has not yet fully emerged in NGC 5419 while the photometric core has already formed. This would suggest that the formation of the photometric core precedes that of the anisotropy (Merritt, 2013).

In the end it is interesting to discuss what is the meaning of the black hole mass estimate of NGC 5419 for the demographics of black holes. Figure (5.14) portrays the scaling relation between the black hole mass and the velocity dispersion inside r_{e} for core and power-law early-type galaxies from the sample of Saglia et al. (2016). It also highlights the estimates of the black hole mass of NGC 5419 from axisymmetric and triaxial models. The figure indicates that the relation overpredicts the black hole mass of NGC 5419. This is in contrast with the steepening of the relation at the high mass end predicted from merger simulations (Boylan-Kolchin et al., 2006). It is too early however to speculate what the overall effect on black hole demographics will be. For instance the black hole masses of triaxial galaxies could scatter around the scaling relation. It may also be that NGC 5419 is an outlier. Only the triaxial stellar dynamical modelling of more galaxies will allow to say something more conclusive. In the near future, the model of NGC 5419 will be completed allowing for different viewing directions and relaxing the hypothesis of a spherical halo. It will be investigated what the effects of these changes will be primarily on the mass of the central black hole.

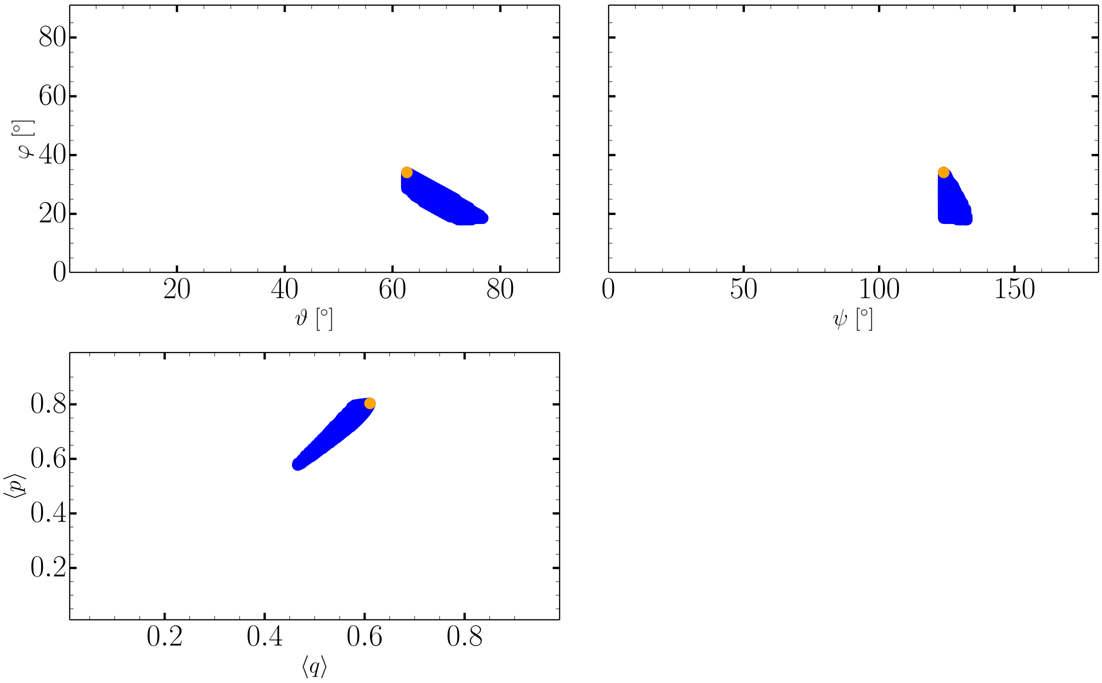

Figure 5.5: Viewing directions corresponding to physically meaningful de-projections for the early-type galaxy NGC 5419. The viewing direction ($\vartheta = 63\,^\circ, \varphi = 33\,^\circ, \psi = 124\,^\circ$) is highlighted by the orange dots. The axes ratios $\langle q \rangle$ and $\langle p \rangle$ are the luminosity weighted averages of the axes ratios of the single components.

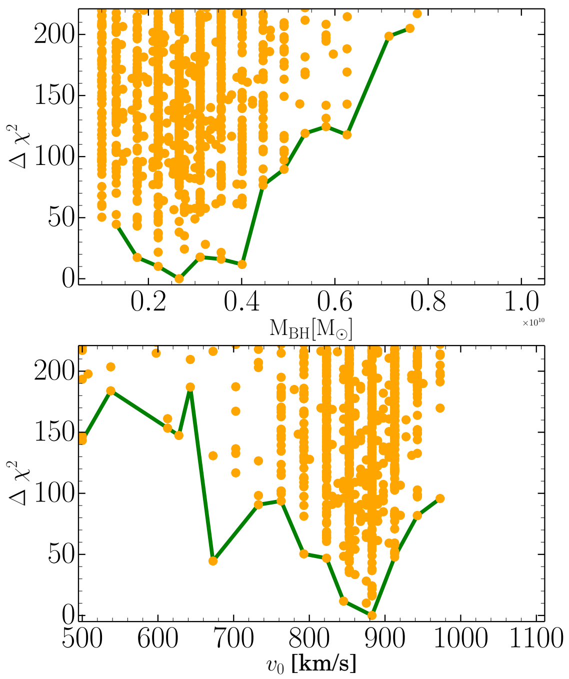

(a) $\Delta\chi^2$ plot

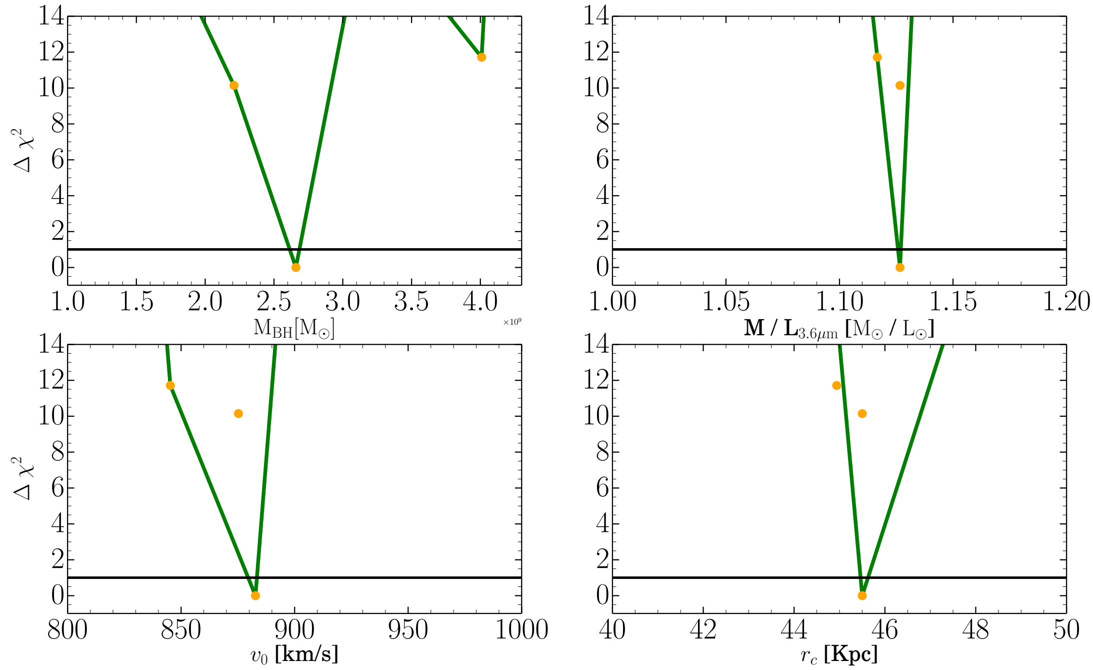

(b) Error plot

Figure 5.6: Figure (5.6(a)) portrays the $\Delta\chi^2 = \chi^2 - \chi^2_{\rm min}$ as a function of the input mass parameters. Figure (5.6(b)) zooms in towards the minimum of the $\Delta\chi^2$ curves and shows for the input mass parameters the 1-σ error as determined in Gebhardt et al. (2000b).

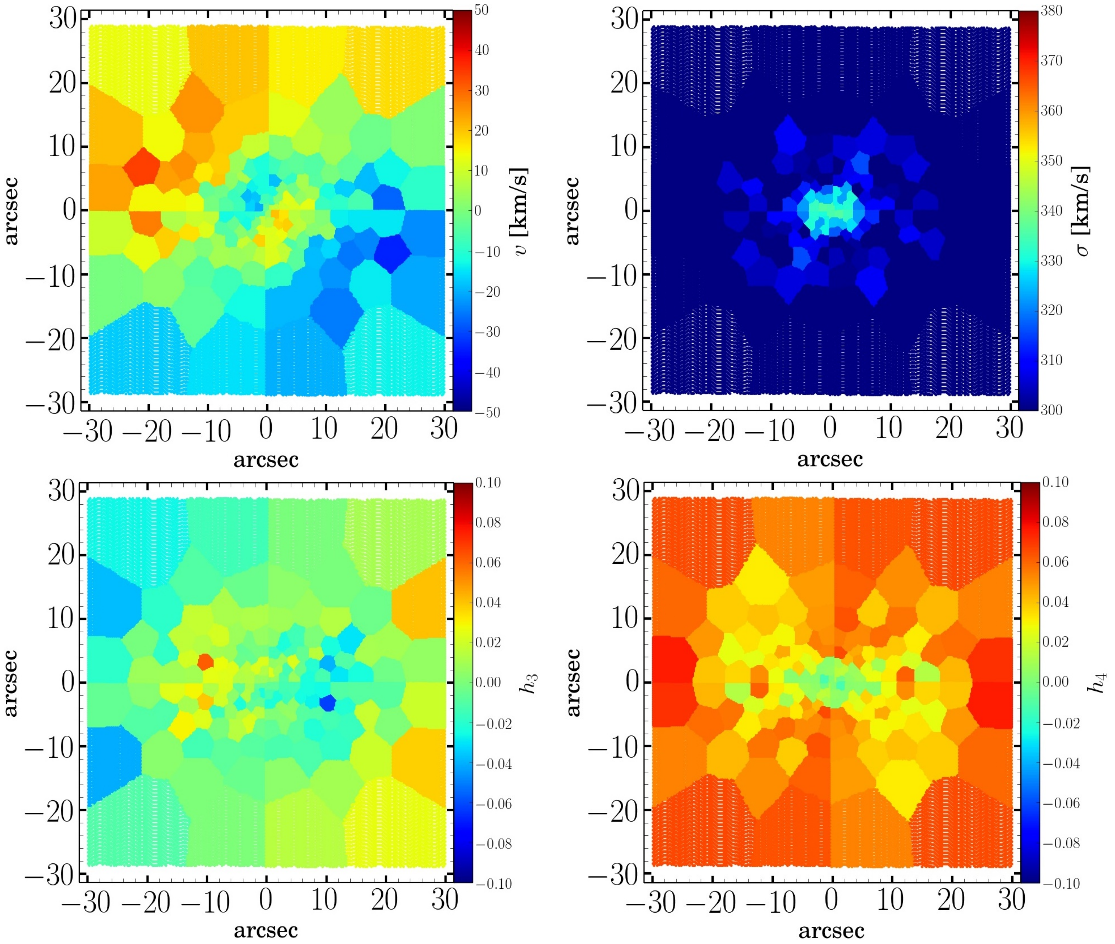

Figure 5.7: Kinematic maps for the best fitting triaxial model of NGC 5419.

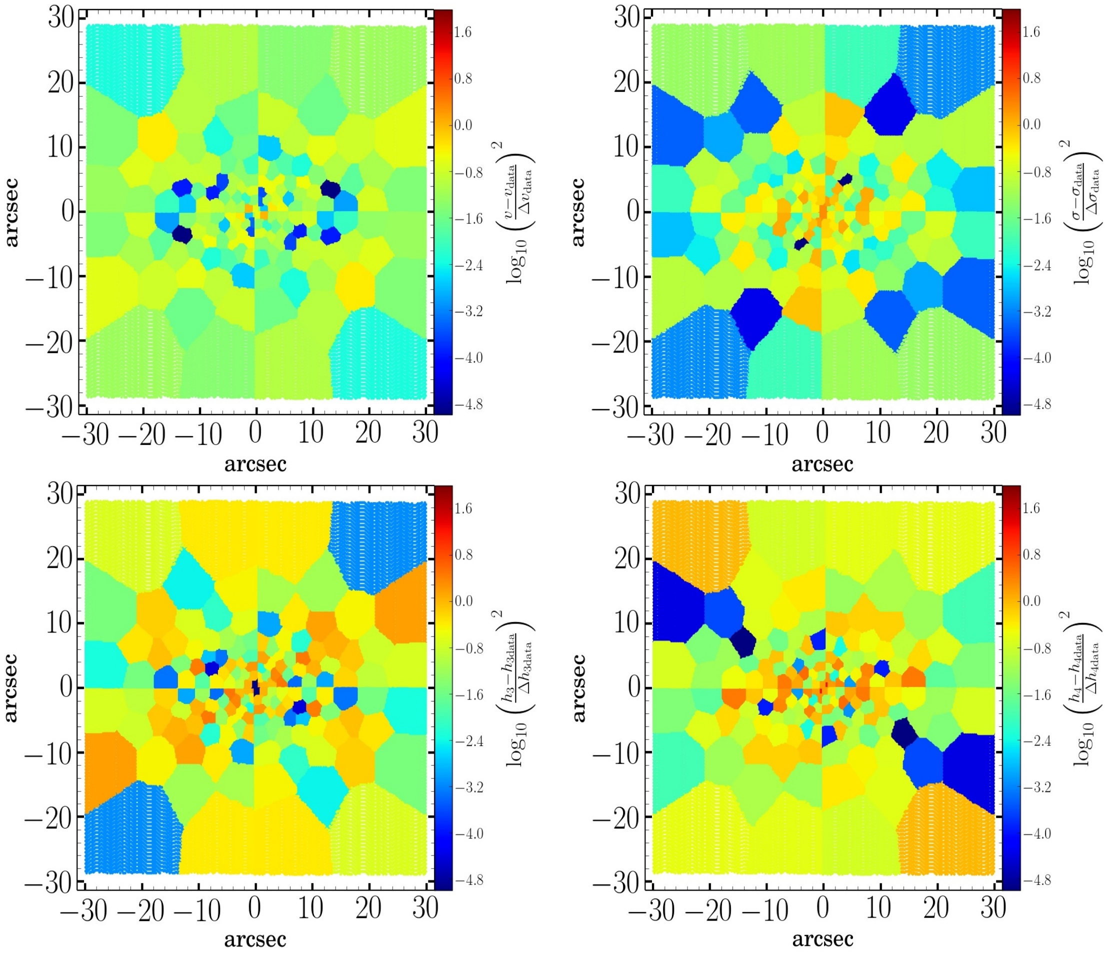

Figure 5.8: Maps of the errors for the best fitting triaxial model of NGC 5419.

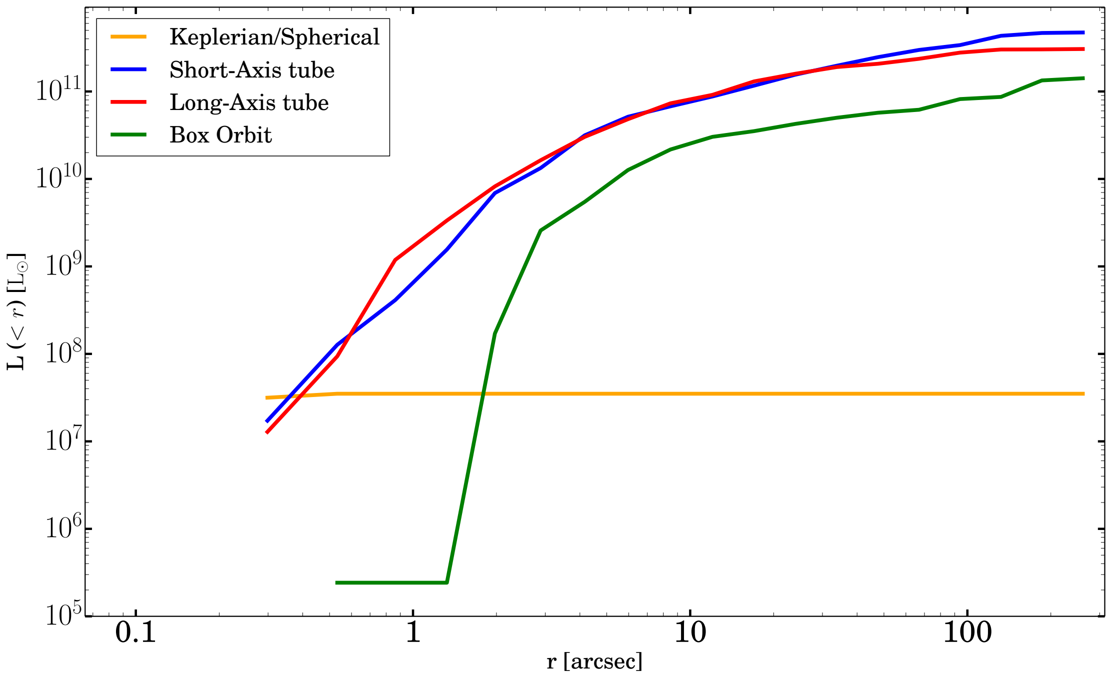

Figure 5.9: Cumulative light carried by the different orbit types in the best fitting triaxial model of NGC 5419 as a function of the average of the peri- and apocentres of the orbits.

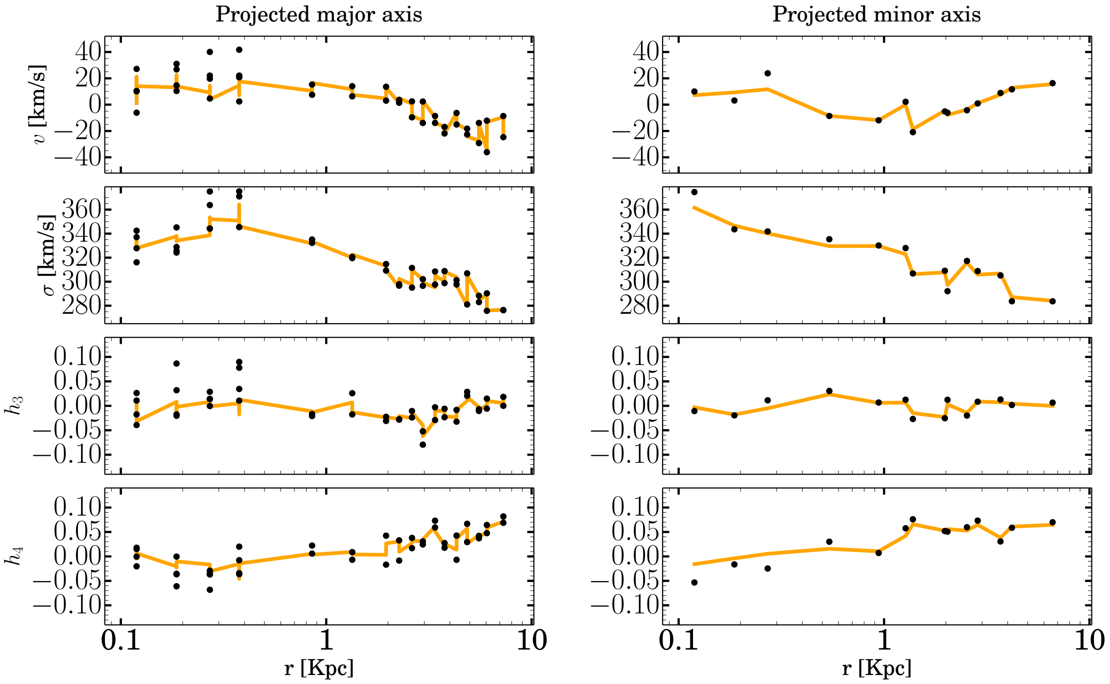

(a) Low regularisation corresponding to $\alpha = 13.42$

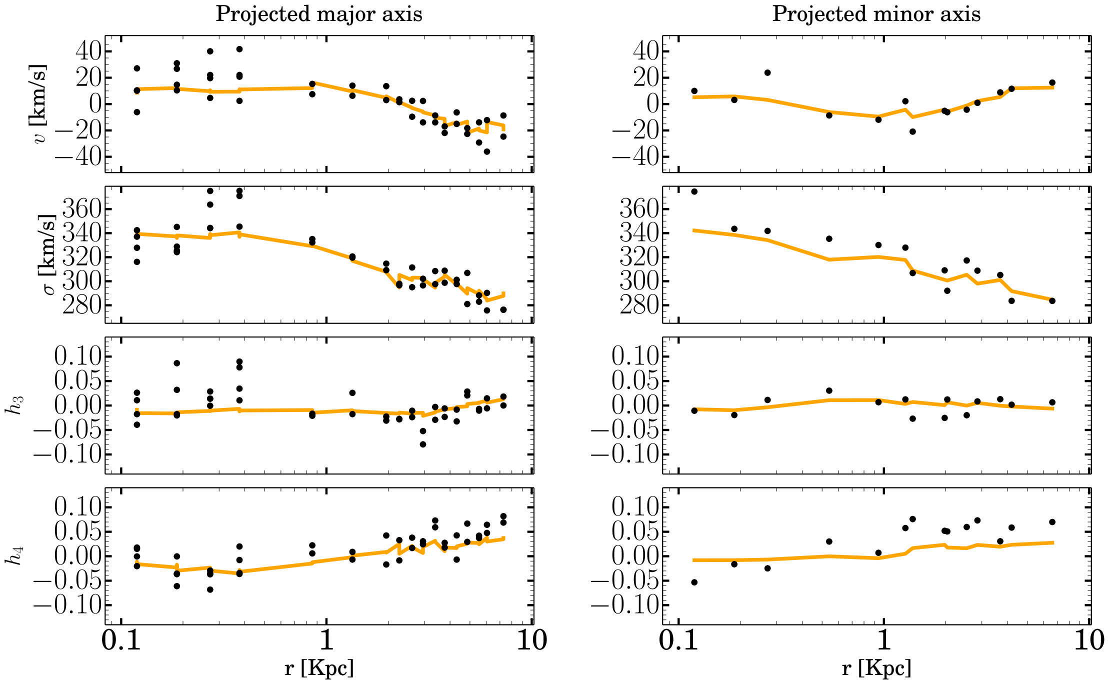

(b) High regularisation corresponding to $\alpha = 1.024\mathrm{E}-04$

Figure 5.10: Fit to the velocity profiles of NGC 5419 along the projected major and minor axes for the best fitting triaxial models. Figure (5.10(a)) portrays the fit corresponding to a low regularisation and Figure (5.10(b)) to a high regularisation. The dots represent the data and the coloured lines the results of the modelling.

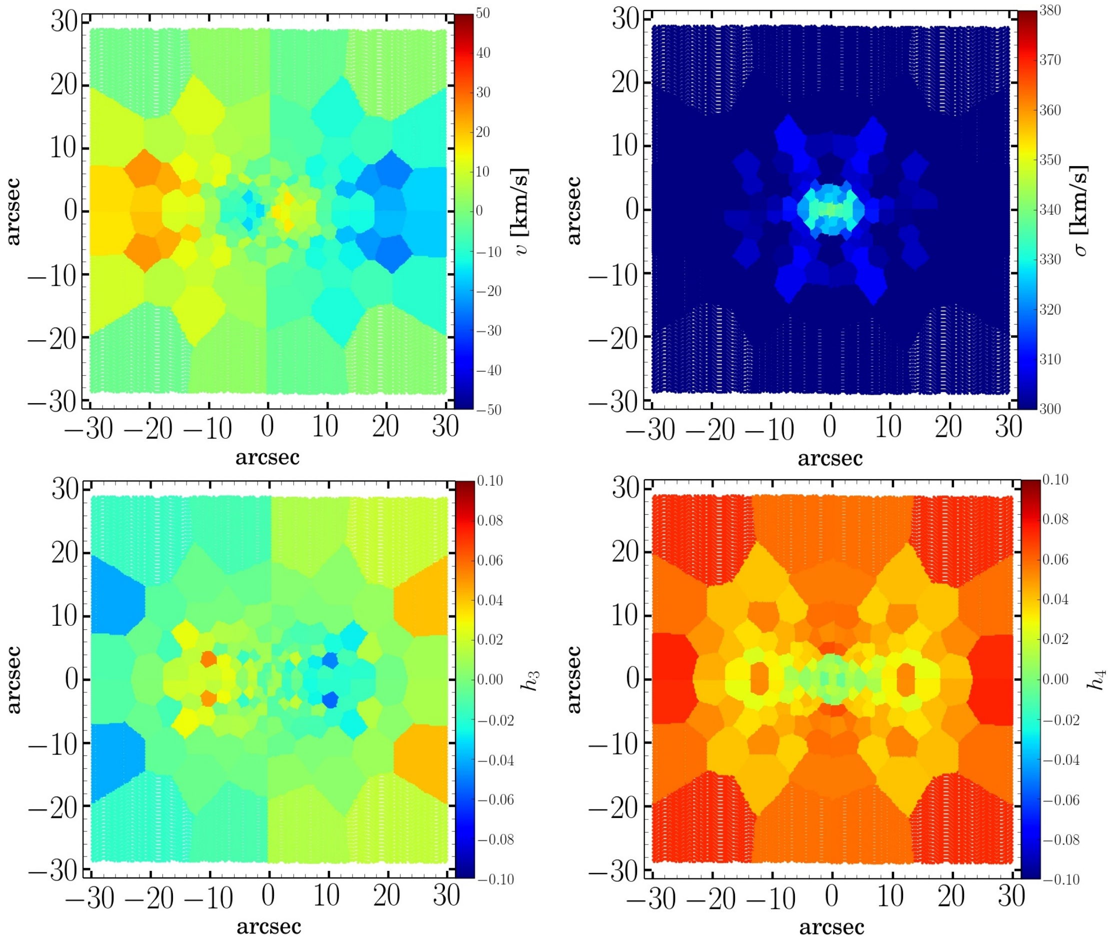

Figure 5.11: Kinematic maps for the best fitting axisymmetric model of NGC 5419.

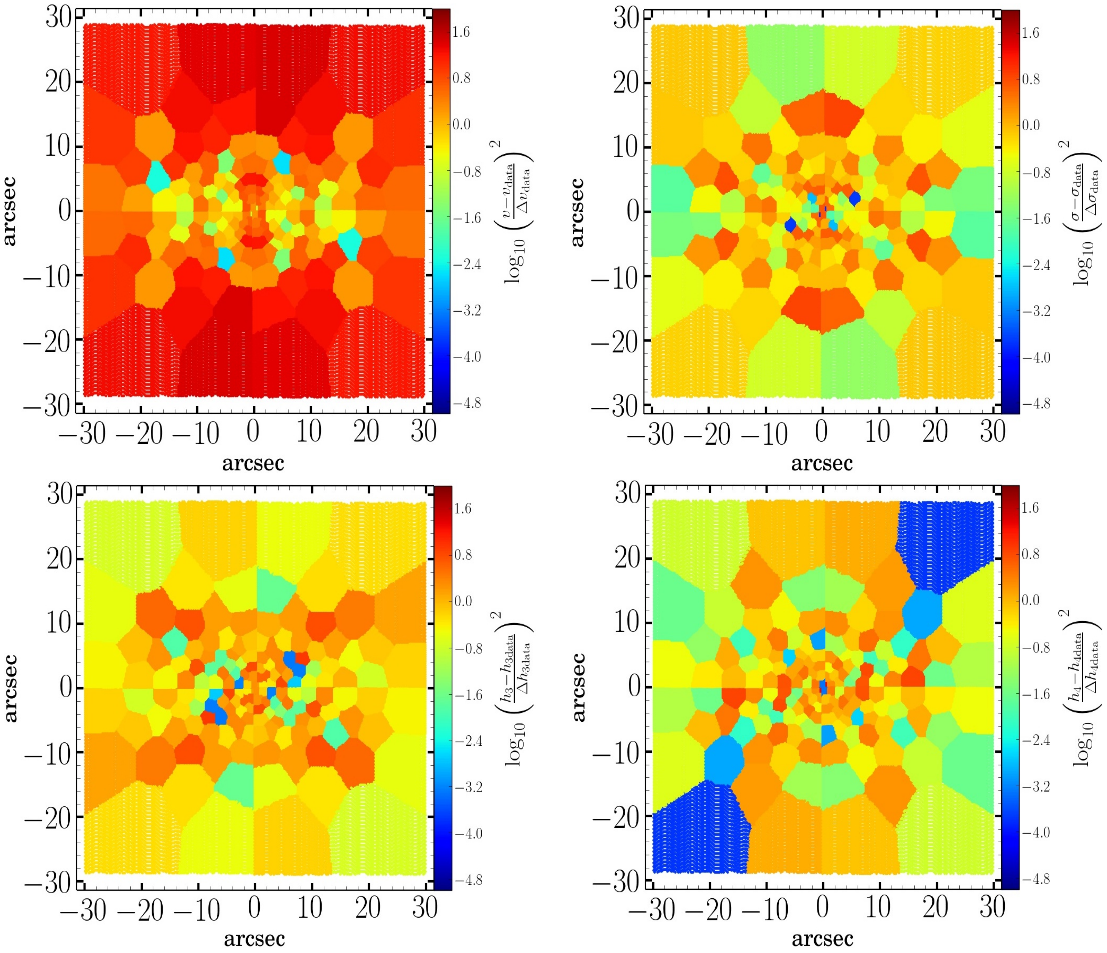

Figure 5.12: Maps of the errors for the best fitting axisymmetric model of NGC 5419.

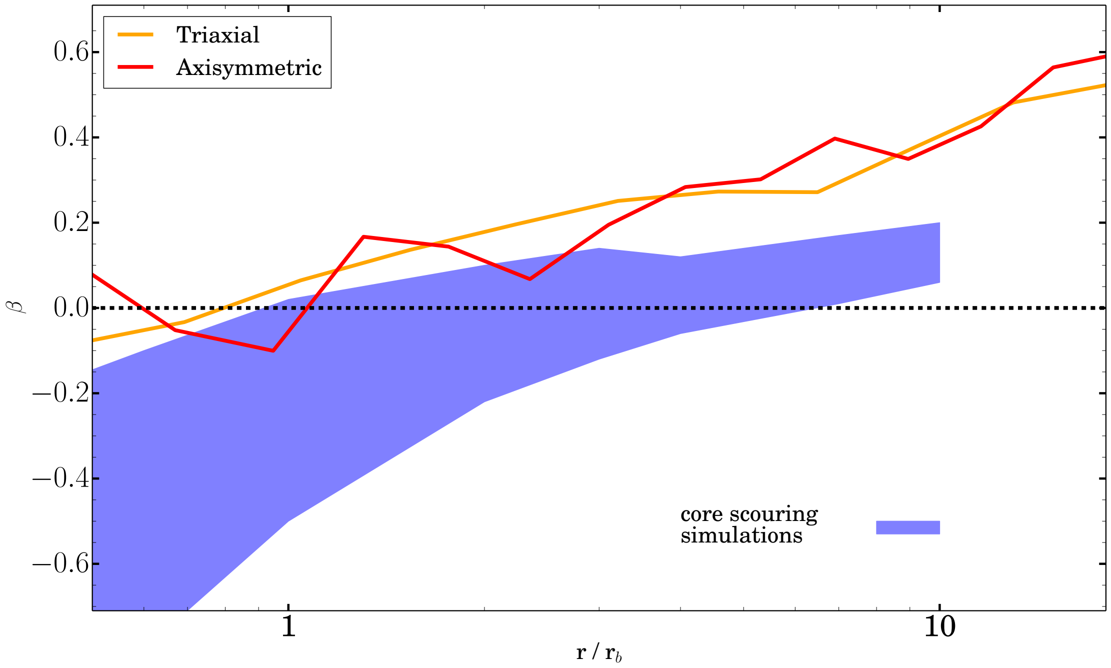

Figure 5.13: Luminosity weighted spherically averaged anisotropy parameter β as a function of the radius for the best fitting triaxial and axisymmetric models of NGC 5419. The radius is scaled by the core radius r_b. The shaded area portrays the prediction of core scouring by equal-mass binary black holes from N-body simulations of Quinlan & Hernquist (1997) and Milosavljević & Merritt (2001).

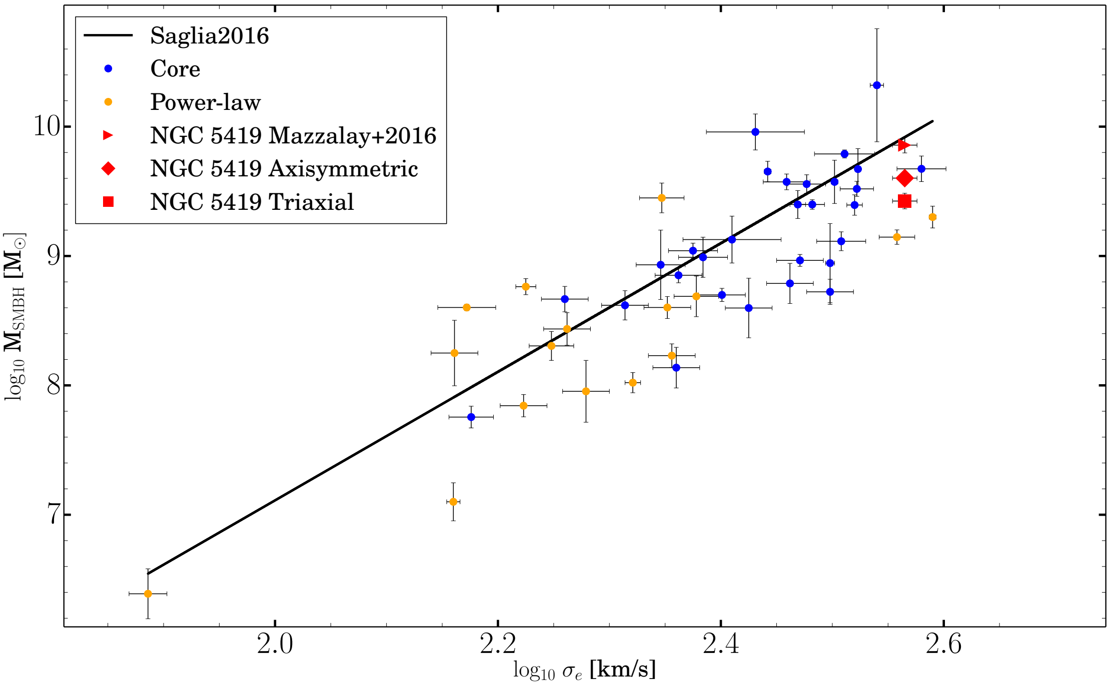

Figure 5.14: Scaling relation between the black hole mass and the velocity dispersion inside $r_{\rm e}$ for core and power-law early-type galaxies from the sample Saglia et al. (2016).

Chapter 6

Conclusions

This work describes the development, testing and first applications of a fully triaxial implementation of the orbit-based Schwarzschild method for the self-consistent stellar dynamical modelling of massive triaxial elliptical galaxies.

The introductory chapter lays the theoretical foundations on which the Thesis is built and deals with the motivational drivers and aims of this project. It also details the theory of collisionless systems and describes their dynamical modelling. A third of all massive elliptical galaxies are thought to be triaxial (Emsellem et al., 2007; Cappellari et al., 2007). They represent the last stage of galaxy evolution and may host the relics of the most massive black holes that are postulated to power the Quasars observed at the early stages of the Universe. Recent studies showed that axisymmetric models are suspected to provide biased reconstructions of the orientation of triaxial galaxies with respect to the line-of-sight and to underestimate their stellar mass-to-light ratio up to 50 % (Thomas et al., 2007a). This results in poorly constrained IMFs and biased black hole masses. These issues justify the implementation of a triaxial version of the Schwarzschild method.

The second chapter describes **SCHERPA**, the **SCH**warzschild m**E**thod for t**R**iaxial early-ty**P**e g**A**laxies, a novel triaxial implementation of the Schwarzschild method. The de-projection of the surface brightness profile is performed by means of the Multi Gaussian Expansion (Cappellari, 2002; van den Bosch et al., 2008). The implementation of the MGE developed over the course of this PhD project has been successfully tested on a toy-model given by the sum of ten Gaussian components. The model has been projected onto the plane of the sky along the viewing direction ($\vartheta = 30\,^\circ, \varphi = 20\,^\circ, \psi = 90\,^\circ$). The implementation recovers accurately the original values of the intrinsic shape parameters σ, p and q of the Gaussian components. Subsequently the chapter delineates how SCHERPA reads-in, interpolates and integrates on appropriate binning grids the input three-dimensional density distribution from Equation (1.27). The calculation of the gravitational potential and force is implemented as an expansion in Spherical Harmonics. The implementation is independent from the method used to de-project the surface brightness profile. The method is tested on spherical and triaxial potentials. It is also compared to a composite potential generated by a triaxial stellar density combined with a central black hole and a spherical dark matter halo. The implementation recovers the theoretical values within 0.6 %. The chapter focuses then on the sampling of the initial conditions and on the integration of the representative stellar orbits. The gravitational potential of galaxies varies from the center to the outskirts. In the center it is dominated by the SMBH and in the outer parts by dark matter. This work provides the first technique able to yield a coverage of phase-space with representative stellar orbits that adapts itself to the changes in the gravitational potential of real galaxies. The number of orbits to be sampled in order to ensure a complete coverage of phase-space may be very large. To shorten the calculation of the orbital time-averaged properties and reduce the number of representative orbits to be computed, the orbits are classified following the scheme of van den Bosch et al. (2008). The orbits are categorised in short- and long-axis tubes (if the orbit conserves respectively the sign of the z-/x-component of the angular momentum), Keplerian/Spherical-like orbits (if the orbit conserves the sign of all components of the angular momentum) and Box orbits (if the orbit does not conserve the sign of any of the components of the angular momentum). The deviations in the conservation of the integrals of motion during the orbit integration is lower than 0.001%. The space of the input mass parameters and viewing angles is explored by means of NOMAD (**N**onlinear **O**ptimisation by **M**esh **A**daptive **D**irect search), a C++ software designed for time-consuming and constrained black-box optimisations (Audet & Dennis, 2006; Le Digabel, 2011). The software investigates the space of the input mass parameters and viewing angles with a direct-search scheme, where the exploration is driven only by the function evaluations. The advantage of NOMAD is its efficiency in converging to the best fitting model regardless of the number of dimensions of the space of parameters. It is also able to execute different function calls in parallel. To shorten each model call, the implementation of SCHERPA has been modified in order to run on multiple computer cores.

The third chapter tests how well SCHERPA estimates the intrinsic kinematics of a spherical and a triaxial reference model while fitting their projected velocity profiles. It validates also the recovery of the values of the input mass parameters and of the viewing angles. The spherical model is an isotropic Hernquist sphere (Hernquist, 1990). It is viewed edge-on and contains no dark matter and no black hole. SCHERPA reproduces within 1.5 % the theoretical values of the intrinsic and projected properties. The verification of the recovery of the mass-to-light ratio and of the orientation is carried out by fitting three noisy realisations of the original velocity profiles, obtained from a Monte-Carlo sampling of the model. For all noisy realisations the best fitting mass-to-light ratio equals the expected value. With respect to the viewing direction, the expectation for a spherical system is that the velocity profiles can be fitted equally well regardless of the line-of-sight. The results from SCHERPA are compared to axisymmetric models obtained using the code from Thomas et al. (2004). While axisymmetric models fit the profiles better for an edge-on view, the models from SCHERPA show no coherent dependence on the viewing angles. This is presumably due to the fact that SCHERPA produces fully three-dimensional models where all four integrals of motion of the spherical potential are sampled. The models have then more freedom in fitting the noisy data. Axisymmetric models are instead two-dimensional. They sample only three integrals of motion, integrate the representative orbits in two-dimensions and smooth them in the azimuthal direction. Face-on axisymmetric models are such that the position angle on the sky corresponds to the intrinsic azimuthal angle, as a function of which they are constant by construction. The triaxial reference model is a four million unequal-mass particles model produced by I. Soeldner-Rembold starting from an initial spherical N-body model. It contains no dark matter and no black hole. The initial model is evolved self-consistently by means of the N-body made-to-measure code NMAGIC (De Lorenzi et al., 2007). NMAGIC squashes the model rigidly along the principal axes. It enforces a triaxiality of $T = \frac{1-p^2}{1-q^2} \approx 0.55$ with $q = 0.7$ and $p = 0.85$. SCHERPA is able to reproduce the input mass-to-light ratio $\mathrm{M/L} = 1\ \frac{\mathrm{M}_\odot}{\mathrm{L}_\odot}$ within 2 % accuracy for all the projections considered and recovers the intrinsic kinematics within 4.5 %. This accuracy is similar to the one reported by Van De Ven et al. (2008) on triaxial separable Abel models. In the end a search in the parameter space spanned by the mass-to-light ratio and viewing angles is carried out with NOMAD by fitting the velocity profiles obtained for the line-of-sight ($\vartheta = 45\,^\circ, \varphi = 45\,^\circ, \psi = 112\,^\circ$). The density comes from an MGE de-projection. SCHERPA recovers the mass-to-light ratio within 0.6 %, the viewing angles within $7\,^\circ$ of the input values and the intrinsic shape within 6 %. The accuracy on the reconstruction of the intrinsic shape is better than the one reported by van den Bosch & Van De Ven (2009) on triaxial separable Abel models.

The fourth chapter reports on the three-dimensional axisymmetric modelling performed with SCHERPA of the massive early-type galaxy NGC 1600. The aim of the chapter is to test SCHERPA in the axisymmetric regime and to verify how the code behaves when fitting the data of a real galaxy. The galaxy has boxy isophotes, an effective radius $r_e = 14.85$ Kpc and one of the largest central cores in the surface brightness profile (Lauer et al., 2007). The galaxy harbours one of the black holes with the highest mass. The galaxy shows also a predominance of stars on tangential orbits inside the core radius and a predominance of radial orbits for larger radii. NGC 1600 has been observed as part of the MASSIVE survey (Ma et al., 2014). The space of parameters spanned by the black hole mass, mass-to-light ratio and two dark matter halo parameters is searched for the best fitting model with NOMAD. SCHERPA confirms that the galaxy hosts a black hole with mass larger than $10^{10}\ \mathrm{M}_\odot$ and recovers the core scouring signature. This suggests that NGC 1600 presumably hosts a dormant descendant of the massive black holes powering distant Quasars. The best fitting input mass parameters are within 20 % of the values found in Thomas et al. (2016). The black hole and mass-to-light ratio are respectively 20 % smaller and larger than previous estimates. The black hole mass decreases in order to compensate for the higher stellar mass (see Section 1.6). The comparison between the luminosity weighted spherically averaged anisotropy profiles of the models from SCHERPA and Thomas et al. (2016) hints to the fact that a smaller black hole mass translates in a system that is less anisotropic. Core scouring changes the orbital distribution in galaxies. The black hole binary slingshots outwards stars on radial orbits that come close to it. Intuitively it is then fair to expect that a less massive black hole will scouter less radial orbits out. A more conclusive answer can be drawn from the analysis of simulated galaxy mergers that explore a wide range of initial conditions.

The fifth chapter reports on the first triaxial model performed with SCHERPA of the massive early-type galaxy NGC 5419. The galaxy rotates slowly, has boxy isophotes, an effective radius $r_e = 14.66$ Kpc (Saglia et al., 2016) and an isophotal twist of $\Delta\text{PA} \approx 20\,^\circ$. HST images of the center ($r < 0.4$ arcsec) of the galaxy from Lauer et al. (2005) show evidence of a double nucleus. The two nuclei correspond presumably to two SMBHs separated in projection by 70 pc (Mazzalay et al., 2016). The center counter-rotates with respect to the outer parts of the galaxy. The low rotation, the boxy isophotes, the isophotal twist and the KDC suggest that NGC 5419 is triaxial. This makes the galaxy an interesting object to be modelled with SCHERPA. The space of parameters spanned by the black hole mass, mass-to-light ratio and the two parameters of a spherical dark matter halo is searched for the best fitting model with NOMAD. As an initial test the line-of-sight is set to $(\vartheta = 63\,^\circ, \varphi = 33\,^\circ, \psi = 124\,^\circ)$. The viewing direction is close to the intrinsic major axis of the galaxy. It corresponds to the roundest of the allowed triaxial intrinsic shapes. The best fitting model corresponds to a black hole with mass $\text{M}_{\text{SMBH}} = 2.659^{+0.041}_{-0.060} \cdot 10^9$ $\text{M}_\odot$ and an enclosed stellar mass within the core radius of $\text{M}_{\text{star,triaxial}}(< r_b) = 6.8 \cdot 10^9$ $\text{M}_\odot$. Keplerian/Spherical-like orbits carry 0.4 % of the light in the region inside the core radius, where instead box orbits play a negligible role. The presence of a massive black hole renders in fact box orbits unstable. Triaxial models from van den Bosch & De Zeeuw (2010) for the early-type galaxy NGC 3379 are instead dominated by box orbits inside the sphere of influence of the black hole (55 % of all orbits). The triaxial best fitting model reproduces accurately the counter-rotation. This is achieved from the interplay in projection of the major families of tube orbits characteristic of a triaxial potential. In fact the short- and long-axis tubes carry respectively about 46 % and 43 % of the total light inside the region of the KDC. Box orbits carry the remaining ≈ 11 % of the light with a small contribution coming from Keplerian/Spherical-like orbits (less than 0.3 %). The results from SCHERPA are compared to an axisymmetric modelling of the galaxy performed with the code from Thomas et al. (2004). The best fitting axisymmetric estimate of the black hole mass overestimates the triaxial value by approximately 50%. The axisymmetric enclosed stellar mass inside the core radius r_b is also ≈ 15 % larger with respect to the triaxial result. This is expected given the fact the galaxy is observed close to its intrinsic major axis. Probably more modelling along different line-of-sights is needed in order to understand if these overestimations are systematic. For the moment it is possible to say that axisymmetric models overestimate the black hole mass of NGC 5419. This is the opposite of what reported in van den Bosch & De Zeeuw (2010) for NGC 3379, where the black hole mass from triaxial models is claimed to be almost two times larger than previous axisymmetric estimates from Shapiro et al. (2006). The anisotropy profiles from the triaxial and axisymmetric best fitting model are not compatible with the core scouring predictions. It seems that the core scouring signature in the anisotropy profile has not yet fully emerged in NGC 5419 while the photometric core has already formed. This would suggest that the formation of the photometric core precedes that of the anisotropy (Merritt, 2013). The scaling relation between the black hole mass and the velocity dispersion inside r_e overpredicts the black hole mass of NGC 5419. It is too early however to speculate what the overall effect on black hole demographics will be. For instance the black hole masses of triaxial galaxies could scatter around the scaling relation. It may also be that NGC 5419 is an outlier. Only the triaxial stellar dynamical modelling of more galaxies will allow to say something more conclusive.

6.1 Future prospects

This work describes the development, testing and first applications of a fully triaxial implementation of the orbit-based Schwarzschild method for the self-consistent stellar dynamical modelling of massive triaxial elliptical galaxies. In the near future it will be tested how well SCHERPA estimates the intrinsic kinematics and the black hole mass of an N-body model containing a central SMBH. Moreover the modelling of NGC 5419 will be completed allowing for different viewing directions and relaxing the hypothesis of a spherical halo. It will be investigated what the effects of these changes will be primarily on the mass of the central black hole. A long term goal will be the implementation of a non-parametric method for the triaxial de-projection of the surface brightness profile. SCHERPA will then be applied to other massive early-type galaxies that can be observationally categorised as triaxial. Another interesting application of the code will be the modelling of galaxies that are observationally classified as axisymmetric (like NGC 1600). This will allow to infer the occurrence of triaxiality in massive elliptical galaxies. Another aim of these studies will be to better constrain the demographics of black holes and to improve the precision in the scaling relations with their host galaxies. As discussed above, the only two triaxial estimates of black hole masses yield opposite results with respect to previous axisymmetric models. It will be interesting to verify if black holes masses scatter around the scaling relation or if they are consistently below it as for NGC 5419. The studies will make use of increasingly higher resolution data coming in the next decade (for example from instruments as MICADO mounted on the Extremely Large Telescope). This will allow to close the circle on the origin and the formation of early-type galaxies.

Appendix A

Code specifications

SCHERPA is a $\approx$ 14.000 lines code. It uses the standard Intel compiler *ifort*. The I/O rate of the code is maximum during the calculation of the orbit library and its storage on the local disk. The I/O rate is usually on the order of 5 GB per core per hour. The final output files are in ASCII format. They have sizes of about 10 MB. As mention in Section (2.1), SCHERPA is implemented in FORTRAN in the F90/F95 standard (Brainerd et al., 1996). Fortran is a portable programming language specifically targeted at scientific and engineering computing. It is equipped with several legacy libraries [1]. The Fortran 90/95 standard contains all the properties of previous versions together with new useful tools. The most important ones used in this work are:

- **Constructs**: the GO TO has been substituted by the CYCLE and EXIT statements for the DO construct. Moreover it is possible to name tag the DO and IF constructs and the CYCLE and EXIT statements. These modifications are particularly useful whenever several constructs are nested;

- **Precision**: it is possible to specify the precision of a variable in a more portable way using the intrinsic functions SELECTED_INT_KIND and SELECTED_REAL_KIND. This makes numeric representations independent from the specifications of the machine on which the code is compiled and executed;

- **Array/Matrix processing**: the operations (sum, subtraction and so on) introduced for scalars are generalisable to arrays and matrices. It is possible to access only subscripts of arrays and matrices. Functions can be array-valued. The standard introduces also intrinsic procedures aimed for example at computing the sum of the elements of an array/matrix or its minimum and maximum values.

---

[1] The link `http://fortranwiki.org/fortran/show/Libraries` provides a list of some of the available libraries.

- **Dynamic allocation of memory**: memory can be allocated dynamically in the Fortran 90/95 standard. This allowed to reduce the memory requirements of SCHERPA up to 30 %.
- **Procedure arguments**: the arguments of subroutines can be made optional or keyword-like. This allows to list the procedure arguments in any order or to specify default values for missing optional arguments;
- **Procedure interface blocks**: interface blocks are important because they allow the compiler to check if the arguments in the procedure call match with those provided in the procedure definition. They guarantee the integrity of the procedure call and are particularly useful when calling procedures of external libraries;
- **Recursive procedures**: the new standard introduces recursive procedures. They simplify the implementation of intrinsically recursive operations as the calculation of the Fibonacci numbers and the factorial;
- **I/O specifications**: it is possible to specify the INTENT of the dummy arguments of the procedures. This allows to avoid unwanted modifications to the values of the input variables. The unit and the format statement of a given input/output file can be name-taged. This is a simplification with respect to Fortran 77 where only numerical tags were allowed;
- **Modules**: Modules make programs easier to comprehend and to maintain. They subdivide codes into coherent program units. Each unit groups logically related variable declarations, procedures and procedure interfaces as for example those for the calculation of the gravitational potential and forces. The information contained in the specification part (i.e. what precedes the CONTAINS statement) is valid for all procedures listed in the module. The information in a module can be accessed from another program unit by means of the USE statement.

Together with the program units detailed in Section (2.1), SCHERPA constitutes also of subsidiary modules devoted to the definition of the global variables and parameters (**mod_scherpadefs.f90**) and the implementation (**mod_nr.f90** and **mod_nrutil.f90**) of the mathematical routines from (Press et al., 1996). Module **mod_changecoord.f90** contains the routines for transforming the components of vectors from one coordinate system to another. Module **mod_polyfunc.f90** is responsible for the calculation of the Legendre and Hermite polynomials. Module **mod_binfunc_lib.f90** implements the binning functions for the spatial grids. Module **mod_binfunc_mod.f90** is devoted to the binning functions used to re-bin three-dimensional arrays into mono-dimensional ones.

Appendix B

Mathematical annotations

B.1 De-projection

The de-projection follows as

$$\begin{pmatrix} x \\ y \\ z \end{pmatrix} = \mathbf{R^{-1}} \cdot \mathbf{P^{-1}} \cdot \begin{pmatrix} x' \\ y' \\ z' \end{pmatrix} \tag{B.1}$$

with

$$\mathbf{P^{-1}} = \begin{pmatrix} -\sin\varphi & -\cos\varphi\cos\vartheta & \cos\varphi\sin\vartheta \\ \cos\varphi & -\sin\varphi\cos\vartheta & \sin\varphi\sin\vartheta \\ 0 & \sin\vartheta & \cos\vartheta \end{pmatrix} \tag{B.2}$$

$$\mathbf{R^{-1}} = \begin{pmatrix} \sin\psi & \cos\psi & 0 \\ -\cos\psi & \sin\psi & 0 \\ 0 & 0 & 1 \end{pmatrix} \tag{B.3}$$

The appendix completes what detailed in Section (2.2.2).

B.2 Coordinate transformation

The components of a vector $\mathbf{v}$ in the spherical coordinates (r, θ, ϕ) used in this thesis ($\theta = 0$ identifies the equatorial plane) are transformed in cartesian coordinates as

$$\begin{aligned} v_x &= v_r \cos(\theta)\cos(\phi) - v_\theta \sin(\theta)\cos(\phi) - v_\phi \sin(\phi) \\ v_y &= v_r \cos(\theta)\sin(\phi) - v_\theta \sin(\theta)\sin(\phi) + v_\phi \cos(\phi) \\ v_z &= v_r \sin(\theta) + v_\theta \cos(\theta). \end{aligned} \tag{B.4}$$

The opposite transformation reads

$$\begin{aligned} v_r &= v_x \cos(\theta)\cos(\phi) + v_y \cos(\theta)\sin(\phi) + v_z \sin(\theta) \\ v_\theta &= -v_x \sin(\theta)\cos(\phi) - v_y \sin(\theta)\sin(\phi) + v_z \cos(\theta) \\ v_\phi &= -v_x \sin(\phi) + v_y \cos(\phi). \end{aligned} \tag{B.5}$$

B.3 Maximum entropy technique

This appendix completes what detailed in Section (2.6.1) and describes how the orbital weights are determined from the maximisation of the entropy-like quantity $\hat{S}$ defined in Equation (2.53) as

$$\hat{S} \equiv S - \alpha\chi^2 \tag{B.6}$$

where the term S is the Boltzmann entropy from Equation (2.54) and

$$\chi^2 \equiv \sum_{b=1}^{N_\mathrm{losvd}} \sum_{g=1}^{N_\mathrm{vel}} \left(\frac{\mathrm{LOSVD}^{b,g}_\mathrm{model} - \mathrm{LOSVD}^{b,g}_\mathrm{data}}{\Delta\mathrm{LOSVD}^{b,g}_\mathrm{data}} \right)^2 . \tag{B.7}$$

It measures the deviations among the model and data LOSVDs in the projected bin $1 \le b \le N_\mathrm{x,sky} \times N_\mathrm{y,sky}$ and in the velocity bin $1 \le g \le N_\mathrm{vel}$. The model predictions $\mathbf{LOSVD}_\mathrm{model}$ are given by

$$\mathrm{LOSVD}^{b,g}_\mathrm{model} = \sum_{i=1}^{N_\mathrm{orbit}} w_i \; \mathrm{LOSVD}^{b,g}_i \tag{B.8}$$

where w_i is the orbital weight. $\mathbf{LOSVD}_\mathrm{data}$ and $\mathbf{LOSVD}_\mathrm{model}$ can be seen as vectors of $N_\mathrm{losvd} \times N_\mathrm{vel}$ elements and so

$$\mathbf{LOSVD}_\mathrm{model} = \mathbf{LOSVD}_\mathrm{orbit} \cdot \mathbf{w} \tag{B.9}$$

with $\mathbf{LOSVD}_\mathrm{orbit}$ being a matrix with $N_\mathrm{losvd} \times N_\mathrm{vel}$ rows and N_orbit columns. Vector $\mathbf{w}$ is the vector of the orbital weights. It has N_orbit elements. The model predictions for the total luminosity can be written as

$$\mathbf{LIGHT}_\mathrm{model} = \mathbf{LIGHT}_\mathrm{orbit} \cdot \mathbf{w} \tag{B.10}$$

where $\mathbf{LIGHT}_\mathrm{model}$ is a vector of N_bin elements and $\mathbf{LIGHT}_\mathrm{orbit}$ a matrix with N_bin rows and N_orbit columns. N_bin is the number of bins in which the three-dimensional space is organised.

$\hat{S}$ is a function of the regularisation parameter α. Therefore the maximisation of $\hat{S}$ is iterated for different values of α until the value of the χ^2 is stable around its minimum (Thomas et al., 2005b). For each value of the regularisation parameter, the maximisation of $\hat{S}$ is performed by the method of the Lagrange multipliers. The Lagrangian function is

$$\mathcal{L}(\mathbf{w}, \mathbf{y}, \boldsymbol{\lambda}) = \hat{S}(\mathbf{w}, \mathbf{y}) - \boldsymbol{\lambda} \cdot \mathbf{g}(\mathbf{w}, \mathbf{y}) \tag{B.11}$$

where $\boldsymbol{\lambda}$ is the $N_\mathrm{bin} + N_\mathrm{losvd} \times N_\mathrm{vel}$ vector of the Lagrangian multipliers. Vector $\mathbf{y}$ is the $N_\mathrm{losvd} \times N_\mathrm{vel}$ vector of the kinematic predictions of the model and reads

$$\mathbf{y} \equiv \mathbf{LOSVD}_\mathrm{model} - \mathbf{LOSVD}_\mathrm{data}. \tag{B.12}$$

Vectors $\mathbf{y}$ and $\mathbf{w}$ are treated as independent variables. The dependence $\mathbf{y} = \mathbf{y}(\mathbf{w})$ is implied. Function $\mathbf{g}(\mathbf{w}, \mathbf{y})$ encloses the photometric and kinematic constraints. It reads

$$\mathbf{g}(\mathbf{w}, \mathbf{y}) \equiv \begin{pmatrix} \mathbf{LIGHT}_{\text{data}} \\ \mathbf{LOSVD}_{\text{data}} \end{pmatrix} - \mathbf{C} \cdot \begin{pmatrix} \mathbf{w} \\ \mathbf{y} \end{pmatrix} \tag{B.13}$$

where $\mathbf{C}$ is a matrix with $n_{\text{rows}} = N_{\text{bin}} + N_{\text{losvd}} \times N_{\text{vel}}$ and $n_{\text{columns}} = N_{\text{orbit}} + N_{\text{losvd}} \times N_{\text{vel}}$. It reads

$$\mathbf{C} = \begin{pmatrix} \mathbf{LIGHT}_{\text{orbit}} & \mathbf{0} \\ \mathbf{LOSVD}_{\text{orbit}} & \mathbf{1} \end{pmatrix} . \tag{B.14}$$

The Lagrange multipliers are the solution of

$$\overrightarrow{\nabla}_{\mathbf{w},\mathbf{y},\lambda}\, \mathcal{L}(\mathbf{w}, \mathbf{y}, \boldsymbol{\lambda}) \equiv 0 \Longrightarrow \begin{array}{l} \overrightarrow{\nabla}_{\mathbf{w},\mathbf{y}}\, \hat{S}(\mathbf{w}, \mathbf{y}) - \boldsymbol{\lambda} \cdot \overrightarrow{\nabla}_{\mathbf{w},\mathbf{y}}\, \mathbf{g}(\mathbf{w}, \mathbf{y}) \equiv 0 \\ \mathbf{g}(\mathbf{w}, \mathbf{y}) \equiv 0. \end{array} \tag{B.15}$$

which can be rewritten as

$$\overrightarrow{\nabla}_{\mathbf{w},\mathbf{y},\boldsymbol{\lambda}}\, \mathcal{L}(\mathbf{w}, \mathbf{y}, \boldsymbol{\lambda}) = \overrightarrow{\nabla}_{\mathbf{w},\mathbf{y}} \hat{S}(\mathbf{w}, \mathbf{y}) - \mathbf{C}^t \cdot \boldsymbol{\lambda} \equiv 0. \tag{B.16}$$

Given its non-linearity, Equation (B.16) is solved with the Newton's method

$$\begin{pmatrix} \Delta\mathbf{w} \\ \Delta\mathbf{y} \end{pmatrix} = -\mathbf{f} \cdot \frac{1}{\overrightarrow{\nabla}_{\mathbf{w},\mathbf{y}} \mathbf{f}}. \tag{B.17}$$

Substituting $\mathbf{f} = \overrightarrow{\nabla}_{\mathbf{w},\mathbf{y}} \hat{S}(\mathbf{w}, \mathbf{y}) - \mathbf{C}^t \cdot \boldsymbol{\lambda}$ leads to

$$\begin{pmatrix} \Delta\mathbf{w} \\ \Delta\mathbf{y} \end{pmatrix} = -\left(\overrightarrow{\nabla}_{\mathbf{w},\mathbf{y}} \hat{S} - \mathbf{C}^t \cdot \boldsymbol{\lambda}\right) \cdot \frac{1}{\Delta_{\mathbf{w},\mathbf{y}} \hat{S}} \tag{B.18}$$

where $\Delta_{\mathbf{w},\mathbf{y}} \hat{S}$ is the Laplacian of $\hat{S}$. Given

$$\begin{pmatrix} \Delta\mathbf{LIGHT}_{\text{data}} \\ \Delta\mathbf{LOSVD}_{\text{data}} \end{pmatrix} = \mathbf{C} \cdot \begin{pmatrix} \Delta\mathbf{w} \\ \Delta\mathbf{y} \end{pmatrix} , \tag{B.19}$$

Equation (B.18) becomes

$$\mathbf{A} \cdot \boldsymbol{\lambda} = \begin{pmatrix} \Delta\mathbf{LIGHT}_{\text{data}} \\ \Delta\mathbf{LOSVD}_{\text{data}} \end{pmatrix} + \mathbf{C} \cdot \overrightarrow{\nabla}_{\mathbf{w},\mathbf{y}} \hat{S} \cdot \frac{1}{\Delta_{\mathbf{w},\mathbf{y}} \hat{S}} , \tag{B.20}$$

$$\mathbf{A} = \mathbf{C} \cdot \mathbf{C}^t \cdot \frac{1}{\Delta_{\mathbf{w},\mathbf{y}} \hat{S}} . \tag{B.21}$$

The square-matrix $\mathbf{A}$ has dimension $n = N_{\text{bin}} + N_{\text{losvd}} \times N_{\text{vel}}$. It is inverted to yield the Lagrangian multipliers. The multipliers are then substituted in Equation (B.18) to adjust the weights under the requirement

$$\sum_{i=1}^{N_{\text{orbit}}} w_i = 1. \tag{B.22}$$

The entropy and its derivatives are computed in the routine **entropy()**. The orbital weights are adjusted in routine **spear()**, where the linear algebra operations are performed by means of the routines from the LAPACK library (`http://www.netlib.org/lapack/`).

Bibliography

Aarseth S.J. & Binney J., 1978, *On the relaxation of galaxies and clusters from aspherical initial conditions*, Monthly Notices of the Royal Astronomical Society, 185, 2, 227. Cited on page 16.

Abramowitz M. & Stegun I.A., 1972, *Handbook of Mathematical Functions: With Formulas, Graphs, and Mathematical Tables*, Courier Dover Publications, New York. Cited on page 50.

Arnold V., 1989, *Mathematical Methods of Classical Mechanics*, volume 80, Springer New York. Cited on pages 21 and 25.

Audet C. & Dennis J.E., 2006, *Mesh Adaptive Direct Search Algorithms for Constrained Optimization*, SIAM Journal on Optimization, 17, 1, 188. Cited on pages 67 and 132.

Bacon R., Bauer S.M., Bower R. et al., 2004, *The second generation VLT instrument MUSE: Science drivers and instrument design*, Proceedings of SPIE - The International Society for Optical Engineering, 5492, PART 2, 1145. Cited on page 117.

Baes M., Dejonghe H. & Buyle P., 2005, *The dynamical structure of isotropic spherical galaxies with a central black hole*, Astronomy and Astrophysics, 432, 2, 411. Cited on page 70.

Balmaverde B., Capetti A. & Grandi P., 2006, *The Chandra view of the 3C/FR I sample of low luminosity radio-galaxies*, Astronomy and Astrophysics, 451, 1, 35. Cited on page 111.

Barnes J.E., 1992, *Transformations of galaxies. I - Mergers of equal-mass stellar disks*, The Astrophysical Journal, 393, 484. Cited on page 16.

Barth A.J., Ho L.C. & Sargent W.L.W., 2002, *A Study of the Direct Fitting Method for Measurement of Galaxy Velocity Dispersions*, The Astronomical Journal, 124, 5, 2607. Cited on page 106.

Beifiori A., Mendel J.T., Chan J.C.C. et al., 2017, *The KMOS Cluster Survey (KCS) I: The fundamental plane and the formation ages of cluster galaxies at redshift $1.4<z<1.6$*, The Astrophysical Journal, 846, 2, 25. Cited on page 13.

Bender R., 1988a, *Rotating and counter-rotating cores in elliptical galaxies*, Astronomy and Astrophysics, 202, L5. Cited on pages 6 and 16.

Bender R., 1988b, *Velocity anisotropies and isophote shapes in elliptical galaxies*, Astronomy and Astrophysics, 193, L7. Cited on page 5.

Bender R., 1990, *Unraveling the kinematics of early-type galaxies - Presentation of a new method and its application to NGC4621*, Astronomy and Astrophysics, 229, 441. Cited on page 9.

Bender R., Burstein D. & Faber S.M., 1993, *Dynamically hot galaxies. II - Global stellar populations*, The Astrophysical Journal, 411, 153. Cited on page 14.

Bender R., Doebereiner S. & Moellenhoff C., 1988, *Isophote shapes of elliptical galaxies. I - The data*, Astronomy and Astrophysics Supplement Series, 74, 385. Cited on pages xv, 5, and 6.

Bender R. & Moellenhoff C., 1987, *Morphological analysis of massive early-type galaxies in the Virgo cluster*, Astronomy and Astrophysics, 177, 71 . Cited on pages xxi, xxiii, 5, 98, and 112.

Bender R., Saglia R.P. & Gerhard O.E., 1994, *Line-of-Sight Velocity Distributions of Elliptical Galaxies*, Monthly Notices of the Royal Astronomical Society, 269, 3, 785. Cited on pages xv, 9, 11, 22, 105, and 108.

Bender R., Saglia R.P., Ziegler B. et al., 1998, *Exploring Cluster Elliptical Galaxies as Cosmological Standard Rods*, The Astrophysical Journal, 493, 529. Cited on page 13.

Bender R. & Surma P., 1992, *Mg2 line-strength profiles of elliptical galaxies with kinematically decoupled cores*, Astronomy and Astrophysics, 258, 250. Cited on page 6.

Bender R., Surma P., Doebereiner S., Moellenhoff C. & Madejsky R., 1989, *Isophote shapes of elliptical galaxies. II - Correlations with global optical, radio and X-ray properties*, Astronomy and Astrophysics, 217, 35. Cited on page 5.

Bertin G., 2014, *Dynamics of galaxies: Second Edition*, Cambridge University Press. Cited on page 19.

Bertin G., Saglia R.P. & Stiavelli M., 1992, *Elliptical galaxies with dark matter. I - Self-consistent models. II - Optimal luminous-dark matter decomposition for a sample of bright objects*, The Astrophysical Journal, 384, 423. Cited on page 22.

Bertola F., Bettoni D., Danziger J. et al., 1991, *Testing the gravitational field in elliptical galaxies - NGC 5077*, The Astrophysical Journal, 373, 369. Cited on page 36.

Bertola F. & Capaccioli M., 1975, *Dynamics of early type galaxies. I - The rotation curve of the elliptical galaxy NGC 4697*, The Astrophysical Journal, 200, 439. Cited on page 9.

Bertola F. & Galletta G., 1979, *Ellipticity and twisting of isophotes in elliptical galaxies*, Astronomy and Astrophysics, 77, 363. Cited on page 15.

Binney J., 1978a, *Elliptical galaxies - Prolate, oblate or triaxial*, Comments on Astrophysics, 8, 27. Cited on page 15.

Binney J., 1978b, *On the rotation of elliptical galaxies*, Monthly Notices of the Royal Astronomical Society, 183, 501. Cited on pages xv, 10, and 12.

Binney J., 1982, *Does Jeans' theorem apply only to spherical systems?*, Monthly Notices of the Royal Astronomical Society, 201, 1, 15. Cited on page 20.

Binney J., 1985, *Testing for triaxiality with kinematic data*, Monthly Notices of the Royal Astronomical Society, 212, 4, 767. Cited on page 33.

Binney J., 2005, *Rotation and anisotropy of galaxies revisited*, Monthly Notices of the Royal Astronomical Society, 363, 3, 937. Cited on page 10.

Binney J., Davies R.L. & Illingworth G.D., 1990, *Velocity mapping and models of the elliptical galaxies NGC 720, NGC 1052, and NGC 4697*, The Astrophysical Journal, 361, 78. Cited on page 21.

Binney J. & de Vaucouleurs G., 1981, *The apparent and true ellipticities of galaxies of different Hubble types in the Second Reference Catalogue*, Monthly Notices of the Royal Astronomical Society, 194, 3, 679. Cited on pages 5, 15, 47, and 77.

Binney J., Gerhard O.E. & Hut P., 1985, *Structure of Surfaces of Section*, Monthly Notices of the Royal Astronomical Society, 215. Cited on page 65.

Binney J. & Mamon G.A., 1982, *M/L and velocity anisotropy from observations of spherical galaxies, or must M87 have a massive black hole?*, Monthly Notices of the Royal Astronomical Society, 200, 2, 361. Cited on pages 9 and 21.

Binney J. & Petrou M., 1985, *Structure of box-shaped bulges and other spheroidal components*, Monthly Notices of the Royal Astronomical Society, 214, 4, 449. Cited on page 5.

Binney J. & Tremaine S., 2008, *Galactic Dynamics: Second Edition*, Princeton. Cited on pages 13, 19, 25, 43, and 49.

Binney, J. and Merrifield M., 1998, *Galactic Astronomy*, Princeton. Cited on pages 7, 9, and 10.

Bissantz N. & Gerhard O., 2002, *Spiral arms, bar shape and bulge microlensing in the Milky Way*, Monthly Notices of the Royal Astronomical Society, 330, 3, 591. Cited on page 33.

Blaña M., Wegg C., Gerhard O. et al., 2016, *Andromeda chained to the Box – dynamical models for M31: bulge and bar*, Monthly Notices of the Royal Astronomical Society, 588, 4, 4279. Cited on page 23.

Blaña M., Wegg C., Gerhard O. et al., 2017, *NMAGIC models for M31*. Cited on page 23.

Blandford R.D., 1990, *Physical processes in active galactic nuclei*, in *20. Saas-Fee Advanced Course of the Swiss Society for Astrophysics and Astronomy: Active galactic nuclei*, pages 161 – 275, Springer-Verlag, Berlin/Heidelberg. Cited on page 3.

Bonnet H., Abuter R., Baker A. et al., 2004, *First light of SINFONI at the VLT*, The Messenger, 117, 17. Cited on page 117.

Box G.E.P. & Muller M.E., 1958, *A Note on the Generation of Random Normal Deviates*, The Annals of Mathematical Statistics, 29, 2, 610. Cited on page 71.

Boylan-Kolchin M., Ma C.P. & Quataert E., 2006, *Red mergers and the assembly of massive elliptical galaxies: The fundamental plane and its projections*, Monthly Notices of the Royal Astronomical Society, 369, 3, 1081. Cited on page 120.

Brainerd W.S., Goldberg C.H. & Adams J.C., 1996, *Programmer's Guide to Fortran 90*, Springer-Verlag, New York. Cited on pages 31 and 137.

Brent R.P., 1971, *An algorithm with guaranteed convergence for finding a zero of a function*, Computer Journal, 14, 4, 422. Cited on page 57.

Burkert A. & Naab T., 2005, *The surprising anisotropy of fast rotating, discy elliptical galaxies*, Monthly Notices of the Royal Astronomical Society, 363, 2, 597. Cited on page 10.

Caon N., Capaccioli M. & D 'onofrio M., 1993, *On the shape of the light profiles of early-type galaxies*, Monthly Notices of the Royal Astronomical Society, 265, 1013. Cited on page 7.

Cappellari M., 2002, *Efficient multi-Gaussian expansion of galaxies*, Monthly Notices of the Royal Astronomical Society, 333, 2, 400. Cited on pages 18, 32, 33, 35, 36, 51, and 131.

Cappellari M., 2008, *Measuring the inclination and mass-to-light ratio of axisymmetric galaxies via anisotropic Jeans models of stellar kinematics*, Monthly Notices of the Royal Astronomical Society, 390, 1, 71. Cited on pages 21 and 33.

Cappellari M., Bacon R., Bureau M. et al., 2006, *The SAURON project–IV. The mass-to-light ratio, the virial mass estimator and the Fundamental Plane of elliptical and lenticular galaxies*, Monthly Notices of the Royal Astronomical Society, 366, 4, 1126. Cited on pages 13, 24, and 119.

Cappellari M. & Copin Y., 2003, *Adaptive spatial binning of integral-field spectroscopic data using Voronoi tessellations*, Monthly Notices of the Royal Astronomical Society, 342, 2, 345. Cited on pages 107 and 117.

Cappellari M., Emsellem E., Bacon R. et al., 2007, *The SAURON project - X. the orbital anisotropy of elliptical and lenticular galaxies: Revisiting the (V/σ, ϵ) diagram with integral-field stellar kinematics*, Monthly Notices of the Royal Astronomical Society, 379, 2, 418. Cited on pages 17 and 131.

Cappellari M., Emsellem E., Krajnović D. et al., 2011, *The ATLAS3D project - I. A volume-limited sample of 260 nearby early-type galaxies: Science goals and selection criteria*, Monthly Notices of the Royal Astronomical Society, 413, 2, 813. Cited on pages 10 and 21.

Cappellari M., McDermid R.M., Alatalo K. et al., 2012, *Systematic variation of the stellar initial mass function in early-type galaxies*, Nature, 484, 7395, 485. Cited on pages 3, 17, and 21.

Cappellari M., McDermid R.M., Alatalo K. et al., 2013, *The ATLAS3D project-XX. Mass-size and mass-σ distributions of early-type galaxies: Bulge fraction drives kinematics, mass-to-light ratio, molecular gas fraction and stellar initial mass function*, Monthly Notices of the Royal Astronomical Society, 432, 3, 1862. Cited on page 17.

Cappellari M., Verolme E.K., van der Marel R.P. et al., 2002, *The Counterrotating Core and the Black Hole Mass of IC 1459*, The Astrophysical Journal, 578, 2, 787. Cited on page 24.

Carter D., 1987, *Weak disks in rapidly rotating elliptical galaxies*, The Astrophysical Journal, 312, 514. Cited on page 5.

Cash J.R. & Karp A.H., 1990, *A variable order Runge-Kutta method for initial value problems with rapidly varying right-hand sides*, ACM Transactions on Mathematical Software, 16, 3, 201. Cited on page 58.

Chandrasekhar S., 1942, *Principles of stellar dynamics*, The University of Chicago Press, Chicago, Illinois (USA). Cited on page 20.

Chokshi A. & Turner E.L., 1992, *Remnants of the quasars*, Monthly Notices of the Royal Astronomical Society, 259, 3, 421. Cited on page 3.

Ciotti L. & Bertin G., 1999, *Analytical properties of the R^(1/m) luminosity law*, Astronomy and Astrophysics, 352, 447. Cited on page 7.

Contopoulos G., 1956, *On the Isophotes of Ellipsoidal Nebulae*, ZA, 39, 126. Cited on pages 16, 28, and 33.

Crane P., Stiavelli M., King I.R. et al., 1993, *High resolution imaging of galaxy cores*, The Astronomical Journal, 106, 1371. Cited on page 5.

Cretton N., de Zeeuw P.T., van der Marel R.P. & Rix H.W., 1999, *Axisymmetric Three-Integral Models for Galaxies*, The Astrophysical Journal Supplement Series, 124, 2, 383. Cited on page 24.

Cretton N. & van den Bosch F.C., 1999, *Evidence for a Massive Black Hole in the S0 Galaxy NGC 4342*, The Astrophysical Journal, 514, 2, 704. Cited on pages 21, 24, and 33.

Das P., Gerhard O., Mendez R.H., Teodorescu A.M. & de Lorenzi F., 2011, *Using NMAGIC to probe the dark matter halo and orbital structure of the X-ray bright, massive elliptical galaxy, NGC 4649*, Monthly Notices of the Royal Astronomical Society, 415, 2, 1244. Cited on pages 23 and 77.

Davies R.L. & Birkinshaw M., 1988, *The orientations of the rotation axes of radio galaxies. II-Stellar rotation curves and velocity dispersion profiles*, The Astrophysical Journal Supplement Series, 68, 409. Cited on page 15.

Davies R.L., Efstathiou G., Fall S.M., Illingworth G. & Schechter P.L., 1983, *The kinematic properties of faint elliptical galaxies*, The Astrophysical Journal, 266, 41. Cited on pages xv, 9, 10, and 12.

Davies R.L., Kuntschner H., Emsellem E. et al., 2001, *Galaxy Mapping with the SAURON Integral-Field Spectrograph: The Star Formation History of NGC 4365*, The Astrophysical Journal, 548, 1, L33. Cited on pages xvi, 3, 6, and 17.

De Lorenzi F., Debattista V.P., Gerhard O. & Sambhus N., 2007, *NMAGIC: a fast parallel implementation of a χ 2 -made-to-measure algorithm for modelling observational data*, Monthly Notices of the Royal Astronomical Society, 376, 1, 71. Cited on pages 23, 66, 77, 82, and 133.

De Lorenzi F., Gerhard O., Coccato L. et al., 2009, *Dearth of dark matter or massive dark halo? Mass-shape-anisotropy degeneracies revealed by NMAGIC dynamical models of the elliptical galaxy NGC 3379*, Monthly Notices of the Royal Astronomical Society, 395, 1, 76. Cited on page 23.

de Vaucouleurs G., 1948, *Recherches sur les Nebuleuses Extragalactiques*, Annales d'Astrophysique, 11, 247. Cited on page 7.

de Zeeuw P.T., 1985a, *Elliptical galaxies with separable potentials*, Monthly Notices of the Royal Astronomical Society, 216, 273. Cited on pages 18, 22, 28, 45, 52, and 58.

de Zeeuw P.T., 1985b, *Motion in the core of a triaxial potential*, Monthly Notices of the Royal Astronomical Society, 215, 4, 731. Cited on page 28.

de Zeeuw P.T. & Franx M., 1991, *Structure and Dynamics of Elliptical Galaxies*, Annual Review of Astronomy and Astrophysics, 29, 1, 239. Cited on page 3.

de Zeeuw P.T. & Merritt D., 1983, *Stellar orbits in a triaxial galaxy. I - Orbits in the plane of rotation*, The Astrophysical Journal, 267, 571. Cited on page 28.

de Zeeuw T., Peletier R. & Franx M., 1986, *Mass models with Stackel potentials*, Monthly Notices of the Royal Astronomical Society, 221, 4, 1001. Cited on page 53.

Dehnen W., 1993, *A Family of Potential-Density Pairs for Spherical Galaxies and Bulges*, Monthly Notices of the Royal Astronomical Society, 265. Cited on pages 22 and 43.

Dehnen W. & Gerhard O.E., 1993, *Three-integral models of oblate elliptical galaxies*, Monthly Notices of the Royal Astronomical Society, 261, 2, 311. Cited on page 22.

Dejonghe H., 1987, *A completely analytical family of anisotropic Plummer models*, Monthly Notices of the Royal Astronomical Society, 224, 1, 13. Cited on page 9.

Dejonghe H. & de Zeeuw T., 1988, *Analytic axisymmetric galaxy models with three integrals of motion*, The Astrophysical Journal, 333, 90. Cited on page 22.

di Tullio G.A., 1979, *On the variation of ellipticity with radius in elliptical galaxies*, Astronomy and Astrophysics Supplement Series, 37, 591. Cited on page 15.

Djorgovski S. & Davis M., 1987, *Fundamental properties of elliptical galaxies*, The Astrophysical Journal, 313, 59. Cited on page 13.

Douglas N., Napolitano N., Romanowsky A.c.d. et al., 2007, *The PN.S Elliptical galaxy survey: Data reduction, planetary nebula catalog, and basic dynamics for NGC 3379*, The Astrophysical Journal, 664, 1 I, 257. Cited on page 10.

Dressler A., 1980, *Galaxy morphology in rich clusters - Implications for the formation and evolution of galaxies*, The Astrophysical Journal, 236, 351. Cited on page 14.

Dressler A., Oemler A., Jr. et al., 1997, *Evolution since Z = 0.5 of the Morphology-Density Relation for Clusters of Galaxies*, The Astrophysical Journal, 490, 577. Cited on page 14.

Ebisuzaki T., Makino J. & Okumura S., 1991, *Merging of two galaxies with central black holes*, Nature, 354, 6350, 212. Cited on page 7.

Eddington A.S., 1916, *The Distribution of Stars in Globular Clusters*, Monthly Notices of the Royal Astronomical Society, 76, 7, 572. Cited on page 77.

Eisenhauer F., Abuter R., Bickert K. et al., 2003, *SINFONI - Integral field spectroscopy at 50 milli-arcsecond resolution with the ESO VLT*, in A.F.M. Iye, Masanori; Moorwood, editor, *Instrument Design and Performance for Optical/Infrared Ground-based Telescopes. Proceedings of the SPIE*, volume 4841, page 1548. Cited on page 117.

Emsellem E., Cappellari M., Krajnović D. et al., 2011, *The ATLAS3D project - III. A census of the stellar angular momentum within the effective radius of early-type galaxies: Unveiling the distribution of fast and slow rotators*, Monthly Notices of the Royal Astronomical Society, 414, 2, 888. Cited on pages 5 and 10.

Emsellem E., Cappellari M., Krajnovi D. et al., 2007, *The SAURON project - IX. A kinematic classification for early-type galaxies*, Monthly Notices of the Royal Astronomical Society, 379, 2, 401. Cited on pages 5, 10, 17, and 131.

Emsellem E., Cappellari M., Peletier R.F. et al., 2004, *The SAURON project - III. Integral-field absorption-line kinematics of 48 elliptical and lenticular galaxies*, Monthly Notices of the Royal Astronomical Society, Volume 352, Issue 3, pp. 721-743., 352, 721. Cited on page 3.

Emsellem E., Monnet G. & Bacon R., 1994a, *The multi-gaussian expansion method: a tool for building realistic photometric and kinematical models of stellar systems I. The formalism*, Astronomy and Astrophysics, , 285, 723. Cited on page 33.

Emsellem E., Monnet G., Bacon R. & Nieto J., 1994b, *The multi-gaussian expansion method: a tool for building realistic photometric and kinematical models of stellar systems II. Application to the central region of the Sombrero Galaxy (NGC 4594)*, Astronomy and Astrophysics, 285, 739. Cited on page 33.

Erwin P., 2015, *Imfit: A fast, flexible new program for astronomical image fitting*, Astrophysical Journal, 799, 2. Cited on page 114.

Erwin P., Saglia R.P., Fabricius M. et al., 2014, *Composite bulges: The coexistence of classical bulges and discy pseudo-bulges in S0 and spiral galaxies*, Monthly Notices of the Royal Astronomical Society, 446, 4, 4039. Cited on page 24.

Faber S.M., Friel E.D., Burstein D. & Gaskell C.M., 1985, *Old stellar populations. II - an analysis of K-giant spectra*, The Astrophysical Journal Supplement Series, 57, 711. Cited on page 14.

Faber S.M. & Jackson R.E., 1976, *Velocity dispersions and mass-to-light ratios for elliptical galaxies*, The Astrophysical Journal, 204, 668. Cited on page 13.

Faber S.M., Tremaine S., Ajhar E.A. et al., 1997, *The Centers of Early-Type Galaxies with HST. IV. Central Parameter Relations.*, The Astronomical Journal, 114, 1771. Cited on page 7.

Fabian A., Thomas P., White R. & Fall S., 1986, *A lower limit to the binding mass of early-type galaxies*, Monthly Notices of the Royal Astronomical Society, 221, 4, 1049. Cited on page 10.

Ferrarese L. & Merritt D., 2000, *A Fundamental Relation between Supermassive Black Holes and Their Host Galaxies*, The Astrophysical Journal Letters, 539, 1, L9. Cited on page 14.

Finozzi F., 2013, *Programming and testing a 3D-Schwarzschild code for the dynamical modeling of galaxies*, Master thesis, Ludwig–Maximilians–Universität, München. Cited on pages 31 and 37.

Ford H.C., Ciardullo R., Jacoby G.H. & Hui X., 1989, *Planetary nebulae in galaxies beyond the Local Group*, in *IAU Symposium No. 131: Planetary nebulae*, volume 131, pages 335–350, Cambridge University Press. Cited on page 10.

Forman W., Jones C. & Tucker W., 1985, *Hot coronae around early-type galaxies*, The Astrophysical Journal, 293, 102. Cited on page 10.

Franx M., Illingworth G. & Heckman T., 1989, *Major and minor axis kinematics of 22 ellipticals*, The Astrophysical Journal, 344, 613. Cited on page 15.

Franx M. & Illingworth G.D., 1988, *A counterrotating core in IC 1459*, The Astrophysical Journal, 327, L55. Cited on page 9.

Galilei G., 1610, *Sidereus Nuncius*, Apud Thomas Baglionum, Venice. Cited on page 1.

Gavazzi R., Treu T., Rhodes J.D. et al., 2007, *The Sloan Lens ACS Survey. IV. The Mass Density Profile of Early*`[U+2010]`*Type Galaxies out to 100 Effective Radii*, The Astrophysical Journal, 667, 1, 176. Cited on page 10.

Gebhardt K., Bender R., Bower G. et al., 2000a, *A Relationship between Nuclear Black Hole Mass and Galaxy Velocity Dispersion*, The Astrophysical Journal Letters, 539, 1, L13. Cited on page 14.

Gebhardt K., Richstone D., Ajhar E.A. et al., 1996, *The Centers of Early-Type Galaxies With HST. III. Non-Parametric Recovery of Stellar Luminosity Distribution*, The Astronomical Journal, 112, 105. Cited on page 5.

Gebhardt K., Richstone D., Kormendy J. et al., 2000b, *Axisymmetric, Three-Integral Models of Galaxies: A Massive Black Hole in NGC 3379*, The Astronomical Journal, 119, 3, 1157. Cited on pages xxiii, 24, 118, and 122.

Gebhardt K., Richstone D., Tremaine S. et al., 2003, *Axisymmetric Dynamical Models of the Central Regions of Galaxies*, The Astrophysical Journal, 583, 1, 92. Cited on pages 24 and 117.

Gebhardt K. & Thomas J., 2009, *The Black Hole Mass, Stellar Mass-To-Light Ratio, and Dark Halo in M87*, The Astrophysical Journal, 700, 2, 1690. Cited on pages 18, 24, and 119.

Gerhard O. & Binney J., 1996, *On the deprojection of axisymmetric bodies*, Monthly Notices of the Royal Astronomical Society, 279. Cited on page 33.

Gerhard O., Kronawitter A., Saglia R.P. & Bender R., 2001, *Dynamical Family Properties and Dark Halo Scaling Relations of Giant Elliptical Galaxies*, The Astronomical Journal, 121, 1936. Cited on page 13.

Gerhard O.E., 1993, *Line-of-sight velocity profiles in spherical galaxies: breaking the degeneracy between anisotropy and mass.*, Monthly Notices of the Royal Astronomical Society, 265, 213. Cited on page 9.

Gerhard O.E. & Binney J., 1985, *Triaxial galaxies containing massive black holes or central density cusps.* Cited on page 28.

Goldstein H., Poole C. & Safko J., 2002, *Classical mechanics*, Addison-Wesley, San Francisco, 3 edition. Cited on page 20.

Goss W.M., McAdam W.B., Wellington K.J. & Ekers R.D., 1987, *The very low-brightness relic radio galaxy 1401-33*, Monthly Notices of the Royal Astronomical Society, 226, 4, 979. Cited on page 111.

Gott J.R., 1977, *Recent Theories of Galaxy Formation*, Annual Review of Astronomy and Astrophysics, 15, 1, 235. Cited on page 3.

Graham A.W., Erwin P., Trujillo I. & Asensio Ramos A., 2003, *A New Empirical Model for the Structural Analysis of Early-Type Galaxies, and A Critical Review of the Nuker Model*, The Astronomical Journal, 125, 6, 2951. Cited on page 8.

Gültekin K., Richstone D.O., Gebhardt K. et al., 2009, *the M -Σ and M - L Relations in Galactic Bulges, and Determinations of Their Intrinsic Scatter*, The Astrophysical Journal, 698, 1, 198. Cited on page 15.

Hamabe M. & Kormendy J., 1986, *Correlations Between R/1/4 - Law Parameters for Bulges and Elliptical Galaxies*, in *Structure and Dynamics of Elliptical Galaxies, Proceedings of IAU Symposium*, volume 127, page 379, Cambridge University Press. Cited on page 14.

Heiligman G. & Schwarzschild M., 1979, *On the nonexistence of three-dimensional tube orbits around the intermediate axis in a triaxial galaxy model*, The Astrophysical Journal, 233, 872. Cited on page 27.

Henault F., Bacon R., Bonneville C. et al., 2003, *MUSE: a second-generation integral-field spectrograph for the VLT*, Instrument Design and Performance for Optical/Infrared Ground-based Telescopes, 4841, 1096. Cited on page 117.

Henon M. & Heiles C., 1964, *The Applicability of the Third Integral of Motion: Some Numerical Experiments*, The Astronomical Journal, 69, 1, 73. Cited on page 27.

Hermite C., 1864, *Sur un nouveau developpement en serie de fonctions*, Comptes Rendus de l'Academie des Sciences, 58, 93. Cited on page 9.

Hernquist L., 1990, *An analytical model for spherical galaxies and bulges*, The Astrophysical Journal, 356, 359. Cited on pages 22, 44, and 132.

Herschel W., 1786, *Catalogue of One Thousand New Nebulae and Clusters of Stars. by William Herschel, LL.D. F. R. S.*, Philosophical Transactions of the Royal Society of London, 76, 457. Cited on page 2.

Hill G., MacQueen P. & Palunas P., 2008, *Present and future instrumentation for the Hobby-Eberly Telescope*, Proc. SPIE, 7014, 701406. Cited on page 106.

Hubble E.P., 1925, *Cepheids in spiral nebulae*, The Observatory, 48, 139. Cited on page 2.

Hubble E.P., 1926, *Extragalactic nebulae.*, The Astrophysical Journal, 64, 321. Cited on page 2.

Hubble E.P., 1936, *Realm of the Nebulae*, Yale University Press. Cited on page 2.

Humphrey P.J., Buote D.A., Gastaldello F. et al., 2006, *A Chandra View of Dark Matter in Early-Type Galaxies*, The Astrophysical Journal, 646, 2, 899. Cited on page 3.

Hunter C., 1975, *Determination of the distribution function of an elliptical galaxy*, The Astronomical Journal, 80, 783. Cited on page 22.

Hunter C. & de Zeeuw P.T., 1992, *Trixaxial galaxy models with thin tube orbits*, The Astrophysical Journal, 389, 79. Cited on pages 22 and 28.

Hunter C. & Qian E., 1993, *Two-integral distribution functions for axisymmetric systems*, Monthly Notices of the Royal Astronomical Society, 262, 401. Cited on page 22.

Illingworth G., 1977, *Rotation in 13 elliptical galaxies*, The Astrophysical Journal, 218, L43. Cited on page 9.

Jaffe W., 1983, *A simple model for the distribution of light in spherical galaxies*, Monthly Notices of the Royal Astronomical Society, 202, 4, 995. Cited on page 22.

Jeans J., 1915, *On the theory of star-streaming and the structure of the universe*, Monthly Notices of the Royal Astronomical Society, 76, 2, 70. Cited on page 20.

Jedrzejewski R. & Schechter P., 1989, *Minor-axis rotation in elliptical galaxies*, Astronomical Journal, 98, 147. Cited on page 15.

Jedrzejewski R.I., 1987, *Isophote shapes*, in *Structure and dynamics of elliptical galaxies; Proceedings of the IAU Symposium, Princeton, NJ, May 27-31, 19866*, volume 127, pages 37–44, Cambridge University Press. Cited on page 84.

Kelson D.D., van Dokkum P.G., Franx M., Illingworth G.D. & Fabricant D., 1997, *Evolution of Early-Type Galaxies in Distant Clusters: The Fundamental Plane from Hubble Space Telescope Imaging and Keck Spectroscopy*, The Astrophysical Journal, 478, L13. Cited on page 13.

King I.R., 1978, *Surface photometry of elliptical galaxies*, The Astrophysical Journal, 222, 1. Cited on page 15.

Kjaergaard P., Jorgensen I. & Moles M., 1993, *The Fundamental Plane and the Surface Brightness Test for the Expansion of the Universe*, The Astrophysical Journal, 418, 617. Cited on page 13.

Kondratev B.P. & Ozernoi L.M., 1979, *What is the intrinsic shape of elliptical galaxies*, Soviet Astronomy Letters, 5, 37. Cited on pages 16 and 28.

Kormendy J., 1977, *Brightness distributions in compact and normal galaxies. II - Structure parameters of the spheroidal component*, The Astrophysical Journal, 218, 333. Cited on pages 14 and 15.

Kormendy J., 1984, *Recognizing merger remnants among normal elliptical galaxies NGC 5813*, The Astrophysical Journal, 287, 577. Cited on page 6.

Kormendy J., 1985, *Brightness profiles of the cores of bulges and elliptical galaxies*, The Astrophysical Journal, 292, L9. Cited on page 5.

Kormendy J. & Bender R., 1996, *A Proposed Revision of the Hubble Sequence for Elliptical Galaxies*, The Astrophysical Journal Letters, 464, 2, L119. Cited on page 5.

Kormendy J., Bender R. & Cornell M.E., 2011, *Supermassive black holes do not correlate with galaxy disks or pseudobulges.*, Nature, 469, 7330, 374. Cited on pages 2 and 14.

Kormendy J. & Gebhardt K., 2001, *Supermassive black holes in galactic nuclei*, in *AIP Conference Proceedings*, volume 586, pages 363–381. Cited on page 14.

Kormendy J. & Ho L.C., 2013, *Coevolution (Or Not) of Supermassive Black Holes and Host Galaxies*, Annual Review of Astronomy and Astrophysics, 51, 511. Cited on pages 2, 13, 14, and 15.

Kormendy J. & Kennicutt R.C., 2004, *Secular Evolution and the formation of pseudobulges in disk galaxies*, Annual Review of Astronomy and Astrophysics, 42, 1, 603. Cited on page 2.

Kormendy J. & Richstone D., 1995, *Inward Bound–The Search for Supermassive Black Holes in Galactic Nuclei*, Annual Review of Astronomy and Astrophysics, 33, 1, 581. Cited on page 3.

Krajnović D., Emsellem E., Cappellari M. et al., 2011, *The ATLAS3Dproject - II. Morphologies, kinemetric features and alignment between photometric and kinematic axes of early-type galaxies*, Monthly Notices of the Royal Astronomical Society, 414, 4, 2923. Cited on page 10.

Kroupa P., 2002, *The Initial Mass Function of Stars: Evidence for Uniformity in Variable Systems*, Science, 295, 5552, 82. Cited on page 17.

Lake G., 1981a, *Dynamical Modeling of Elliptical Galaxies - Part Two - Numerical Prolate Models*, The Astrophysical Journal, 243, 121. Cited on page 22.

Lake G., 1981b, *Dynamical modeling of elliptical galaxies. I - Analytical prolate models. II - Numerical prolate models*, The Astrophysical Journal, 243, 111. Cited on page 22.

Lanzoni B., Ciotti L., Cappi A., Tormen G. & Zamorani G., 2004, *The Scaling Relations of Galaxy Clusters and Their Dark Matter Halos*, The Astrophysical Journal, 600, 2, 640. Cited on page 13.

Lauer T.R., 1985, *Boxy isophotes, discs and dust lanes in elliptical galaxies*, Monthly Notices of the Royal Astronomical Society, 216, 2, 429. Cited on page 5.

Lauer T.R., Ajhar E.A., Byun Y. et al., 1995, *The Centers of Early-Type Galaxies with HST.I.An Observational Survey*, Astronomical Journal, 110, 2622. Cited on page 7.

Lauer T.R., Faber S.M., Gebhardt K. et al., 2005, *The Centers of Early-Type Galaxies with HST. V. New WFPC2 Photometry*, The Astronomical Journal, 129, 2138. Cited on pages 5, 111, and 134.

Lauer T.R., Gebhardt K., Faber S.M. et al., 2007, *The Centers of Early-Type Galaxies with Hubble Space Telescope. VI. Bimodal Central Surface Brightness Profiles*, The Astrophysical Journal, 664, 1980, 226. Cited on pages xv, 7, 8, 105, and 133.

Le Digabel S., 2011, *Algorithm 909: NOMAD: Nonlinear Optimization with the MADS Algorithm*, ACM Transactions on Mathematical Software, 37, 4, 1. Cited on pages 67 and 132.

Lees J. & Schwarzschild M., 1992, *The orbital structure of galactic halos*, The Astrophysical Journal, 384, 491. Cited on page 28.

Li H., Li R., Mao S. et al., 2016, *Assessing the jeans anisotropic multi-gaussian expansion method with the illustris simulation*, Monthly Notices of the Royal Astronomical Society, 455, 4, 3680. Cited on page 21.

Loewenstein M. & Mathews W., 1987, *Evolution of hot galactic flows*, The Astrophysical Journal, 319, 614. Cited on page 10.

Loewenstein M. & White R.E., 1999, *Prevalence and properties of dark matter in elliptical galaxies*, The Astrophysical Journal, 518, 50. Cited on page 10.

Lokas E.L., 2002, *Dark matter distribution in dwarf spheroidal galaxies*, Monthly Notices of the Royal Astronomical Society, 333, 3, 697. Cited on page 21.

Longobardi A., Arnaboldi M., Gerhard O. & Mihos J.C., 2015, *The build-up of the cD halo of M 87: evidence for accretion in the last Gyr*, Astronomy & Astrophysics, 579, L3. Cited on page 10.

Longobardi A., Arnaboldi M., Gerhard O. et al., 2013, *The planetary nebula population in the halo of M 87*, Astronomy & Astrophysics, 558, A42. Cited on page 10.

Lynden-Bell D., 1962a, *Stellar Dynamics: Exact Solution of the Self-Gravitation Equation*, Monthly Notices of the Royal Astronomical Society, 123, 5, 447. Cited on page 22.

Lynden-Bell D., 1962b, *Stellar dynamics. Only isolating integrals should be used in Jeans theorem*, Monthly Notices of the Royal Astronomical Society, 124, 1, 1. Cited on page 21.

Ma C.P., Greene J.E., McConnell N. et al., 2014, *The MASSIVE Survey. I. A volume-limited integral-field spectroscopic study of the most massive early type galaxies within 108 Mpc*, The Astrophysical Journal, 795, 2, 158. Cited on pages 106 and 133.

Magorrian J., 1999, *Kinematical signatures of hidden stellar discs*, Monthly Notices of the Royal Astronomical Society, 302, 3, 530. Cited on pages 33, 77, and 107.

Magorrian J. & Binney J., 1994, *Predicting line-of-sight velocity distributions of elliptical galaxies*, Monthly Notices of the Royal Astronomical Society, 271, 4, 949. Cited on page 21.

Magorrian J., Tremaine S., Richstone D. et al., 1998, *The Demography of Massive Dark Objects in Galaxy Centers*, The Astronomical Journal, 115, 6, 2285. Cited on page 21.

Makino J. & Ebisuzaki T., 1996, *Merging of Galaxies with Central Black Holes. I. Hierarchical Mergings of Equal-Mass Galaxies*, The Astrophysical Journal, 465, 527. Cited on page 7.

Malin D.F. & Carter D., 1983, *A catalog of elliptical galaxies with shells*, The Astrophysical Journal, 274, 534. Cited on page 6.

Matthias M. & Gerhard O., 1999, *Dynamics of the Boxy Elliptical Galaxy NGC 1600*, Monthly Notices of the Royal Astronomical Society, 310, 879. Cited on pages 105 and 108.

Mazzalay X., Thomas J., Saglia R.P. et al., 2016, *The supermassive black hole and double nucleus of the core elliptical NGC 5419*, Monthly Notices of the Royal Astronomical Society, 462, 3, 2847. Cited on pages 24, 111, 114, 117, 119, and 134.

McConnell N.J., Ma C.P., Gebhardt K. et al., 2011, *Two ten-billion-solar-mass black holes at the centres of giant elliptical galaxies*, Nature, 480, 7376, 215. Cited on pages 3, 17, and 105.

McConnell N.J., Ma C.P., Murphy J.D. et al., 2012, *Dynamical measurements of black hole masses in four brightest cluster galaxies at 100 Mpc*, The Astrophysical Journal, 756, 2, 179. Cited on page 106.

Melville A.D., 1998, *Metamorphoses Ovid ; translated by A.D. Melville ; with an introduction and notes by E.J. Kenney.*, Oxford University Press, Oxford. Cited on page 1.

Merritt D., 2013, *Dynamics and Evolution of Galactic Nuclei*, Princeton University Press. Cited on pages 120 and 135.

Message P Forum, 2012, *MPI: A Message-Passing Interface Standard*, University of Tennessee. Cited on page 68.

Messier C., 1781, *Catalogue des Nébuleuses & des amas d'Étoiles (Catalog of Nebulae and Star Clusters)*. Cited on page 2.

Milosavljević M. & Merritt D., 2001, *Formation of Galactic Nuclei*, The Astrophysical Journal, 563, 1, 34. Cited on pages xxii, xxiv, 6, 106, 109, 120, and 129.

Miralda-Escude J. & Schwarzschild M., 1989, *On the orbit structure of the logarithmic potential*, The Astrophysical Journal, 339, 752. Cited on pages xvi, 28, and 29.

Monnet, G., Bacon, R., Emsellem E., 1992, *Modelling the stellar intensity and radial velocity fields in triaxial galaxies by sums of Gaussian functions*, Astronomy and Astrophysics, 253, 366. Cited on page 33.

Morganti L. & Gerhard O., 2012, *Regularizing made-to-measure particle models of galaxies*, Monthly Notices of the Royal Astronomical Society, 422, 2, 1571. Cited on page 23.

Morse P.M. & Feshbach H., 1953, *Methods of theoretical physics*, McGraw-Hill, New York. Cited on page 49.

Napolitano N.R., Romanowsky A.J., Coccato L. et al., 2009, *The Planetary Nebula Spectrograph elliptical galaxy survey: The dark matter in NGC 4494*, Monthly Notices of the Royal Astronomical Society, 393, 2, 329. Cited on page 10.

Navarro J.F., Frenk C.S. & White S.D.M., 1996, *The Structure of Cold Dark Matter Halos*, The Astrophysical Journal, 462, 563. Cited on page 43.

Nieto J.L. & Bender R., 1989, *Boxiness in elliptical galaxies*, Astronomy and Astrophysics, 215, 266. Cited on page 15.

Norman C.A., May A. & van Albada T.S., 1985, *Black holes and the shapes of galaxies*, The Astrophysical Journal, 296, 20. Cited on page 28.

Nowak N., Saglia R.P., Thomas J. et al., 2007, *The supermassive black hole in NGC 4486a detected with SINFONI at the Very Large Telescope*, Monthly Notices of the Royal Astronomical Society, 379, 3, 909. Cited on pages 24 and 117.

Nowak N., Saglia R.P., Thomas J. et al., 2008, *The supermassive black hole of FornaxA*, Monthly Notices of the Royal Astronomical Society, 391, 1629. Cited on pages 24 and 117.

Nowak N., Thomas J., Erwin P. et al., 2010, *Do black hole masses scale with classical bulge luminosities only? The case of the two composite pseudo-bulge galaxies NGC 3368 and NGC 3489*, Monthly Notices of the Royal Astronomical Society, 403, 2, 646. Cited on pages 24 and 117.

Opitsch M., 2016, *The bar of the Andromeda galaxy revealed by integral field spectroscopy*, Ph.D. thesis, Ludwig-Maximilians Universität München. Cited on page 23.

Opitsch M., Fabricius M.H., Saglia R.P. et al., 2017, *Evidence for non-axisymmetry in M31 from wide-field kinematics of stars and gas*. Cited on page 23.

Peletier R.F., Davies R.L., Illingworth G.D., Davis L.E. & Cawson M., 1990, *CCD surface photometry of galaxies with dynamical data. II - UBR photometry of 39 elliptical galaxies*, The Astronomical Journal, 100, 1091. Cited on pages 5 and 107.

Pérez-Villegas A., Portail M. & Gerhard O., 2017a, *The Stellar Halo in the Inner Milky Way: Predicted Shape and Kinematics*, Monthly Notices of the Royal Astronomical Society: Letters, 464, 1, L80. Cited on page 23.

Pérez-Villegas A., Portail M., Wegg C. & Gerhard O., 2017b, *Revisiting the Tale of Hercules: How Stars Orbiting the Lagrange Points Visit the Sun*, The Astrophysical Journal Letters, 840, L2. Cited on page 23.

Pierce M., Beasley M.A., Forbes D.A. et al., 2006, *Gemini/GMOS spectra of globular clusters in the Leo group elliptical NGC 3379*, Monthly Notices of the Royal Astronomical Society, 366, 4, 1253. Cited on page 10.

Plummer H.C., 1911, *On the Problem of Distribution in Globular Star Clusters*, Monthly Notices of the Royal Astronomical Society, 71, 5, 460. Cited on page 43.

Portail M., Gerhard O., Wegg C. & Ness M., 2016, *Dynamical Modelling of the Galactic Bulge and Bar: Pattern Speed, Stellar, and Dark Matter Mass Distributions*, Monthly Notices of the Royal Astronomical Society, Volume 465, Issue 2, p.1621-1644, 24, 1. Cited on page 23.

Portail M., Wegg C. & Gerhard O., 2015a, *Peanuts, brezels and bananas: Food for thought on the orbital structure of the Galactic bulge*, Monthly Notices of the Royal Astronomical Society: Letters, 450, 1, L66. Cited on page 23.

Portail M., Wegg C., Gerhard O. & Martinez-Valpuesta I., 2015b, *Made-to-measure models of the Galactic box/peanut bulge: stellar and total mass in the bulge region*, Monthly Notices of the Royal Astronomical Society, 448, 1, 713. Cited on page 23.

Press W.H., Vetterling W.T., Metcalf M., Flannery B.P. & Teukolsky S.A., 1996, *Numerical Recipes in Fortran 90 Vol. 2 - The Art of Parallel Scientific Computing: Second Edition*, Cambridge University Press, Cambridge. Cited on pages 44, 57, 58, 71, and 138.

Quinlan G. & Hernquist L., 1997, *The dynamical evolution of massive black hole binaries - II. Self-consistent N-body integrations*, New Astronomy, 2, 533. Cited on pages xxii, xxiv, 6, 106, 109, 120, and 129.

Richstone D.O., 1982, *Scale-free models of galaxies. II - A complete survey of orbits*, The Astrophysical Journal, 252, 496. Cited on page 27.

Richstone D.O. & Tremaine S., 1984, *A general method for constructing spherical galaxy models*, The Astrophysical Journal, 286, 27. Cited on page 24.

Richstone D.O. & Tremaine S., 1988, *Maximum-entropy models of galaxies*, The Astrophysical Journal, 327, 82. Cited on page 65.

Rix H.W., de Zeeuw P.T., Cretton N., van der Marel R.P. & Carollo C.M., 1997, *Dynamical Modeling of Velocity Profiles: The Dark Halo around the Elliptical Galaxy NGC 2434*, The Astrophysical Journal, 488, 2, 702. Cited on page 24.

Rix H.W. & White S.D., 1990, *Disks in elliptical galaxies*, The Astrophysical Journal, 362, 52. Cited on page 5.

Rix H.W. & White S.D., 1992, *Optimal estimates of line-of-sight velocity distributions from absorption line spectra of galaxies - Nuclear discs in elliptical galaxies*, Monthly Notices of the Royal Astronomical Society, 254, 389. Cited on page 9.

Romanowsky A.J., Douglas N.G., Arnaboldi M. et al., 2003, *A Dearth of Dark Matter in Ordinary Elliptical Galaxies*, Science, 301, 5640, 1696. Cited on page 10.

Ross W.D. & Smith J.A., 1912, *The works of Aristotele translated into English*, Oxford, Clarendon Press. Cited on page 1.

Rusli S.P., Erwin P., Saglia R.P. et al., 2013a, *Depleted Galaxy Cores and Dynamical Black Hole Masses*, The Astronomical Journal, 146, 6, 160. Cited on pages 24 and 117.

Rusli S.P., Thomas J., Erwin P. et al., 2011, *The central black hole mass of the high-σ but low-bulge-luminosity lenticular galaxy NGC 1332*, Monthly Notices of the Royal Astronomical Society, 410, 2, 1223. Cited on pages 24 and 117.

Rusli S.P., Thomas J., Saglia R.P. et al., 2013b, *The influence of dark matter halos on dynamical estimates of black hole mass: 10 new measurements for high-σ early-type galaxies*, The Astronomical Journal, 146, 3, 45. Cited on pages 18, 24, and 117.

Rybicki G.B., 1987, *Deprojection of galaxies - how much can be learned*, Structure and Dynamics of Elliptical Galaxies, page 397. Cited on page 32.

Saglia R.P., Bertin G., Bertola F. et al., 1993, *Stellar dynamical evidence for dark halos in elliptical galaxies - The case of NGC 4472, IC 4296, and NGC 7144*, The Astrophysical Journal, 403, 567. Cited on page 10.

Saglia R.P., Bertin G. & Stiavelli M., 1992, *Elliptical Galaxies with Dark Matter. II. Optimal Luminous–Dark Matter Decomposition for a Sample of Bright Objects*, The Astrophysical Journal, 384, 433. Cited on page 10.

Saglia R.P., Kronawitter A., Gerhard O. & Bender R., 2000, *The Orbital Structure and Potential of NGC 1399*, The Astronomical Journal, 119, 153. Cited on page 10.

Saglia R.P., Opitsch M., Erwin P. et al., 2016, *The SINFONI Black Hole Survey: The Black Hole Fundamental Plane revisited and the paths of (co-) evolution of supermassive black holes and bulges*, The Astrophysical Journal, 818, 47. Cited on pages xxiv, 7, 9, 14, 24, 111, 117, 120, 130, and 134.

Salpeter E.E., 1955, *The Luminosity Function and Stellar Evolution.*, The Astrophysical Journal, 121, 161. Cited on page 17.

Sandage A., Freeman K.C. & Stokes N.R., 1970, *The Intrinsic Flattening of e, so, and Spiral Galaxies as Related to Galaxy Formation and Evolution*, The Astrophysical Journal, 160, 831. Cited on page 5.

Schaeffer R., Maurogordato S., Cappi A. & Bernardeau F., 1993, *The Fundamental Plane of Galaxy Clusters*, Monthly Notices of the Royal Astronomical Society, 263, L21. Cited on page 13.

Schwarzschild M., 1979, *A numerical model for a triaxial stellar system in dynamical equilibrium*, The Astrophysical Journal, 232, 236. Cited on pages 16, 23, and 28.

Schwarzschild M., 1982, *Triaxial equlibrium models for elliptical galaxies with slow figure rotation*, The Astrophysical Journal, 263, 599. Cited on pages 16 and 23.

Schwarzschild M., 1993, *Self-Consistent models for galactic halos*, The Astrophysical Journal, 409, 563. Cited on pages 18, 28, and 58.

Schweizer F., 1982, *Colliding and merging galaxies. I - Evidence for the recent merging of two disk galaxies in NGC 7252*, The Astrophysical Journal, 252, 455. Cited on page 6.

Sérsic J.L., 1963, *Influence of the atmospheric and instrumental dispersion on the brightness distribution in a galaxy*, Boletin de la Asociacion Argentina de Astronomia, 6, 41. Cited on page 7.

Sérsic J.L., 1968, *Atlas de galaxias australes*, Cordoba. Cited on page 7.

Shapiro K.L., Cappellari M., De Zeeuw T. et al., 2006, *The black hole in NGC 3379: A comparison of gas and stellar dynamical mass measurements with HST and integral-field data*, Monthly Notices of the Royal Astronomical Society, 370, 2, 559. Cited on pages 119 and 135.

Siopis C., Gebhardt K., Lauer T.R. et al., 2009, *A Stellar Dynamical Measurement of the Black Hole Mass in the Maser Galaxy NGC 4258*, The Astrophysical Journal, 693, 1, 946. Cited on pages 24, 43, 61, and 65.

Stark A.A., 1977, *Triaxial Models of the Bulge of M31*, The Astrophysical Journal, 213, 368. Cited on page 33.

Statler T.S., 1987, *Self-consistent models of perfect triaxial galaxies*, The Astrophysical Journal, 321, 113. Cited on pages xvi, 16, and 29.

Statler T.S., 1991, *On the velocity fields of elliptical galaxies*, The Astronomical Journal, 102, 3, 882. Cited on page 16.

Subrahmanyan R., Beasley A.J., Goss W.M., Golap K. & Hunstead R.W., 2002, *PKS B1400-33: an unusual radio relic in a poor cluster*, The Astronomical Journal, 125, 3, 1095. Cited on page 111.

Syer D. & Tremaine S., 1996, *Made-to-measure N-body systems*, Monthly Notices of the Royal Astronomical Society, 282, 1, 223. Cited on page 23.

Thomas D., Maraston C., Bender R. & de Oliveira C.M., 2005a, *The Epochs of Early Type Galaxy Formation as a Function of Environment*, The Astrophysical Journal, 621, 673. Cited on page 3.

Thomas D., Maraston C., Schawinski K., Sarzi M. & Silk J., 2010, *Environment and self-regulation in galaxy formation*, Monthly Notices of the Royal Astronomical Society, 404, 4, 1775. Cited on page 3.

Thomas J., Jesseit R., Naab T. et al., 2007a, *Axisymmetric orbit models of N-body merger remnants: A dependency of reconstructed mass on viewing angle*, Monthly Notices of the Royal Astronomical Society, 381, 4, 1672. Cited on pages 17, 74, 119, and 131.

Thomas J., Ma C.P., McConnell N.J. et al., 2016, *A 17-billion-solar-mass black hole in a group galaxy with a diffuse core*, Nature, 532, Ngc 4874, 1. Cited on pages xxii, 3, 15, 24, 105, 107, 108, 109, and 133.

Thomas J., Saglia R., Bender R., Erwin P. & Fabricius M., 2014a, *Massive Elliptical Galaxies: BH Scouring or a Bottom-Heavy IMF?*, Proceedings of the International Astronomical Union, 10, S311, 36. Cited on page 17.

Thomas J., Saglia R.P., Bender R., Erwin P. & Fabricius M., 2014b, *The Dynamical Fingerprint of Core Scouring in Massive Elliptical Galaxies*, The Astrophysical Journal, 782, 1, 39. Cited on pages 6, 24, 106, and 117.

Thomas J., Saglia R.P., Bender R. et al., 2004, *Mapping stationary axisymmetric phase-space distribution functions by orbit libraries*, Monthly Notices of the Royal Astronomical Society, 353, 2, 391. Cited on pages xix, 18, 24, 62, 65, 68, 74, 76, 119, 132, and 134.

Thomas J., Saglia R.P., Bender R. et al., 2005b, *Regularized orbit models unveiling the stellar structure and dark matter halo of the Coma elliptical NGC 4807*, Monthly Notices of the Royal Astronomical Society, 360, 4, 1355. Cited on pages 66 and 140.

Thomas J., Saglia R.P., Bender R. et al., 2007b, *Dynamical modelling of luminous and dark matter in 17 Coma early-type galaxies*, Monthly Notices of the Royal Astronomical Society, 382, 2, 657. Cited on page 118.

Thomas J., Saglia R.P., Bender R. et al., 2009, *Dark matter scaling relations and the assembly epoch of Coma early-type galaxies*, The Astrophysical Journal, 691, 1, 770. Cited on page 24.

Thomas J., Saglia R.P., Bender R. et al., 2011, *Dynamical masses of early-type galaxies: a comparison to lensing results and implications for the stellar initial mass function and the distribution of dark matter*, Monthly Notices of the Royal Astronomical Society, 415, 1, 545. Cited on pages 3, 17, and 24.

Tremaine S., Richstone D.O., Byun Y.I. et al., 1994, *A family of models for spherical stellar systems*, The Astronomical Journal, 107, 634. Cited on page 22.

Tremblay B. & Merritt D., 1995, *The Frequency Function of Elliptical Galaxy Intrinsic Shapes*, The Astronomical Journal, 110, 1039. Cited on pages 5 and 15.

Tremblay B. & Merritt D., 1996, *Evidence From Intrinsic Shapes for Two Families of Elliptical Galaxies*, The Astronomical Journal, 111, 2243. Cited on pages 5, 15, 47, and 77.

Tremblay B., Merritt D. & Williams T., 1995, *Planetary nebulae as probes of dark matter in NGC 3384*, Astrophysical Journal, Part 2-Letters, 443, 1, L5. Cited on page 10.

Treu T. & Koopmans L.V.E., 2004, *Massive Dark Matter Halos and Evolution of Early-Type Galaxies to* $z \approx 1$, The Astrophysical Journal, 611, 2, 739. Cited on page 10.

Trujillo I., Burkert A. & Bell E., 2004a, *The Tilt of the Fundamental Plane: Three-Quarters Structural Nonhomology, One-Quarter Stellar Population*, The Astrophysical Journal Letters, 600, L39. Cited on page 13.

Trujillo I., Erwin P., Asensio Ramos A. & Graham A.W., 2004b, *Evidence for a New Elliptical-Galaxy Paradigm: Sérsic and Core Galaxies*, The Astronomical Journal, 127, 4, 1917. Cited on page 8.

Tully R.B. & Fisher J.R., 1977, *A new method of determining distances to galaxies*, Astronomy and Astrophysics, 54, 661. Cited on page 13.

Valluri M., Merritt D. & Emsellem E., 2004, *Difficulties with Recovering the Masses of Supermassive Black Holes from Stellar Kinematical Data*, The Astrophysical Journal, 602, 1, 66. Cited on page 24.

Van De Ven G., De Zeeuw P.T. & Van Den Bosch R.C.E., 2008, *Recovery of the internal orbital structure of galaxies*, Monthly Notices of the Royal Astronomical Society, 385, 2, 614. Cited on pages 77, 83, and 133.

van den Bergh S., 2009, *Lenticular Galaxies and Their Environments*, The Astrophysical Journal, 702, 2, 1502. Cited on page 2.

van den Bosch R.C.E. & De Zeeuw P.T., 2010, *Estimating black hole masses in triaxial galaxies*, Monthly Notices of the Royal Astronomical Society, 401, 3, 1770. Cited on pages 17, 24, 58, 118, 119, and 134.

van den Bosch R.C.E., Gebhardt K., Gültekin K. et al., 2012, *An over-massive black hole in the compact lenticular galaxy NGC 1277.*, Nature, 491, 7426, 729. Cited on page 24.

van den Bosch R.C.E. & Van De Ven G., 2009, *Recovering the intrinsic shape of early-type galaxies*, Monthly Notices of the Royal Astronomical Society, 398, 3, 1117. Cited on pages 18, 77, 103, and 133.

van den Bosch R.C.E., van de Ven G., Verolme E.K., Cappellari M. & de Zeeuw P.T., 2008, *Triaxial orbit based galaxy models with an application to the (apparent) decoupled core galaxy NGC 4365*, Monthly Notices of the Royal Astronomical Society, 385, 2, 647. Cited on pages 18, 24, 32, 33, 36, 39, 51, 58, 61, 77, 81, 131, and 132.

van der Marel R.P., Cretton N., de Zeeuw P.T. & Rix H., 1998, *Improved Evidence for a Black Hole in M32 from HST /FOS Spectra. II. Axisymmetric Dynamical Models*, The Astrophysical Journal, 493, 2, 613. Cited on page 24.

van der Marel R.P. & Franx M., 1993, *A new method for the identification of non-Gaussian line profiles in elliptical galaxies*, The Astrophysical Journal, 407, 525. Cited on page 9.

Verolme E.K., Cappellari M., Copin Y. et al., 2002, *A SAURON study of M32: Measuring the intrinsic flattening and the central black hole mass*, Monthly Notices of the Royal Astronomical Society, 335, 3, 517. Cited on page 24.

Vincent R.A. & Ryden B.S., 2005, *The Dependence of Galaxy Shape on Luminosity and Surface Brightness Profile*, The Astrophysical Journal, 623, 1, 137. Cited on pages 15, 47, 77, and 117.

Wilkinson A. & James R.A., 1982, *A stationary and a slowly rotating model of a triaxial elliptical galaxy*, Monthly Notices of the Royal Astronomical Society, 199, 2, 171. Cited on page 16.

Wilkinson A., Sharples R.M., Fosbury R.A.E. & Wallace P.T., 1986, *Stella dynamics of Cen A*, Monthly Notices of the Royal Astronomical Society, 218, 2, 297. Cited on page 10.

Williams T.B., 1981, *Spectroscopy, surface photometry, and three-dimensional models for NGC 596*, The Astrophysical Journal, 244, 2, 458. Cited on pages 15 and 36.

Williams T.B. & Schwarzschild M., 1979, *A photometric determination of twists in three early-type galaxies*, The Astrophysical Journal, 227, 56. Cited on page 15.

Wilson C.P., 1975, *Dynamical models of elliptical galaxies*, The Astronomical Journal, 80, 175. Cited on page 22.

Wilson G., Kaiser N., Luppino G. & Cowie L., 2001, *Galaxy Halo Masses from Galaxy-Galaxy Lensing*, The Astrophysical Journal, 555, 572. Cited on page 10.

Winsall M.L. & Freeman K.C., 1993, *Velocity distributions in spherical elliptical galaxies. II - Measuring line-of-sight stellar velocity distributions*, Astronomy and Astrophysics, 268, 443. Cited on page 9.

Ziegler B.L. & Bender R., 1997, *The Mgb- relation of elliptical galaxies at z 0.37*, Monthly Notices of the Royal Astronomical Society, 291, 3, 527. Cited on page 14.

Acknowledgments

I would like to thank Ralf Bender and my thesis supervisors Roberto Saglia and Jens Thomas for giving me the opportunity to work on this exciting project at a world-class institute as the Max Planck Institute for Extraterrestrial Physics (MPE) and for proofreading and improving this dissertation. I am thankful to Alexey Krukau and Frederik Beaujean for the technical assistance and the support with the C^{2}PAP cluster and the parallelisation of the code. A special thanks goes also to all the members of the OPINAS group, in particular to Francesco Montesano, Matteo Fossati, Jeffrey Chan, Peter Erwin and Ximena Mazzalay.

I am very grateful to my fellow officemates Jiamin Hou, Martha Lippich, Michael Opitsch, Salvador Salazar, Jan Grieb, Sandesh Kulkarni and Kianusch Mehrgan for the nice working atmosphere and the lively discussions about other things than science. I am grateful also to Matias Blaña, Jethro Ridl, Christopher Wegg, Manuel Behrendt, Carolina Agurto, Corina Tataru, Matthieu Portail, Mohit Tanga, Florian Hofman, Claudia Pulsoni, Angeles Pérez, Anna Brucalassi, Laura Morselli, Alessia Longobardi, Sotiris Chatzopoulos, María José Bustamante, Alessandro Ballone, Torben Simm, Jonathan Clarke and Shola Wylie for their constant support and friendship and the many lunch, coffee and tea breaks that provided an always much needed distraction. I would like to acknowledge in particular Isabella Söldner-Rembold for the N-body triaxial reference model she so kindly provided. I would also like to thank all the members of the group MCC (Monaco Che Conta) and Marco Häuser, Alexander Arth, Ralph Müller, Thomas Maier, Björn Sörgel and Dominika Boneberg for being a constant and reliable presence in these many years in Munich.

Last by not least I would like to thank my friends back home Andrea, Gianluca, Filippo and Orso for being always there, regardless of the time and distance. I thank Dario and Valentina for the many relaxing moments we spent together. My gratitude goes also to my uncles, aunts, cousins, my grandparents and to my sister Nicoletta and my parents-in-law Cesare and Luisa. They all never missed the opportunity of supporting and encouraging me. My deepest gratitude goes to my wife Federica for being always by my side throughout this PhD and for her constant motivation and inspiration. I thank my parents Maurizio and Pina for the fantastic opportunities they have given me to pursue my dreams.

This research was supported by the DFG cluster of excellence ‘Origin and Structure of the Universe’ (`www.universe-cluster.de`).